THE UNIVERSITY *of* EDINBURGH

Searches for new physics using low energy electron recoils in the LUX and LZ experiments

Elizabeth Leason

Doctor of Philosophy
The University of Edinburgh
June 2021

Abstract

There is evidence, on a range of astrophysical and cosmological scales, that most of the matter in the universe is comprised of invisible dark matter. The particle nature of this dark matter is inconsistent with the Standard Model (SM) of particle physics and, along with other unexplained phenomena, implies the existence of new physics beyond the SM. A range of dark matter models and SM extensions exist, predicting a broad range of new phenomena. One popular dark matter candidate is Weakly Interacting Massive Particles (WIMPs), but after several decades of experimental efforts there has been no conclusive detection. As a result, there is increased interest in alternative models, such as axions or hidden sector dark matter, motivating broader search strategies.

Direct detection experiments typically aim to detect WIMPs scattering off nuclei in a terrestrial detector. However, they can also be used to search for electron recoil signals resulting from other new physics models. The LUX experiment, and its successor LUX-ZEPLIN (LZ), use xenon dual phase time projection chamber technology to search for dark matter.

In this work the mirror dark matter (MDM) model will be examined, with the world's first direct detection search for MDM, using LUX data. The result, published in Physical Review D [1], rules out much of the allowed parameter space for this model. LZ will have a larger exposure and lower backgrounds than LUX, giving improved sensitivity to rare events. A general approach for low energy electron recoil analyses in LZ has been used to find projected confidence limits for seven signal models, preprint [2]. The solar axion and MDM analyses will be described in detail here. If a new physics signal is detected it is important to characterise the model, often involving multiple model parameters. In this work a Bayesian approach is investigated for analysis with multiple parameters of interest, using a solar axion analysis as a test case.

Lay Summary

Cosmological and astrophysical observations show an inconsistency between the calculated total mass of matter in the universe and the mass contained in the stars, dust etc. that we can see. This indicates that 84% of the mass of the universe is invisible — it does not emit or absorb light. The current best understanding of particle physics, the Standard Model (SM), does not contain any particle which can explain dark matter. Whilst it successfully explains most phenomena in particle physics, there is increasing evidence that the SM is not the full picture. Therefore, the big question confronting cosmology and particle physics today is the nature of the new physics beyond the SM and how dark matter fits into this.

There are many possible theories and many ways they can be tested, this work aims to investigate a small part of this space. Specifically, direct detection experiments — aiming to detect dark matter passing through the Earth, via its interaction with atoms in an experiment. The LUX and LZ experiments are the focus of this work, these are large liquid xenon detectors located deep underground used to carry out dark matter searches. Whilst the most commonly studied dark matter candidate is the Weakly Interacting Massive Particles (WIMPs), this is not the only appealing model and many others exist including much lighter axions and hidden sector particles.

In this work, data from the LUX experiment is used to carry out the first direct detection search for mirror dark matter (MDM), a hidden sector model with specific symmetry to the SM. Following this, the expected sensitivity of the upcoming LZ experiment to MDM, and other dark matter models which give similar signals, is studied. If a signal is discovered it is important to determine which model it comes from and what the properties are. The final part of this thesis looks at a Bayesian approach to characterising possible signals with multiple parameters.

Declaration

I declare that this thesis was composed by myself, that the work contained herein is my own except where explicitly stated otherwise in the text, and that this work has not been submitted for any other degree or professional qualification except as specified.

Chapter 4 – 6 highlight the original work of this author. I led the analysis in Chapter 4 — a search for mirror dark matter using LUX data. The data used was collected by the LUX collaboration prior to the start of this PhD. I developed the analysis framework used for the LZ low energy electron recoil searches in Chapter 5. This uses some of the same principles and common tools with the low energy nuclear recoil WIMP search. I was responsible for the mirror dark matter and solar axion analyses, whilst the other five searches were the work of others using the framework. The work in Chapter 6 used and extended the Bayesian analysis capabilities of the LZ statistical analysis package. I led this work and the tools are now available for the whole collaboration to use.

Parts of this work have been published in [1, 2].

(*Elizabeth Leason, June 2021*)

Acknowledgements

To acknowledge everyone who played a part in this journey would be impossible. I am grateful to so many people, from those who inspired me to do physics and this PhD, to those who listened to me moan about it over a run or coffee. I will try to avoid listing people for fear of missing someone out, but that does not diminish my gratitude.

First and foremost, I would like to thank my supervisor Alex Murphy, for providing invaluable guidance and a wealth of knowledge. His confidence in me, often exceeding my own, encouraged me to make the most of opportunities throughout the PhD. As part of the EdiDM group I have had the opportunity to meet and work with some fantastic people, many thanks to every one of them. Especially to Maria Francesca for getting me started with analysis, Xin for introducing me to cleanroom life and Athoy for companionship day in, day out. More widely I would like to thank the PPE group in Edinburgh for making me feel so welcome, providing a cheerful and supportive work environment.

One of the great privileges of the past few years has been collaborating with so many talented members of LUX and LZ. Again, I was welcomed right from the beginning and have had an invaluable source of help and support. Thank you for teaching me so much — especially during visits to Berkely and onsite in South Dakota. I want to specifically thank Quentin Riffard for helping with the LUX analysis, Scott Hertel for guiding the low energy ER work (never missing a detail in my plots) and Ibles Olcina for helping me untangle Bayesian statistics,

Outside of physics I want to thank friends for their support from near and afar. Friends from growing up in Glossop, undergraduate days in Durham and here in Edinburgh have kept me going and I indebted to all of you. In Edinburgh, Carnethy running club immediately made me feel at home and has been one of the highlights of life here. I have met incredible people and explored great places — gaining friends and memories that will last a lifetime.

I am thankful to my family for being a constant source of support and giving me the confidence to be ambitious. But importantly, thank you to my parents and siblings for teaching me to laugh at myself.

Above all thank you to Dominic for being by my side every step of the way.

Contents

List of Figures

List of Tables

Chapter 1

Introduction

Particle physics, cosmology and astrophysics today all face an unresolved problem — the nature of dark matter. Evidence on a range of astrophysical scales has uncovered a gravitationally interacting, non-luminous substance, which makes up 84% of the mass of the universe. However, the nature of dark matter remains a mystery and only the amount of it is conclusively known, along with some general constraints from observations. With many macroscopic candidates ruled out, the most common assumption is that dark matter consists of one or more fundamental particles. The Standard Model (SM) of particle physics does not contain any suitable candidates, strongly suggesting the need for new physics beyond the SM. Additional evidence that the SM is incomplete arises in various experimental and theoretical problems — indicating that it is part of a bigger underlying theory which could also explain dark matter.

In this chapter the evidence for dark matter will be reviewed, along with the problems in the SM that together build a picture of the need for a new underlying theory in particle physics. Chapter 2 discusses the approaches to solving these problems, starting with the requirements for dark matter models and the ways models can be constructed. Specific dark matter models will be discussed, beginning with the most popular WIMP and axion dark matter models, then considering other hidden sector and effective field theories. Any proposed model should be tested to rule out or confirm its existence and establish the relevant parameters. Chapter 2 ends with a review of the complimentary methods used to probe dark matter and new physics models.

Chapter 3 focuses on the direct detection approach, searching for dark matter

interactions in terrestrial experiments. Large noble liquid experiments have led this effort over the past decade and this technology will be discussed in detail, in particular the LUX and LUX-ZEPLIN(LZ) xenon experiments.

Chapters 4 – 6 go through a chronology of possible non-WIMP dark matter searches, carried out by this author, using low energy electron recoil events to probe lower mass particles in these experiments.

In Chapter 4 the first ever direct detection search for mirror dark matter is presented. The phenomenology of mirror dark matter detection is discussed, including new calculations of the effects of Earth capture and shielding. Then the data taking and analysis are described, resulting in a limit on mirror dark matter kinetic mixing, which rules out much of the allowed parameter space for the theory.

LUX will be replaced by the next generation LZ experiment and Chapter 5 presents the sensitivity of LZ to a broader range of models, which could result in a low energy electron recoil signal. Here, a common analysis framework is used to determine the sensitivity of LZ to a variety of models. Modelling of electron recoils in liquid xenon, background simulations and statistical approaches to limit setting and discovery are also discussed.

In the case of discovery of one of these models it is important to characterise the signal, often determining multiple model parameters. Chapter 6 investigates a Bayesian approach to signal characterisation, which is particularly powerful in the case of models with multiple free parameters or multiple components. However, it could also be used to distinguish between multiple low energy electron recoil models which give similar signals.

Finally, Chapter 7 summaries the findings of this thesis, discussing the conclusions and future outlook.

1.1 Dark Matter History

Whilst discussions of dark matter generally begin with Zwicky in 1933, the term "dark matter" was coined by Poincare in 1906 and research in this area had been going on for over a century beforehand [3]. John Michell proposed, in 1783, that if light is affected by the laws of gravity there could exist objects whose

gravitational field was too strong for light to escape — invisible astrophysical objects later known as black holes. In 1904, Lord Kelvin had the idea that velocities of stars in a galaxy can be used to infer the density of the galaxy. An idea which was applied to the Milky Way by Poincare in 1906, it was here that the term "dark matter" was first seen — describing the extra non-luminous matter that these measurements suggested.

Jan Oort carried out the first kinematic analysis of local stars in 1932 and Fritz Zwicky used the virial theorem to determine the mass of the Coma galaxy cluster in 1933 (Section 1.2.2). He found that this did not match the mass observed in luminous matter and proposed that there must be additional non-luminous matter. In the 1970s measurements of galaxy rotation curves provided further evidence for dark matter and the idea became more widely accepted. These began with the measurement of the M31 galaxy rotation curve by Vera Rubin and Kent Ford in 1970, followed by measurements of M33, NGC300, IC342, M101 and NGC6946 throughout the decade [4].

This initiated efforts across multiple disciplines to better understand the dark matter — from observational astronomy to theory and cosmology, then particle physics. Over the past several decades a variety of independent estimates of the matter density of the universe, described in Section 1.2, point to a large non luminous, non baryonic component. In parallel to this many theories for the nature of dark matter were proposed, (Sections 2.2,2.3) and experiments constructed to search for them (Section 2.4). Interplay between these fields is key, with developments in one area informing another. In Chapters 4 – 6 the latest developments in one branch of the experimental efforts will be described, with searches for dark matter and new physics using low energy electron recoil signals in large xenon based direct detection experiments.

1.2 Dark Matter Evidence

1.2.1 Galaxy Rotation Curves

Evidence for dark matter exists across a range of astrophysical scales. On a galactic scale galaxy rotation curves show the circular velocity profile of stars and gas as a function of distance from the galactic centre. Given Newtonian dynamics gravity must equal centripetal acceleration in circular orbits. This

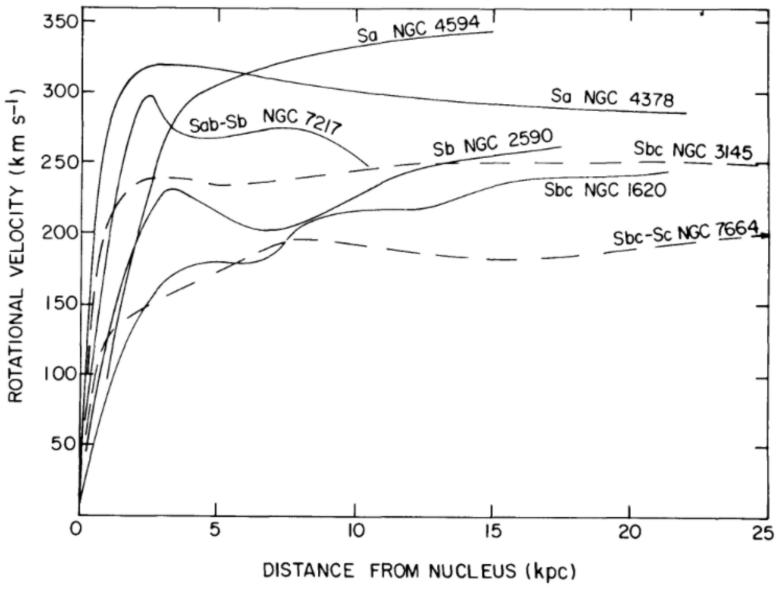

Figure 1.1 *Rotation curves of seven galaxies observed by Rubin and Ford, all showing constant trend at large radii, taken from Ref. [4].*

gives the velocity of gravitationally bound objects at radius r:

$$v(r) = \sqrt{\frac{GM(r)}{r}}, \tag{1.1}$$

where $M(r) = 4\pi \int \rho(r) r^2 dr$ is the mass enclosed at some radius r. Luminous matter is observed to be concentrated at the centre of the galaxy, so $M(r)$ is expected be constant at large radii and the velocity would fall as $v \propto r^{-1/2}$. But observations show rotation curves to be flat at large radii as seen in the curves made by Rubin and Ford, shown in Fig. 1.1. This can be explained if there is another mass component with $M(r) \propto r$, forming a spherical halo of non-luminous matter that extends much beyond the galactic disk. The different distribution of dark matter in the galaxy was the first strong evidence of dark matter with very different behaviour and properties to ordinary matter — rather than a dark phase of ordinary matter.

1.2.2 Galaxy Clusters

There is also evidence for dark matter on the scale of clusters of hundreds to thousands of gravitationally bound galaxies. Different methods can be used to

determine the mass of cluster: applying the virial theorem to galaxy velocities, X-ray emission or weak gravitational lensing.

The virial theorem states that the potential energy is twice the kinetic energy for a system in virial equilibrium, $2K = |U|$. Kinetic energy is given by:

$$K = \frac{1}{2}\sum mv^2 = \frac{1}{2}M\sigma^2, \tag{1.2}$$

where m and v are the mass and velocity of a given galaxy. Assuming that all N cluster galaxies have the same mass m the total cluster mass is $M = Nm$ and σ is the velocity dispersion. The total potential energy is given by:

$$|U| = \sum_{i=1}^{N} < \bar{r}_i \cdot \bar{F}_i >, \tag{1.3}$$

where $\bar{F}$ is the total force on the ith particle at position $\bar{r}_i$

In 1933 Zwicky first estimated the mass of the Coma cluster as the product of the 800 observed galaxies and the typical mass of a galaxy, 10^9 solar masses ($M_\odot$) [5]. Then the potential energy was calculated, assuming a physical size of 10^6 light years for the cluster. Using the virial theorem to infer the kinetic energy from this, and assuming the previously estimated mass, the expected velocity dispersion was 80 km/s. However this was much smaller than the observed velocity dispersion of 1000 km/s. As a result, Zwicky concluded that there must be much more dark matter than luminous matter in the cluster in order to account for the much higher velocity dispersion.

Zwicky carried out a second analysis in 1937, using the virial theorem to find a lower limit on the average mass of individual galaxies in the cluster [6]. This time, assuming 1000 galaxies in a 2×10^6 light year radius, with velocity dispersion 700 km/s, Zwicky calculated the potential energy and solved for the galaxy mass. The resulting average mass of $4.5 \times 10^{10} M_\odot$ per galaxy gave a mass-to-light ratio of ~ 500, assuming average luminosity of 8.5×10^7 solar luminosity ($L_\odot$). This was ~ 5 times greater than the mass-to-light ratio for the Milky Way, implying again that the cluster contained much more mass than that in luminous objects. A similar study by Smith, investigating the Virgo cluster in 1936, also found a higher than expected mass per galaxy and a mass-to-light ratio of ~ 200 [7].

Measurements of X-rays emitted by hot gas in clusters, by thermal Bremsstrahlung, provide further evidence for dark matter in galaxy clusters. For a gas in

hydrostatic equilibrium:

$$\frac{dP}{dr} = -G\frac{M(r)\rho(r)}{r^2}, \tag{1.4}$$

where $M(r)$ is the total mass contained within radius r and $\rho(r)$ is the gas density. For an ideal gas pressure is given by:

$$P = \frac{\rho kT}{\mu m_p}, \tag{1.5}$$

where T is temperature, m_p is proton mass and μ is the mean molecular weight (≈ 0.6 for an ionised plasma). Combining these two equations, the observed X-ray gas temperature can be used to find the cluster density and mass, giving a mass (1 - 2)$\times 10^{15} M_\odot$ from all hot gas and galaxies in the Coma cluster [8]. This can be compared to the mass of stars inferred from observed luminosity, plus the mass of gas inferred from X-ray emissivity. Again the total mass is greater than that observed in stars and gas, providing evidence for dark matter in clusters. For example Ref. [9] finds a total baryon fraction of 13.6% for 12 galaxy clusters at $z \sim 0.1$ with masses $M = (1 - 5) \times 10^{14} M_\odot$.

1.2.3 Gravitational Lensing

Further evidence on the scale of galaxy clusters comes from measurements of cluster mass using gravitational lensing — distortions in the paths of photons due to mass in between the source and observer. Photons propagate along null geodesics (straight line paths) in spacetime causing apparent curvature of their trajectory if passing a massive object, which distorts spacetime. The resulting deflection angle is given by [10]:

$$\hat{\alpha} = \frac{4GM}{c^2\zeta}, \tag{1.6}$$

for a ray of light deflected off the exterior of a spherically symmetric mass M with impact parameter ζ. Deflection of multiple light rays, converging them towards a point, means the mass between the source and observer effectively acts as a lens. The extent of the lensing depends on the relative positions of the source, lens and observer as well as the mass and shape of the lens. Strong lensing, when the mass is high and angular separation small, gives multiple images and arcs. Weak lensing results from smaller masses and larger separations, giving distortions and small magnifications. This is studied statistically with averages over ensembles

of many galaxies. Microlensing occurs on the scale of stars where the observed brightness of an object fluctuates due to changes in the allignment with respect to a mass. All types of lensing can be used to probe the projected mass profile of clusters; strong lensing in the central regions and weak lensing allowing mass measurements out to larger radii.

Another key use of weak lensing observations was studies of the "bullet cluster" (1E0657-558) merger, where two galaxy clusters at z = 0.296 collided [11]. Cluster mass is comprised of: $\sim 1 - 2\%$ galaxies, $\sim 5 - 15\%$ hot baryonic plasma, which emits X-rays, and the rest is postulated to be dark matter. When the cluster exists in isolation these three components are expected to form similar symmetric distributions, tracing the gravitational potential. But during a merger of two clusters the galaxies are expected to behave as collision-less point particles whilst the plasma behaves like a fluid, experiencing ram pressure. This should result in spatial decoupling of the galaxies and plasma, as interactions cause the plasma to slow down. If the cluster does not contain any dark matter the gravitational potential would trace the dominant matter component — the plasma. Whereas for a cluster containing dark matter, which would be coincident with the galaxies, the gravitational potential would trace this component.

Weak lensing was used to map the gravitational potential of the clusters by measuring the distortion of images of background galaxies. The baryonic matter was imaged in visible light and the plasma in the clusters was imaged in X-rays — then the maps were compared, as shown in Fig. 1.2. For the IE0657-558 merger it was found that the two peaks in the potential map were offset at $\sim 8\ \sigma$ from

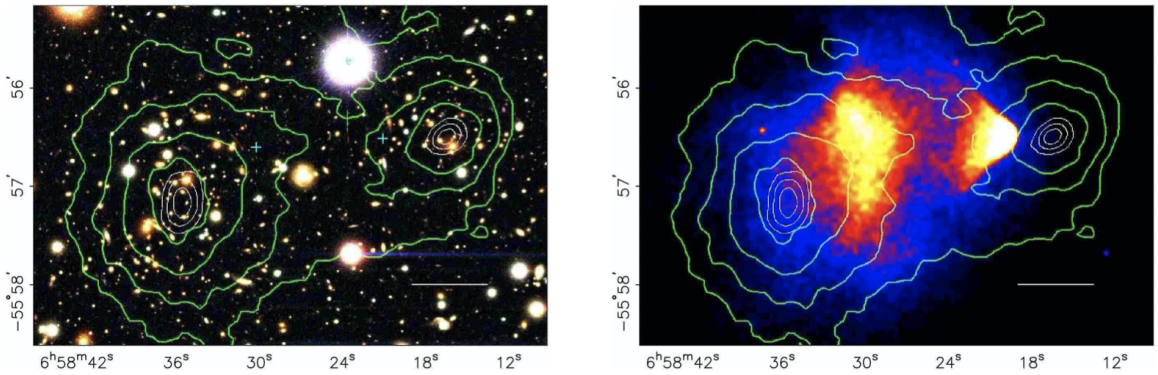

Figure 1.2 *Images of the 1E0657-558 cluster merger, taken from Ref. [11]. Left shows the colour image in visible light and right shows the X-ray image, both have green contours from weak lensing indicating gravitational potential.*

the centre of mass of the plasma clouds [11]. This provided evidence that most of the mass is not in the plasma component of the cluster, suggesting a dark matter component. Compared to the evidence for dark matter considered so far this is unique as it is independent of any assumptions about gravity.

1.2.4 Cosmic Microwave Background

Evidence for dark matter is present on cosmological scales in the Cosmic Microwave Background (CMB) — microwave radiation originating from the epoch of recombination [12]. Following its prediction in the 1940s, this nearly isotropic background of microwave photons was first discovered by Wilson and Penzias in 1965 [13].

Prior to recombination, photons are coupled to the ionised plasma, constantly scattering off free electrons. Once the temperature of the universe cooled to $\sim$ 3000 K (approximately 380,000 years after the big bang), free protons and electrons could form neutral hydrogen atoms. At this point photons decouple from the plasma and propagate freely through the universe. These photons are visible today, however they have been significantly redshifted due to the expansion of the universe.

The COBE experiment measured the temperature and uniformity of the CMB in the 1990s, finding a near perfect blackbody spectrum with temperature $\sim$ 2.7 K [14]. However, a full sky map of the CMB, accounting for galactic sources and dipole effects, showed very faint anisotropies in the CMB at the level of one part per 10,000. In the 2000s, the WMAP experiment refined measurements of the anisotropies and determined cosmological parameters using properties of the CMB power spectrum [15]. These measurements were further refined by the Planck experiment, mapping the CMB across the entire sky with unprecedented angular resolution [16]. The resulting map, in Fig. 1.3, shows that the CMB now corresponds to a black body spectrum with a temperature of 2.726 K and has been found to be isotropic at a 10^{-5} level. Foreground emission in the galactic plane can disturb CMB observations, so a mask is applied — as indicated by the grey lines in Fig. 1.3.

The observed temperature anisotropies arise from temperature and density fluctuations at the last scattering surface when recombination occurs. A conflict between inward gravitational attraction and photon pressure outwards lead to

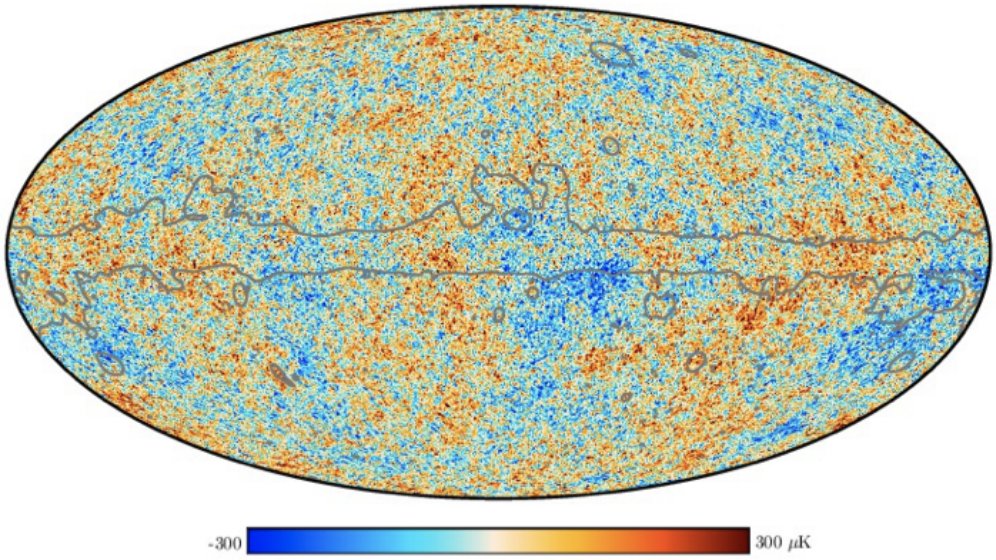

(a) *All sky temperature map of CMB anisotropies, with grey lines indicating the masked region around the galactic plane.*

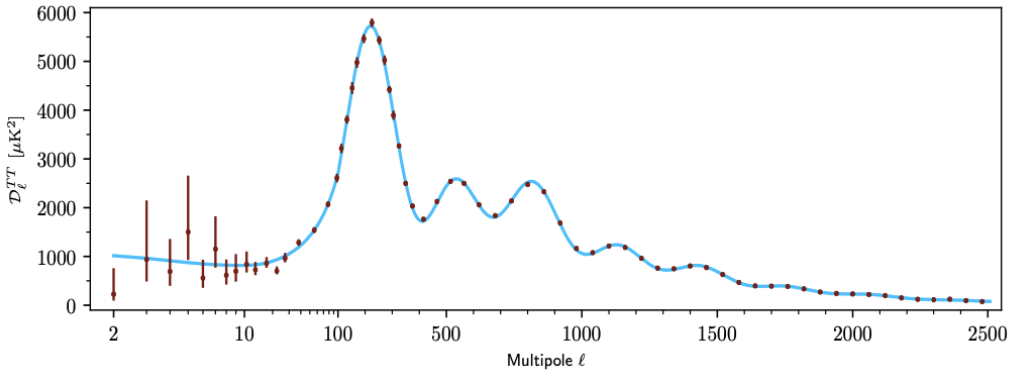

(b) *Angular power spectrum of primary anisotropies.*

Figure 1.3 *Planck 2018 results, taken from Ref. [16], which use data taken between 2009 and 2013.*

acoustic oscillations, which continued until the universe became transparent to photons. The magnitude of the acoustic oscillations is damped by viscosity and heat conduction in the fluid. These small temperature anisotropies can be used to determine cosmological parameters, by fitting a cosmological model with a fixed number of parameters to the observed power spectrum of temperature fluctuations.

The lower part of Fig. 1.3 shows the angular power spectra of the primary anisotropies measured by the Planck experiment [16]. Fitting of the peaks and parameters can be used to determine cosmological characteristics. The

broad peak at $l \approx 220$, and the subsequent peaks, result from the acoustic oscillations, with the odd numbered peaks showing baryon gravitational collapse and the even ones pressure expansion. Since decoupling and recombination are not instantaneous the oscillations continue whilst the fraction of baryons in the coupled fluid increases, resulting in higher odd peaks compared to even. The oscillation froze out when all photons were eventually released.

The angular spectrum can be fitted to a full cosmological model to determine parameter values. In general the position of the first peak gives information about the curvature of the universe, the second peak the baryon density and the third peak the dark matter density. WMAP and Planck have used this approach to determine cosmological parameters from CMB anisotropies, with the most recent Planck results, [16], giving density parameters:

$$\Omega_m = 0.3153 \pm 0.0073, \quad \Omega_b = 0.0493 \pm 0.0002. \tag{1.7}$$

This indicates that 31.53% of the energy density of the universe consists of matter, with only 4.93% of this being baryonic matter. As a result it can be inferred that $(1 - 4.93/31.53) = 84.36\%$ of matter is the universe is dark matter, as mentioned at the beginning of this chapter.

1.2.5 Big Bang Nucleosynthesis

The baryon density of the universe can be determined using big bang nucleosynthesis (BBN), which describes the production of light elements: D, ^{3}He, ^{4}He and ^{7}Li, in the early universe when $T \sim 100$keV. Abundances of the light elements can be predicted based on known SM processes and compared to abundances determined using spectroscopic measurements of various astrophysical targets (quasars for D, extra galactic ionised regions for ^{4}He and metal poor stars for ^{7}Li). The production and decay rates depend on the density of baryons, usually expressed relative to the relic blackbody photon density $\eta = n_b/n_\gamma$. Higher baryon density means deuterium production starts earlier, so the yield of ^{4}He, ^{7}Li is increased. For standard BBN with three neutrino species η is the only free parameter, so any abundance measurement can be used to constrain η, with additional measurements as consistency checks. The concordant range of η from D and ^{4}He measurements gives baryon density parameter range:

$$0.046 \leq \Omega_b h^2 \leq 0.053, \tag{1.8}$$

which is in agreement with the CMB measurement.

1.2.6 Large Scale Structure

The observed baryonic density fluctuations in the CMB at recombination are $\delta\rho_b/\rho_b|_{rec} \sim 10^{-5}$. If these grew linearly with scale factor we would expect fluctuations of $\sim 10^{-2}$ today, inconsistent with the large scale inhomogeneities and structure observed in the universe $\delta\rho_b/\rho_b|_{obs} \gg 1$. However, if there is a dominant non-relativistic, pressureless dark matter component which decouples before recombination it can grow to larger perturbations, allowing faster gravitational collapse and forming the observed structure.

The evolution of structure in the universe is very complex to model — the most common approach is the use of numerical N-body simulations e.g. the "Millenium simulation" carried out by the Virgo consortium [17]. This simulation assumes dark matter is made up of elementary particles that only interact gravitationally, following $2160^3 \approx 10^{10}$ particles through progressive redshifts from $z = 127$ to the present day. The structure formed by gravitational amplification of small density fluctuations in the early universe gives a complex "cosmic web" topology. Comparisons of galaxy clustering properties from the simulation results with survey data, from both high and low redshifts, allows cosmological model and dark matter parameters to be tested.

1.3 ΛCDM Model

The Standard Model of cosmology is a comprehensive cosmological model for big bang cosmology, CMB observations and dark matter. This is based on a universe that originates from a hot big bang then expands, so that it is now statistically uniform on large scales. Three main components of dark energy, dark matter and ordinary matter populate the universe and gravity is governed by general relativity.

The statistical homogeneity and isotropy of the universe can be described using the space time metric:

$$ds^2 = -c^2dt^2 + a(t)^2\left(\frac{dr^2}{1-kr^2} + r^2d\Omega^2\right). \tag{1.9}$$

This relates the spacetime interval ds to time t and spatial (r, Ω) coordinates, where $d\Omega = d\theta^2 + \sin^2\theta d\phi^2$. Time dependence of the spatial part comes from the dimensionless scale factor $a(t)$ which is used to determine proper distances in comoving coordinates and k is a constant describing the curvature of the universe. The Einstein equations relate the geometry of the universe to its matter and energy content:

$$R_{\mu\nu} - \frac{1}{2}g_{\mu\nu}R = -\frac{8\pi G_N}{c^4}T_{\mu\nu} + \Lambda g_{\mu\nu}. \tag{1.10}$$

Here, $R_{\mu\nu}$ is the Ricci tensor, R is Ricci scalar, $T_{\mu\nu}$ is the energy momentum tensor, Λ is the cosmological constant and $g_{\mu\nu}$ is the spacetime metric. This means the right left hand side describes the geometry of the universe, relating it to the energy content described by the right hand side. For a perfect fluid: $T_{\mu\nu} = -pg_{\mu\nu} + (p+\rho)u_\mu u_\nu$, where p is the isotropic pressure, ρ is the energy density and u is the velocity vector for the isotropic fluid in co-moving coordinates.

The Einstein's equations for a perfect fluid give the Friedmann equations:

$$H^2 = \left(\frac{\dot{a}}{a}\right)^2 = \frac{8\pi G_N \rho}{3} - \frac{k}{a^2} + \frac{\Lambda}{3}, \tag{1.11}$$

$$\frac{\ddot{a}}{a} = \frac{\Lambda}{3} - \frac{4\pi G_N}{3}(\rho + 3p), \tag{1.12}$$

where $H(t)$ is the Hubble parameter. From this the critical density, which results in a flat universe (k=0), can be determined:

$$\rho_{crit} = \frac{3H^2}{8\pi G_N}. \tag{1.13}$$

This critical density can be used to define the energy density of a given species:

$$\Omega_i = \frac{\rho_i}{\rho_{crit}}. \tag{1.14}$$

The total energy density is given by: $\Omega = \sum_i \Omega_i$, and from the Friedmann equation we can write: $\Omega - 1 = k/H^2a^2$. This shows that for:

- $\Omega < 1$ (or $\rho < \rho_{crit}$), $k = -1$: an open universe,
- $\Omega > 1$ (or $\rho > \rho_{crit}$), $k = +1$: a closed universe,
- $\Omega = 1$ (or $\rho = \rho_{crit}$), $k = 0$: a flat universe.

Different Ω_i evolve differently with time, depending on the equation of state of the

component: $\omega = p/\rho$. The different components can be distinguished with density parameters Ω_m for pressureless/ordinary matter, Ω_r for relativistic particles and Ω_Λ for vacuum energy. The matter component consists of both baryonic matter Ω_b and cold dark matter Ω_c.

In general the density and scale factor are related to the equation of state by; $\rho \propto a^{-3(1+\omega)}$ and $a(t) \propto t^{2/3(1+\omega)}$. For relativistic particles or radiation $\omega = 1/3$, giving the evolution of density $\rho_r \propto a^{-4}$ and scale factor $a(t) \propto t^{1/2}$. For pressureless gas or matter (i.e. ordinary baryonic matter or cold dark matter) $\omega = 0$, so the density evolves as $\rho_m \propto a^{-3}$ and scale factor as $a(t) \propto t^{2/3}$. This shows that even if radiation dominates in the early universe the matter density will dominate at later times due to faster growth. The vacuum energy Λ component $\omega = -1$ and ρ_ω is constant, so this will eventually dominate at late times.

The Standard Model of cosmology, or ΛCDM model, can be described by a set of parameters, with the smallest set being six parameters describing the universe in a way that can be compared to current cosmological data. These parameters include:

1. the density of baryons $\Omega_b h^2$,
2. the density of cold dark matter $\Omega_c h^2$,
3. the amplitude of adiabatic perturbations A_s,
4. the spectral index of adiabatic perturbations n_s,
5. the angular scale of acoustic oscillations θ_*,
6. optical depth of re-ionisation τ.

Here, the two densities are given in terms of the reduced Hubble constant $h = H/(100 \text{ km s}^{-1}\text{Mpc}^{-1})$. This set of parameters is not unique, the cosmological model can also be described in terms of parameters derived from these. Fitting equations describing the cosmological model to the measured power spectrum of CMB anisotropies allows determination of the parameters, as done using the Planck experiment [16], giving $\Omega_b \sim 0.0493$ and $\Omega_c \sim 0.2642$.

Dark matter can be produced thermally or non-thermally in the early universe, or it can result from particle-antiparticle asymmetry. Thermal production can occur via freeze out, with particle species decoupling when the interaction rate drops

below expansion rate. Particles which freeze out when relativistic are hot thermal relics and those which freeze out when non-relativistic are cold thermal relics. The Boltzmann equation governs the time evolution of the number density of a species pair annihilating with particles in the thermal bath by two-two processes. An approximate numerical solution of the Boltzmann equation gives the relic density of cold dark matter:

$$\Omega_\chi h^2 \approx \frac{3 \times 10^{-27} \mathrm{cm}^3 \mathrm{s}^{-1}}{\langle \sigma v \rangle}. \tag{1.15}$$

This is a function of the product of the thermally averaged cross section and relative velocity $\langle \sigma v \rangle$. For the relic density to match the Planck value of 0.0493 the value must be $\langle \sigma v \rangle \sim 3 \times 10^{-26}$ cm^3 s^{-1}.

An alternative thermal production mechanism is freeze in, where particles in equilibrium in the thermal bath very slowly produce dark matter via decay or annihilation processes [18]. The coupling between the bath and the dark matter is so weak that, unlike freeze-out, the dark matter remains thermally decoupled and is never in equilibrium with the bath. As the temperature of the universe drops, dark matter production will cease once the temperature of the thermal bath drops below the dark matter mass, fixing the dark matter abundance. In contrast to freeze out, there is initially negligible dark matter density and it builds up gradually. This means that stronger coupling will lead to higher abundance, as more dark matter is produced, whilst in freeze out higher coupling reduces the abundance as equilibrium is maintained to a lower temperature.

Non-thermal production occurs via processes which are not in thermal equilibrium, such as particle decay or topological or gravitational effects. For asymmetric dark matter the relic abundance comes from from asymmetry between DM and anti-dark matter (which may or may not be related to baryon anti-baryon asymmetry).

The evidence outlined above indicates the presence of dark matter in the universe and this in turn is required in the cosmological model in order reproduce the observed universe. Very little is known about the nature of the dark matter, but it is most commonly considered to be a new fundamental particle or particles — required properties and possible models will be discussed in Sections 2.1 – 2.3.

1.4 Standard Model of Particle Physics

The Standard Model of cosmology requires extensions to the Standard Model of particle physics to explain the presence of dark matter and dark energy.

During the 20th century elementary particle physics evolved, simultaneously but completely separately to the developments in dark matter observations, leading to the Standard Model of particle physics. Beginning with J.J. Thomson's discovery of the electron in 1897 and Planck's work on photons in 1900, further theoretical and experimental work deepened the understanding of fundamental particles and forces. Hypothesized particles were discovered and unexpected particles explained with new properties and symmetries, culminating in the SM; twelve matter fermions with interactions via three fundamental forces mediated by bosons.

Matter fermions have half integer spin, with fundamental fermions having spin 1/2 and composite particles having a combination of constituent fermion spins. The fundamental fermions are six quarks and six leptons, arranged in three generations each containing two quarks, a charged lepton and a lepton neutrino. Each fermion has an associated antifermion with opposite quantum numbers. Quarks combine to form hadrons — either baryons containing three quarks or mesons containing a quark and an antiquark. Charged leptons carry $\pm$1e charges, whilst quarks have +2/3e or -1/3e charges, resulting in $\pm$1e or 0e in hadrons. Strong interactions are mediated by eight gluons and electroweak by photons, $W^{\pm}$, Z and Higgs. Bosons have integer spin, with the Higgs having spin 0 and the others having spin 1. This makes the Higgs boson, discovered in 2012 by the ATLAS and CMS experiments the only fundamental scalar and it provides the mechanism by which the $W^{\pm}$, Z bosons and charged fermions acquire masses.

The theory has a $SU(3)_C \times SU(2)_L \times U(1)_Y$ gauge structure, with the $SU(3)_C$ group for strong interactions and $SU(2)_L \times U(1)_Y$ for electroweak interactions. In total there are 19 free parameters for the gauge couplings, masses and mixings of these particles and interactions.

1.5 Physics Beyond the Standard Model

1.5.1 Evidence for New Physics

The SM explains physics on the fundamental level and successfully describes many experimental results, with the discovery of the Higgs boson in 2012 by the ATLAS and CMS experiments verifying its final predicted particle [19, 20]. However, there are also indications that it is not the full picture and new physics beyond the SM must exist. Phenomena which cannot be explained by the SM include; neutrino masses, matter-antimatter asymmetry, cosmological inflation, dark energy and the problem of dark matter introduced above.

Neutrino masses: Neutrinos are neutral leptons in the SM which do not have strong or electromagnetic interactions, with one corresponding to each charged lepton. Neutrinos are produced via weak interactions in flavour eigenstates, which can also be written as superpositions of mass eigenstates: $|\nu_\alpha\rangle = \sum_i U_{\alpha i}|\nu_i\rangle$, for flavours α and masses i, where U is the PMNS matrix. The flavour eigenstates will oscillate if at least one has mass, however in the SM there are no neutrino masses (as the absence of right handed neutrinos means there is no Yukawa term, which generates fermion masses). Observation of neutrino flavour oscillations is now well established using a variety of neutrino sources and detection techniques e.g. studies of solar neutrinos with Super-Kamiokande [21] and SNO [22] or accelerator neutrinos using T2K [23]. This indicates that neutrinos have mass, however measurements of tritium β decay by the KATRIN experiment constrain this to be very small with $m_{\nu_e} < 0.8$ eV/c^2 [24]. Since neutrinos are massless in the SM this indicates that some extension to the theory is needed to explain the neutrino masses, how they are generated and why they are much smaller than those of quarks and charged leptons.

Baryon asymmetry: Each SM particle has an associated antiparticle with the same mass, but opposite quantum numbers. There is no observed astrophysical signature of matter–antimatter annihilation, which indicates negligible antimatter content in the universe. Also, equal numbers of baryons and antibaryons would result in a much lower baryon density than is observed now. However, the SM does not give any explanation for the baryon–antibaryon asymmetry, indicating the need for an extension which explains baryogenesis — the origin of asymmetry from an initially baryon symmetric state. Three conditions, known as the Sakharov

conditions, are required for baryogenesis: baryon number violation, C and CP violation and departure from thermal equilibrium.

Dark matter: As outlined in Section 1.2, there is evidence that 84% of the matter in the universe is non-luminous, non-baryonic dark matter that is not explained by the SM. In addition, CMB and other cosmological observations point to a big bang model followed by inflation, which the SM provides no mechanism for. Neither does it explain the dark energy required to explain the observed accelerating expansion of the universe.

All of these factors motivate the need for something beyond the SM. Further hints are also provided by experimental and theoretical problems — but these are more indicative of an incomplete theory than being fundamental motivations for new physics.

Muon magnetic anomaly: On the experimental side, measurements of the muon magnetic anomaly show discrepancy with SM predictions. The magnetic moment of charged leptons is given by: $\bar{\mu} = (g-2)/2m\bar{s}$, and tree level interactions give $g = 2$ from the Dirac equation. However, loop contributions give a very small correction — the anomalous magnetic moment $a = (g-2)/2$. Precise theoretical predictions of the SM value have been made using state of the art lattice and data driven techniques to improve calculations of the hadronic contributions, in addition to the QED and electroweak parts which are well known.

In order to determine the anomaly experimentally, muon spin precession is measured in a magnetic storage ring. This has been done by successive experiments at BNL [25] and more recently using the same ring at Fermilab [26]. High energy positrons emitted by muon decay are measured inside the ring to measure the difference between spin precession and cyclotron frequency. This, along with very precise measurement of the magnetic field to determine equivalent proton spin precession frequency, is used to find the magnetic anomaly. The BNL experiment originally measured a_μ as 3.7 σ above the SM prediction [25]. The Fermilab measurement is consistent with the BNL result, being 3.3 σ above the SM prediction with a 15% smaller error [26]. Combining the two results gives a magnetic anomaly 4.2 σ above the SM value, indicating tension with the SM and a need for new physics to explain this result.

Strong CP: Another problem which arises from an experimental result is the strong CP problem, described in detail in Section 2.2.3. This is the unnaturally

small value of the CP violating parameter in QCD, as inferred from measurements of the neutron electric dipole moment.

Theoretical: From a theoretical viewpoint, one problem of the SM is the large difference in energy scale between electroweak and gravitational interactions, with the electroweak scale $O(100)$ GeV being much smaller than the $O(10^{19})$ GeV Planck scale on which gravity dominates. This is called the hierarchy problem as there is some unexplained between the two scales. Additionally the SM is theoretically unsatisfactory — it does not explain the quantum numbers and contains at least 19 arbitrary parameters. This suggests that it describes only part of some other underlying physics, which perhaps unifies all known forces.

In summary, we have seen the wealth of evidence for dark matter as one part of physics beyond the Standard Model. This provides the context for the models and searches discussed in the rest of this work.

Chapter 2

Solving the Puzzle

Given evidence presented in Section 1.2, the question naturally arises about the nature of the invisible, gravitationally interacting matter present in large quantities throughout the universe. The favoured dark matter (DM) candidate has evolved over time, since first hints observed in first half of 20th century. Initially, from the evidence for additional non-luminous matter in galaxies, it was possible that it could be a different invisible phase of ordinary matter. But more conclusive evidence in the 1970s, with studies of rotation curves, indicated a spherical dark matter halo composed of matter which does not gravitationally collapse in the same way as ordinary matter. At this point separate matter in dark stars, gas or brown dwarfs was the favoured explanation. It wasn't until the 1980s that the idea of particle dark matter became the preferred paradigm, following studies of neutrino cosmology. Once experimental evidence showed that neutrinos were too light to form all of the dark matter, in the 1990s the weakly interacting massive particle (WIMP) became the favoured candidate. However, following two decades of experimental searches there has been no discovery of WIMP dark matter or other particles related to the SUSY models which can motivate it. There is now increased interest in a range of other dark matter models including axion and hidden sector models.

In this chapter an overview of dark matter models will be given, focusing on the most popular models and those that can be probed by electron recoil searches, followed by a review of the complementary search strategies used to probe these models. The energy/mass scales covered by these models along with the associated searches are shown in Fig. 2.1.

2.0.1 Properties

Little is known about the nature of dark matter, despite the compelling evidence for its existence presented in Section 1.2. This is because most of the evidence for dark matter comes from gravitational interactions, which are not included in the Standard Model (SM) of particle physics. However the gravitational interactions with baryons, inferred from the observations outlined in Chapter 1, do give a set of basic properties which any dark matter model must have.

Dark: The dark matter does not give observable light emission or absorption, so any coupling to photons must be very weak and it is essentially neutral.

The question of *how dark* the dark matter must be can be constrained using the observed density perturbations in the CMB, introduced in Section 1.2.4. Dark matter with even a small millicharge would couple to the photon baryon plasma in the early universe. If this was still in equilibrium at recombination DM density perturbations would be washed out due to radiation pressure and photon diffusion. To avoid this the DM must be decoupled at recombination, indicating charges less than $\sim 10^{-6}$ e and $\sim 10^{-4}$ e for 1 GeV and 10 TeV dark matter masses respectively [27].

Cold: The observed large scale structure in the universe implies that the dark matter particles must have been non-relativistic at the time of structure formation. If this was not the case structure would be washed out and gravitational collapse into stars, galaxies and clusters would not occur. As discussed in Section 1.3 cold dark matter is a key part of the ΛCDM standard model of cosmology. This requirement of coldness constrains masses of thermally produced DM to be $\lesssim$ keV, however lighter dark matter particles may be produced non thermally.

Stable: In order for dark matter to play a role in structure formation and have observable astrophysical effects today it should have a lifetime comparable to the age of the universe. If significant dark matter decay takes place structure formation is affected and the abundance at recombination must increase to give the correct abundance today. This would alter the CMB observables discussed in Section 1.2.4. Simulations with varying dark matter model parameters fitted to CMB data give a conservative lower limit on the DM lifetime of 160 Gyr, for the case where DM decays to dark radiation only [28].

Collisionless: Studies of merging clusters constrain dark matter self interactions, which would result in deceleration or scattering and loss of the dark matter in the galaxy cluster. The most stringent constraint comes from observations of the bullet cluster merger, described in Section 1.2.2, which constrains the dark matter self interaction cross section: $\sigma/m < 0.47$ cm^2/g [29]. Dark matter self interactions would also lead to non-spherical distribution of dark matter in galactic halos, in contrast to the spherical halos inferred from observations.

Non-baryonic: Determination of the baryon and dark matter energy densities from BBN and CMB oscillations indicate that the energy density in dark matter is about five times the energy density in baryons. Therefore dark matter should be composed of something other than baryons.

Some models do contain properties such as charge or DM self interactions (e.g. hidden sector dark matter discussed in Section 2.3.1), but these are strongly constrained or use other mechanisms to explain the property.

Mass scale: In principle dark matter mass can take any value from the present day value of the Hubble constant in natural units $\sim 10^{-33}$ eV (smaller particle masses cannot be determined due to the uncertainty principle), to the Planck scale $\sim 10^{28}$ eV.

These 60 orders of magnitude can be reduced slightly by considering quantum effects, depending on the nature of the particle and requiring it to be confined to the dark matter halo. For bosonic dark matter the de Broglie wavelength must be smaller than the virialized structure, otherwise the wavepacket cannot be localized inside the DM halo. This gives a lower limit on dark matter mass: $m_{DM} \gtrsim 10^{-22}$ eV for bosons. A similar argument exists for fermionic dark matter using the Pauli exclusion principle, with discrete states filled until the velocity/momentum exceeds the escape velocity for the halo. This plus the requirement to explain the mass of the halo results in a lower limit: $m_{DM} \gtrsim 400$ eV/c^2 for fermions. Another mass limit, discussed above, is the requirement of $m_{DM} \gtrsim$ keV/c^2 for thermally produced dark matter.

2.1 Dark Matter Model Building

The above constraints are not sufficient to define a dark matter model — there are a large number of models, spanning a large mass range, which reproduce the

correct basic properties.

Model building can be approached in two different ways: looking at dark matter candidates embedded in models which solve one or more of the problems described in Section 1.5, or a bottom up approach to create a model that explains a specific observation. These approaches lead to a variety of different particle types being postulated, spread right across the large mass range introduced in Section 2.0.1 and shown in Fig. 2.1.

Similarly to the fundamental SM particles, dark matter particles can be characterised by their mass and spin — mass determining whether they behave like waves or particles and spin distinguishing fermions and bosons. Dark matter particles can behave like waves if inter particle separation is greater than the de Broglie wavelength and occupation number in the de Broglie volume (λ_{dB}^3) is much greater than 1. This is the case for dark matter bosons with masses $m_{DM} \lesssim 30$ eV/c^2 in the Milky Way. Typically these candidates are ultralight bosons such as axions, axion-like particles or hidden photons. Searches for these particles can use coherent effects of the entire field rather than hard particle scatterings. Dark matter with occupation number less than 1 in λ_{dB}^3 behaves as individual quanta and is treated as discrete particles in phenomenology, which is the case for masses above ~ 30 eV/c^2.

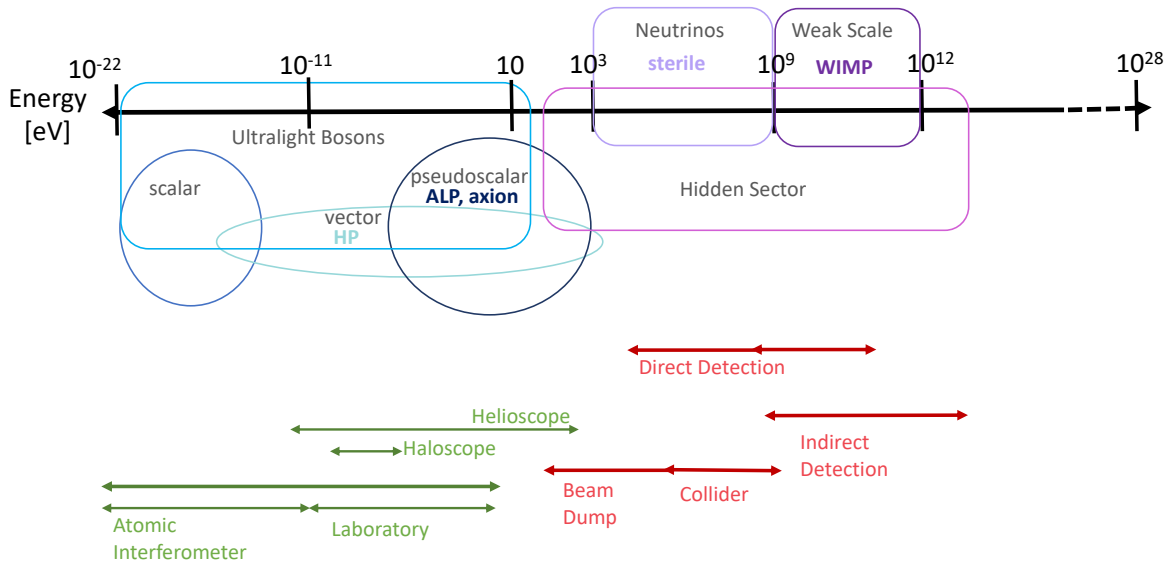

Figure 2.1 *Mass/energy scales of different classes of DM models, with the associated search strategies shown below.*

Two other key characteristics for DM are the production mechanism and whether it is hot/warm/cold in the structure forming epoch. As described in Section 1.3, DM can be produced thermally or non-thermally depending on whether it is in equilibrium in the early universe. Whether DM relics are hot/warm/cold depends on how relativistic they are at the time of matter radiation equality and the resulting free streaming length. As discussed in Section 2.0.1 hot dark matter is disfavoured as the long free streaming length washes out structure, but cold dark matter with $\gg$ keV/c^2 mass or warm dark matter with $\sim$ keV/c^2 mass are possible candidates.

2.1.1 Macroscopic Dark Matter

Whilst the above discussion has focussed on particle dark matter, it is important to note that there are some macroscopic dark matter models, with candidates at much higher mass scales. These include "Massive Astrophysical Compact Halo Objects" (MACHOs) — large, non luminous objects made from baryonic matter. Such objects could be detected through gravitational microlensing, where the flux of a background star would appear amplified if a MACHO passed through the line of sight. The EROS-2 collaboration searched for microlensing events using a sample of 7 million stars and constrained the contribution of MACHOs to the Milky Way halo mass to be less than 8% [30].

Another macroscopic dark matter candidate is primordial black holes (PBHs), which formed shortly after the big bang from the collapse of density perturbations during radiation domination [31]. The LIGO Virgo discovery of gravitational waves from mergers of $\sim 10 M_{\odot}$ black holes in 2016 [32], which could possibly be of primordial rather than stellar origin, renewed interest in this model. Since PBHs are not formed from stellar gravitational collapse they can have masses much below stellar masses, however many observational constraints exist on the dark matter fraction at various PBH masses. It is found that planetary to stellar mass PBHs can only form a subdominant contribution to DM, but asteroid mass scale PBHs remain viable (this lower mass regime is more observationally challenging) [31]. In order to probe the lowest parameter space for PBHs improved theoretical calculations and new observational techniques are required.

Since these macroscopic models are heavily constrained and do not answer the other SM problems discussed in Section 1.5, dark matter comprised of one or more new fundamental particles remains the preferred paradigm.

2.2 Popular Particle Dark Matter Models

A plethora of different models arise from different approaches to model building in the particle dark matter paradigm. Three of the most popular models: neutrinos, WIMPs and axions, will be discussed here.

2.2.1 Neutrinos

One obvious DM candidate to consider are the SM neutrinos, they are known to exist, have mass and are the only weakly interacting neutral, long-lived SM particles. However, the neutrino mass is very small, ≤ 0.8 eV/c^2, as described in Section 1.5, which means that neutrinos cannot contribute sufficient energy density to be the dominant component of dark matter. As collisionless relativistic particles neutrinos would erase small scale structure on scales below ~ 40 Mpc by free streaming from higher to lower density regions. This would imply that the observed structure in the universe arose from "top down" formation with large structures forming first rather than building up from small scales, but this disagrees with observations. Therefore, neutrinos can contribute at most 1.6% of the total dark matter mass (and at least 0.5% from oscillation mass constraints). Since neutrinos cannot contribute 100% of the dark matter, we can conclude that the SM does not contain a viable candidate to explain dark matter fully.

Since SM neutrino masses are too small, a new approach may be to propose heavier neutrinos with weaker SM couplings as DM candidates. These right-handed (RH) "sterile" neutrino(s) are added to the SM left-handed (LH) "active" neutrinos. The neutrino minimal standard model (νMSM) is a bottom up approach to minimally extend the SM to include sterile neutrinos — adding three RH neutrinos to the SM. Different mass neutrinos explain the dark matter ($\sim$ keV/c^2), neutrino masses and baryon asymmetry (both 100 MeV/c^2 – electroweak scale). Sterile neutrinos arise in many new physics models and keV scale sterile neutrinos also provide a viable dark matter candidate, first suggested by Dodelson and Widrow in 1993 [33].

The RH neutrinos only have direct SM couplings to active neutrinos, so production and decay must be via mixing with active neutrinos. If the production via mixing is slower than expansion the sterile neutrinos are never in thermal equilibrium. They are produced non-thermally, either via oscillations at $\sim$ 100

MeV or decay of heavy particles at higher temperatures [33]. Early calculations assumed that sterile neutrinos would constitute cold dark matter, but it has been shown that they can be cold, warm or hot depending on the masses and energy distributions.

2.2.2 WIMPs

A commonly discussed class of dark matter candidate is weakly interacting massive particles (WIMPs). Thermal WIMPs are produced by freeze out, described in Section 1.3, with average cross section $\langle \sigma v \rangle \sim 3 \times 10^{-26}$ cm^{3}s^{-1} required to give the correct relic density of cold dark matter. For typical velocities $v \sim 0.1$c this corresponds to $\sigma \sim 10^{-36}$ cm^2, which is the order of weak scale interactions. This is the so called "WIMP miracle" — the coincidence of the required cross section and the electroweak scale. A thermal WIMP with mass $\sim$ 10 GeV/c^2 – 1 TeV/c^2 could be part of some new physics not far above the scale of the SM, solving the hierarchy problem introduced in Section 1.5. WIMP dark matter also meets the required properties of being stable and weakly interacting, only having interactions with W, Z bosons but not photons or gluons. The additional advantage that it is potentially detectable has led to lots of interest in WIMP dark matter over the past few decades, making it the most studied dark matter candidate.

There are various WIMP candidates, arising from different theoretical frameworks such as supersymmetry (SUSY). In SUSY generators are introduced to relate SM integer spin bosons and half integer spin fermions, associating a superpartner, of opposite spin type, to each SM particle [12]. The Minimal Supersymmetric extension of the SM (MSSM) has the smallest field content necessary to be consistent with the SM. Here, fermionic superpartners are associated to all gauge fields (gluinos, binos, winos) and scalar superpartners are associated to fermions (squarks, sleptons). There is also an additional Higgs field to give two Higgs doublets with a spin 1/2 Higgsino being associated to each Higgs boson. In order to maintain conservation of baryon and lepton number R-parity is conserved in SUSY. R-parity is given by:

$$R = (-1)^{3B+L+2S}, \tag{2.1}$$

where B is baryon number, L is lepton number and S is spin. This means that

$R = 1$ for SM particles and $R = -1$ for superpartners. Heavy superpartners can only decay to odd numbers of lighter superpartners and there exists a stable Lightest Supersymmetric Particle (LSP), which makes an attractive WIMP dark matter candidate. Sneutrinos were one possibility for the LSP, but have been ruled out as their scattering cross section with nucleons would lie above the limits found by direct detection experiments [34]. Alternatively, the LSP could be the gravitino or four neutralinos — fermionic mass eigenstates which are a mixture of wino, bino and higgsinos.

An alternative non-SUSY theory containing WIMPs is Universal extra dimensions (UED) [35], where flat compact extra dimensions are added, with all SM particles free to propagate in all dimensions. This is a generalisation of the original idea by Kaluza and Klein of five dimensional space time. Particles moving in the hidden fifth dimension appear very massive as their extra dimensional momentum appears as an extra contribution to rest mass. For many extra dimensions the SM fields propagating in these extra dimensions appear as towers of Kaluza Klein (KK) states. There is associated KK-parity which acts similarly to R-parity in SUSY, conserving the evenness or oddness of the number of KK states. This implies the existence of a stable lightest KK state, which is a weakly interacting cold dark matter candidate produced by thermal freeze out which gives the correct relic abundance for $\sim$ 100 GeV/c^2 – TeV/c^2 particle masses.

Different models giving rise to WIMP dark matter include other models with extra dimensions, little Higgs [36], technicolour and composite Higgs theories. Whilst these WIMPs are astrophysically equivalent, being cold, collisionless and thermally produced in freeze out, they can have very different phenomenology in collider, indirect and direct searches.

Electroweak scale WIMPs arise naturally in theories motivated by solving the gauge hierarchy problem. However, the cross section dependence: $\sigma \propto g^4/m^2$, means that it is also possible for sub GeV WIMPs possible to give correct relic density if the coupling g is below the electroweak scale. There is no firm lower limit on WIMP mass, other than $\sim$ 10 keV/c^2 for it to constitute cold dark matter, and several variations on the WIMP model exist such as superWIMPs. Alternatively light thermal WIMPs may be contained within other theories such as hidden sectors, described in Section 2.3.1.

Whilst WIMP dark matter is both theoretically and experimentally appealing, no evidence for WIMPs or SUSY after several decades of searches has lead to

increased interest in other models.

2.2.3 Axions

Axions are an alternative dark matter candidate — ultralight bosons with wave-like behaviour, primarily motivated by the Peccei Quinn solution to the strong CP problem. This problem in the SM, described below, arose in the 1970s when QCD was being developed to describe the strong sector. The subsequent theoretical and experimental efforts developed over the next several decades, in parallel to those for WIMPs.

The QCD Lagrangian, describing strong interactions, is given by:

$$\mathcal{L}_{QCD} = \bar{\phi}(i\gamma^{\mu}D_{\mu} - m)\phi - \frac{1}{4}G^{a\mu\nu}G^{a}_{\mu\nu}. \tag{2.2}$$

The first term gives the quark kinetic energy, where $D_{\mu} = \partial_{\mu} - igA^{a}_{\mu}t^{a}$, the second term gives quark mass and the final term describes the gluon dynamics, where $G^{a}_{\mu\nu} = \partial_{\mu}A^{a}_{\nu} + \partial_{\nu}A^{a}_{\mu} + gf_{abc}A^{b}_{\mu}A^{c}_{\nu}$ are the field strength tensors of the gluon fields A^{a}_{μ}. For N quark flavours with vanishing mass $m_q \to 0$, this has $U(N)_V \times U(N)_A$ symmetry. Since the first generation of quarks (u, d) have mass much below the QCD scale, strong interactions in the SM are expected to have $U(2)_V \times U(2)_A$ symmetry. The vector symmetry $U(2)_V = SU(2)_l \times U(1)_B$, corresponding to isopsin and baryon number, is observed. However, the $U(2)_A = SU(2)_A \times U(1)_A$ symmetry is not observed. The $SU(2)_A$ symmetry is spontaneously broken, with pions as the generated Nambu Goldstone bosons, but the $U(1)_A$ symmetry is not observed in nature. This lack of $U(1)_A$ symmetry in QCD was termed the $U(1)_A$ problem [37].

Solving this problem required the realisation that the QCD vacuum has a more complicated structure, described by an additional phase parameter θ [38]. An extra term was added to the QCD Lagrangian:

$$\mathcal{L}_{\theta} = \frac{\alpha_S \theta}{8\pi} G_{\mu\nu}\tilde{G}^{a\mu\nu}, \tag{2.3}$$

where $\tilde{G}^{a\mu\nu} = 1/2\varepsilon^{\mu\nu\alpha\beta}G^{a}_{\alpha\beta}$ and α_S is the fine structure constant. This additional term is invariant under charge conjugation (C), but violates parity and time invariance (PT), so there is CP violation. If weak interactions are added, an additional term must be included — a new parameter is defined:

$\bar{\theta} = \theta + arg(detM)$, for quark mass matrix M. As a result the QCD Lagrangian is now:

$$\mathcal{L}_{QCD} = \bar{\phi}(i\gamma^{\mu}D_{\mu} - m)\phi - \frac{1}{4}G^{a\mu\nu}G^{a}_{\mu\nu} + \frac{\alpha_S\bar{\theta}}{8\pi}G_{\mu\nu}\tilde{G}^{a\mu\nu}. \tag{2.4}$$

The final term gives CP violation, which would induce a neutron electric dipole moment [39]:

$$d_n \approx \theta\frac{em^*}{\Lambda_{QCD}m_n}, \tag{2.5}$$

where $m^* = m_u m_d/(m_u + m_d)$ is the reduced mass of the up and down quark and $\Lambda_{QCD} \sim 1$GeV is the QCD energy scale. The measured upper limit: $|d_n| < 3 \times 10^{-26}$ e cm [40], implies that $\theta \leq 10^{-9}$. There is no physical reason for this parameter to be so small — this non-observation, or incredibly small CP violation, in the strong interaction is the *strong CP problem*.

Three possible solutions to the problem are: unconventional dynamics, spontaneously broken CP and additional chiral symmetry [39]. The first two are unsatisfactory — the first requires zero quark masses and the second has θ at loop level, both of which require additional justification. The third option forms the basis of the solution proposed by Peccei and Quinn in 1977 [41]. Their approach promotes $\bar{\theta}$ from a parameter to a dynamical variable with different values for different vacuum states and a minimum at $\bar{\theta} = 0$. This is achieved by adding an additional global symmetry $U(1)_{PQ}$, under which the axion field transforms as: $a(x) \to a(x) + \alpha f_a$. Spontaneous symmetry breaking (SSB), at scale f_a, results in a Goldstone boson — the axion.

Three additional terms are added to the QCD Lagrangian, in order to make it $U(1)_{PQ}$ invariant [39]:

$$\mathcal{L}_{axion} = -\frac{1}{2}\partial_{\mu}a\partial^{\mu}a + l_{int}[\partial^{\mu}a/f, \psi] + \frac{a}{f_a}\zeta\frac{\alpha_S}{8\pi}G^{a}_{\mu\nu}\tilde{G}^{\mu\nu a}. \tag{2.6}$$

These terms describe axion kinetic energy, interactions and chiral anomaly, respectively. The chiral anomaly of $U(1)_{PQ}$ is also the effective potential of the axion field, which has a minimum value at $\langle a \rangle = -f_a\frac{\bar{\theta}}{\zeta}$. Writing the full QCD Lagrangian in terms of the physical axion $a_{phys} = a - \langle a \rangle$, cancels the CP violating term.

The mass of the resulting axion is given by: $m_a f_a = \sqrt{\chi}$, where χ is the topological susceptibility in QCD. Evaluating this using chiral perturbation theory (to next-

to-next-to leading order) gives axion mass [42]:

$$m_a = 5.691\left(\frac{10^9}{f_a[\mathrm{GeV}]}\right)\mathrm{meV/c^2}. \tag{2.7}$$

Axion Models

In the original PQ axion model, the breaking scale was assumed to be the same as the electroweak scale: $f_a = v_{EW} \approx 250$ GeV. This corresponds to m_a >150 keV, and since SM particle couplings are also inversely proportional to f_a these would also be large giving a heavy or "visible" axion. However, this was quickly ruled out by a combination of direct experimental searches (rare kaon and quarkonia decays [43]) and astrophysical arguments (stellar evolution or supernova neutrino emission). Experimental upper limits showed that $f_a \geq 10^3$ GeV ($m_a \leq 6$ keV/c^2), so the visible QCD axion was excluded.

Since the value of f_a is arbitrary, axion production from SSB at a higher scale is allowed with $f_a \gg v_{EW}$. This results in much smaller couplings and mass — the "invisible axion", with two main benchmark invisible axion models: KSVZ and DFSZ. The KSVZ model is a "hadronic" axion model, which introduces a scalar field σ, with $f_a = \langle\sigma\rangle \gg v_{EW}$ and an exotic heavy quark Q with $M_Q = f_a$ [44, 45]. The two new fields are the only fields carrying a PQ charge, whilst the quarks, leptons and Higgs fields have zero PQ charge. At low energies the axion SM interactions occur via axion-gluon coupling to the heavy quark and at high energies there may be higher order interactions with light quarks. The DFSZ model adds a new complex scalar field ϕ, with $f_a = \langle\phi\rangle \gg v_{EW}$ [46, 47]. Here, the PQ symmetry is treated as a chiral rotation, so all SM quarks and leptons have a PQ charge and can couple to axions at tree level. The interactions of axions with ordinary matter depend on the axion model, this is discussed below.

Axion Interactions

The interaction Lagrangian for axions can be split into terms describing their couplings to fermions and photons:

$$\mathcal{L}_{int} = \mathcal{L}_{af} + \mathcal{L}_{a\gamma}, \tag{2.8}$$
$$\mathcal{L}_{af} = \frac{g_{af}}{2m_f}\left(\bar{\psi}_f\gamma^\mu\gamma_5\psi_f\right)\partial_\mu a, \qquad \mathcal{L}_{a\gamma} = -\tfrac{1}{4}g_{a\gamma}\tilde{F}_{\mu\nu}F^{\mu\nu}a.$$

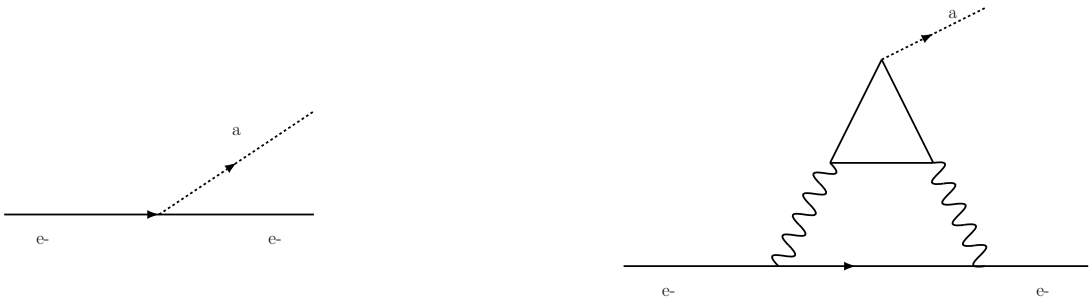

Figure 2.2 *Feynman diagrams showing the axion-electron coupling. Left is the tree level coupling — possible in non-hadronic models, right is the loop level radiative coupling.*

Axion-Electron Coupling:

The axion-electron interaction is described by the term [39]:

$$\mathcal{L}_{ae} = \frac{g_{ae}}{2m_e}\big(\bar{\psi}_e\gamma^\mu\gamma_5\psi_e\big)\partial_\mu a = i\frac{g_{ae}}{2m_e}\partial_\mu a(\bar{e}\gamma^\mu\gamma_5 e), \tag{2.9}$$

where g_{ae} is the axion-electron coupling:

$$g_{ae} = \frac{C_e m_e}{f_a}, \tag{2.10}$$

with effective PQ charge C_e. For generic/non-hadronic axion models (e.g. DFSZ) there are tree level axion-electron interactions, whereas for hadronic models (e.g. KSVZ) with $C_e = 0$ the axion-electron interactions only occur at loop level, both are shown in Fig. 2.2.

Axion-Nucleon Coupling:

The axion-nucleon interaction is described by the term:

$$\mathcal{L}_{aN} = \frac{g_{aN}}{2m_N}\big(\bar{\psi}_N\gamma^\mu\gamma_5\psi_N\big)\partial_\mu a = i\frac{g_{aN}}{2m_N}\partial_\mu a(\bar{N}\gamma^\mu\gamma_5 N). \tag{2.11}$$

Figure 2.3 *Feynman diagrams showing the axion-nucleon coupling. Left is the direct coupling, right is via pion mixing.*

Figure 2.4 *Feynman diagrams showing the axion-photon coupling. Left is the direct coupling, right is via a fermion loop.*

Similarly to the electron case, the axion-nucleon coupling is:

$$g_{aN} = \frac{C_N m_N}{f_a}, \tag{2.12}$$

where C_N is the effective PQ charge for the nucleon N, which depends on the axion model. There are two equal contributions to the nucleon coupling: direct coupling to light quarks at tree level and couplings due to pion mixing, shown in Fig. 2.3.

Axion-Photon Coupling:

There is a direct axion-photon coupling in all models and an additional fermion loop if fermions have non-zero PQ charge (in non-hadronic models), shown in Fig. 2.4. The axion-photon interaction is described by the term:

$$\mathcal{L}_{a\gamma} = -\frac{1}{4} g_{a\gamma} \tilde{F}_{\mu\nu} F^{\mu\nu} a = g_{a\gamma} \bar{E}.\bar{B}a, \tag{2.13}$$

where F is the electromagnetic field strength tensor. The coupling is given by:

$$g_{a\gamma} = \frac{\alpha}{2\pi f_a} \left(\frac{E}{N} - 1.92 \right), \tag{2.14}$$

where E and N are the electromagnetic and colour anomalies respectively. The value of E/N depends on the axion model e.g. E/N = 8/3 for DFSZ and E/N = 0 for KSVZ if the electric charge of the new heavy quark is assumed to vanish.

Axion-like Particles

There is also a more general class of axion-like particles (ALPs) which share properties with axions. Many beyond the SM theories introduce new symmetries, and any global symmetry which is spontaneously broken results in a Goldstone

or pseudoscalar Goldstone boson — these additional light particles are ALPs. They couple to ordinary matter in the same way as axions, but f_a is replaced by the ALP decay constant and there is no a-priori relationship between the coupling strength and mass [39]. The ALPs do not solve the strong CP problem, but they may be dark matter candidates. ALPs arise in different theories with various fundamental motivations, for example string theories which contain many additional pseudoscalar and scalar fields in compacted extra dimensions.

Axions in Nature

Cosmological axions:

As introduced above, axions produced non-thermally in the early universe provide a cold dark matter candidate, see Ref. [48] for a recent review of axions as DM.

Spontaneous symmetry breaking happens as a result of a PQ phase transition in early universe, at some very high energy either before or after the universe reaches its maximum temperature. Whether the PQ symmetry breaking occurs before or after inflation determines the dynamics of the axion field and subsequent dark matter density. For pre-inflationary symmetry breaking, the axion field is smoothed out and a simple wave equation can be used to describe the evolution of the field. However, for post-inflationary symmetry breaking the axion field is not smooth, leaving a more complex configuration where topological defects need to be considered.

The symmetry breaking produces initial fluctuations of the axion field. Once the expansion of the universe drops below the natural frequency of axion oscillations (after some time scale depending on axion mass $t \sim 1/m$) the axion field becomes highly dynamical and begins to oscillate. Oscillations of the axion field produce non relativistic axions, with the population growing up to some later time. After production ceases the comoving axion number density is conserved and is diluted by expansion with $\rho \sim 1/a^3$. As a result axions can populate the universe in a coherent wave-like state that is slow moving and cold. On scales larger than the de Broglie wavelength axions behave as cold dark matter and reproduce the structure formation observed in the universe. This production mechanism is called the misalignment mechanism, due to vacuum misalignment of the axions oscillating in the potential.

The same non-thermal production mechanism can be generalised to all ultralight

bosons, including ALPs. Similarly, the time at which ALP field oscillations begin is determined by the ALP mass and this determines the relic abundance. ALPs with large occupation numbers can also be treated as a coherent classical field below the de Broglie wavelength.

If axions are assumed to contribute all of the dark matter, their mass is required to be $\gtrsim \mu$ eV/c^2, with the exact value depending on the details of the PQ symmetry breaking and subsequent production. An upper limit of ~ 20 meV/c^2 can be placed on the mass from limits on the g_{aNN} coupling derived using observations of SN1987A [39]. However, not all of the dark matter has to necessarily take the form of axions — both axions and ALPs could exist and form all/some/none of the dark matter.

Stellar axions:

In addition to cosmological relics, axions from astrophysical sources can also be considered. The couplings of axions to electrons, nucleons and photons, described in Section 2.2.3, would allow axions to be produced in hot astrophysical plasmas such as stars and supernovae. For example, axions could be produced in the Sun by ABC, Primakoff and ^{57}Fe processes described in Section 5.1.3.

Observations of lifetimes and stellar energy losses can be used to constrain axion production and therefore couplings to normal matter. Direct searches for axion flux from these objects can also be carried out using terrestrial experiments. Search strategies for both dark matter and stellar ultralight bosons will be discussed further in Sections 2.4 and 3.2, followed by an LZ analysis in Chapter 5 which includes solar axions and cosmological ALPs.

2.3 Widening the Net

After several decades of experimental searches, there have been no discoveries of any of the three leading dark matter candidates discussed above, only exclusion limits and ever-tightening constraints on the parameter space. This has motivated new approaches to dark matter model building — alternative theories have been proposed along with more model independent approaches to phenomenology.

2.3.1 Hidden Sector

A class of model which has been considered historically, and recently become more popular due to the lack of conclusive signals of DM interactions, is the idea that dark matter resides in a "hidden sector" (HS). This sector does not interact with any of the SM gauge fields [49] and any stable particle(s) it contains could naturally explain dark matter. In addition, neutrino masses and baryon asymmetry could be explained using additional particles or gauge symmetries in the hidden sector. As well as being qualitatively appealing, and potentially solving multiple SM problems, there is top down motivation for hidden sectors from string theory, SUSY or composite Higgs models.

The hidden nature of the new physics allows for a lot of model building freedom — hidden sectors with simple or rich structures are possible, giving rise to a variety of phenomenology. Since particles in the hidden sector are not charged under the SM gauge group they can only interact with SM particles via gravity and possible weak "portal" interactions. The three main types of renormalizable portal interactions allowed by the SM symmetries are: vector, scalar and neutrino portals [50], with interaction terms described by the singlet operators:

$$\mathcal{L} \subset \begin{cases} -\frac{\epsilon}{2cos\theta_W} B_{\mu\nu} F'^{\mu\nu} & \text{vector,} \\ (\mu\phi + \lambda\phi^2) H^\dagger H & \text{scalar,} \\ y_n L H N & \text{neutrino.} \end{cases} \tag{2.15}$$

Vector: The vector portal arises if there is an additional U(1)′ symmetry and associated vector mediator in the HS, which may couple to the SM U(1) via photon or Z interactions. In the vector portal Lagrangian term: $B^{\mu\nu}$ is the hypercharge field strength tensor and $F'_{\mu\nu}$ is the field strength tensor of the U(1)′ vector boson.

Any interaction between the HS and SM particles via electromagnetic interaction, of the new U(1)′ vector bosons with photons, is described as a kinetic mixing interaction. The interaction strength depends on the kinetic mixing parameter ϵ. Hidden sector particles which have U(1)′ charge will therefore appear to have eϵ millicharges in the SM. Kinetic mixing is the simplest way to couple a new vector field to the SM without charging the SM under new gauge fields, but alternative vector portals are also possible, such as a mediator coupled directly to baryonic,

lepton or (B-L) currents [51].

A simple model is a HS containing a minimal kinetically mixed hidden photon (HP) A' as the vector mediator. This model is parametrized by the HP mass $m_{A'}$ and kinetic mixing strength ϵ. The hidden sector may contain only the HP or be more complex – with HPs as the dark matter candidate or mediator. Interactions between additional DM and SM could be mediated by the HP with an interaction term: $\epsilon/2F'^{\mu\nu}F_{\mu\nu}$. These interactions with ordinary matter may be observable in experiments, as described in Section 2.4.

Light HPs can be produced in the early universe by scattering or annihilation processes, resonant photon-HP conversion or a misalignment mechanism similar to the one described in Section 2.2.3. Dark matter in the hidden sector could be produced via thermal freeze out and the "WIMP miracle" described in Section 2.2.2 can apply equally well for HS particles with a thermally averaged cross section $\langle\sigma v\rangle \sim 3 \times 10^{-26}$ cm^{3}s^{-1}. The DM can either undergo "secluded" annihilation to pairs of mediators which subsequently decay to SM particles or "direct" annihilation to SM final states via a virtual mediator. Dependence of the cross section on the couplings and masses is given by [50]:

$$\langle\sigma v\rangle \sim \begin{cases} \frac{g_D^4}{m_\chi^2} & \text{secluded,} \\ \frac{g_D^2 g_{SM}^2 m_\chi^2}{m_{A'}^2} & \text{direct.} \end{cases} \tag{2.16}$$

Here, g_D is the mediator-DM coupling, $g_{SM} = e\epsilon$ is the SM-DM coupling and m_χ is the DM mass and $m_{A'}$ is the mediator mass. These parameters are fixed in order to produce the correct relic abundance from thermal production. Couplings can be on the weak scale as for WIMPs, but other parameter combinations are possible and m_χ can take a broad range of values. Alternatively the HS DM can be produced by freeze in where the HS is never in thermal equilibrium with the SM and non-equilibrium processes will gradually populate the DM [50].

Scalar: The discovery of the Higgs showed that fundamental scalars exist and many SM extensions predict the existence of new scalars or pseudoscalars, including extended Higgs or SUSY models. These scalars can be light and very weakly coupled to the SM, if they are singlets under the SM gauge symmetry. A singlet scalar mediator ϕ in the HS can couple to the square of the SM Higgs field H resulting in mixing between the singlet scalar and Higgs doublet. In the Lagrangian term for this interaction, in Eq. 2.16, μ and λ are dimensionless and dimensional couplings respectively.

The scalar mediator can either mediate DM SM interactions or constitute the DM itself as a stable particle. As above, DM states in the HS can undergo either secluded or direct decays to SM states with the scalar mediator being either an intermediate step or virtual mediator. For the scalar mediator to be the DM it must be stabilised by a discrete Z_2 symmetry, so the Lagrangian reduces to $\mathcal{L} \subset \phi^2|H|^2$ [52]. The mediator undergoes annihilations to SM states, such as light fermions, vector bosons or Higgs pairs, via the Higgs interaction. In the early universe ϕ will be in thermal equilibrium with the SM due to the Higgs portal, then as the universe expands freeze out will give a constant comoving DM density, as described in Section 1.3. Alternatively, if the Z_2 is broken a small amount, through operators that couple ϕ to H and other stable neutral DM states χ, the coupling may be smaller and ϕ, χ would be out of equilibrium. Here, the correct abundance of combined ϕ, χ can be achieved by freeze in from decays of H and ϕ.

Neutrino: Mixing of SM neutrinos with some new heavy neutral leptons (HNLs) is the basis for the neutrino portal interactions given in Eq. 2.16. Here, the HNL fermionic mediator N mixes with the lepton doublet L with Yukawa coupling y_n. Only the right handed component of N couples to the SM sector, so the HNL is a right handed/sterile neutrino as introduced in Section 2.2.1. This can be a viable DM candidate in the narrow $m_N \sim$ keV mass range, however the mass is strongly constrained outside of this by a range of experimental and BBN constraints, described in Section 2.2.1. This model explains both neutrino masses and dark matter and as above production occurs via mixing with the SM neutrinos.

In summary there are a wide range of possible hidden sector structures, resulting in a variety of possible dark matter candidates, some of which overlap with the classes of dark matter described in Section 2.2. The predicted particles and forces cover a large parameter space, a shown in Fig. 2.1. These give a range of expected phenomena, so complementary searches are needed, as described below in Section 2.4. A problem with HS models is that it is not necessary for them to have any SM couplings at all, meaning that a theory could be very difficult to test.

2.3.2 Mirror Dark Matter

Mirror dark matter (MDM) is a specific example of a hidden sector model, with a particularly rich dark sector which is isomorphic to the SM [53–55]. This

means that the mathematical structure of the gauge symmetries is the same (isomorphism preserves sets and relations between elements with one-to one mapping). The full Lagrangian is extended to included the mirror sector term [55]:

$$\mathcal{L} = \mathcal{L}_{SM}(e, u, d, \gamma, W, Z, ...) + \mathcal{L}_{SM}(e', u', d', \gamma', W', Z', ...) + \mathcal{L}_{mix}, \tag{2.17}$$

where $\mathcal{L}_{SM}(e...)$ and $\mathcal{L}_{SM}(e'...)$ are the SM and mirror sector Lagrangians respectively. The mirror sector contains a mirror partner of each SM particle (denoted $'$), which have the same masses, lifetimes and self-interactions as SM particles.

The mixing term $\mathcal{L}_{mix}$ contains any non-gravitational portal interactions between mirror and SM particles, this is the only place where new parameters are introduced in this model. With the two sectors related by a discrete Z_2 symmetry transformation, the allowed vector and scalar portal interactions in this model can be written as:

$$\mathcal{L}_{mix} = \frac{\epsilon}{2} F^{\mu\nu} F'_{\mu\nu} + \lambda H'^2 H^2. \tag{2.18}$$

As described for general hidden sector vector portal interactions, the first term describes the kinetic mixing interaction with strength ϵ. Kinetic mixing induces tiny SM electromagnetic charges $\pm\epsilon e$ for mirror protons and electrons. Since the mirror Higgs (H') is the only scalar in the mirror sector, the second term describes the $H' - H$ mixing. The neutrino portal term is not included in the model by default as it requires non-degenerate mirror neutrino and SM neutrino masses. However, if there is some symmetry breaking massive, right handed neutrinos can be added. These could generate SM neutrino masses via a seesaw mechanism, with the form of the portal interaction depending on the type of seesaw mechanism.

In the MDM model all of the inferred non-baryonic dark matter is some type of mirror matter, from the spectra of mirror particles and atoms. This MDM would exist as a multi-component plasma halo (predominantly $\mathrm{e}', \mathrm{He}'$), assuming that the mirror electron temperature exceeds the binding energy of a mirror hydrogen atom and the cooling time exceeds the Hubble time [56]. The process of MDM production in the mirror sector is completely analogous to particle production in the SM, just with shifted timescales due to the different temperature.

Despite some very different properties to more conventional WIMP or axion models, the required properties from BBN, CMB and structure constraints can

be all fulfilled by MDM. One difference to the models discussed above, is that the MDM is collisional due to its self interactions. However, it is also dissipative and as long as cooling is sufficient the gravitational collapse of perturbations is not prevented. The complex dark sector can also lead to the formation of exotic structures, such as mirror stars and supernovae. Constraints and searches for hidden sector models are discussed below as part of Section 2.4, then a direct detection search for MDM is the subject of Chapter 4 and future prospects are described in Chapter 5.

2.3.3 Effective Field Theories

A different approach to studying dark matter, in a model independent way, is to construct effective field theories (EFTs) of all possible interactions between DM candidates and the SM [57, 58]. Since almost nothing is known about the non-gravitational interactions of dark matter, any assumptions made about the scale of couplings by a given model are arbitrary and for composite dark matter multiple scales might arise. Outside of a model based the electroweak scale or minimal SM extensions, there are numerous possible DM-SM interactions on a range of scales. Dark matter which interacts with the SM via mediators at a higher energy scale Λ, allows the heavy mediators to be integrated out, leaving effective point interactions. In general, the effective Lagrangian can be written as [59]:

$$\mathcal{L}_{eff} = \mathcal{L}_{SM} + \sum \frac{f_i^{(5)}}{\Lambda} O_i^{(5)} + \sum \frac{f_i^{(6)}}{\Lambda} O_i^{(6)} + ... \quad , \tag{2.19}$$

where $O_i^{(n)}$ is a n-dimensional operator, which consists of a gauge invariant combination of SM and DM fields, and f_i are coefficients. Suppression of higher dimension terms by the energy scale of new physics means that the lowest allowed dimension will dominate.

An EFT can be constructed for scalar, fermion or vector dark matter describing the phenomena of interest e.g. DM-DM annihilation, DM-SM scattering or SM-SM production, as long as the interaction energy scale is much smaller than Λ. Searches using these channels aim to constrain the f_i coefficients. In the EFT framework this can be done in a model independent way which allows for comparison between the different types of searches described in Section 2.4.

Whilst EFTs are simple and flexible, they are a bottom up approach and don't motivate new physics or solve any of the other problems in the SM. They can

be used to guide model building and be complimented by complete models with many parameters, for which narrow benchmark searches can be performed.

Bridging these two types of modelling are simplified models, which expand the effective operator to include a mediator [60]. This retains some degree of model independence and keeps the number of parameters small, whilst providing a more detailed model and kinematic descriptions of the interactions. It also allows searches for the mediator to be carried out. Again these searches can be used to constrain the parameter space in which complete models can be constructed. The different approaches to model building are summarised in Fig. 2.5 and the scales of the resulting models are shown in Fig. 2.1.

2.4 Dark Matter Searches

The defining properties of dark matter, described in Section 2.0.1, make it inherently difficult to search for — weak interactions and no emission of light. In addition, the wide variety of possible models, described in Sections 2.2, 2.3, means the predicted signatures are incredibly varied.

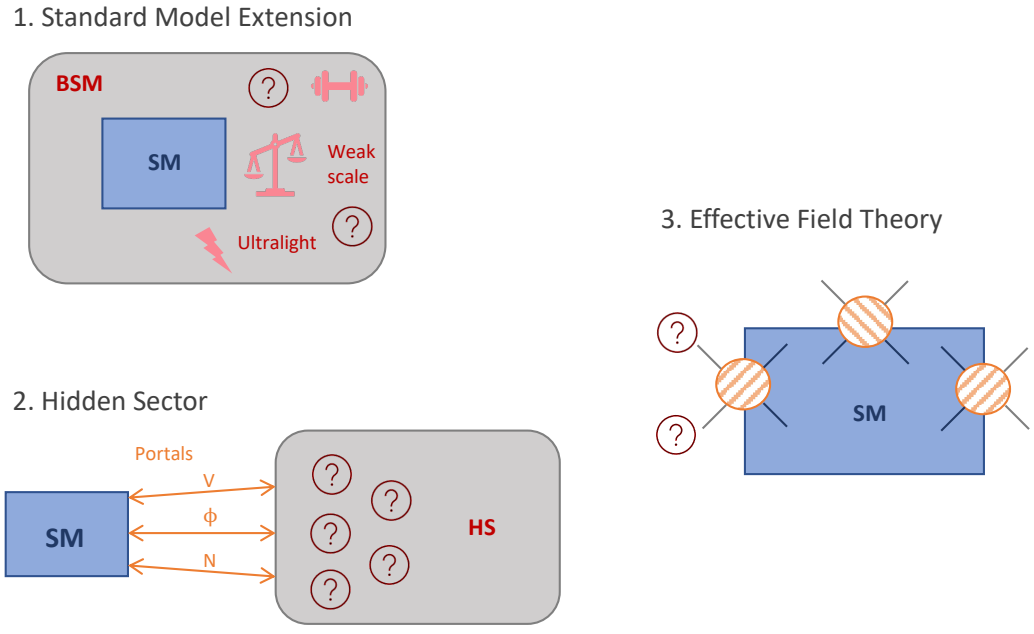

Figure 2.5 *Schematic showing three different approaches to dark matter model building.*

Fundamental dark matter candidates can be divided into two classes — particle-like and wave-like. Much of the experimental effort in the past decades has focused on searches for particle-like DM around the weak scale. Particle-like dark matter can be probed using its interaction as individual quanta in three ways, as shown by the red arrows in Fig. 2.6:

1. **Collider:** search for DM production from SM particles in colliders, fixed target or beam dump experiments.
2. **Indirect:** search for annihilation of DM to SM particles, which may subsequently decay to observable particles or be observed directly.
3. **Direct:** search for scattering of DM particles off SM particles on Earth.

Constraints can be set for thermally produced dark matter which interacts with SM particles prior to freeze out, as indicated by the grey arrow. Depending on dark matter mass, coupling sizes and astrophysical distribution not all of these three channels may be available. But complimentary approaches using all three can cover different models and areas of parameter space, as shown in Fig. 2.1. In order to confirm a discovery, detection in more than one of these channels would be required. For example, a collider signal does not confirm the galactic nature of dark matter, whilst indirect signals are not easy to definitively attribute to dark

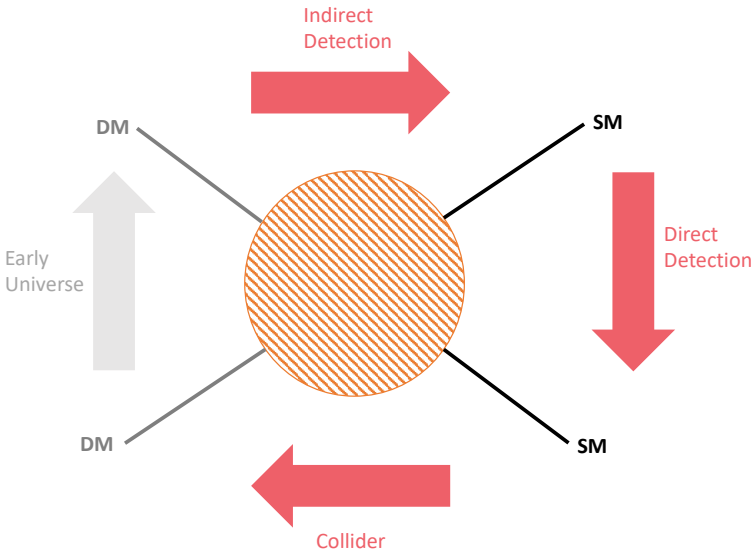

Figure 2.6 *Possible dark matter and standard model interactions, which allow different search strategies.*

matter particles. In Sections 2.4.1, 2.4.2 collider and indirect searches respectively will be described, whilst direct detection will be the subject of Chapter 3.

Bosons with sub-eV mass behave like waves rather than individual quanta, so a different approach must be taken in searches for them, using coherent effects of the oscillating field. Similar principles to those employed to search for particle-like DM are employed — the particles may be produced in laboratory based experiments or particles of astrophysical origin can be detected either indirectly or directly. As with particle-like DM, the different approaches are complimentary, probing different areas of parameter space and enabling checks in the case of discovery. The difference here is in the technology used to achieve this. Many experiments designed to search for axions rely on the axion-photon coupling and inverse Primakoff effect, described in Section 2.4, to detect conversion photons in strong magnetic fields. This technology can also be used to search for ALPs, HPs and more general weakly interacting ultralight particles. Both ALPs and hidden sector particles may cross the eV – keV energy range. So for higher masses they also be detectable in particle scattering experiments, via an effect analogous to the photoelectric effect or in collider/beam dump searches. Searches for ALP/HPs in the LZ direct detection experiment will be discussed in detail in Chapter 5.

2.4.1 Collider and Accelerator

Collider and accelerator searches can be used to test all three types of models shown in Fig. 2.5, with different experimental configurations covering a range of models and parameter space. At the energy frontier, colliders can provide high energy collisions, whilst fixed target and beam dump experiments can probe the intensity frontier. Here, searches for DM models will be discussed in the reverse order to above, going from a more general EFT based approach to searches tailored to complete models.

Coupling of dark matter particles to SM particles would allow their production at high energy particle colliders. At the Large Hadron Collider (LHC) dark matter searches can be performed, most commonly using the two general purpose detectors, CMS and ATLAS. Collider searches fall into two categories: final states with dark matter, where a mono-X signature accompanied by missing transverse energy is expected, and final states without dark matter, where a heavy mediator is searched for. The mono-X signature arises from production of a pair of invisible dark matter particles plus some other particle or photon from

initial state radiation. In the mediator searches the heavy mediator is assumed to decay into a pair of particles and the signature would be a peak in the mass distribution of two jets. Dark matter analyses, including mono-photon, mono-jet and di-jet searches, have been carried out by CMS and ATLAS, [61, 62], with an EFT approach usually used in these searches.

If dark matter couples to leptons, it can be produced by e^+e^- colliders, such as LEP and SuperKEKB. The analysis by the DELPHI experiment at LEP used a mono-photon search, interpreted in an EFT framework to constrain the dark matter couplings to electrons, the cross section and the annihilation rate [63].

Hidden sector searches at colliders and accelerators probe one of the portals introduced in Section 2.3.1, often focusing on the vector portal with hidden photon searches. Production of HPs can occur via [64]:

- Bremsstrahlung: $e^-Z \to e^-ZA'$ (fixed target or beam dump),
- annihilation: $e^+e^- \to \gamma A'$ (collider),
- meson decay: $\pi^0/\eta/\eta' \to \gamma A'$ (fixed target or collider).

The resulting HP may undergo invisible decays to dark matter particles χ, if the HP mass is greater than twice the dark matter mass $m_{HP} > 2m_\chi$, otherwise it can only undergo visible decays to SM final states. For invisible decays the analysis will be a bump hunt in the missing mass distribution, whilst visible decays can use a bump hunt in final state invariant mass e.g. di-lepton resonance searches. For visible decays with short decay lengths, searches for displaced vertices can also be performed.

Fixed target experiments pass a beam through a thin target, then use a set of downstream detectors to measure the products. In electron beam dump experiments HPs are produced via Bremsstrahlung and detected using missing energy searches. For example, the NA64 experiment at CERN used a 100 GeV electron beam to search for sub-GeV HPs [65].

In beam dump experiments particles are also created by collision processes of an incident beam on a primary target and detected in a downstream detector through scattering or decays. The difference to fixed target experiments is a thick target followed by substantial shielding to absorb SM particles and essentially stop the beam. For electron beam dump experiments production is via Bremsstrahlung

and for proton beams it is via a similar process plus meson decays. Many limits from beam dump experiments come from reinterpretation of previous results. For example, the E137 electron beam dump experiment at SLAC and CHARM proton beam dump experiment at CERN [66] were used to set limits for HPs with masses below ~ 1 GeV/c^2. A new experiment which should improve these limits is the BDX electron beam dump experiment at Jefferson Lab [67]. Here, an 11 GeV electron beam incident on a thick target would produce HPs via Bremsstrahlung, which subsequently decay to DM particles $A' \to \chi\bar{\chi}$. The DM particles are then detected in a DsI(TI) crystal detector through scattering processes $\chi a \to \chi e$ or $\chi N \to \chi N$.

An example using annihilation is the planned search by Belle 2, at SuperKEKB, for A' produced in $e^+e^- \to \gamma A'$ [68]. The dark photon is expected to decay to SM particles $A' \to l^+l^-, h^+h^-$ or dark matter $A' \to \chi\bar{\chi}$, giving an energetic photon plus either two oppositely charged tracks (SM decay) or missing energy (dark matter decay). Analogous searches for $pp \to \gamma A'$ followed by $A' \to \chi\bar{\chi}$ can be carried out at the LHC.

An example using meson decays is the NA62 experiment at CERN which uses a high intensity kaon source to search for invisible pion decay $\pi^0 \to A'\gamma$ [69]. The pions are produced in kaon decay $K^+ \to \pi^+\pi^0$ and missing mass is calculated as: $M^2_{miss} = (P_K - P_\pi - P_\gamma)^2$, where P_K, P_π are the kaon and pion momenta measure in track detectors and P_γ is the photon momentum measured in the calorimeter. Missing mass would peak at $M^2_{A'}$ for HP production and at zero for the main $\pi^0 \to \gamma\gamma$ background. This analysis probes the 20 – 120 MeV/c^2 HP mass range, setting limits on the coupling ϵ^2. Meson decay searches have also been carried out by the LHCb collaboration, using both invariant mass and displaced vertex searches for rare $D^* \to D^0 A'(\to e^+e^-)$ decays [70], probing MeV/c^2 – GeV/c^2 HP masses.

Figure 2.7 shows the limits on HP kinetic mixing set by current collider and accelerator experiments, in addition to the projected sensitivities of future experiments.

The Higgs portal can be probed using searches for exotic Higgs decays for example, the analysis carried out by the CMS collaboration in Ref. [71], which searches for Higgs to invisible ZZ' decays.

Sterile neutrinos, as HNL in hidden sectors or as a standalone SM extension, can be probed in processes containing active neutrinos due to their mixing. Searches

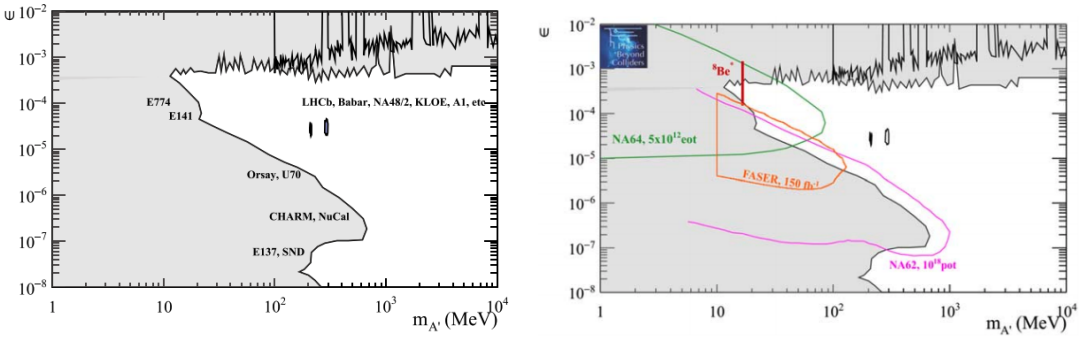

Figure 2.7 *Limits on hidden photon kinetic mixing, ϵ, vs. hidden photon mass. Results from current experiments (left) and projections for future experiments (right), taken from Ref. [64].*

can either be done for missing energy or RH neutrino decay products, if they decay to active neutrinos or other visible final states such as pions, muons or electrons. An example is the NA62 HNL search [72] which looks for $K^+ \to l^+N$ decays through a missing mass ($M^2_{miss} = (P_K - P_l)^2$) search. Neutrino accelerator beams can also be used to search for sterile neutrino mixing or decays. For example, the SBN experiment at Fermilab will be placed in the booster neutrino beam, with multiple identical detectors in the same beam to carry out precise neutrino oscillation experiments [73]. The main aim is to search for new oscillations caused by mixing with eV/c^2 mass sterile neutrinos, however searches for decays of heavier sterile neutrinos are also possible.

Collider searches cannot conclusively detect DM, but they can scan the parameter space of a variety of models to search for hints, which could be searched for in experiments that test the nature of the cosmological particles. Conversely if a direct or indirect detection experiment did detect a dark matter signal, this can be tested by colliders to rule out astrophysical background sources and determine its properties such as mass and spin.

2.4.2 Indirect

Indirect detection aims to detect SM particles produced in the decay or annihilation of dark matter particles, most commonly γ-rays, neutrinos or antimatter. The rdetection ate today depends on: the annihilation or decay rate, the DM density in the area of interest and the number of final state particles produced. This makes indirect searches very model dependent, as both

the astrophysical distribution and interaction cross sections of the DM must be specified.

For models with thermal production via freeze out, such as WIMPs, annihilation had to happen in early universe and should therefore be possible today, even if at a lower rate due to reduced density. WIMP annihilation cross sections determine both relic density and indirect detection signals, so the relic density constrains the rate of indirect detection signals. However, for hidden sector models the relic density is governed by hidden sector annihilation, whilst indirect signals depend on the portal interactions, so the indirect signal rate is less constrained. In hidden sector models the DM annihilates to unstable dark sector particles, which will eventually decay to a mediator that couples, and subsequently decays to, SM particles. This process may take several steps within the hidden sector, forming a multi-step decay cascade. These searches can be less model dependent as the processes within the hidden sector are hidden and what is observed is only the result of the portal interaction. Decays of specific dark matter states, such as sterile neutrinos, can also be considered. These will again be model dependent as the signal depends on the lifetime of the dark matter and the density in the area of interest. For indirect searches observational targets are selected which are expected to have high DM densities and low backgrounds — these include dwarf spheroidal galaxies and the Milky Way centre.

Gamma-ray measurements of these targets have been made by both space and ground based experiments. Direct annihilation to photons: $\chi\chi \rightarrow \gamma\gamma$, would result in a monoenergetic line in the γ-ray spectrum, with energy close to the DM particle mass. Since no astrophysical process is known to produce $\gtrsim$ GeV γ-ray lines this would be a strong indication for a dark matter signal. However, for neutral DM with no electromagnetic interactions this process can only happen at loop level and is highly suppressed. More commonly, DM particles would annihilate to other SM particles which subsequently emit photons, giving a smooth continuous γ-ray spectrum.

Cosmic γ-rays can only be observed directly from space, as their interaction length in the atmosphere is too short for them to reach the Earth before interacting (via e^+e^- pair production). But it is possible for ground based imaging atmospheric Cherenkov telescopes (IACTs) to observe γ-rays indirectly. These detect the Cherenkov light from particles produced in electromagnetic cascades initiated by high energy photons ($\gtrsim$ 100 GeV) in the atmosphere. Simulations are used to reconstruct the energy and position of the initial particles, but uncertainties arise

from atmospheric density profiles.

An example of an IACT is the VERITAS telescope in Arizona, which carried out a search for γ-rays resulting from WIMP annihilation in four dwarf spheroidal galaxies [74]. Limits were placed on the annihilation cross section to $b\bar{b}$, $\tau^+\tau^-$ and $\gamma\gamma$ for WIMP masses 100 GeV/c^2 – 100 TeV/c^2, as shown in 2.8. The next generation IACT γ-ray observatory, the Cherenkov Telescope Array (CTA), will consist of two arrays in Chile and La Palma. This will cover a large fraction of the sky, using three different telescope sizes to observe γ-ray energies 10 GeV – 300 TeV[75]. This will allow the CTA to test thermal annihilation cross sections for DM masses at the $\sim$ TeV scale, providing a stringent test of the WIMP paradigm.

Space based telescopes offer the advantage of directly detecting γ-rays, but their limited size means they can only cover energies $\lesssim$ TeV. The space based Fermi Large Area Telescope (LAT) detects γ-rays, using conversion to e^+e^- pairs, with a conversion tracker and calorimeter. The LAT search for DM annihilations in 15 dwarf spheroidal galaxies gave the strongest limits to date on DM annihilation cross sections to $b\bar{b}$, $\tau^+\tau^-$ for 1 GeV/c^2 – 10 TeV/c^2 masses [76], as shown in Fig. 2.8. These constraints lie below the canonical thermal relic cross section for WIMP masses less than 100 GeV/c^2.

The galactic centre is expected to provide higher annihilation signal rates than dwarf spheroidal galaxies, due to the high dark matter density and proximity to Earth. But the Milky Way has a more complex structure and the galactic centre is bright in all wavelengths, so backgrounds are higher and more difficult to estimate. An excess of γ-rays, over the expected emission from diffuse and point sources, was observed by the LAT experiment at energies of 1 – 3 GeV [77]. Whilst this could indicate WIMP annihilation, there is an argument attributing the excess to a population of milli-second pulsars and attempts to resolve these two explanations have proved inconclusive [78, 79]. These searches also have strong dependence on the galactic DM density profile, which provides a large uncertainty.

Another possible excess was observed within $\sim$ 1 kpc of the galactic centre, in an all sky map of 511 keV γ-ray line emission, using observations from the Integral-SPI space based spectrometer [80]. This could be consistent with DM annihilation directly to e^+e^-pairs or via an excited state [81], but there are also valid astrophysical explanations [78, 82].

At lower energies, X-rays could also be used as an indirect detection signal,

produced by inverse Compton scattering of SM charged DM annihilation products or in the decay of $\sim$ keV dark matter such as sterile neutrinos. Whilst the dominant decay mode of sterile neutrinos would be two neutrinos, a radiative decay to a neutrino plus a photon is also possible, resulting in a line feature at half the neutrino mass. A 3.55 keV X-ray signal was observed in the stacked XMM-Newton spectrum of 73 galaxy clusters [83], which could be attributed to sterile neutrino decay. However, this is in tension with non-observation of the feature in a separate study of 81 and 89 galaxies using Chandra and XMM-Newton [84]. Future studies with improved energy resolution are required to conclusively determine the nature of the 3.55 keV feature.

Neutrinos from dark matter annihilation provide an alternative indirect detection channel, produced when DM annihilates to SM particles which subsequently decay to neutrinos. Neutrino experiments can be used to observe the galactic centre and place limits on the annihilation cross section, as done using γ-rays. The IceCube experiment, a cubic kilometre of instrumented ice at the South Pole, which detects Cherenkov light emitted by secondary particles produced in

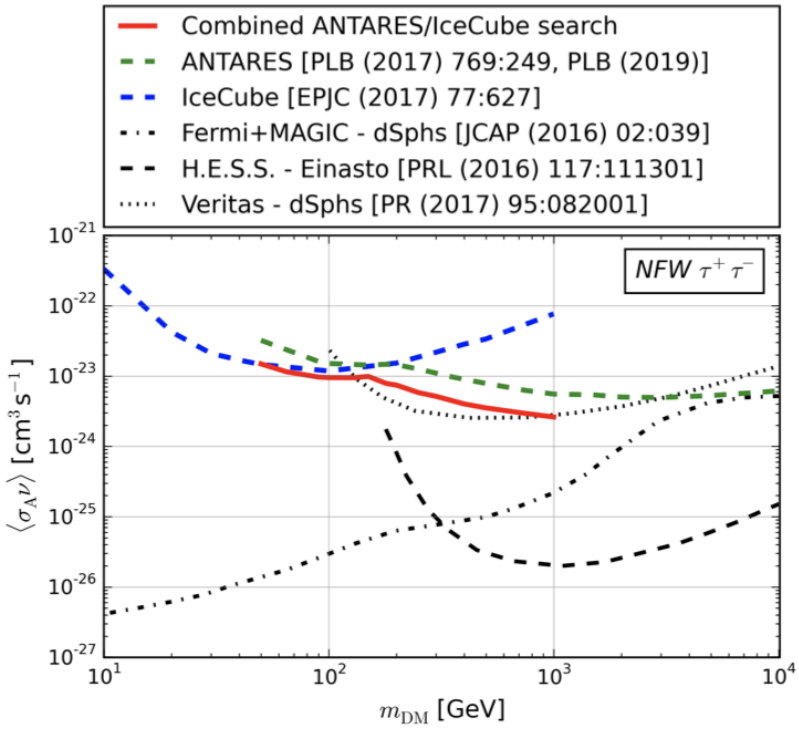

Figure 2.8 *Limits on WIMP annihilation cross sections set by VERITAS, Fermi, IceCube and ANTARES individual and joint analyses, taken from Ref. [85].*

neutrino interactions with the ice, can be used to search for >10 GeV neutrinos. A joint analysis has been carried out by IceCube and the ANTARES experiment, an underwater neutrino telescope in the Mediterranean Sea which also detects Cherenkov light from secondary particles produced by neutrino interactions. No excess was observed and limits were set on the DM annihilation cross section, in the $b\bar{b}$, $\mu^+\mu^-$, W^+W^- and $\tau^+\tau^-$ channels, for 10 GeV/c^2 – 1 TeV/c^2 WIMPs shown in Fig. 2.8, improving on the individual limits by a factor of two [86]. The Super-Kamiokande experiment is a water Cherenkov detector holding 50 tonnes of ultrapure water, which has also carried out a search for excess neutrinos from the galactic centre. Again, no excess was found and limits were set on the same neutrino annihilation channels plus $\nu\bar{\nu}$ for dark matter masses in the range 1 GeV/c^2 – 10 TeV/c^2 [87], as shown in Fig. 2.8.

Unlike photons, neutrinos are able to pass through matter without absorption, so neutrino signals could also arise from DM captured in celestial bodies. Depending on the incident flux, dark matter mass and nucleon scattering cross section DM can be captured in bodies such as the Sun or Earth. Higher density within the body increases DM annihilation rates and equilibrium between the capture and annihilation may be reached. This means the annihilation rate, and therefore neutrino flux, can be completely determined by the capture rate or the DM-nucleon scattering cross section. This gives a unique probe of scattering, rather than annihilation cross section, allowing direct comparison with direct detection experiments. The IceCube experiment has set a limits on spin independent and spin dependent WIMP-nucleon cross sections for 20 GeV/c^2 – 10 TeV/c^2 WIMP masses, for the $b\bar{b}$, W^+W^- and $\tau^+\tau^-$ annihilation channels for this captured Solar neutrino population [85]. Searches for neutrino annihilations from DM captured in the Sun have the advantage of no dependence on the DM halo profile and no confusing foreground sources.

A different prospect for indirect detection are stable charged particles, produced as the end point of DM annihilation or decay. In order to minimise the background, relatively rare antimatter particles such as positrons, antiprotons or antinuclei are typically used. These are expected to be produced in equal quantities to their matter counterparts in DM annihilation or decay, but exist in much lower quantities from other sources. The main disadvantage of using charged particles is that they are deflected by galactic magnetic fields during propagation, so pointing to the source is not possible. They can also be scattered and absorbed — detailed particle transport modelling is required to minimise

uncertainties from propagation and energy losses. Searches have been carried out by the space based PAMELA [88] and AMS [89] experiments, with both observing a positron excess in the $1 - 500$ GeV energy range. However, there are also viable astrophysical sources which cannot be ruled out, as it is difficult to accurately resolve the source of positrons.

As discussed above, there are good prospects for indirect detection of hidden sector dark matter, with a plethora of different models offering a wide variety of phenomenology. Since all of the annihilation details occur in the hidden sector it is possible to have a detectable indirect detection signals if the cross section is large, even if the portal coupling is small and direct or collider searches are heavily suppressed. However, model building in light of the constraints can be challenging given the wide variety of possible models. In Ref. [90] a model independent approach is taken to parametrize existing constraints and consider potential signals in terms of hierarchical decay cascades.

A different approach also has to be taken for non-thermally produced dark matter, such as axions. For ALPs photon-axion conversion is expected in strong intergalactic magnetic fields and this would distort the observed spectra of γ-ray sources. The CTA has proposed using blazars with different densities and flare diractions to search for any spectra anomalies which would indicate axion production [91].

Mirror dark matter has poor indirect detection prospects as it arises from mirror baryon asymmetry, so there would be too few mirror antibaryons to give observable annihilation signals. The only possible signal could be an excess of positrons produced via kinetic mixing in mirror supernovae [55].

In summary, indirect detection can constrain dark matter models and provide hints at the existence of a given candidate. However, whilst there have been a few anomalies observed there are many modelling challenges in terms of both backgrounds and the astrophysical DM distributions, which make a conclusive detection difficult. Complementarity between different types of indirect detection experiment and direct/collider searches will be key in establishing the detection of a dark matter candidate.

2.4.3 Novel/Wave Searches

For wave-like dark matter candidates, discussed in Section 2.2, searches can make use of coherent wave effects. Axion searches have typically made use of the axion-photon coupling in either laboratory experiments, haloscopes or helioscopes. These techniques can be generalised to search for other ultralight bosons including ALP and HP searches.

The laboratory searches are analogous to collider searches for weak scale dark matter — with dark matter created and detected under special conditions. These fall into three categories: regeneration or light-shining through wall (LSW) experiments, polarization experiments and long range force experiments.

The ALPS-II experiment at DESY is an example of a LSW experiment which injects a powerful laser into a cavity containing a strong magnetic field that could convert photons to axions. After a wall there is a second cavity with a strong field to reconvert the axions into photons, which are then detected. This follows on from the ALPS-I experiment, which carried out searches from weakly interacting sub-GeV particles including ALPs, HPs and hidden sector "mini-charged" particles with U(1) charges [92]. ALPS-II aims to improve on the ALPs-I sensitivity by three orders of magnitude, probing ALP masses below 10^{-4} eV/c^2, HP masses $< 10^{-3}$ eV/c^2 and mini-charged particles with masses 10^{-2} – 1 eV/c^2 [93].

Polarization experiments, such as PVLAS, use the laser beam itself to detect conversion — with ALPs or millicharged ($\pm\epsilon$e) particles expected to cause anomalous polarisation effects in light propagating in a transverse magnetic field. Limits were placed on axion-photon coupling for ALP masses $10^{-4} - 10^{-2}$ eV/c^2 and ϵ for scalar and fermion millicharged particles with masses $10^{-4} - 1$eV/c^2 [94].

Long range or fifth force experiments search for interactions mediated by new bosons. The ARIADNE experiment plans to do this using an NMR method, where the axion coupling mediates fermion interactions, driving spin precession in polarised ^{3}He [95]. This will probe the axion-nucleon coupling for axion masses $10^{-4} - 10^{-2}$ eV/c^2.

Laboratory searches offer the advantage of having no dependence on the astrophysical particle distribution (in either the Sun or DM halo). But producing

the particles in the experiment means there is extra suppression from weak couplings, which will enter the rate term twice. They also suffer the same problem as collider and accelerator searches — there is no guarantee that any new particles detected constitute astrophysical dark matter.

For even smaller masses, atom interferometry can be used, measuring the relative phase difference induced by perturbations in atomic transition frequency by ultralight bosonic dark matter fields. The AION programme has a staged plan to build 10 – 1000 m baseline atom interferometers with cold strontium atom sources. This will give sensitivity to scalar DM interactions with electrons, photons and the Higgs portal for DM masses below 10^{-10} eV/c^2 [96]. A longer term plan is to extend this technology to the space based AEDGE programme. This would use two cold atom interferometers on separate satellites, with a very long (4.4×10^7m) baseline, to measure the differential phase shift, significantly improving sensitivity at the lowest masses [97].

Haloscopes aim to detect relic particles in the halo, whilst helioscopes aim to detect those produced in the Sun, as described in Section 2.2.3. These are analogous to weak scale direct detection experiments. Detection is via the same principle of regeneration in a magnetic field as LSW experiments, using the inverse Primakoff effect, but the source of particles is not terrestrial.

Haloscopes can either use microwave cavities or dielectrics to resonantly enhance photon production of photons at a certain frequency, determined by the axion mass. In both cases the resonant frequency can be tuned and a scan over axion masses is performed. The ADMX experiment, at the University of Washington, is a haloscope which has reported results for 2.81 – 3.31 μeV/c^2 ALP masses and should have sensitivity up to 10 μeV/c^2 [98]. Larger cavities are needed to probe higher frequencies and therefore masses. This can be problematic due to higher energy losses for high volumes, so cavity haloscopes can only probe masses up to $\sim$ 70 μeV/c^2. Dielectric haloscopes use stacked dielectric disks in a strong magnetic field, arranged so that coherent emission constructively interferes, allowing tuning by varying disk separation. This technique allows larger volumes with less energy loss to be used. The planned MADMAX dielectric cavity experiment should be able to probe ALP masses in the 40 – 400 μeV/c^2 range [99].

Haloscopes probe the $g_{a\gamma}$ coupling from conversion, whilst helioscopes can probe all three couplings, due to different production mechanisms in the Sun, described in Section 5.1.3. Helioscopes use the same idea of resonant axion-photon

conversion in a strong field, but the $\sim$ keV energies of axions produced in the Sun mean that X-ray photons are produced. Experiments consist of a dipole magnetic with the aperture pointed to track the Sun and a vacuum cavity in the magnetic field instrumented using X-ray optics. The CAST helioscope experiment, based at CERN using an LHC protoype magnet, has set limits on $g_{a\gamma}, g_{ae}, g_{aN}$ for axion masses up to 1 eV/c^2 [100]. The next generation IAXO helioscope plans to improve on the CAST sensitivity by 4 – 5 orders of magnitude using stronger magnets and a larger volume [101].

Direct searches for ALPs can be reinterpreted as HP searches, where the HP photon conversion occurs due to kinetic mixing, allowing limits to be set on the kinetic mixing strength for different HP masses. Another approach used for HP searches are dish antenna, where HPs induce oscillation of free electrons in a conductor, resulting in photon emission from the surface and a spherical mirror conductor will focus these photons enabling their detection. The FUNK experiment has searched for HPs in the 2.5 – 7 eV/c^2 mass range using this method [103].

Current limits on the axion-photon coupling, $g_{a\gamma}$, arising from the methods discussed above are shown in Fig. 2.9, indicating the complementarity of these

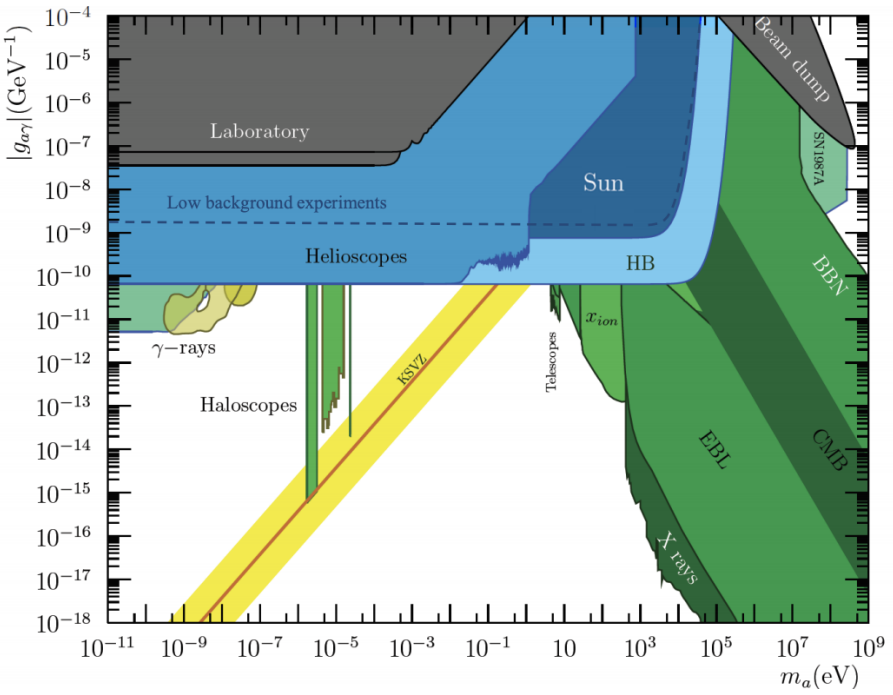

Figure 2.9 *Current limits on axion-photon coupling, from different experiemtnal approaches and astrophysical constraints, taken from Ref. [102].*

searches. Constraints on a single coupling can easily be compared in a model independent way, but similarly to the particle searches, model dependence is introduced when comparing different couplings.

In this chapter we have seen that the required properties for dark matter in Section 2.0.1 lead to different model building approaches, shown in Fig 2.5. These approaches lead to models on a range of scales as shown in Fig. 2.1, which have varied phenomenology and require a range of complimentary search strategies. The searches aim to detect or rule out models, and need to cover as much parameter space as possible. Pushing down sensitivity or extending it to new parameter space is achieved by improving existing experiments or using completely new technology. Here, collider and indirect searches for particle dark matter, plus laboratory and halo/helio-scope searches for wave dark matter have been discussed. The remainder of this thesis will focus on direct detection searches, in particular those using electron recoils to probe non WIMP models.

Chapter 3

Direct Detection

As introduced in Section 2.4, direct detection searches aim to detect signals from galactic dark matter (DM) interacting with ordinary matter in a terrestrial detector. Historically, these searches have focused on nuclear recoils induced by WIMP dark matter, but the wide range of possible models, outlined in Sections 2.2, 2.3, give much more diverse phenomenology. This has led to a range of experimental innovations, with different techniques optimised to probe different models and areas of parameter space.

3.1 Interaction Types

Galactic dark matter incident on a detector can scatter off an atomic nucleus or electrons, or be absorbed by electrons, depending on the characteristics of the dark matter particle. Expected interaction rates will depend on detector properties, plus the dark matter particle characteristics and astrophysical properties. The three types of interaction between incoming dark matter and the target, which would lead to a signal, are shown in Fig. 3.1 (note that this is a simplistic diagram and sub leading order loop contributions will be discussed later).

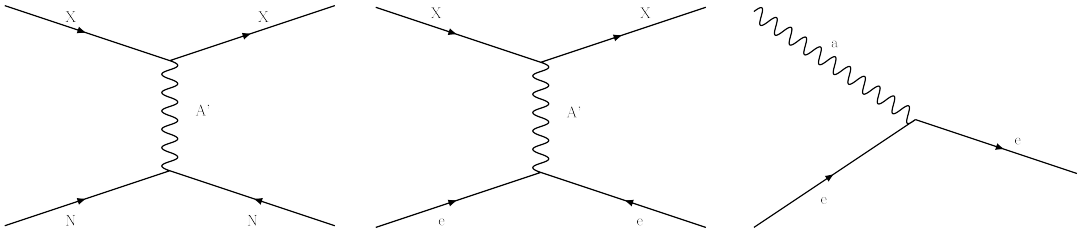

(a) *DM-nucleon scattering* **(b)** *DM-electron scattering* **(c)** *DM-electron absorption*

Figure 3.1 *Feynman diagrams showing the possible interactions of dark matter with particle in the target in a direct detection experiment.*

3.1.1 Nucleus Scattering

The idea of detecting neutrinos [104] and dark matter [105], via elastic scattering with atomic nuclei, was first proposed in the 1980s. This interaction with the nucleus results in a nuclear recoil (NR) event, for either elastic or inelastic scattering. Expected interaction rates for WIMPs in the galactic halo and idea of modulation studies, were first outlined in Ref. [106]. The subsequent discussion follows Ref. [107], with recent reviews provided by Refs. [108, 109].

For elastic scattering of incoming dark matter with a target particle, the momentum and energy transfer can be calculated non-relativistically in the centre of mass frame, as shown in Fig. 3.2. The momentum and energy transfer are given by: $|\bar{q}|^2 = 2\mu^2 v^2(1-\cos\theta)$ and $E_R = 2\mu^2 v^2(1-\cos\theta)/m_N$, where v is the incoming particle velocity, m_N is the nuclear mass and θ is the angle between the incident and scattered particles. The reduced mass is given by: $\mu = (m_N m_\chi/(m_N + m_\chi)$,

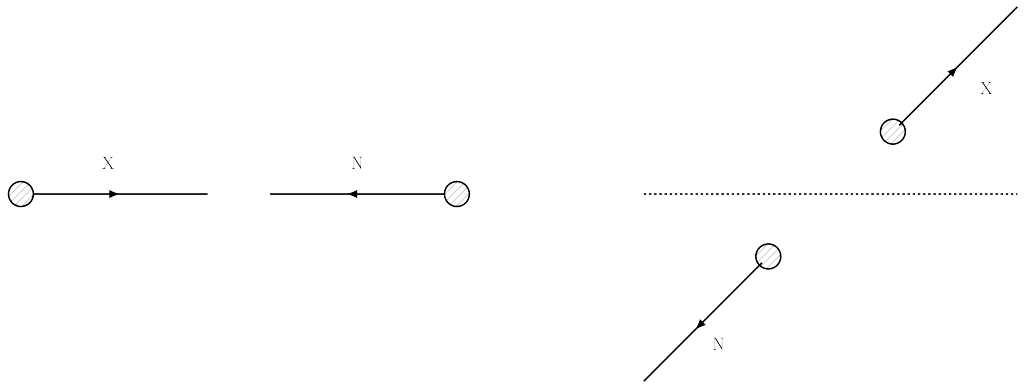

Figure 3.2 *Elastic scattering of dark matter χ with target particle N in the centre of mass frame.*

where m_χ is the dark matter particle mass.

Energy spectra as a function of nuclear recoil energy E_{nr} are calculated using the differential rate of elastic scattering of incoming dark matter off the target nucleus:

$$\frac{dR}{dE_{nr}} = \frac{\rho_0 M}{m_N m_\chi} \int_{v_{min}}^{v_{esc}} v f(\bar{v}) \frac{d\sigma}{dE_{nr}} dv. \tag{3.1}$$

Here, the detector parameters are: detector target mass M and target nucleus mass m_N. The dark matter particle properties are: mass m_χ and cross section σ. The astrophysical properties are: local dark matter density ρ_0 and velocity distribution $f(\bar{v})$.

The product of velocity, weighted by distribution, and the differential cross section, with respect to energy, is integrated over dark matter velocities from minimum velocity, v_{min}, to escape velocity, v_{esc}. Minimum velocity, needed to induce a recoil of energy E_{nr}, is given by:

$$v_{min} = \sqrt{\frac{E_{nr} m_N}{2\mu^2}}. \tag{3.2}$$

Escape velocity is the speed above which objects are no longer bound in the gravitational potential of the galactic halo, estimated to be $v_{esc} = 553^{+54}_{-41}$ km/s [110].

Astrophysics Input

As seen in Eqn. 3.1, the local density ρ_0 and velocity distribution $f(\bar{v})$ of dark matter are important for predicting signal rates.

The local density can be determined either using the vertical motion of stars close to the Sun or by extrapolating the galactic rotation curve. In both methods there is uncertainty from the contribution of baryons (gas, stars, stellar remnants), which must be subtracted to infer ρ_0. Generally, a canonical value of $\rho_0 = 0.3$ GeV/cm^3 has been used [107], however recent Gaia data suggests a value in the range 0.4 – 1.5 GeV/cm^3 [111].

Typically, the Standard Halo Model is used for the velocity distribution. This assumes dark matter is distributed as an isothermal sphere with an isotropic

Maxwell Boltzman velocity distribution, truncated at the escape velocity:

$$f(\bar{v}, \bar{v}_E) = Ne^{-(\bar{v}+\bar{v}_E)^2/\bar{v}_0^2}. \tag{3.3}$$

Here, N is the normalisation, $\bar{v}$ is the dark matter velocity on the target, $\bar{v}_E$ is the velocity of the Earth with respect to the dark matter halo and $\bar{v}_0$ is the galactic rotation velocity. This velocity distribution gives the flat rotation curves seen in Section 1.2 and is a simple reference model which allows for easy comparison of results. However, recent observational data suggests this model is not entirely accurate and other models with asymmetric, flat or rotating dark matter halos exist.

As the Earth orbits the Sun its velocity with respect to the dark matter halo varies, with a Galilean boost depending on direction. The Earth velocity with respect to the dark matter halo is the sum contributions from the galactic rotation velocity, the Sun's peculiar velocity $\bar{v}_{pec}$ and the Earth's orbital velocity $\bar{v}_{orb}(t)$:

$$\bar{v}_E(t) = \bar{v}_0 + \bar{v}_{pec} + \bar{v}_{orb}(t). \tag{3.4}$$

Galactic coordinates can be used for these vectors, where x points towards the galactic centre, y is in the direction of galactic rotation and z points towards the North Pole. The galactic circular velocity vector is $\bar{v}_0 = (0, v_c, 0)$, with a standard value $v_c = 220$ km/s determined from many independent measurements [107]. Peculiar motion of the Sun (relative to the galactic rest frame) is determined from parallaxes and proper motions of stars close to the Sun, giving $\bar{v}_{pec} = (10.0 \pm 0.4, 5.2 \pm 0.6, 7.2 \pm 0.4)$ km/s [107].

The orbital velocity introduces modulation: $|\bar{v}_{orb}(t)| = v_+ \cos(\theta)[\omega(t - t_0)]$, with amplitude $v_+ = 30$ km/s and angle between the Earth's orbit and galactic plane $\theta \approx 60°$. The angular frequency is: $\omega = 2\pi/T$, with period $T = 1$ year, where $t_0 =$ 2nd June is the date at which both speeds add up maximally. This modulation is expected to give $\sim 5\%$ variation in the magnitude of the velocity.

Particle Physics Input

The particle physics input to the rate calculation is the interaction cross section. Here, the WIMP-nucleon differential cross section is the sum of spin-independent

(SI) and spin-dependent (SD) contributions:

$$\frac{d\sigma}{dE_{nr}} = \frac{m_N}{2\mu^2 v^2}\left(\sigma_0^{SI} F_{SI}^2 + \sigma_0^{SD} F_{SD}^2\right), \tag{3.5}$$

where F^2 are the form factors and σ_0 are the cross sections in the limit of zero momentum transfer. The form factors for specific target nuclei are calculated in Ref. [112] and [113] for the SI and SD cases respectively. Typically, the phenomenological Helm form factor is used for SI calculation in direct detection experiments, whilst the full shell-model calculation is required for SD form factors. For the SI interactions all nucleons contribute coherently to the cross section, whereas for the SD interactions nuclear spin contents, due to protons and neutrons, must be considered. This means that the SI cross section depends on target mass, whilst the SD cross section depends on target spin — hence different target nuclei are better suited to probing each.

These SI and SD WIMP-nucleon interactions are a specific subset of more general effective field theory operators. As described in Section 2.3.3, these can be used to construct a large number of possible four point interactions and sum over all contributions.

3.1.2 Electron Scattering

For light dark matter (with $m_\chi \ll m_N$), the energy transferred in an elastic recoil with the nucleus is: $E_{nr} = q^2/2m_N \sim m_\chi^2 v^2/2m_N$ [114]. For sub-GeV scale dark matter masses this will give NR energies below the lowest possible thresholds. However, the total energy available from the incoming dark matter kinetic energy is larger: $E_{tot} = 1/2 m_\chi v^2$ (with no $1/m_N$ factor), and it is possible for DM to scatter off atomic electrons to make use of this full energy. These electron recoil (ER) events can happen via ionisation and excitation, which require $\sim$ eV energy transfer — so they are possible for $\sim$ MeV/c^2 dark matter.

3.1.3 Electron Absorption

Another interaction type, accessible for (pseudo)scalar DM candidates such as ALPs or HPs, is absorption by bound electrons in the target [115]. This occurs via an effect analogous to the photoelectric effect, resulting in ejection of the

electron from the atom, giving an ER event. The energy deposited is equal to the mass of the particle, plus a negligible incident kinetic energy, resulting in a single monoenergetic peak signal, rather than a continuous spectrum as seen for scattering.

3.2 Direct Detection Technologies and Experiments

Direct detection aims to measure one of three signal types, shown in Fig. 3.3, which can arise from energy deposition:

- Ionisation — energy transferred in scattering results in an electron being released from the target atom. A signal of one or more electrons can be measured in semiconductors, noble liquids or low pressure gas detectors.
- Scintillation — prompt emission of a photon when an excited target atom de-excites. A signal of one or more photons can be measured in scintillators

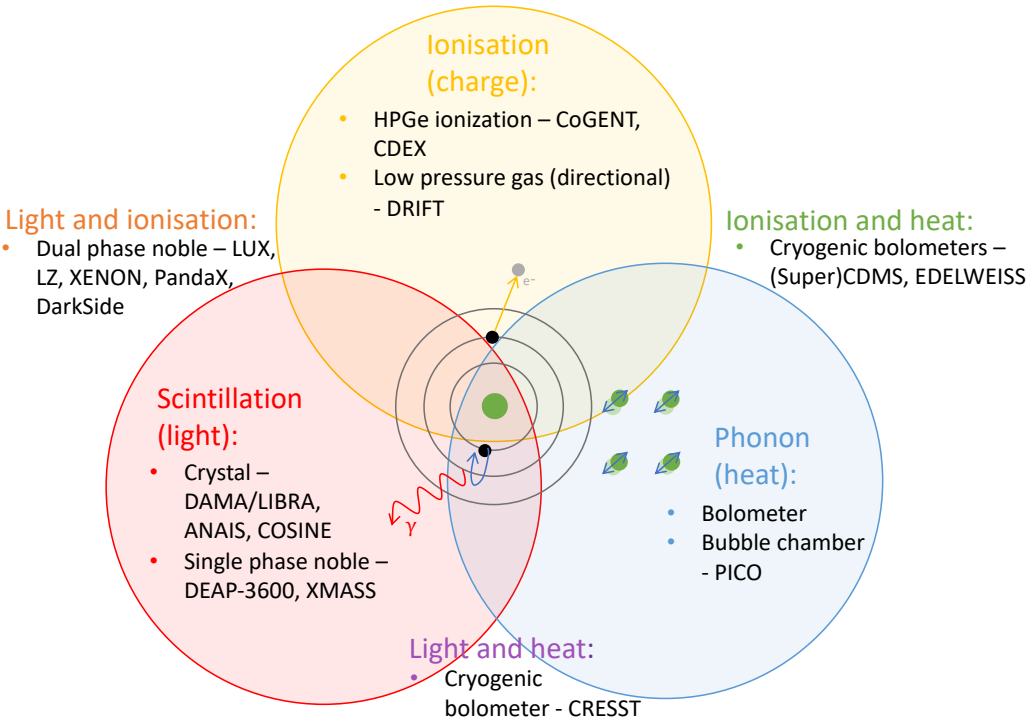

Figure 3.3 *Different types of signal in direct detection experiments with examples of technologies and experiments using each.*

such as noble liquids or crystals.

- Phonon — recoil energy is converted to a collective excitation causing vibrational motion of the lattice. A heat or acoustic signal can be detected in superconductors, superfluids or cryogenic bolometers.

For a recent review of WIMP direct detection see Ref. [108] and for new ideas in the field see Ref. [116].

3.2.1 General Backgrounds

Particles from radioactive decays in detector materials, cosmogenic particles and various neutrino populations can also interact with target atoms. These cause backgrounds to the dark matter event search — inducing both NR and ER events. Mitigation of the backgrounds, by minimising and characterising them, is essential when searching for rare ($10^{-3} - 1$ event/kg/day) dark matter interactions.

Experiments are generally located deep underground to suppress cosmic rays, which makes the hadronic component of the cosmic ray flux negligible. However, cosmic ray muons can penetrate deep underground, creating high energy neutrons which can give rise to NR events. Shielding around the detector reduces this background, along with other neutron and γ-ray backgrounds from the laboratory environment. Radioisotope decays can result in γ-rays or β particles entering the detector — causing ER events. Due to the absorption length, γ-rays from outside the detector and β particles from internal radioisotope decays inside the detector are the biggest concerns. These can be minimised by choosing the most radiopure materials for detector construction.

The final set of backgrounds arise from neutrino interactions. Solar neutrinos from the pp chain and ^{7}Be give rise to ERs, whilst ^{8}B neutrinos as well as atmospheric and supernova origins will give NRs. Scattering of incoming neutrinos with nucleons, via weak neutral current interactions, is coherently enhanced giving coherent elastic neutrino-nucleus scattering (CEνNS), with the cross section enhanced by a factor proportional to the square of the number of nucleons [117].

Since most of the background will be ERs from radioisotope decays, the ability to discriminate between ER and NR events is beneficial in a search for NRs from WIMP scattering. If position information is available fiducialisation may also be

used to exclude data in outer regions of the target, where background rates will be higher.

Once backgrounds from radioactive decays become subdominant, irreducible backgrounds from physics processes become important. Nuclear recoils from CEνNS form an irreducible background which fundamentally limits the sensitivity an experiment can achieve — this is the so called "neutrino floor". Detailed description of the backgrounds, specific to the LUX and LZ experiments, are given in Sections 4.3.3 and 5.1.2.

3.2.2 Detection Techniques

A direct detection experiment will make use of at least one of the ionisation, scintillation or phonon channels introduced above. Using two allows greater discrimination between event types, with different technologies utilising different channels and combinations. The general properties required for a detector searching for these signals from rare dark matter interactions are:

- Low threshold — ability to detect $\sim$ keV energy transfers.
- Scalable mass — large exposure needed for statistical significance in rare event searches.
- Background mitigation — important to have low background and ability to discriminate signal and background events.

Technology developed with the primary aim of detecting NR events from WIMP scattering will be discussed here. Then in Section 3.2.3 alternative searches using electron interactions will be outlined.

Ionisation:

The first direct detection search, carried out in 1987, used a high purity germanium ionisation detector [118]. More recently the CoGENT [119] and CDEX [120] experiments used p-type point contact germanium detectors, with CDEX-10 currently running and CDEX-1T upgrade planned. The small ($\sim$ eV) band gap in Ge gives low energy thresholds and good energy resolution. Low target nucleus mass and low thresholds make this technology well suited for probing low mass WIMPs (below 10 GeV/c^2). However, measuring ionisation

only does not allow for discrimination between ER and NR events. The high capacitance of Ge diodes above $\sim$ 1 kg scale makes large detector masses difficult to achieve, instead an array of 1 kg detectors can be used, as proposed for CDEX-1T [120].

The NEWS-G experiment also makes use of ionisation signals, in spherical proportional counters containing noble gas, with a radial electric field which drifts ionisation charges to a central anode sensor. Different light noble gas targets (H, He, Ne) can be used to probe a range of sub-GeV dark matter masses. A prototype ran at Modane Underground Laboratory (LSM), with a 9.7 kg day total exposure, reporting results in 2018 [121]. The next phase of NEWS-G involves installing a larger detector at SNOLAB.

A different ionisation detector technique is used by directional detectors, with low pressure gas time projection chambers used to measure the direction of a recoiling nucleus from ionisation tracks. A dark matter signal coming from the direction of the constellation Cygnus would confirm the galactic origin and provide powerful discrimination against backgrounds. An example is the DRIFT experiment at Boulby Mine — a 1 m^3 multi wire proportional chamber holding 139 g target gas, which contains CS_2 negative ions to transport ionisation tracks to readout planes [122]. However, this technology is currently limited by target size and backgrounds from the wire grid.

Scintillation:

Another single phase technology which can achieve a large mass, using an array of detectors, is scintillator arrays. Thalium doped sodium iodide, NaI(Tl), crystals are commonly used, with light readout using photomultiplier tubes (PMTs). The advantage of this is a stable and scalable detector, which has low mass target nuclei and low thresholds. But there is a problem of high intrinsic backgrounds and ER/NR discrimination or fiducialisation, which would reduce these, are difficult. Therefore, a search for a modulation signal above background is often carried out, rather than an event level analysis. The most prominent example of this type of detector is DAMA/LIBRA, using 250 kg of highly radiopure NaI(Tl), located at Laboratori Nazionali del Gran Sasso (LNGS) [123]. A total exposure of 2.46 tonne years in the 2 – 6 keV energy range, shows evidence for a modulating signal at 12.9 σ significance (with a slightly smaller significance in the 1 – 6 keV range, after the threshold was lowered in phase 2). Other experiments have been constructed to test this claim of dark matter scattering, via ERs or NRs. These

include NaI detectors ANAIS at Canfranc [124] and COSINE-100 at Yangyang Underground Laboratory [125]. Neither of these experiments have seen evidence of modulation. The most recent ANAIS result shows incompatibility with the DAMA modulation at 3.3 σ and 2.6 σ for the 1 – 6 keV and 2 – 6 keV energy ranges [126].

Scintillation signals can also be detected using liquid noble elements, such as liquid xenon (LXe) or liquid argon (LAr). These materials are good scintillators, have self shielding properties and can be used to make dense and compact targets. Typically the liquid scintillator is contained in a spherical chamber, surrounded by PMTs for maximum light collection efficiency. Photon timing and PMT position allow for 3D position reconstruction, so fiducialisation of the target volume is possible. In LAr pulse shape discrimination can also be used to distinguish between ER and NR events. High thresholds mean these experiments are best suited to searches for WIMP masses above 10 GeV/c^2. Examples include the XMASS experiment, located at Kamioka Observatory, with a 97 kg fiducial volume of LXe [127]. An example using LAr is DEAP-3600 located at SNOLAB, with a 758 tonne day exposure resulting in the best SI limit in liquid argon [128].

Phonon:

Alternatively, heat/phonons from interactions can be detected using bubble chambers, where heat triggers phase changes in a superheated liquid. This results in the formation of bubbles, which can be detected acoustically and optically. A target containing a nucleus with uneven total angular momentum can be used to investigate the spin dependent interactions. The PICO bubble chamber, located at SNOLAB, using a C_3F_6 target, gives the most stringent DM-proton SD limits [129]. An upgrade to a tonne-scale detector, PICO-500, is underway.

Two channels:

In order to improve background discrimination detectors may utilise two of these channels — the ratio of energy deposited in the two channels will vary between ER and NR events.

Cryogenic bolometers use crystals (typically Ge or Si) cooled down to $\sim$ mK temperatures, coupled to a thermal bath to detect heat deposited within the detector, along with either light or charge readout. For example the CDMS-II experiment, at Soudan Underground Laboratory, used Ge and Si detectors to detect phonons and ionisation [130]. An energy deposition in one of the

six cylindrical Ge or Si detectors would lead to creation of electron-hole pairs (ionisation) and phonons. An applied electric field drifts the charges to be detected at electrodes, whilst the phonons are detected using superconducting transition edge sensors. The higher ionisation yield of NR events, compared to ER, means the phonon to ionisation signal ratio can be used for discrimination and the two channels also allow for accurate energy measurement independent of interaction type. The CDMS programme is continued with SuperCDMS, which has increased target mass using 15 detectors with interleaved electrodes [131]. First results have been obtained from running at Soudan [132] and the experiment will move to SNOLAB to benefit from greater cosmic ray shielding deeper underground. The experiment has also been run as CDMSLite, with a high bias voltage to amplify the ionisation signal. This reduces the threshold in order to probe lower WIMP masses down to ~ 0.2 GeV/c^2, but this also reduces the discrimination power [133].

The EDELWEISS experiment, at LSM, also uses phonon and charge detection in cylindrical germanium bolometers [134]. A 33.4 g high purity Ge crystal is operated at ~ 20 mK, with electrodes to read out ionisation charge and heat sensors for phonon detection. Again the low threshold and good energy resolution make this experiment well suited to low mass WIMPs.

The CRESST experiment at LNGS, uses the phonon channel along with scintillation light in calcium tungstate, $CaWO_4$, crystals operated at ~ 15 mK [135]. Both the phonon and scintillation light signal, absorbed in a silicon-on-saphire light absorber, are measured with transition edge sensors. Scintillation light yield is higher for ER events than NR events, so the ratio of energies in the light and phonon channels can be used for event by event discrimination and precise energy determination. Dark matter masses as low as 160 MeV/c^2 can be probed, due to low energy threshold, good energy resolution and low atomic mass of oxygen.

Dual phase noble liquid experiments, operating as time projection chambers, use the ionisation and scintillation channels. The different light and charge yields of ER and NR events allow for event level discrimination. These experiments typically use xenon (e.g. LUX, LZ, XENON, PandaX) or argon (e.g. DarkSide). Analysis using the charge signal only can also be carried out, lowering the threshold below 1 keV, as done by XENON1T [136]. More details on the operating principle and results from dual phase TPCs are given in Section 3.3.

3.2.3 Electron Interaction Searches

As introduced in Section 3.1.2, the kinematics of electron interactions allow greater energy transfer than nucleus interactions for light dark matter. Electron interactions can also result in the three channels shown in Fig 3.3, so technology developed for weak scale (WIMP NR) direct detection can be adapted to use electron interactions for light dark matter searches. However, in these searches radioactive backgrounds cannot be as effectively suppressed using ER/NR discrimination, as most will be ERs.

Electron Scattering Searches

Scattering of an electron, as shown in Fig. 3.1, allows keV/c^2 – GeV/c^2 dark matter masses to be probed. The full energy deposit can be transferred to ionisation and excitation, unlike the less efficient transfer of energy to surrounding electrons following a nuclear recoil. These signals can be detected in semiconductors, superconductors or liquid noble elements. Ionisation of the target electron in a semiconductor (Ge or Si) would result in it being excited from the valence band to the conduction band, where it can be drifted and detected. A semiconductor with a $\sim$ eV bandgap allows dark matter masses as low as $\sim$ MeV/c^2 to be probed [114]. For example, the EDELWEISS experiment carried out electron recoil searches for solar axions [137], dark photons and dark matter interacting with electrons via either a heavy or light mediator [138]. Whilst noble liquid detectors do not benefit from thresholds as low as those in semiconductors, they can also detect ionisation signals from ER events. The XMASS, LUX and XENON1T experiments have carried out solar axion analyses using electron recoils [139–141]. More details of solar axion searches in liquid xenon will be given in Chapters 5 and 6.

Electron Absorption Searches

Absorption processes, introduced in Section 3.1.3, allow even lighter bosonic dark matter candidates (see Section 2.1) to be probed in the same experiments, since all of the energy of the incoming particle is absorbed.

Semiconductor experiments, using Ge or Si, can probe masses as low as $\sim$ meV/c^2. When dark matter mass exceeds the $\sim$ eV band gap absorption results in electrons

being excited to the conduction band. Dark matter with mass below the band gap energy, in the 0.01 – 1 eV/c^2 range, can also be detected since multi-phonon excitations enable absorption [142]. The electron hole pairs can either be observed directly after being drifted by an electric field, or converted to phonons in an amplification process. CDMSLite carried out a search for electron recoils from bosonic superWIMP absorption [143].

Bosonic dark matter can also be absorbed by conduction electrons in superconductors via phonon emission if the energy deposition exceeds the $\sim$ meV superconducting gap [144]. Aluminium is a possible target, with a 0.6 meV superconducting gap.

Noble liquids allow for absorption by atomic electrons, which can be detected using ionisation only or light and ionisation signals. The XMASS experiment used this technique to search for bosonic superWIMPs [145], LUX carried out an ALP analysis [140] and XENON1T carried out ALP and HP searches using ionisation only [136] and both channels [141].

As described in Section 2.4.3, resonant cavity searches provide an alternative techniques for ultralight bosonic dark matter searches. The coupling to photons is utilised in both haloscopes, such as ADMX [146, 147], and helioscopes such as CAST [148]. Whilst these methods are also searching for direct interactions of particles in a terrestrial detector, they typically probe much lower masses then the electron scattering or absorption experiments.

New Ideas

New direct detection technologies and analysis techniques can be used to probe new parameter space.

Helium is of interest as a new target for low mass dark matter due to better kinematic matching, high radiopurity and good production of scintillation light and phonon/roton signals. This allows small scale (sub-kg) experiments to probe new areas of parameter space [149].

In conventional noble liquid direct detection experiments an inelastic NR event in liquid xenon may be accompanied by an ER event due to Bremsstrahlung or the Migdal effect [150]. For low mass dark matter the NR may be below threshold, whilst the ER is above threshold. The LUX experiment has probed

these sub-GeV dark matter masses with this effect using an ER analysis [151].

3.3 Dual Phase Time Projection Chambers

The principle of the time projection chamber (TPC) is to give 3D position reconstruction by drifting an ionisation signal/track to a 2D (x, y) readout plane, using an electric field, and determining the z coordinate using the drift time. This was initially done for a gas target in the late 1970s, followed by liquid noble elements, then both — with the use of a dual phase TPC pioneered by the ZEPLIN-II experiment. As introduced in Section 3.2.2, the use of two phases allows readout of both light and charge signals.

Noble liquids are used due to their combination of good scintillation and ionisation properties, with ionisation electrons able to drift long distances despite relatively high density [152]. A dual phase TPC is usually a cylindrical volume containing liquid noble scintillator, with a gaseous phase above it and a vertical electric field applied. As shown in Fig. 3.4, the interaction of a particle with a target atom in the liquid results in a prompt scintillation signal (S1) from de-excitation. Electrons liberated from the atom in ionisation can be drifted upwards by a

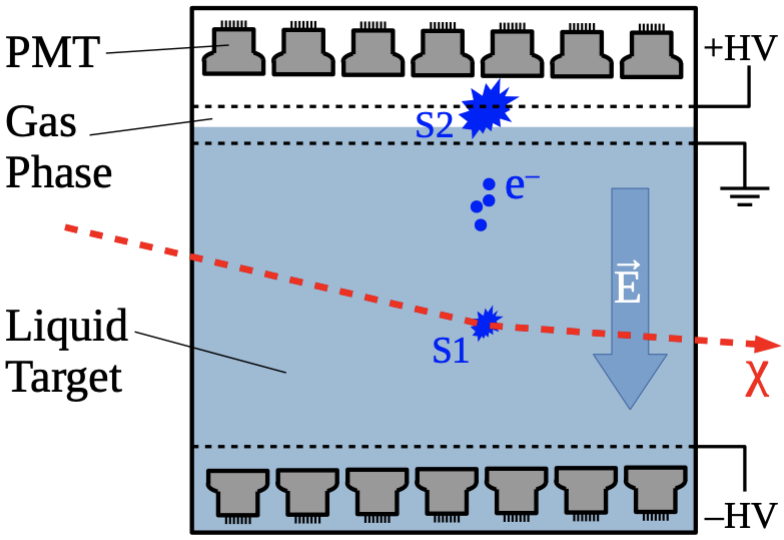

Figure 3.4 *Schematic of a dual phase time projection chamber with S1 scintillation light signal in the liquid and secondary S2 signal in the gas phase, taken from Ref. [108].*

$\sim$ 1 kV/cm electric field and extracted into the gas phase by a $\sim$ 10 kV/cm field applied at the boundary. Here, a secondary light signal (S2) is created by electroluminescence, giving a signal proportional to the number of ionisation electrons. These two light signals are collected by arrays of PMTs, above and below the target volume. Measurement of the S2 signal in the top PMT array indicates the x, y position of the interaction, as electrons are not expected to scatter significantly as they move through the liquid. Depth (z position) of the interaction can be determined from the time delay between the S1 and S2 signal, giving 3D position reconstruction. Energy can be determined from the size of the S1 and S2 signals, as described in Section 3.3.1. The detector threshold is determined by the S1 scintillation signal — this can be reduced in an "S2-only" analysis, but backgrounds will be higher.

Liquid argon and xenon targets are the most commonly used noble elements. Argon was used in early TPCs, having the advantage of being the most abundant noble element and cheap to obtain in large volumes. Argon detectors also allow for very good ER discrimination using pulse shape discrimination. However, a big disadvantage is the presence of the ^{39}Ar radioisotope in natural atmospheric Ar, which undergoes β decays with a 565 keV end point, providing an intrinsic background in the WIMP search region.

Liquid xenon technology has overtaken argon, leading direct detection searches over the past decade. This target offers the advantages of:

1. higher WIMP-nucleon cross section, due to higher atomic mass,
2. self shielding from background radiation, with a shorter gamma-ray attenuation length than Ar ($\sim$ 6 cm, compared to $\sim$ 18 cm for a 1 MeV γ-ray [153]) due to higher density,
3. few long lived radioisotopes in natural Xe.

The DarkSide collaboration uses argon TPC technology — the DarkSide-50 experiment, at LNGS, used a 46 kg active mass of argon. The TPC was surrounded by a liquid scintillator veto and water cherenkov detector to mitigate backgrounds and pulse shape discrimination was used for ER/NR discrimination. DarkSide-50 published first results using atmospheric argon in 2015 [154]. Then a second run was carried out with argon from underground sources, which had a factor 1.4×10^3 less ^{39}Ar. The improved limit of 1.09×10^{-44} cm^2 for 126 GeV/c^2

WIMP mass, was the most stringent dark matter nucleon cross section limit set by an Ar experiment [155]. An ionisation only analysis was also carried out, probing WIMP masses down to 1.8 GeV/c^2 [156]. An upgrade to DarkSide-20k is currently taking place, this will have a 40 tonne fiducial mass of underground argon [157].

The PandaX collaboration uses Xe TPC technology, with a series of experiments located at Jinping Underground Laboratory. The PandaX-II experiment ran from 2016–2018 with a 360 kg target mass, to give a total exposure of 132 tonne days [158]. An upgrade to PandaX-4T is now underway [159], with a 5.6 tonne year exposure expected.

Another example of Xe TPC technology is used by the XENON collaboration with the successive XENON10 [160], XENON100 [161] and XENON1T [162] experiments, located at LNGS. The upper limit of 4.1×10^{-47}cm^2 at 30 GeV/c^2 WIMP mass, set by XENON1T, is the most stringent SI WIMP-nucleon cross section limit to date. Currently work is being undertaken to upgrade to the XENONnT experiment, which aims to have a 20 tonne year exposure [163].

In the UK the ZEPLIN program, with experiments located at Boulby Mine, ran dual phase Xe experiments ZEPLIN-II [164] and ZEPLIN-III [165]. Following this, the LUX experiment ran at Sanford Underground Research Facility (SURF),

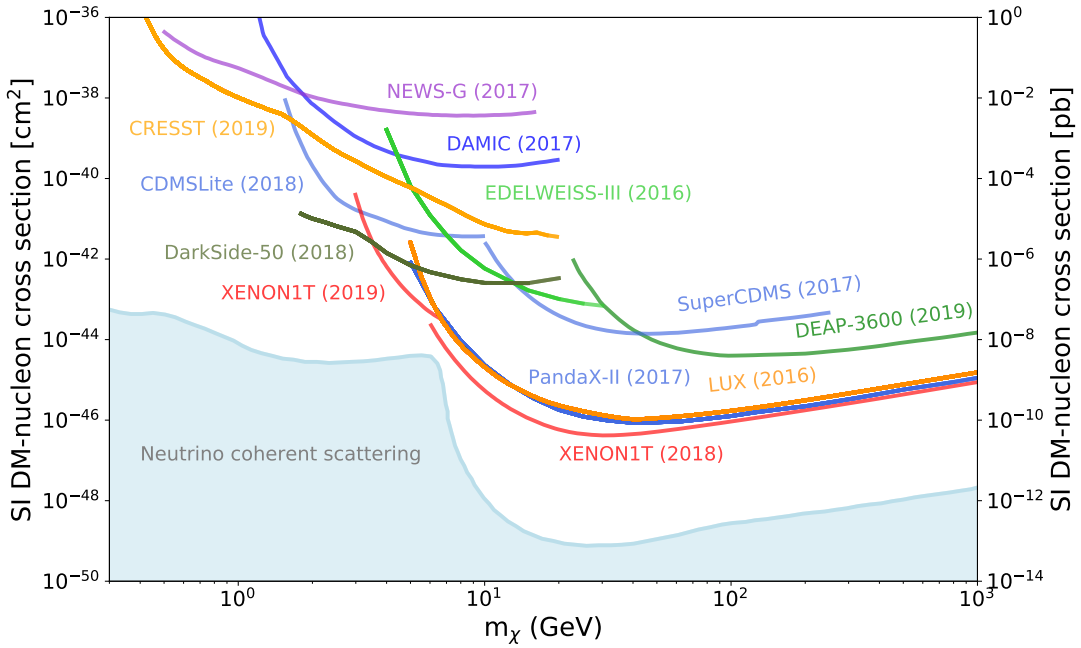

Figure 3.5 *Current upper limits on the spin-independent WIMP-nucleon cross section from direct detection experiments, taken from Ref. [110]*

Table 3.1 *Existing and projected upper limit on spin-independent cross section for direct detection experiments probing WIMP masses greater than 5 GeV/c^2. The lowest limit and corresponding WIMP mass is given.*

Experiment	Target	Exposure	Limit [cm^2]	WIMP mass [GeV/c^2]
DEAP-3600	Ar	758 t day	3.9×10^{-45}	100
DarkSide-50	Ar	1.4 t day	1.14×10^{-44}	100
XMASS	Xe	685 t day	2.2×10^{-44}	60
PandaX	Xe	5.4 t day	8.6×10^{-47}	40
LUX	Xe	33.5 t day	2.2×10^{-46}	50
XENON1T	Xe	365 t day	4.1×10^{-47}	30
DarkSide-20k	Ar	200 t yr	7.4×10^{-48}	1000
PandaX-4T	Xe	5.6 t yr	6×10^{-48}	40
LZ	Xe	15 t yr	1.6×10^{-48}	40
XENONnT	Xe	20 t yr	1.4×10^{-48}	50

South Dakota from 2013–2016. The full 3.34×10^4 kg day exposure gave a SI cross section limit of 1.1×10^{-46}cm^2 for 50 GeV/c^2 WIMP mass [166]. The LUX detector will be described in detail in Section 3.4 and analysis of LUX data is the focus of Chapter 4. Curently the LUX-ZEPLIN (LZ) experiment is under construction at SURF, replacing LUX. The LZ detector will contain 7 tonnes LXe, with a 5.6 tonne fiducial mass, and aims to have world leading sensitivity of 1.6×10^{-48}cm^2 for 40 GeV/c^2 WIMP mass with a 1000 live day run [167]. The LZ detector is described in more detail in Section 3.5 and projections of the sensitivity of LZ to electron recoil searches are the focus of Chapter 5.

Recent direct detection results for WIMP-nucleon scattering are show in Fig. 3.5, with results and projections for future experiments also outlined in Table 3.1.

3.3.1 Xenon Microphysics

Dual phase TPC technology, described in Section 3.3, detects ionisation and scintillation signals, produced by particle interactions with a liquid noble gas. In this section, the microphysics of light and charge production in liquid xenon, along with the resulting signal characteristics, will be described.

3.3.2 Light and Charge Production

Energy deposited in a particle interaction in liquid xenon is split between the three channels outlined in Section 3.2.2, in variable proportions for ER and NR events. In a dual phase TPC only the scintillation light and ionisation charge are detected — their production is described below.

Primary Scintillation Signal

Most of the prompt scintillation light is emitted by excited diatomic molecules, created in exciton luminescence or recombination luminescence processes. Exciton luminescence occurs when a single atom undergoes impact excitation to form an exciton Xe^*, which subsequently binds to another Xe atom to form an excited diatomic molecule or excimer Xe_2^* [152]:

$$\begin{aligned}
e^- + Xe &\rightarrow Xe^* + e- && \text{impact excitation,}\\
Xe^* + Xe &\rightarrow Xe_2^{*v} && \text{excimer formation,}\\
Xe_2^{*v} + Xe &\rightarrow Xe_2^* + Xe && \text{relaxation,}\\
Xe_2^* &\rightarrow 2Xe + \gamma && \text{VUV photon emission.}
\end{aligned}$$

Here, the * superscript indicates electronic excitation and the ^{v} superscript indicates vibrational excitation. Vibrational relaxation is non-radiative, occurring via atomic collisions. The electronic relaxation of the excimer is radiative, accompanied by the emission of a vacuum ultraviolet (VUV) photon, with $\sim$ 178 nm wavelength.

The second process, recombination luminescence, occurs when recombination of an ionisation electron with a molecular ion forms an excimer:

$$\begin{aligned}
e^- + Xe &\rightarrow Xe^+ + 2e^- && \text{ionisation,}\\
Xe^+ + Xe + Xe &\rightarrow Xe_2^+ + Xe &&\\
e^- + Xe_2^+ &\rightarrow Xe^{**} + Xe && \text{recombination,}\\
Xe^{**} + Xe &\rightarrow Xe^* + Xe &&\\
Xe^* + Xe + Xe &\rightarrow Xe_2^* + Xe &&\\
Xe_2^* &\rightarrow 2Xe + \gamma && \text{VUV photon emission.}
\end{aligned}$$

The molecular ion Xe_2^+ is created $\sim$ ps after the ionisation, and following recombination an atom in a higher electronic excited state Xe^{**} is formed. The final stage is similar to exciton luminescence, so the emitted photon has a similar wavelength and lifetime. But recombination also adds a time delay, as it is slow compared to de-excitation times.

The VUV photon is emitted in the transition from one of the two lowest excited states of the excimer: triplet $^3\Sigma_u^+$ or singlet $^1\Sigma_u^+$, to the ground state $^1\Sigma_g^+$. Since the ground state potential is repulsive at the short interatomic distances, it results in dissociation of the molecule in this transition. This means the photon is not reabsorbed, since there is a low probability of it finding another Xe_2. Transitions from the triplet and singlet states have decay times of 27 ns and 2.2 ns respectively. The exciton and recombination processes can result in different proportions of the two excited states being populated, depending on the initial particle causing the recoil. In argon the triplet decay time is much longer $\sim \mu$s, allowing for discrimination between ER and NR events using the shape of the S1 pulse. The high refractive index of liquid xenon causes total internal reflection at the liquid gas boundary, so most prompt scintillation light is collected by the bottom PMT array.

Ionisation Signal

An ionisation electron which is not recaptured can escape the interaction site as a free charge. In order to produce an ionisation/secondary scintillation S2 signal the free charge must have a high mobility in the electric field and a low probability to form low mobility states along the drift path. A high gain amplification mechanism is also needed to produce a measurable signal.

The band structure and hole-type conductivity in liquid xenon gives high mobility free electrons in the conduction band and positive vacancies in the valence band. Free electrons can drift relatively quickly in liquid noble gases, with 2.25 mm/μs drift velocity measured for an applied field of 1 kV/cm in liquid xenon. Good purity is required to reduce the formation of low mobility states, when electronegative species (such as O_2) capture free electrons forming negative ions. Amplification is achieved by extracting free electrons from the liquid to the gas phase using an electric field. Electrons in the gas can be accelerated to sufficient energies to excite gas atoms, producing secondary scintillation/electroluminescence photons and possible secondary ionisation electrons. Avalanches of

secondary electrons allow very high amplification gains, with a single extracted electron able to produce hundreds of photons. Secondary scintillation photons are produced when single excited atoms (or excimers in higher density gas) de-excite to the ground state. This results in a similar spectrum to primary scintillation, with a small difference in peak position and width.

Energy and Yields

For nuclear recoils a significant proportion of the incident particle energy is dissipated to kinetic energy of the target atom (heat) and is not available as light or charge. This effect is called nuclear quenching [168] and is not present for electron recoil interactions.

At higher energies there are additional processes which can reduce the number of scintillation photons, such as bi-excitonic quenching where two free excitons collide and emit an electron [169]:

$$\mathrm{Xe}^* + \mathrm{Xe}^* \rightarrow \mathrm{Xe} + \mathrm{Xe}^+ + \mathrm{e}^-.$$

This reduces the number of excitons available for VUV photon production — at most one photon can be produced by the ion, rather than one from each exciton. At high energies this becomes important due to increased track density which enables the collisions to occur.

Scintillation and ionisation are strongly anti-correlated, due to the removal of free charges by recombination. The applied electric field and deposited energy both affect the amount of recombination — it is small for low recoil energies (due to low track density) and high applied fields (which move charges away quickly).

The split of the deposited energy E_0 into ionisation, excitation and heat can be described using:

$$E_0 = N_i E_i + N_{ex} E_{ex} + N_i \varepsilon. \tag{3.6}$$

Here, $N_{i/ex}$ is the initial number of ions/excitons, $E_{i/ex}$ is the mean ionisation/excitation energy and ε is the mean energy of sub-excitation electrons, which can interact elastically increasing the temperature. This can be rewritten in terms of the ionisation potential, I (= 12.13 eV for Xe):

$$\frac{E_0}{I} = N_i \frac{E_i}{I} + N_{ex} \frac{E_{ex}}{I} + N_i \frac{\varepsilon}{I}. \tag{3.7}$$

The band structure of liquid noble gases means I can be replaced by the band gap, E_g (= 9.22 eV for Xe):

$$\frac{E_0}{E_g} = N_i \frac{E_i}{E_g} + N_{ex} \frac{E_{ex}}{E_g} + N_i \frac{\varepsilon}{E_g}. \tag{3.8}$$

The W-value is defined as the average energy needed to produce a single excited or ionised atom: $W = E_0/N_i$, giving:

$$\frac{W}{E_g} = \frac{E_i}{E_g} + \frac{N_{ex}}{N_i} \frac{E_{ex}}{E_g}. \tag{3.9}$$

The ratio of excitons to ions N_{ex}/N_i depends on the interaction type: a value of 0.06 is calculated for electrons, whilst 0.2 is measured. For nuclear recoils fewer ions are produced and a value of ~ 1 is measured.

Recombination means that the observed ionisation and scintillation signals are not equal to N_i, N_{ex}. The quantities that can be measured are the number of scintillation photons n_γ and number of electrons which escape the interaction site n_e. These are related to the initial number of quanta produced by:

$$\begin{aligned} n_\gamma &= (N_{ex} + rN_i), \\ n_e &= (1-r)N_i, \end{aligned} \tag{3.10}$$

where r is the recombination probability. However, all excitons and ions create one photon or free electron, so the total initial and observed number of quanta are equal:

$$N_i + N_{ex} = n_e + n_\gamma. \tag{3.11}$$

The mean energy needed to produce scintillation photons W_s can be defined analogously to the W-value:

$$W_s = \frac{E_o}{N_{ph}} = \frac{W}{1 + N_{ex}/N_i}. \tag{3.12}$$

Here, $N_{ph} = N_i + N_{ex}$ assumes no quenching effects.

The measured quanta can be used to estimate the energy in an interaction, for

electron and nuclear recoils these are [170]:

$$\begin{aligned} E_{ER} &= W(n_e + n_\gamma), \\ E_{NR} &= (W/f_n)(n_e + n_\gamma). \end{aligned} \tag{3.13}$$

The nuclear recoil energy includes quenching factor f_n which is the fraction of energy transferred to electronic excitation, accounting for the energy lost to atomic motion/heat. A measured W-value of 13.7 ± 0.7 eV is commonly used [171]. However, a range of differing measurements have been made, such as the EXO-200 experiment finding: $W = 11.5 \pm 0.5(\text{syst}) \pm 0.1(\text{stat})$ eV, using MeV γ-rays [172]. The Lindhard model is used for theoretical calculation of the quenching factor [168]. To account for this fractional $1/f_n$ factor, two energy scales are often defined to express electron and nuclear recoil energies, keV_{ee} and keV_{nr} respectively.

Understanding the light and charge yields is important for determining detection efficiencies in analysis. Light yield L_y is defined as the number of photons emitted per unit energy and charge yield Q_y is the number of electrons emitted per unit energy:

$$L_y = \frac{n_\gamma}{E_0}, \qquad Q_y = \frac{n_e}{E_0}. \tag{3.14}$$

Both yields are a function of the energy transfer and applied electric field — Fig. 3.6 shows the dependence of scintillation yield on linear energy transfer (LET). The reduction in yield for both low and high nuclear recoil energies shows the importance of quenching. For intermediate LET values the scintillation yield is approximately constant, as each of the excited and ionised species gives a photon in this region .

The number of quanta that can be detected will be less than the number released in the particle track. This means that whilst S1 and S2 are proportional to the number of photons and free charges, they will be lower and can be written:

$$S1 = g_1 n_\gamma, \qquad S2 = g_2 n_e. \tag{3.15}$$

The S1 and S2 signals are measured in units of photons detected, phd, and g_1, g_2 are detector gains with units of phd/quanta. Specifically, g_1 gives phd per emitted scintillation photon, accounting for the light collection efficiency (at the centre of the detector) and PMT quantum efficiency. The g_2 value gives

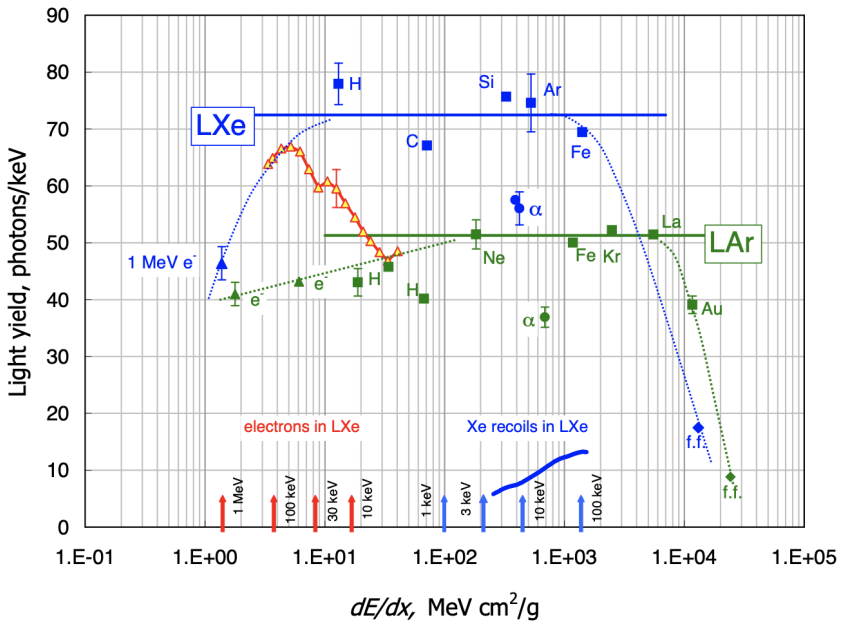

Figure 3.6 *Scintillation light yield as a function of linear energy transfer for liquid xenon (blue) and argon (green). Circle, square or diamonds are data points with associated error bars. The plateaus indicate constant W_s needed to produce photons, with the dashed lines showing quenching effects at low or high energies. The filled triangles come from Compton electron measurements. The energies next to the red and blue vertical lines show the recoil energy in keV, indicating key points for liquid xenon dark matter experiments. Image taken from Ref. [152]*

phd per free electron which escapes the interaction region, this is the product of the electron extraction efficiency and the average single electron pulse size. Calibration measurements are used to determine the values of g_1 and g_2 for a particular detector, this method will be described in Section 4.3.1.

The total energy is therefore given by:

$$E = \frac{W}{f_n}\left(\frac{S1}{g_1} + \frac{S2}{g_2}\right). \tag{3.16}$$

Here, the quenching factor is $f_n = 1$ for electronic recoils (no loss from nuclear quenching) and $f_n < 1$ for nuclear recoils.

Light and charge yields in noble gases can be modelled using the Noble Element Simulation Technique (NEST) [173]. Detector response is predicted as a function of the particle type and energy as well as the detector electric field, temperature

and pressure. A wide range of parameters are covered using a collection of models and extensive available data from a range of experiments. The analyses presented in Chapters 4 and 5 use NESTv.2.0.0 [174], with details and a study of the electron recoil models presented in Section 5.2.1.

3.4 LUX Experiment

The Large Underground Xenon (LUX) experiment was a dual phase xenon time projection chamber, introduced in Section 3.2.2. Data from the LUX experiment is used in Chapter 4 to carry out a search for electron recoils induced by mirror dark matter. Sections 4.2 and 4.4 describe the calibration and data selection. Here, the LUX detector, operation and key results will be described.

LUX was located at SURF, South Dakota, at a depth of $\sim$ 1.5 km (4300 metres water equivalent) underground, taking science data from 2013 – 2016. The LUX-ZEPLIN (LZ) experiment, described in Section 3.5, will operate in the same space.

3.4.1 Detector

The LUX detector will now be described, beginning at the liquid xenon target and moving outwards. As shown in Fig. 3.7, the detector contained 370 kg liquid xenon inside a titanium cryostat — the inner vessel, which was housed inside a second cyrostat — the outer vessel. Inside the inner vessel the TPC had a dodecagonal structure, 50 cm in diameter and 60 cm high, with 12 PTFE panels to aid light collection. The volume of xenon between the cathode and gate grids and these PTFE faces formed a 250 kg active mass. Two arrays of PMTs, mounted in copper blocks above and below the xenon, collected light from this region. The two arrays each contained 61 Hamamatsu R8778 5.6 cm diameter PMTs, chosen due to low radioactivity and good quantum efficiency (33%) at 178 nm wavelength.

Five electrodes were used to generate the electric fields needed to drift and extract electrons. These consisted of bottom and top grids, 2 cm above and below the bottom and top PMT arrays, to protect the PMTs from high fields. Cathode (4 cm above the bottom PMT array) and gate (5 mm below the liquid surface)

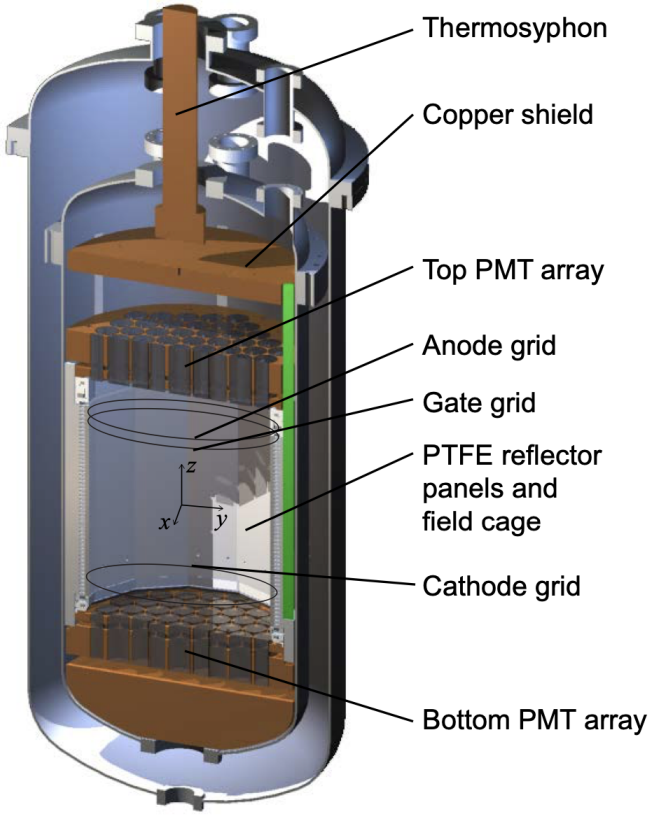

Figure 3.7 *Schematic of the LUX detector, taken from Ref.[175], showing the grids, PMT arrays and PTFE panels surrounding the active region contained within the two vessels.*

grids created the drift field, with 48 copper field shaping rings, located behind the PTFE panels, used to ensure field uniformity. The gate and anode (1 cm above the boundary) grids created high fields need to extract electrons into the gas phase and accelerate them to cause electroluminescence. During Run3 LUX operated with cathode, gate and anode voltages of: -10 kV, -1.5 kV and +3.5 kV. This resulted in an average drift field of 180 V/cm and extraction fields of 2.84 $\pm$ 0.16 kV/cm and 5.55 $\pm$ 0.30 kV/cm in the liquid and gas respectively [175].

The thermosyphons, shown in Fig. 3.5, connected to a liquid nitrogen bath to allow precise control of the detector temperature. A range of sensors in the inner and outer vessel were used to monitor temperature, pressure and liquid level. In order to ensure that the purity (and electron drift length) remained high, the xenon was continuously circulated and purified. The xenon was evaporated and passed through a hot getter, before being condensed and returned to the active volume. Purification was monitored during operation, using both electron drift

lifetime measurements and in situ sampling.

The outer vessel was immersed in a 7.6 m diameter and 6.1 m high water tank, providing shielding of 3.5 m at the sides, 2.75 m at the top and 1.2 m below the detector [176]. Water provides good shielding from γ-rays and neutrons produced in the cavern walls, reducing these backgrounds to a negligible level compared with those from radioisotopes in detector components.

3.4.2 Results Highlights

The LUX experiment began cool down in January 2013, with the first WIMP search and calibration data (Run 3) taken from March – October 2013 [175]. Later in 2013, the first spin independent WIMP analysis limit, of 7.6×10^{-46}cm^2 at 33 GeV/c^2, was published [177]. Following further background and calibration studies this was improved to 6×10^{-46}cm^2 at 33 GeV/c^2, published in 2016 [178]. The second WIMP search data taking (Run 4) extended the exposure to 332 days, improving the limit to 2.2×10^{-46}cm^2 at 33 GeV/c^2 and a minimum of 1×10^{-46}cm^2 at 50 GeV/c^2 [179].

Other analyses looking for a nuclear recoil signal included the spin-dependent WIMP search [180], which set limits on the WIMP-neutron and WIMP-proton cross sections. An effective field theory analysis has been carried out [181], placing limits on 14 independent couplings using Run3 data. The data can also be utilised to search for electron recoil signals. Run3 data was used to place world leading limits on the axio-electric coupling for both solar axions and axion-like particles in the 1 – 16 keV/c^2 mass range [140]. Low mass WIMPs can be probed using the electron recoil signal from Bremsstrahlung or Migdal effects [182], giving results for WIMP masses as low as 0.4 GeV/c^2, using Run3 data. Another technique is to use the double photoelectron emission effect in order to lower the detector threshold, allowing WIMP masses down to 2.5 GeV/c^2 to be probed [183]. The use of Run3 data to set the first direct detection limit on mirror dark matter kinetic mixing will be presented in Chapter 4.

3.5 LZ Experiment

The LUX experiment has now been replaced by LZ, constructed in the same location. LZ, introduced in Section 3.3, will be one of the next generation of tonne scale noble liquid direct detection experiments, aiming to achieve an order of magnitude improvement in SI WIMP-nucleon cross section sensitivity. Analyses for other dark matter models, similar to those described in Section 3.4, will also be possible. Low energy electron recoil searches using LZ will be the topic of Chapters 5 and 6. Here, the detector design, its optimisation for rare event searches and improvements compared to LUX will be described.

3.5.1 Detector

The key requirements for improving the sensitivity of a dark matter detector to smaller cross sections are increased exposure and reduced backgrounds. LZ will have a fiducial volume $\sim$ 40 times larger than that used in LUX. To improve background mitigation, LZ will use skin and outer detector (OD) vetoes and improved selection of radiopure construction materials. Figure 3.8 shows a schematic of the LZ detector, which will be described starting with the liquid

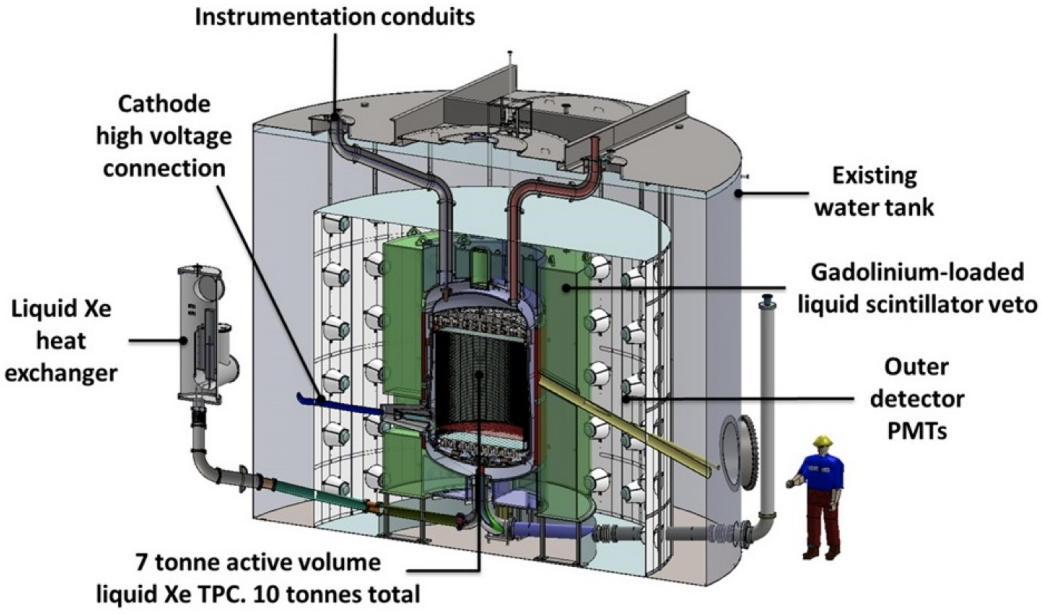

Figure 3.8 *Schematic of the LZ detector, taken from Ref.[184], showing the components of the outer detector and TPC contained within the water tank.*

xenon target moving outwards, as detailed in Ref. [184].

The detector contains 10 tonnes of liquid xenon in total — an active volume with a diameter and height of 1.46 m gives a 7 tonne active mass. Liquid xenon and the TPC are contained in a cryostat made of radiopure titanium [185], consisting of inner (ICV) and outer (OCV) cryostat vessels. The ICV is suspended inside the OCV by three tie bar assemblies, with a vacuum space in between the two vessels. A thermosyphon system, using liquid nitrogen, keeps the liquid xenon in the TPC at an operating temperature of 175.8 K. Insulation of the inner vessel is provided by the vacuum space, which reduces thermal conduction. Multilayer insulator (MLI) is wrapped around the ICV and thermosyphon lines, as shown in Fig. 3.9, to further reduce thermal radiation. Similarly to LUX, the inside of the TPC is coated with highly reflective PTFE ($\geq$ 97.3 % reflectivity when immersed in LXe), to maximise light collection.

Vertical electric fields are controlled by three electrodes in the TPC: a cathode grid at the bottom of the active region operating at -50 kV, a gate grid below

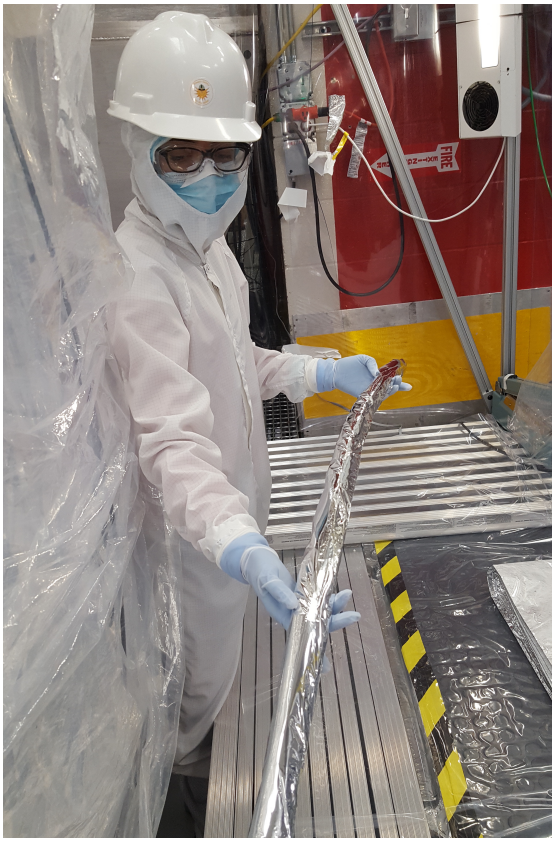

Figure 3.9 *This author preparing an MLI wrapped thermosyphon line for installation on the ICV.*

the liquid boundary and an anode grid above the liquid boundary 13 mm apart operating at ∓ 5.75 kV. This configuration should achieve a uniform 310 V/cm drift field in the TPC, shaped by 57 field shaping rings embedded in the PTFE. An additional electrode below the cathode creates a reverse field region to shield the bottom PMT array from the cathode potential.

Photons created in the TPC are detected by 494 Hamamatsu R11410-22 3 inch diameter PMTs, chosen for their low radioactivity and high quantum efficiency at 178 nm wavelength. The bottom PMT array contains 241 PMTs within the liquid, arranged in a close packed hexagonal configuration to maximise S1 light collection efficiency. The top array contains 253 PMTs, arranged to optimise S2 x, y position reconstruction.

An important feature of the LZ detector is the skin and OD veto system. The skin region is the layer of xenon between the PTFE and the ICV, it is 4 – 8 cm in thickness around the cylinder and thicker below the bottom PMT array. This 2 tonne region of liquid xenon is optically segregated from the TPC, instrumented with 93 Hamamatsu 1 inch PMTs at the top and 38 Hamamatsu 2 inch PMTs at the bottom. The main aim of the skin is to detect scattered γ-rays, which enables TPC events coincident with a skin signal and events outside the TPC where light may leak in, to be vetoed.

The OD forms the second part of the veto system — 17.3 tonnes of gadolinium loaded liquid scintillator, contained in 10 acrylic tanks that surround the cryostat, shown in Fig. 3.8. This forms a near hermetic neutron and γ-ray anti-coincidence system around the cryostat. The main aim of the OD is to tag neutrons which emerge after causing a nuclear recoil in the TPC. Neutron capture on gadolinium atoms triggers a 8 MeV γ-ray cascade, which can be detected by 120 Hamamatsu R5912 8 inch PMTs. These are mounted in a cylindrical array of ladders, 1 m away from the acrylic tanks, within the water tank. The OD and cryostat are housed within the water tank that was used for the LUX experiment. Water provides extra shielding from radiation, from both the cavern environment and the OD PMTs.

To maintain a charge attenuation length greater than 1.46 m, low levels of electronegative impurities are required, in addition to a high electric field. Electronegative impurities can be introduced by outgassing of detector materials, particularly the PTFE. Therefore, continuous circulation and purification of the xenon is required to keep them at an acceptable level ($\sim$ 0.1 ppb). Liquid in the

detector is continuously circulated to a purification tower outside the water tank, where it is evaporated and passed through a hot zirconium getter,before being re condensed and returned to the detector.

Calibrations of the TPC, skin and OD, with a variety of β, γ and neutron sources of different energies, are planned. These are vital to understand the detector response to various particle interaction types, enabling accurate reconstruction of the interaction properties. Internal sources are required for electron recoil calibrations, due to the self shielding nature of Xe, such as β emitting ^{3}H, ^{14}C, ^{220}Rn. Internal γ-ray sources, such as ^{83m}Kr and ^{131m}Xe, can also be used for position reconstruction, field and g1/g2 calibrations. These are all injected into the Xe gas circulation via a source injection panel upstream of the getter.

For other calibrations, sealed radioactive sources can be delivered to the region in between the ICV and OCV, using three dedicated source tubes. These include AmLi and AmBe (α,n) sources for NR efficiency and various γ-ray emitting isotopes for skin and OD studies. An external deuterium-deuterium neutron source outside the water tank is used to produce neutrons, which are fired down air filled conduits into the detector. These monoenergetic neutrons are used to determine the NR light and charge yield of the detector. Photoneutron sources can be introduced to the detector via a lifting system which lowers them through a hole in the acrylic vessel to the top of the OCV. Sources such as YBe and BiBe, which undergo (γ, n) reactions, can be used to calibrate the low energy NR response.

3.5.2 Sensitivity Projections

In the full 5.6 tonne $\times$ 1000 live day exposure. LZ is projected to have exclusion sensitivity (90% confidence level) to spin independent WIMP-nucleon cross sections as low as 1.4×10^{-48}cm^2 for a 40 GeV/c^2 WIMP [167].

The detector threshold is determined by the number of detected S1 photons. The nominal WIMP search analysis requires a three-fold PMT coincidence, where photons must be recorded on three different channels to avoid dark count coincidences. Two techniques can be used to lower the threshold: relaxing the requirement from three-fold to two-fold when double photoelectron emission (DPE) occurs or dropping the requirement of an S1 altogether for an S2 only analysis [186]. The DPE effect can be used since VUV photons have a 20%

probability of emitting two photoelectrons from the PMT photocathode, a larger response than dark counts. This improves sensitivity to 2.5 GeV/c^2 WIMPs by a factor of 4 and sensitivity to ^{8} B neutrinos by a factor of 1.6. The S2 only analysis, along with additional background mitigation strategies, improves the sensitivity to 2.5 GeV/c^2 WIMPs by two orders of magnitude and gives a similar improvement for ^{8}B neutrinos.

Non dark matter searches for new physics can also be carried out. One example is neutrinoless double beta decay — an as yet unobserved process which is only allowed if the neutrino is a Majorana particle (its own antiparticle). The resulting signal would be a mono-energetic peak at the double beta decay Q-value (2458 keV). For the full 1000 day exposure LZ is projected to achieve median exclusion sensitivity to ^{136}Xe neutrinoless double beta decay half life of 1.06×10^{26} years at 90% confidence level [187].

Chapter 4

LUX Mirror Dark Matter Search

The main aim of the LUX experiment, described in Section 3.4, was to search for dark matter in the form of weakly interacting massive particles (WIMPs), placing limits on spin-independent WIMP-nucleon cross-sections for WIMP masses above 4 GeV/c^2 [177, 178]. However, the data has been used for other studies, including searches for spin-dependent WIMP-nucleon interactions [180], electron recoil searches for solar axions and axion-like particles [140] and sub-GeV dark matter via the Bremsstrahlung and Migdal effects [182]. Here, a search for electron recoils originating from mirror dark matter interactions within the detector will be presented. This is the first direct detection search for mirror dark matter, which has been published in Ref. [1].

4.1 Mirror Dark Matter Phenomenology

Mirror dark matter (MDM), introduced in Section 2.3, could result in keV scale electron recoils in the LUX detector, due to kinetic mixing interactions between mirror electrons and Xe atomic electrons. The MDM would exist as a multi-component plasma halo, assuming that the mirror electron temperature exceeds the binding energy of a mirror hydrogen atom [56]. This halo is predominantly composed of mirror electrons e$'$ and mirror helium nuclei He$'$. The He$'$ mass fraction is higher (and mirror hydrogen H$'$ lower) than for ordinary matter because freeze out happens earlier, due to a lower initial temperature in the mirror sector [55].

For a dark matter halo in hydrostatic equilibrium, the local mirror electron temperature (in energy units) is given by [188]:

$$T = \frac{\overline{m} v_{rot}^2}{2}, \tag{4.1}$$

where $\overline{m}$ is the average mass of halo particles and v_{rot} is the galactic rotational velocity. Arguments from early universe cosmology in the mirror model give a mirror helium mass fraction of 90% [189] and, assuming a completely ionised plasma, this gives $\overline{m} \approx 1.1$ GeV. Therefore, using $v_{rot} \approx 220$ kms^{-1} and assuming the halo is in hydrostatic equilibrium, a local mirror electron temperature of ~ 0.3 keV is expected.

The scattering rate for the electron – mirror electron interactions, expected for direct detection, is calculated, following Ref. [55, 56]. Note that nuclear recoils, from scattering of mirror nuclei on xenon nuclei in the detector are also expected, but there is a large uncertainty in the rate, as the fractions of different nuclei in the mirror halo is unknown.

The general expression for the mirror – ordinary electron scattering rate is the product of the target electron density N_e, halo mirror electron density $n_{e'}$ and the integral over the differential cross section $d\sigma/dE_R$, multiplied by the velocity distribution $f_e(v; v_E)$. This gives the expression for the differential rate:

$$\frac{dR_e}{dE_R}(x,t) = N_e n_{e'}(x, v_E) \int_{|v|>v_{min}}^{\infty} \frac{d\sigma}{dE_R} f_e(v; v_E)|v| d^3v. \tag{4.2}$$

The Coulomb scattering cross section is given by:

$$\frac{d\sigma}{dE_R} = \frac{\lambda}{E_R^2 v^2}, \qquad \lambda = \frac{2\pi\epsilon^2\alpha^2}{m_e}, \tag{4.3}$$

where v is the incoming particle velocity, ϵ is the kinetic mixing parameter, introduced in Section 2.3, and α is the fine structure constant. The minimum velocity, needed for a recoil of energy E_R, is given by:

$$v_{min} = \frac{1}{\mu}\sqrt{\frac{m_e E_R}{2}}, \qquad \mu = \frac{m_e m_{e'}}{m_e + m_{e'}}, \tag{4.4}$$

where μ is the reduced mass. A Maxwell Boltzmann distribution is assumed for

the velocity distribution:

$$f_e(v) = \left(\frac{1}{\pi v_0^2}\right)^{\frac{3}{2}} \exp\left(\frac{-(v - v_E)^2}{v_0^2}\right). \tag{4.5}$$

Here, v_0 is the velocity dispersion, given by $v_0 = \sqrt{2T/m_e}$ and v_E is the Earth velocity, taken to be 232 km/s.

Evaluating the velocity integral gives:

$$\frac{dR_e}{dE_R} = \frac{N_T g_T n_{e'} \lambda}{2E_R^2 |v_E|} \left[\text{erf}\left(\frac{v_{min} + |v_E|}{v_0}\right) - \text{erf}\left(\frac{v_{min} - |v_E|}{v_0}\right)\right]. \tag{4.6}$$

Here, g_T is the effective number of free electrons (with binding energy less than 1 keV, 44 in Xe), N_T is the number of target atoms per kg of detector material and $n_{e'}$ is the local number density of mirror electrons. Integrating over recoil velocities from energy threshold E_t to infinity gives rate:

$$R_e = N_T g_T n_e \lambda \left(\frac{2m_e}{\pi T}\right)^{\frac{1}{2}} \left(\frac{e^{-\frac{E_t}{T}}}{E_t} - \frac{\Gamma[0, E_t/T]}{T}\right). \tag{4.7}$$

But this has limitations — for plasmas, such as mirror dark matter, the velocity and density distributions are position dependent, rather than constant as assumed here. It is important to account for terrestrial effects, which alter the local distribution and therefore flux.

4.1.1 Capture and Shielding

In plasma dark matter models, it is important to consider capture of the dark matter by the Earth [190]. Mirror dark matter is captured when it loses energy due to kinetic mixing interactions with ordinary matter. Once a significant amount has accumulated, further capture occurs due to mirror dark matter energy loss from self interactions. Subsequently, mirror dark matter will thermalise with normal matter in the Earth to form an extended distribution. This can affect the incoming mirror dark matter in two ways. Firstly collisional shielding, due to mirror particle interactions identical to the standard model version, suppresses the rate and alters the incoming velocity distribution. Secondly the outer layers of captured mirror dark matter can be ionised — forming a dark ionosphere. The mirror electric field in this dark ionosphere can deflect incoming mirror electrons,

reducing the rate. The second effect is very difficult to model, but the collisional shielding can be accounted for. This effect is calculated below, for the first time for a xenon experiment.

As seen in Eq. 4.2, the electron recoil rate depends on the integral of the velocity distribution and can be re-written as:

$$\frac{dR}{dE} = g_T N_T n_{e'} \frac{\lambda}{E_R^2} I(v_E, \theta), \tag{4.8}$$

where:

$$I(v_E, \theta) = \int_{|v|<v_{min}}^{\infty} \frac{f(v; v_E, \theta)}{|v|} d^3v. \tag{4.9}$$

The velocity distribution, $f(v; v_E, \theta)$, depends on the velocity of the halo wind as measured from Earth v_E and the angle between the halo wind and zenith at the detector location θ.

Expanding $n_{e'} I$ in a Taylor series around the yearly average $\langle n_{e'} I \rangle$, gives rate:

$$\frac{dR}{dE} = g_T N_T n^0_{e'} \frac{\lambda}{v_c^0 E_R^2} [1 + A_v \mathrm{cos}\omega(\mathrm{t} - \mathrm{t}_0) + \mathrm{A}_\theta(\theta - \bar{\theta})]. \tag{4.10}$$

Here, the effective number of free electrons $g_T(E_R)$, with binding energy less than E_R is modelled as a step function for the atomic shells in Xe. The mirror electron number density at the Earth is given by $n^0_{e'}$ and the modified velocity dispersion at Earth given by v^0_c. The A_v and A_θ terms are due to modulation.

Equation 4.3 shows that $d\sigma/dE_R \propto 1/v^2$, so the collision length $\propto v^2$. This means that the effect of collisions becomes negligible for sufficiently large v, above some cutoff velocity v_{cut} the collision length will exceed the Earth diameter. Below this velocity collisions are important until mirror electron energy is reduced to $E_b \approx$ 25 eV, after which energy loss to captured mirror helium is no longer important. The cutoff velocity can be found by considering the mirror electron energy loss due to collisions with mirror helium. The total energy loss, integrated over the path, is equated to the incoming kinetic energy, as it will exceed this below v_{cut}.

As calculated in Appendix A.1.1, the energy loss integrated over the mirror electron path, due to collisions with mirror helium is given by:

$$E'^2 = -4\pi\alpha^2 \Sigma ln\Lambda. \tag{4.11}$$

Here, the column density is $\Sigma = \int n_{He'} dl$ and $\Lambda = E/E_b = T/E_{min}$. At the cutoff

velocity $E' = 1/2mv_{cut}^2$, which gives:

$$v_{cut}^4 = \frac{16\pi}{m^2}\alpha^2 \Sigma log\Lambda. \tag{4.12}$$

This relates the cutoff velocity, above which shielding effects are negligible, to the captured He′ distribution and the local mirror electron temperature.

The column density can be found by considering the path of incoming mirror dark matter through the atmosphere. In the Earth's atmosphere ($r \geq R_E$) the number density of mirror helium, found by solving the equation for hydrostatic equilibrium, is given by:

$$n_{He'}(r) = n_{He'}(R_E)e^{-\lambda(r-R_E)}. \tag{4.13}$$

This means the column density can be written:

$$\Sigma(\psi) = n_{he'}(R_E)\int e^{-\lambda_s d(\psi)}dl, \tag{4.14}$$

$$d(\psi) = \sqrt{l^2 + R_E^2 - 2lR_E\cos\psi}. \tag{4.15}$$

This is valid for $90° \leq \psi \leq 180°$, where ψ is the angle from the incoming particle direction to the zenith. Figure 4.1 shows the column density as a function of incoming particle angle. This is maximum for $\psi = 90°$ and minimum for $\psi = 180°$, which corresponds to a particle travelling vertically downwards. The resulting angular dependence of the cutoff velocity, given by Eq. 4.12, is shown

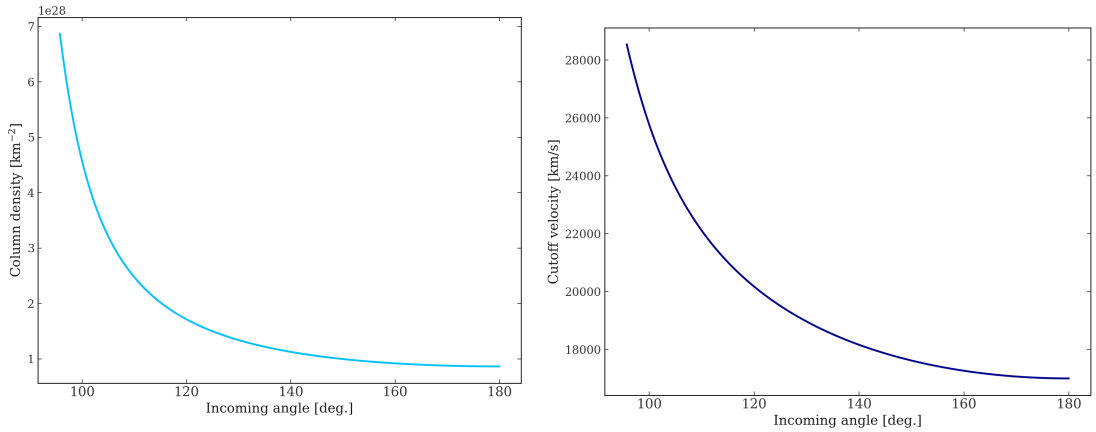

(a) *Column density.* **(b)** *Cutoff velocity.*

Figure 4.1 *Column density and cutoff velocity as a function of incoming particle angle, measured with respect to the zenith at the detector location.*

in Fig. 4.1b. This is also maximum at 90° and decreases as the amount of atmospheric matter traversed by the incoming particle increases.

The Maxwellian velocity distribution for mirror electrons, assumed above in Eq. 4.5, is altered by collisional shielding below the cutoff velocity. The velocity dispersion is replaced by an energy dependent term:

$$\frac{1}{v_c^0} = \frac{1}{N}\int_{|v|>y}^{\infty} \frac{e^{-v^2/v_0^2}}{v_0^3\pi^{3/2}|v|} d^3v = \frac{1}{Nv_0\sqrt{\pi}}\int e^{-y^2/v_0^2} d\cos\psi, \tag{4.16}$$

where $y = MAX[v_{cut}(\phi), v_{min}(E_R)]$. Here, a change to polar coordinates has been used, see Appendix A.1.2 for details. The normalization N is given by:

$$N = \int_{|v|<v_{cut}}^{\infty} \frac{e^{-v^2/v_0^2}}{v_0^3\pi^{3/2}} d^3v. \tag{4.17}$$

Only the surviving high velocity component arrives at Earth with number density: $n_{e'}^0 = N n_{e'}^{far}$, where $n_{e'}^{far} = 0.2$ cm^{-3} is the number density far from the Earth [190].

Both v_c^0 and $n_{e'}^0$ depend on the mirror helium density at the Earth's surface, $n_{He'}(R_E)$ (through column density Σ), electron recoil energy, E_R (through v_{min}), mirror electron temperature and T (through v_0). Figure 4.2a shows v_c^0 as a

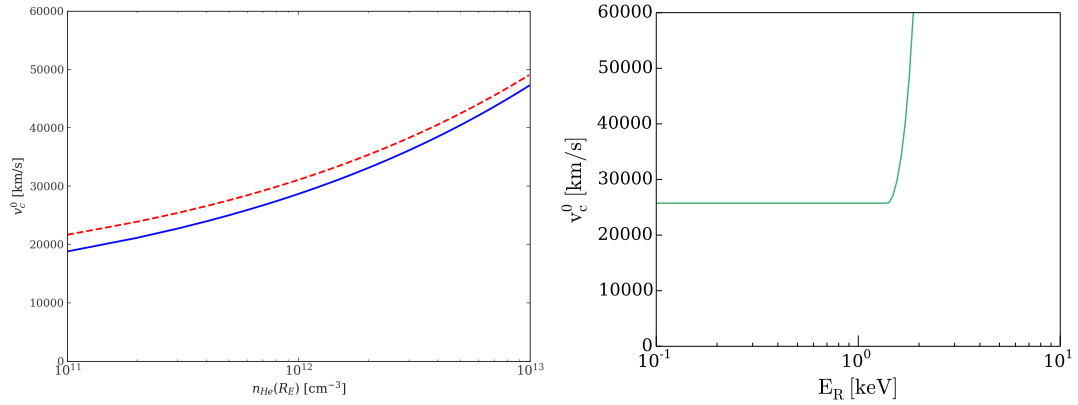

(a) *v_c^0 as a function of the mirror helium number density at the Earths surface, shown for T=0.3 keV (solid line) and T = 0.6 keV (dashed line).*

(b) *v_c^0 as a function of electron recoil energy, this rises sharply for large energies where few mirror electrons meet the minimum energy required.*

Figure 4.2 *The parameter v_c^0 as a function of helium number density, for validation, and energy, for use in energy spectra calculations.*

function of the mirror helium number density at the Earth's surface, used to validate the calculation by comparison to Fig.1a in Ref. [190]. Figure 4.2b shows v_c^0 as a function of the recoil energy — at low E_R the average velocity exceeds the minimum $|v| \gg v_{min}$ so most particles can produce recoils with energy E_R. For large E_R the average particle velocity is lower than v_{min} and few mirror electrons will have sufficient energy to give recoil energy E_R, so the integral is suppressed and there is a sharp rise in v_c^0.

4.1.2 Modulation

Significant modulation, both annual and sidereal, is expected for plasma dark matter models. This will be larger than for WIMP dark matter due to the spatially dependent density and velocity distributions near the Earth [56]. The A_V term in Eq. 4.2 describes annual modulation due to the variation in speed of the Earth with respect to the dark matter halo. This gives a Galilean boost to the incoming dark matter velocity (as with the WIMP case), in addition to changes in the local density and velocity distributions for plasma dark matter. The A_θ term describes modulation due to variation of the angle between the Earth's spin axis and the incoming dark matter wind — both annual modulation from solar orbits and sidereal modulation from rotation are included.

In the first term: $A_v cos\omega(t - t_0)$, the angular frequency is $\omega = 2\pi/1$ year, the

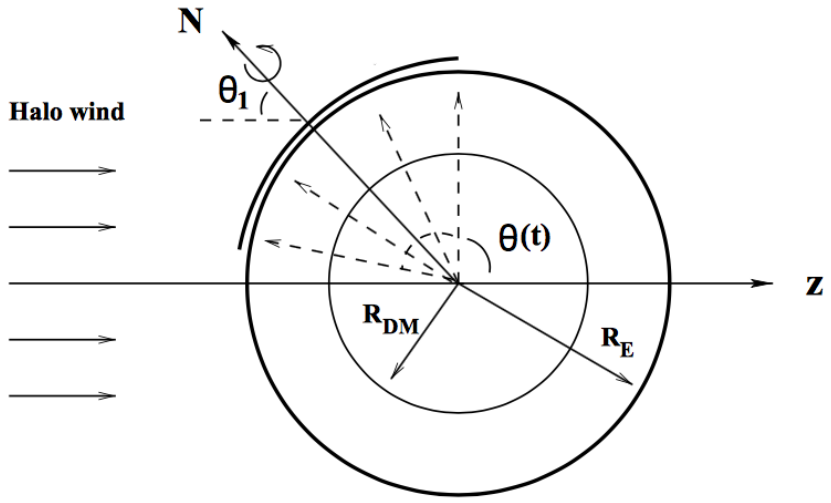

Figure 4.3 *The geometry of the incoming plasma dark matter halo wind with respect to various angles relative to the detector location, taken from Ref. [56].*

date with maximum relative speed is $t_0 = 152$ (2nd June) and the modulation amplitude is $A_v \sim 0.7$ [190] . The second term: $A_\theta(\theta - \bar{\theta})$, requires calculation of the time dependent angle between the halo wind and zenith θ, shown in Fig. 4.3. This is calculated using:

$$\cos\theta(\mathrm{t}) = -\sin\theta_1(\mathrm{t})\cos\theta_{\mathrm{lat}}\cos\left(\frac{2\pi \mathrm{t}}{\mathrm{T_{day}}}\right) - \cos\theta_1(\mathrm{t})\sin\theta_{\mathrm{lat}}, \tag{4.18}$$

where $T_{day} = 1$ is a sidereal day, θ_{lat} is the latitude of the detector location (44° for LUX) and θ_1 is the angle of the Earth's direction of motion through the halo with respect to the spin axis, as shown in Fig. 4.3. The time dependence of θ_1 is given by:

$$\cos\theta_1(\mathrm{t}) = \cos\bar{\theta_1} + \mathrm{y}\left[\cos\bar{\theta_1}\cos\gamma\sin\left(\frac{2\pi(\mathrm{t} - \mathrm{T_1})}{\mathrm{year}}\right) + \sin\theta_{\mathrm{tilt}}\sin\left(\frac{2\pi(\mathrm{t} - \mathrm{T_2})}{\mathrm{year}}\right)\right], \tag{4.19}$$

where $\bar{\theta}_1 = 43°$ is the yearly average, $\theta_{tilt} = 23.5°$ is the angle of Earth's spin axis relative to the normal of the ecliptic plane, $\gamma = 60°$ is the angle of halo wind relative to the normal of the ecliptic plane. The times are $T_1 = t_0 + 1/4$ year = 244 days and $T_2 = 172$ days (summer solstice). The ratio of the parallel and

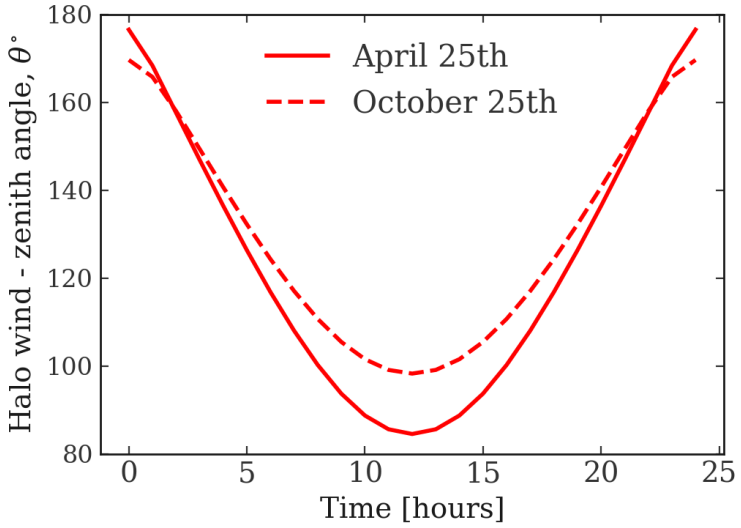

Figure 4.4 *Angle between halo wind and zenith at detector location as a function of time over the course of one day, shown for April 25 (solid line) and October 25 (dashed line).*

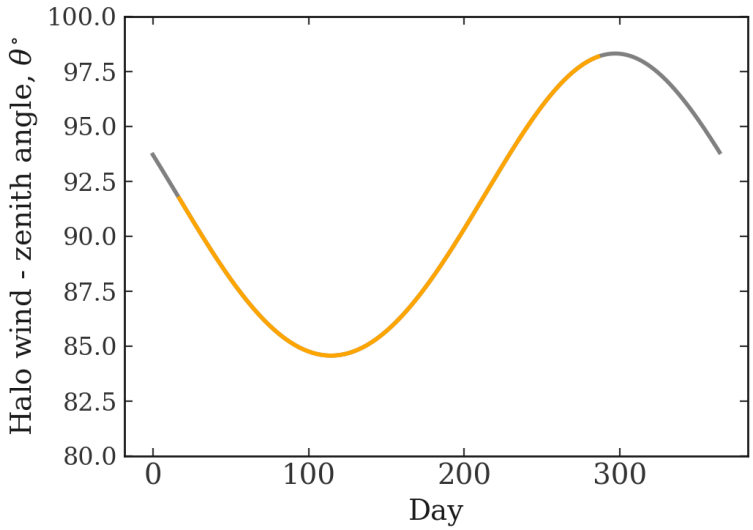

Figure 4.5 *Angle between halo wind and zenith at detector location as a function of time over the course of 1 year (grey) with the LUX Run3 data taking period highlighted (orange).*

perpendicular Earth velocity is given by $y = 0.13$ and the modulation amplitude is $A_\theta \sim 1.0$.

The calculation of $\theta(t)$ was validated by finding the angle at hourly intervals over the course of one day, for Sanford Lab, for the 25th of April and 25th October as these dates show maximum/minimum variation. The resulting Fig. 4.4 can be compared to Fig. 5 in Ref. [56] for validation. Figure 4.5 shows the average angle between halo wind and zenith at detector location for each day over the course of one year, highlighting the LUX Run3 data taking period.

In order to find the expected rate in LUX, for a given livetime, the weighted average of these modulation terms was calculated. This was done by evaluating the terms for each day and multiplying by the fractional livetime for that day, summing over all and then dividing by the total livetime. The mean modulation terms for LUX Run3 were found to be: $A_v\langle cos\omega(t-t_0)\rangle = 0.056$ and $A_\theta\langle\theta-\bar{\theta}\rangle = 0.015$.

4.1.3 Expected rate

Putting all of the above into Eq. 4.10, the differential rate can be calculated, noting that this introduces dependence on the kinetic mixing parameter ϵ,

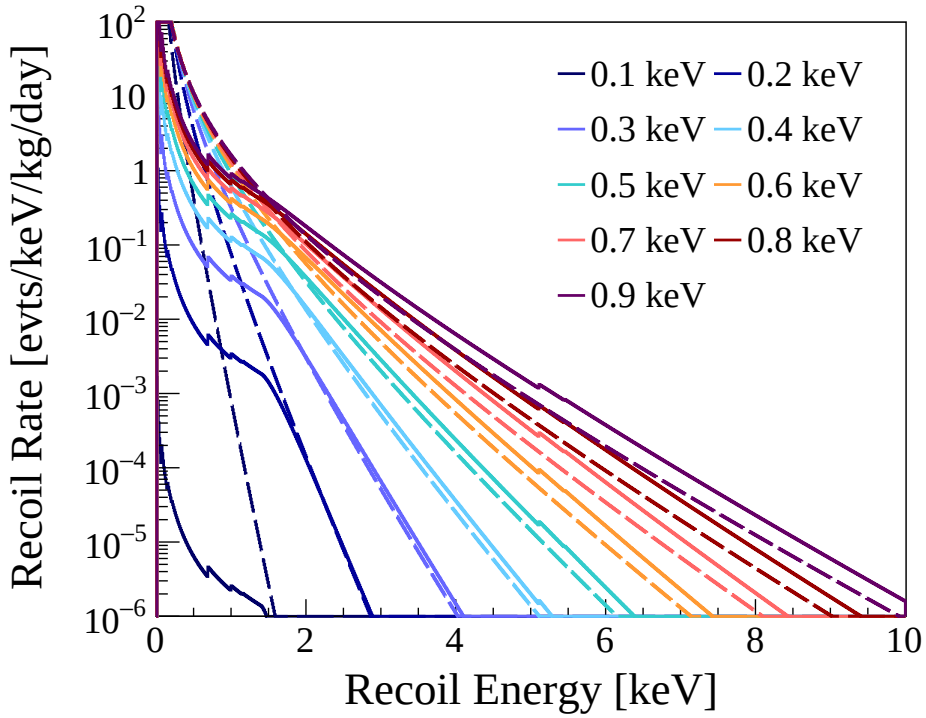

Figure 4.6 *Electron recoil energy spectra from mirror electron kinetic mixing interactions in the LUX experiment, with epsilon* $= 10^{-10}$ *for local mirror electron temperatures 0.1 – 0.9 keV. Dashed lines do not include terrestrial capture and shielding effects, whilst solid lines do.*

through λ. In general, we can set $n_{He'} = 5.8 \times 10^{-11}\text{cm}^{-3}$ [190], then for given values of temperature and kinetic mixing, the rate is calculated as a function of recoil energy. Figure 4.6 shows these differential rates for different local mirror electron temperatures, both with shielding Eq. 4.10 and without Eq. 4.7. When shielding is included there is a 'shoulder' at $\sim$ 2 keV, since energies below this correspond to scattering lengths shorter than the diameter of the Earth.

4.2 Analysis overview

The following sections will describe the mirror dark matter analysis carried out using LUX Run3 (2013) data, reported in Ref. [1]. The general work flow was:

1. Signal energy spectra calculated — phenomenology, accounted for the halo distribution, terrestrial effects and atomic effects, see Section 4.1.

2. Energy spectra used to simulate distributions of detector observables (r, z , S1, S2), see Section 4.3.

3. Distributions of detector observables simulated for background components, see Section 4.3.

4. Datasets of the observables created and data quality cuts applied, see Section 4.4.

5. Statistical test carried out — profile likelihood ratio test used for limit setting, see Section 4.5.

6. Limit on the number of signal events converted to a limit on the kinetic mixing parameter to constrain the model, see Section 4.6.

4.3 Simulations

To allow comparison with data it is important to have simulated distributions of detector observables for both signal and background events. Monte Carlo simulation methods are used to simulate particle interactions within the LUX detector. Energy deposits from these interactions used to simulate the resulting VUV photon scintillation photon and ionisation electron production. These simulations are used to create four dimensional probability density functions (pdfs) for observables in the LUX detector — the prompt scintillation (S1), electroluminesence (S2), radial position (r) and vertical position (z). The simulated data sets are then passed through data selection cuts matching those applied to the real data.

4.3.1 Detector Response/Calibrations

Calibrations are essential for characterising the detector response to particle interactions. The response to ER and NR interactions in the LUX detector, was measured using a range of internal and external sources. Electron recoil calibrations required dispersed sources to be put into the liquid xenon: ^{83m}Kr, a metastable krypton isotope which decays monoenergetically, and tritium, which undergoes low energy beta decay. The NR response, determined using a DD neutron generator, is described in Ref. [175].

The ^{83m}Kr calibration was used to determine electron lifetime and 3D corrections for photon detection efficiency. This accounted for geometric effects and impurities — correction maps normalise the S1 size to that at the centre of the detector and the S2 size to that at the liquid gas interface.

The tritium calibration was used to characterise the low energy electron recoil response of the LUX detector, as described in Ref. [191]. An injection of tritiated methane (CH_3T) into the gas circulation occurred in December 2013, immediately following the science data taking. The CH_3T was used as a host molecule for tritium (^{3}H), which has a β decay spectrum with a 2.5 keV peak and 18.6 keV end point. This calibration gave a large sample of electron recoils ($\sim 10^5$ events) from β decays in the energy range of interest, used to precisely measure light and charge yields in the detector. These yields show good agreement with the Noble Element Simulation Technique (NEST) package v2.0.0 [173, 174]. NEST provides models for scintillation and electroluminescence in noble elements, for given detector characteristics — allowing calculation of light and charge yields and the corresponding S1, S2. More details of ER modelling using NEST will be given in Section 5.2.1.

As shown in Section 3.3.2, the energy deposited by a single scatter ER event in

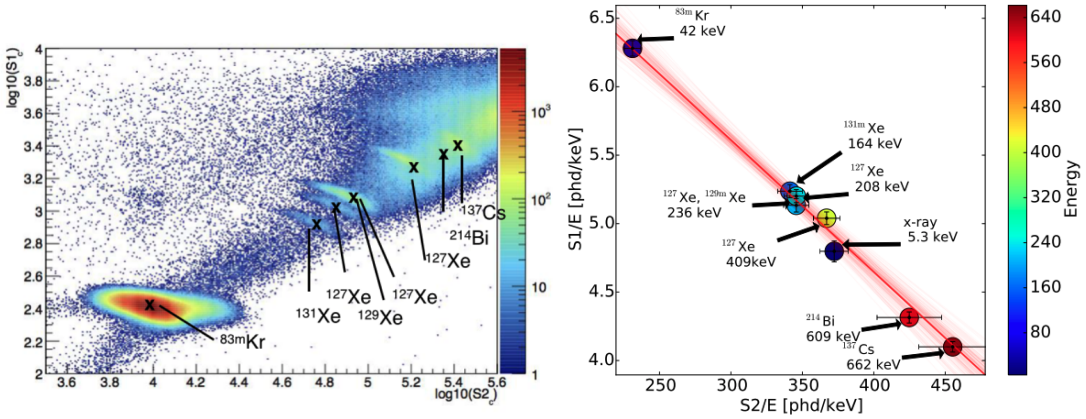

(a) *S1 vs. S2 for line sources in LUX — with ^{83m}Kr and ^{137}Cs data from dedicated calibrations and all other data from background measurements.*

(b) *Plot of sources used for line fitting to extract detector gain values.*

Figure 4.7 *Monoenergetic sources used for detector gain calibrations, taken from Ref. [175].*

the TPC can be described by the combined energy model [192]:

$$E = W(n_e + n_\gamma) = W\left(\frac{S1}{g_1} + \frac{S2}{g_2}\right). \tag{4.20}$$

Here, n_e and n_γ are the number of electrons and photons produced, respectively and $W = (13.7 \pm 0.2)$ eV is the work function for producing these quanta in liquid xenon. Parameters g_1 and g_2 are the gain factors for scintillation photons and extracted electrons, respectively.

For LUX, these gain factors were determined by observing monoenergetic ER sources of known energy. Nine sources were used including injected ^{83m}Kr and external ^{137}Cs, plus background ^{214}Pb and Xe isotopes. The measured S1 and S2 for these sources are shown Fig. 4.7a. For each source a 2D Gaussian was fitted to find the mean $\langle$S1$\rangle$, $\langle$S2$\rangle$. A Doke plot of $\langle$S1$\rangle$/E vs. $\langle$S2$\rangle$/E for all sources, shown in Fig. 4.7b, was then used to perform a linear fit to determine g_1 and g_2. In LUX Run3 this gave: $g_1 = 0.117 \pm 0.003$ phd/photon and $g_2 = 12.1 \pm 0.8$ phd/electron (where phd is photons detected).

Figure 4.8 shows the tritium energy spectrum measured by LUX, using the combined energy model, along with the tritium spectrum convolved with the detector resolution. The ratio of the measured to predicted spectrum gives the ER efficiency in LUX [191].

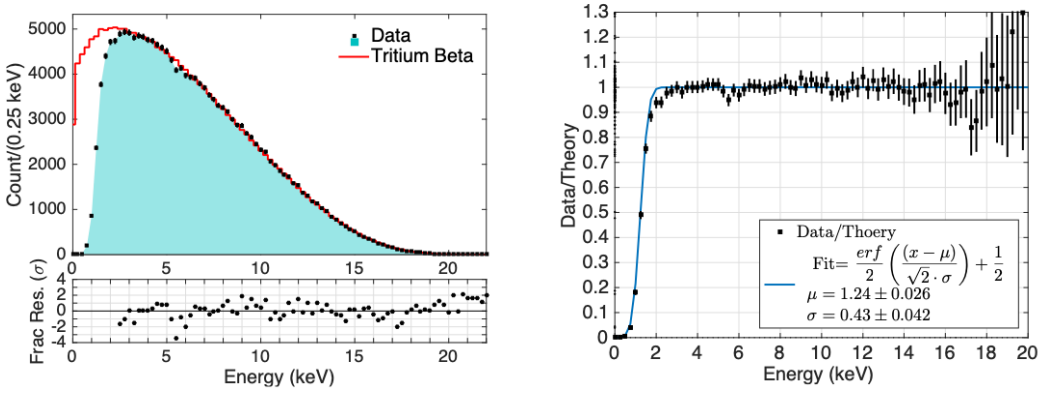

Figure 4.8 *Left: the measured tritium energy spectrum in LUX (black) compared to the expected tritium spectrum convolved with the detector resolution (red). Right: the electron recoil efficiency in LUX, from the ratio of these. Figures taken from Ref. [191].*

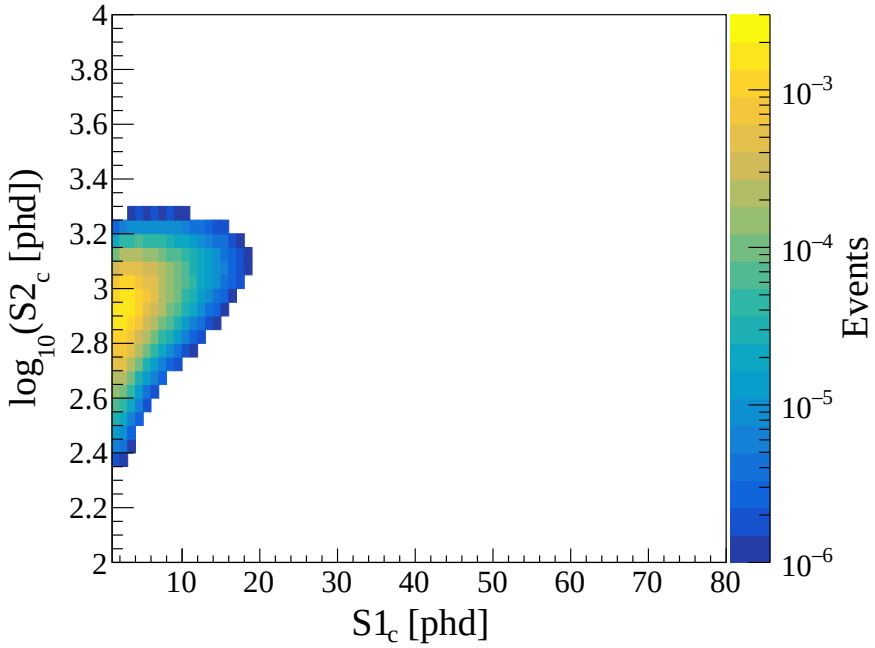

Figure 4.9 *Signal model distribution of detector observables log(S2) vs. S1, for mirror electron temperature $T = 0.3$ keV and kinetic mixing parameter $\epsilon = 1 \times 10^{-10}$.*

4.3.2 Signal

The energy spectra calculated in Eq. 4.10, shown in Fig. 4.6, give the expected energy distribution of mirror dark matter signal events in LUX. No spatial features (radial or depth) are expected for electron recoils induced by mirror electron interactions. A GEANT4 based detector simulation was used to simulate energy depositions deposited uniformly throughout the detector. NEST was then used to model the distributions of the detector observables $(r, z, S1, S2)$, taking into account the detector resolution and efficiency. The resulting distribution in $\log_{10}(S2)$ vs. $S1$ is shown in Fig. 4.9, for mirror electron temperature $T = 0.3$ keV and kinetic mixing parameter $\epsilon = 10^{-10}$.

4.3.3 Backgrounds

In any rare event search experiment it is essential to have precise control over background events which can mimic the signal. The LUX experiment aimed to have less than one WIMP-like background event in 30,000 kg days [176]. Contributions to the background in LUX came from different sources, both

external and internal to the detector. External backgrounds consist of neutrons generated by cosmic ray muon interactions and γ-rays or neutrons from the cavern rock [193]. Shielding by the 300 tonne water tank reduced these to be sub-dominant to internal backgrounds — radioactive decays in the detector components and decays of contaminants within the liquid xenon.

Whilst electron and nuclear recoil events can be discriminated between, using the light to charge ratio (S2/S1), leakage of ER events into the NR band is the dominant background for the WIMP search, due to the much higher ER rate. In ER analyses the signal is amongst these ER backgrounds and the much lower NR backgrounds are not considered.

The largest source of ER backgrounds is Compton scattering of γ-rays from detector components, generated in the decay chains of ^{238}U, ^{232}Th and ^{40}K radioisotopes. During surface assembly cosmogenic activation of Ti and Cu led to ^{46}Sc and ^{60}Co, which also emit γ-rays. Construction materials for LUX were screened prior to use in the detector, see Ref. [193] for details, allowing the γ-ray background rate to be estimated. Following data taking this was refined further by fitting the spectra to measured γ-ray data (see Fig. 2 in Ref. [193]).

In the LUX Run3 data there was found to be an excess of 500 – 1500 keV energy ER events in the lowest 10 cm of the active region, compared to Monte Carlo. These events could be explained by simulating ^{238}U, ^{232}Th, ^{60}Co γ-rays originating from a large copper block below the lower PMTs [178]. Therefore the detector component γ-ray population was subdivided into two spatial distributions: one generated by the bottom PMT array and its support structure and one from the rest of the detector.

Construction materials also provide the largest contribution to the NR background. Neutrons from fission and (α, n) reactions in the ^{238}U, ^{232}Th decay chains and α particles from the PTFE walls can cause NRs in the active volume.

For radioactive decays in detector materials outside of the active volume, β decays do not need to be considered due to absorption. However, β decay (and X-ray emission) from isotopes within the liquid xenon itself are an important background to consider. One source of internal decays is cosmogenic xenon radioisotopes — primarily produced by thermal neutron capture during transport and storage of the xenon above ground [193]. The radioisotopes of interest are: ^{127}Xe, ^{129m}Xe, ^{131m}Xe, ^{133}Xe, all observed in early LUX data. For Run3 only ^{127}Xe has a long enough half life (36 days) to be of interest, and by Run4 it

decayed to a negligible level. The ^{127}Xe isotope decays via electron capture, creating an orbital vacancy which is filled by an electron transition from a higher shell. This causes emission of X-rays or Auger electrons — K shell capture (85%) gives 33 keV energy, L shell (12%) 5.3 keV and the rest from higher shells have $\leq$ 1.2 keV energy. A further internal background arises from ^{37}Ar electron capture decays — with a peak at 2.8 keV possibly seen in data. The ^{37}Ar could come from air surrounding the detector and can be constrained by measurements of its concentration in the lab air, together with limits from the xenon sampling.

The decay cascades of Rn and Kr contaminants in the liquid xenon lead to low energy β emission. If not accompanied by γ-ray emission these cannot be tagged and removed, providing a significant ER background contribution. The two radon isotopes of interest are ^{222}Rn and ^{220}Rn, which decay via ^{214}Pb, ^{214}Bi and ^{212}Pb. These daughter isotopes can undergo naked β decay (with no accompanying EM emission) or semi-naked β decay (accompanied by high energy γ-rays). The Rn daughters cannot be directly measured, but can be constrained by measurements of parent and daughter α decays [193]. Decay rates of ^{214}Pb and ^{214}Bi are expected to be 3.5 – 14 mBq in the active region and ^{212}Pb below 2.8 mBq. However, ^{212}Pb has a longer (10.6 hour) half life, so is expected to leave the active region before it decays. Decay of ^{214}Bi to short lived ^{214}Po, which undergoes α decay within 1 ms means it also does not produce a single β within LUX event window. This leaves only the ^{214}Pb β decay as a background of concern.

The other intrinsic radioisotope which can undergo β decay to produce low energy ER events is ^{85}Kr. Research grade Xe used in LUX contained 130 ppb g/g ^{nat}Kr/Xe when acquired and natural krypton contains the unstable ^{85}Kr isotope at an estimated concentration 2×10^{-11} g/g. The ^{85}Kr undergoes β decay with a 687 keV endpoint, at the acquired concentration this would give 5 DRU$_{ee}$ ER background rate [193]. Since ^{85}Kr would not be removed by the LUX getter (as it is a noble gas), a separate krypton removal system was built to reduce the concentration. The removal system used chromatographic separation based on adsorption on activated charcoal [194]. This reduced the Kr concentration to 3.5 ppt, as measured by weekly sampling during data taking, giving a corresponding ER background rate of 0.17 ± 0.1 mDRU$_{ee}$ (note that DRU is differential rate unit 1 event/kg/day/keV and DRU$_{ee}$ uses keV$_{ee}$ as defined in section 3.3.1).

Similarly to the signal model, four dimensional pdfs in S1, S2, r, z, were generated for each of the background components — the same were used as in Ref. [178]. For this analysis the statistical fluctuations of the simulated pdfs were smoothed

with kernel density estimators [195], using Gaussian kernels with width calculated adaptively from the local density of events. Simulated background sources were summed into five subsets:

- low origin z γ-rays: bottom PMT array, lower copper block (^{60}Co, ^{226}Ra, ^{208}Tl),
- other γ-rays: top PMT array, all other detector components,
- internal β decay: intrinsic ^{85}Kr, ^{220}Rn, ^{222}Rn within the liquid xenon,
- ^{127}Xe electron capture,
- ^{37}Ar electron capture.

These were then weighted using measurements from component screening, Xe sampling and data analysis, to give the full background model, shown in Fig. 4.10.

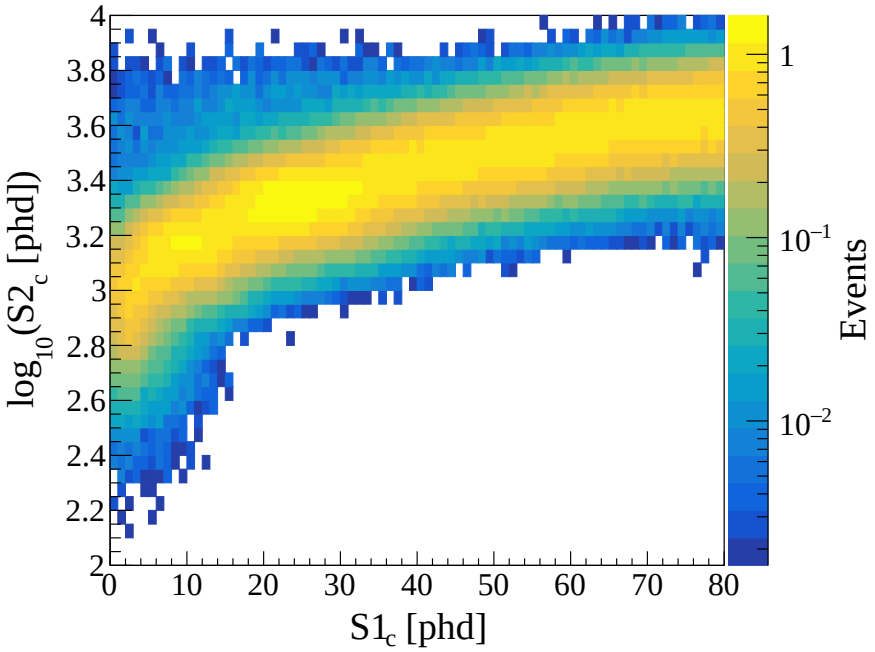

Figure 4.10 *Background model, shown in log(S2) vs. S1 space, from weighted sum of individual components.*

4.4 Data

This analysis used data from LUX Run 3, collected between 24th April and 1st September 2013 — which gave 118 kg × 95 live days, as used primarily for the WIMP search presented in Ref. [177, 178]. Single scatter events consisting of a single S2 preceded by a single S1 are used in this analysis. Events must also come from within a fiducial radius of 18 cm and z range of 8.5 – 48.6 cm above the bottom PMT array (drift time 305 – 38 μs). The S1 pulses in this analysis were required to have two PMTs in coincidence and size 1 – 80 detected photons: the S2 pulses were required to be in the range 100 – 1000 photons. Corrected signal amplitudes $S1_c$, $S2_c$ are used which account for non uniform response throughout the active volume of the detector based on ^{83m}Kr calibrations — with the same applied to simulations. This data is shown in Fig. 4.11 along with 95% signal contours.

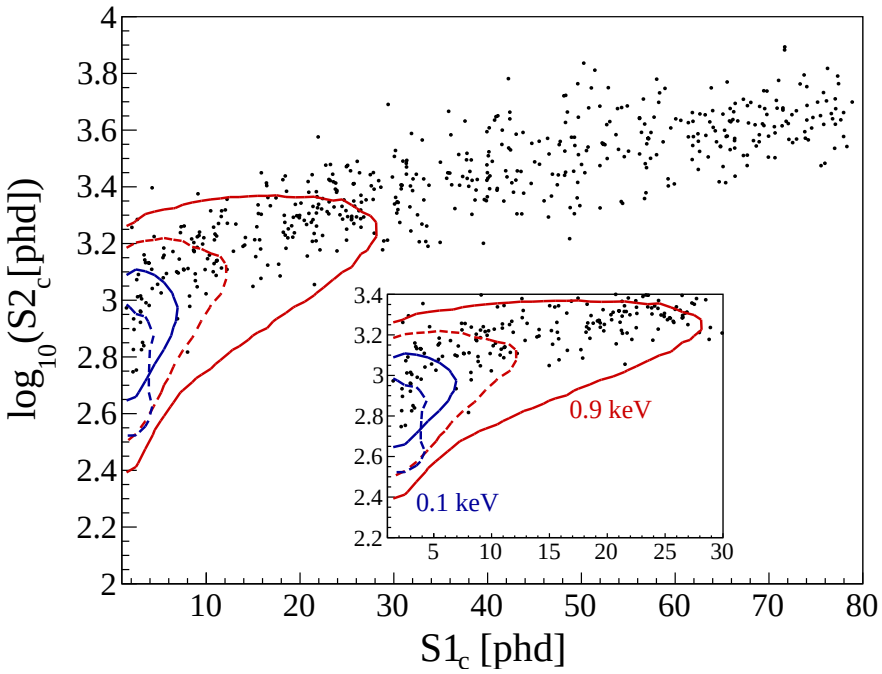

Figure 4.11 *LUX data with contours containing 95% of the expected signal for mirror electron temperatures of 0.1 keV and 0.9 keV. Both are shown for kinetic mixing $\epsilon = 10^{-10}$, the solid line with shielding effects and the dashed line without.*

4.5 Statistical Analysis

Once data has been selected and cuts applied to select suitable candidate events, we want to test a model — either determining discovery significance or excluding the model. A frequentist hypothesis test can be used to compare the model to observations, providing criteria for accepting or rejecting a hypothesis based on measured data. The following describes frequentist hypothesis testing used for rare event searches, including LUX dark matter analyses, based on Refs. [109, 196]. A null hypothesis must be defined, which is assumed to be true until proven otherwise — we can either reject or fail to reject the null hypothesis. For discovery a null hypothesis H_0, of background only, is tested against an alternative hypothesis H_1 of signal plus background — rejecting H_0 means the presence of a signal is favoured. Whilst for limit setting we have a null hypothesis H_0 of signal plus background and an alternative hypothesis H_1 of background only.

The statistical model gives the event probability, normally expressed as a pdf: $f(\bar{x}, \bar{\theta})$, where $\bar{x}$ are the observables and $\bar{\theta}$ are the model parameters, including both parameters of interest and nuisance parameters. For a model containing multiple background components and a signal, each with pdf $f_j(\bar{x}, \bar{\theta})$, and mean μ_j the event probability model is the sum:

$$f(\bar{x}, \bar{\theta}) = \sum_j \frac{\mu_j}{\mu} f_j(\bar{x}, \bar{\theta}), \tag{4.21}$$

where μ is the mean total number of events.

If there are multiple independent measurements/events the probability distributions are multiplied to give the full probability. When the observed number of events n is expected to have Poisson fluctuations around the mean a Poisson term must also be included:

$$f(\bar{x}, \bar{\theta}) = \frac{\mu^n}{n!} e^{-\mu} \prod_{i=1}^{n} f(\bar{x}_i, \bar{\theta}). \tag{4.22}$$

Nuisance parameters $\bar{\nu}$ can improve a model by reducing systematic uncertainties, but their presence may increase statistical uncertainties. Auxiliary measurements can be used to constrain the values of nuisance parameters and pdfs of global

observables $\bar{g}$ are added to constrain the total event model:

$$f(\bar{x}, \bar{\theta}) = \frac{\mu^n}{n!} e^{-\mu} \prod_{i=1}^{n} f(\bar{x}_i, \bar{\theta}) \prod_{j=1}^{N_c} f(\bar{g}_j, \bar{\nu}). \tag{4.23}$$

Values of the model parameters are determined by the hypothesis that is being tested e.g. the signal strength/number of signal events would be zero for a background only null hypothesis.

The likelihood function describes the compatibility of a given data set with different hypotheses — it is the total event model for a given observed data set: $L(\bar{\theta}) = f(\bar{x}_{obs}|\bar{\theta})$, as a function of the model parameters only.

The values of data $\bar{x}$ which lead to rejection of the hypothesis are defined by the critical region w. This region depends on the significance of the test α, it is the area of $\bar{x}$ space where the probability of finding $\bar{x}$ is no more than α; $P(\bar{x} \in w|H_0) \leq \alpha$. In such tests a type I error is defined as rejecting the null hypothesis H_0 if it is true – this has probability α. A type II error is not rejecting the null H_0 if the alternative hypothesis H_1 is true — this has probability $\beta = P(\bar{x} \notin w|H_1)$ and the power of the test is $1 - \beta$. A test statistic $q(\bar{x})$ is used to define the boundary of this critical region, as a scalar function of the data. The Neyman-Pearson Lemma states that the test statistic which maximises the power, for a given significance, is the likelihood ratio:

$$q = \frac{L(H_1)}{L(H_0)}. \tag{4.24}$$

In order to remove dependence on the nuisance parameters the profile likelihood is used — this maximises the likelihood, for a fixed parameter of interest, by varying the nuisance parameters. Therefore, the test statistic used is the Profile Likelihood Ratio:

$$q(\mu) = \frac{L(\mu, \hat{\hat{\nu}})}{L(\hat{\mu}, \hat{\nu})}. \tag{4.25}$$

Here, $L(\mu, \hat{\hat{\nu}})$ is the conditional/profile maximum likelihood for a given value of μ and $L(\hat{\mu}, \hat{\nu})$ is the global maximum likelihood with both μ and ν varying. The test statistic takes values in the range: $0 \leq q \leq 1$, with values close to one indicating good agreement between the data and the hypothesis for a given value

of μ. However, it is more convenient to use the test statistic:

$$t(\mu) = -2\ln\left(\frac{\mathrm{L}(\mu, \hat{\hat{\nu}})}{\mathrm{L}(\hat{\mu}, \hat{\nu})}\right), \tag{4.26}$$

which can take values: $0 \leq t(\mu) \leq \infty$, where higher values correspond to greater incompatibility between the hypothesized value of μ and the data.

To quantify the level of disagreement between the hypothesis and data we compute the p-value:

$$p_\mu = \int_{t_{obs}}^{\infty} f(t|\mu) dt_\mu, \tag{4.27}$$

where $f(t|\mu)$ is the pdf of the test statistic for some value of μ specified by the hypothesis. The test statistic distribution is computed by generating Monte Carlo toys of the dataset, under a given hypothesis, and evaluating the test statistic. The p-value gives the probability of finding t in a region of equal or less compatibility with the hypothesis than the value observed on real data t_{obs}. A low p-value indicates poor agreement between the hypothesis and data. For a one

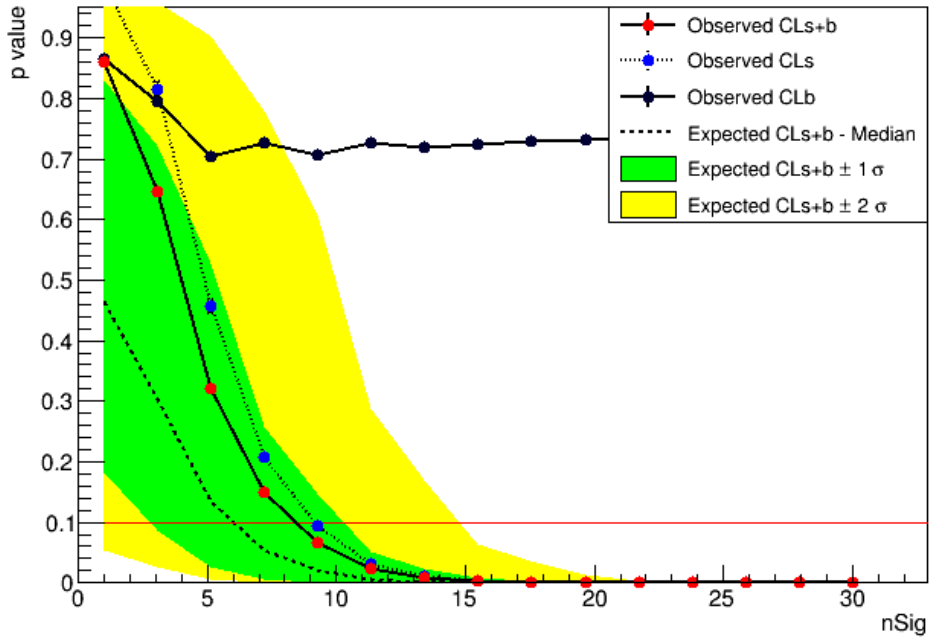

Figure 4.12 *P-value as a function of the number of signal events (parameter of interest). The distributions for signal plus background, background only and the ratio or these are shown. The dashed line shows the expected (median) under the null hypothesis and the coloured bands show the $\pm 1\sigma$ and $\pm 2\sigma$ deviations from this.*

sided test this occurs if the estimated signal strength from data $\hat{\mu}$, is found to be less than the hypothesized value μ. In the case of a two sided test the estimated $\hat{\mu}$ can be either less or greater than hypothesized μ. Note that the p-value depends on the observed data, whilst the significance of a test is chosen beforehand.

For LUX analyses the number of signal events is used as the parameter of interest μ. In a discovery significance test the null hypothesis has $\mu = 0$, whilst for limit setting $\mu > 0$ and the test statistic and p-value are computed for different values of μ. The resulting p-values can be plotted as a function of the number of events, as shown in Fig. 4.12. Here, the p-values for the test statistic under the null hypothesis (CLs+b), the alternative (CLb) and a ratio of these (CLs) are shown. To find an upper limit on the parameter of interest we invert the statistical test for the null hypothesis distribution. A line is drawn at some p-value corresponding to $\alpha = 1 - \mathrm{CL}(\%)$, and the value of the parameter of interest where the plotted curved crosses this line is the upper limit at the given confidence level, CL(%).

This analysis was carried out using four observables: $\bar{x} = (S1, \log_{10} S2, r, z)$. The nuisance parameters were the rates of different classes of background components (described in Section 4.3.3): low-z γ, other γ, internal β, ^{127}Xe and ^{37}Ar. Mean values for each of these were estimated as detailed in Section 4.3 and Gaussian constraint functions were used, with widths corresponding to the uncertainties on each estimate.

4.6 Results

In the LUX Run3 mirror dark matter analysis, the best fit model (global maximum likelihood) was found to have zero signal model contribution. The

Table 4.1 *Nuisance parameters used in the PLR test, the means and standard deviations of the Gaussian constraints are shown along with the value from the best fit to data.*

Parameter	Constraint	Fit Value
Low-z-origin γ counts	157 ± 78	160 ± 17
Other γ counts	217 ± 108	179 ± 18
β counts	65 ± 32	115 ± 17
^{127}Xe counts	35 ± 18	41 ± 8
^{37}Ar counts	10 ± 5	10 ± 7

input and fit value for each nuisance parameter is shown in Table 4.1, and the projections, with corresponding normalisations, are shown in Fig. 4.13. For $T = 0.3$ keV, the background only model gives KS test p-values of: 0.27, 0.68, 0.71 and 0.60, for the projected distributions in $S1$, $\log_{10}(S2)$, r and z, respectively.

Once the 90% confidence limit on the number of signal events had been calculated, as described above, it was converted to a 90% confidence limit on kinetic mixing parameter using:

$$\epsilon(90\%CL) = \epsilon(0)\left(\frac{nSig(90\%CL)}{nPDF(0)}\right)^{\frac{1}{2}}. \tag{4.28}$$

Here, $\epsilon(0)$ is the arbitrary value of kinetic mixing used to generate the signal model, $nPDF(0)$ is the corresponding number of signal events and $nSig(90\%CL)$

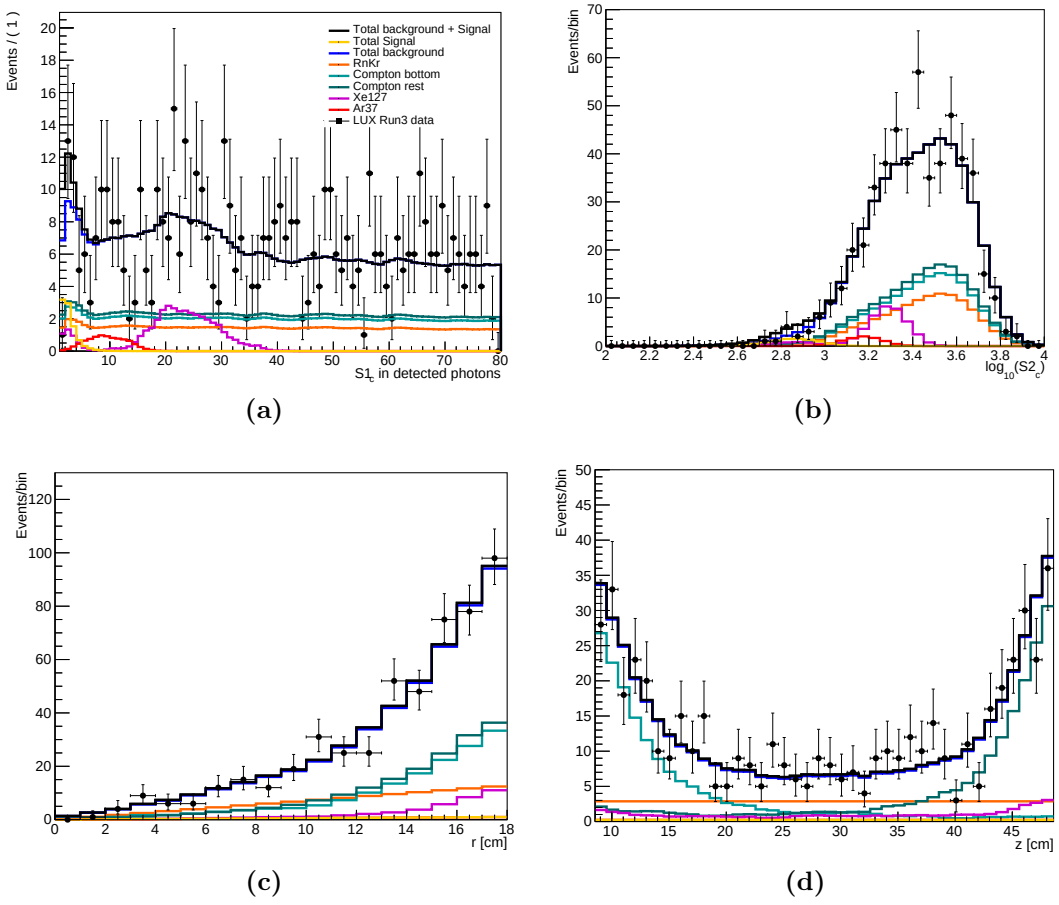

Figure 4.13 *Distributions of the detector observables for the signal and background components, solid lines show the simulations normalised to the best fit values and the black points show the data with errorbars.*

is the 90% confidence limit on the number of signal events. The power of 1/2 comes from the dependence of rate on ϵ^2 in Eq. 4.10, 4.3.

This was repeated to find limits on the kinetic mixing parameter for mirror dark matter temperatures 0.1 – 0.9 keV, the upper limit shown by the blue line in Fig. 4.14. The astrophysical constraint on kinetic mixing within the mirror dark matter theory: $10^{-11} \leq \epsilon \leq 4 \times 10^{-10}$, is also shown – with only the white band allowed. The 90% confidence limit, along with the theory limits on kinetic mixing, excludes mirror electron temperatures above 0.3 keV and constrains the kinetic mixing below this.

The previous experimental constraint onkinetic mixing comes from invisible decays of orthopositronium in a vacuum [197]. If positronium – mirror positronium mixing were to occur, decay to missing photons would leave a missing energy signal. The upper limit placed on the branching fraction of orthopositronium to invisible states gives a 90% upper confidence limit on the

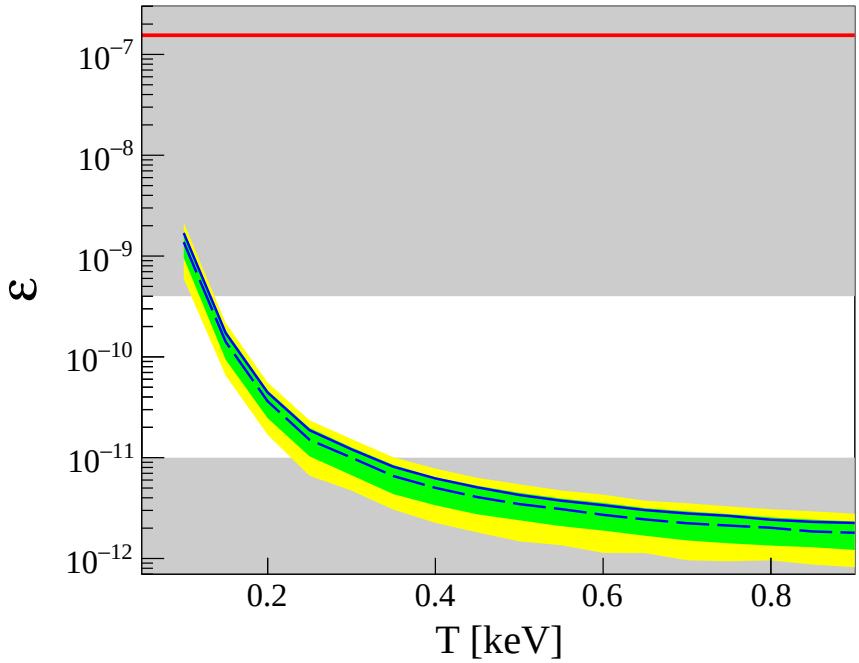

Figure 4.14 *Upper limit on kinetic mixing, at 90% confidence level, as a function of local mirror electron temperature. The solid blue line shows this result, dashed blue is LUX sensitivity with green and yellow bands being 1 and 2 σ respectively. The red line is the upper limit from orthopositronium decays and the grey regions are disallowed by the theory.*

kinetic mixing parameter of: $\epsilon \leq 3.1 \times 10^{-7}$.

In Ref. [198], a constraint on the results from DAMA [199] in terms of mirror dark matter was presented. This study used electron recoil data from the XENON100 experiment to examine leptophilic dark matter models as possible cause of the annual modulation signal, ruling out mirror dark matter as an explanation at a 3.6 σ confidence level.

In summary, the phenomenology of mirror dark matter direct detection has been described, with the effects of mirror dark matter capture by the Earth, and subsequent shielding, calculated for the first time for xenon. This analysis was the first dedicated direct detection search for mirror dark matter, and with no signal observed, a significant proportion of the parameter space allowed by the theory was excluded. Experimental improvements should allow even more of this parameter space to be probed, the projected sensitivity of the LZ experiment to mirror dark matter will be presented in Chapter 5.

However, there are also possible extensions to the theoretical work — the present treatment makes quite simple assumptions for the local mirror electron temperature (thermal equilibrium with nuclei in the halo) and density [56, 200]. The effect of deflection by the captured dark ionosphere is not included and this could significantly alter the signal model. Furthermore, the extent of these shielding effects may have significant dependence on the detector elevation relative to sea level, if the captured distribution is assumed to be spherically symmetric.

Chapter 5

LZ Projected Sensitivity To New Physics Using Low Energy Electron Recoils

The LUX ZEPLIN (LZ) experiment, introduced and described in detail in Chapter 3, is the multi-tonne successor to the LUX experiment. As one of the next generation of liquid xenon experiments, along with XENONnT and PandaX-4T, the main aim is to improve sensitivity to WIMP dark matter by an order of magnitude [184]. The ultimate goal is to explore as much as possible of the experimentally accessible parameter space, pushing down to the "neutrino floor" where the rate is dominated by irreducible neutrino interactions. Features designed to achieve this unprecedented sensitivity: low threshold, high exposure and low backgrounds (from design and veto), also give sensitivity to other rare interactions. In this chapter the low energy electron recoil signals that LZ can probe are examined, along with the important backgrounds and simulation techniques, as presented in Ref. [2]. The projected 90% confidence limit (CL) exclusion sensitivity is found for each signal model and the projected 3σ evidence for selected models is presented, along with the variation in sensitivity with dominant background levels.

5.1 Low Energy Electron Recoil Searches

As the parameter space for WIMP dark matter diminishes, there is increased interest in probing alternative dark matter models and other new physics processes. Many of these processes result in electron recoil (ER) events instead of, or in addition to, the nuclear recoil (NR) events expected for WIMP interactions — as described in Section 3.2.3. In LUX electron recoil analyses for solar axions and axion-like particles [140], sub-GeV dark matter (via Migdal and Bremsstrahlung) [182] and mirror dark matter [1] (described in Chapter 4) were carried out independently. LZ aims to have an even more comprehensive program of low energy ER searches, all using a common analysis framework.

5.1.1 Common analysis framework

The general analysis methodology is similar to that outlined in Section 4.2 for the LUX mirror dark matter analysis, however each stage is modular so that any

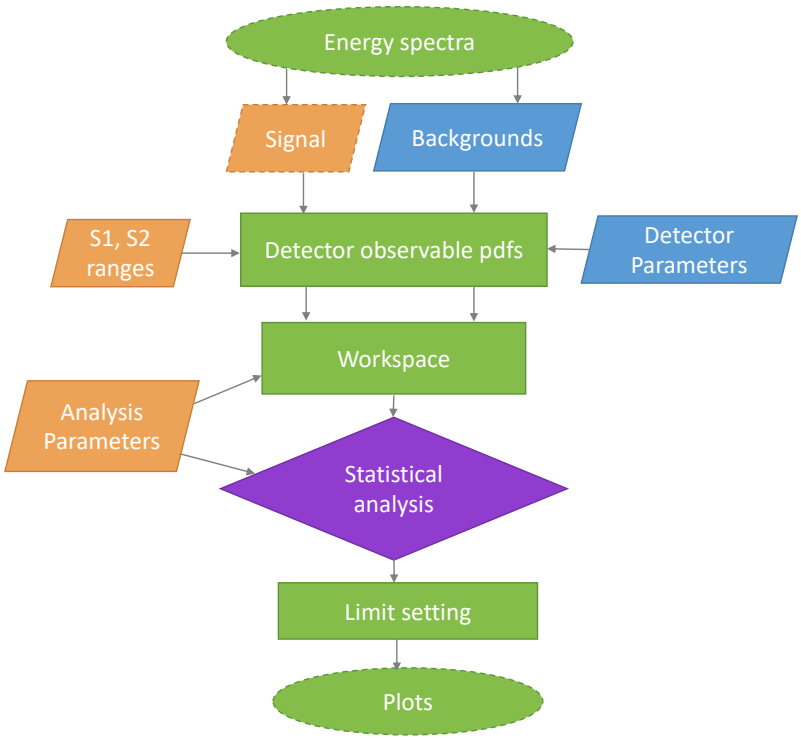

Figure 5.1 *General work flow for low energy electron recoil analysis. The orange stages are input independently for each separate analysis, with the stages with dashed outlines being unique to each analysis.*

low energy electron recoil signal can be put in. Figure 5.1 shows the work flow for the analysis, each signal model search requires unique energy spectra to be generated and will result in a unique limit plot for some physics parameter in that model (indicated by the dashed lines). In between these two points there are common stages:

1. Calculation of background energy spectra — common to all analyses.
2. Generation of detector observable (S1, S2) probability density functions (PDFs).
3. Simulated signal and background PDFs combined in a workspace — also defines analysis parameters.
4. Statistical analysis — profile likelihood ratio test using external package.
5. Conversion of limit on number of signal events to limit on some model parameter.
6. Generation of limit plots, scanning over values of the model parameter where appropriate.

The signal energy spectra must be uniquely generated for each analysis, shown in Fig. 5.6. The PDF ranges and analysis parameters are also input by the person doing each analysis, but they may be common to multiple searches. Statistical analysis, described in Section 5.3, is carried out using the LZStats package which allows the user to run a frequentest profile likelihood ratio test. The result of this test is used to find a limit on the value of some parameter of the signal model, which can then be uniquely plotted for each analysis. Background energy spectra and projected detector parameters are inputs which are common to all analyses, with Figure 5.3b showing the spectra and Table 5.1 giving the expected rates in LZ.

5.1.2 Backgrounds

Since most of the backgrounds expected in LZ will result in ER events, the sensitivity to rare ER signals is limited by a combination of radiogenic and cosmogenic backgrounds. These backgrounds are minimised using a stringent background control strategy consisting of: underground operation and a water

tank (to mitigate cosmogenic backgrounds), target self shielding and outer detector veto (to mitigate backgrounds from external radioactivity) and low radioactivity material selection plus xenon purification (to mitigate internal backgrounds). However, some level of backgrounds will remain, so it is vital to have an accurate background model. Since this background model is common to all low energy (ER and NR) searches, the work here largely follows that done for the WIMP search analysis [167] with a few modifications and additions. The relative importance of the different electron recoil background components and energy spectra are shown in Fig. 5.3a. 5.3b.

Radiogenic and cosmogenic

Similar to the LUX backgrounds, described in Section 4.3.3, there are expected to be ER backgrounds in LZ from internal β decays and external γ-ray emission.

Detector materials contain radioisotopes: ^{40}K, ^{137}Cs, ^{60}Co and ^{238}U, ^{235}U, ^{232}Th, which emit γ-rays that can penetrate the detector causing ER events in the fiducial volume. The U, Th isotopes also produce neutrons through spontaneous fission and (α, n) reactions, which can cause NR backgrounds. A comprehensive screening campaign, involving almost 2000 radio-assays, was used to select the most radiopure detector materials and inform the background model [201]. For example, the Hamamatsu R11410 PMTs (introduced in Section 3.5.1) were chosen due to their low radioactivity. The choice of titanium for the cryostat, which is a factor of 2 lower in U/Th contamination than that used in LUX, was the result of a 2 year material search campaign [184]. This strict quality control, and the xenon self-shielding, means that radioactivity from detector components is not the dominant background source, in contrast to LUX.

Surface contamination of detector materials is another source of radiogenic backgrounds. Stable ^{222}Rn exists at levels of tens to hundreds of Bq/m^3 in air, and charged daughters can plate out onto surfaces during detector construction and installation. This can result in NR backgrounds due to (α,n) processes and ions from the ^{210}Pb subchain being mis-reconstructed within the fiducial volume. The latter effect is an important driver in determining the fiducial cut used. Any γ-rays produced in the decay chains of these radioisotopes will be a source of ER backgrounds if they penetrate the fiducial volume. Dust that accumulates on surfaces is a further cause of radon contamination. To minimise surface backgrounds, the exposure of detector components to radon rich air is

limited, radon proof storage materials are used and surface cleaning techniques are employed. This aims to ensure that strict limits on the radon plate out on xenon wetted surfaces are met.

Backgrounds from the environment must also be considered — neutrons and γ-rays can be produced by U, Th decays in the cavern walls or atmospheric muon induced reactions in the rock or detector. Neutrons from muon induced electromagnetic and hadronic cascades in rock, water and scintillator, can result in NR backgrounds. Neutrons from the cavern walls are attenuated efficiently by the water and scintillator shields — the maximum thickness of 70 cm homogeneous shielding gives a 6 order of magnitude reduction. Any γ-rays produced in these cascades may penetrate the detector more effectively and the γ-ray flux has been measured at various places in the Davis campus at SURF, where LZ is located [202]. The resulting spectral shape of these combined detector, surface and environmental backgrounds is approximately flat in the 0 – 100 keV energy range as shown in Fig. 5.3b.

Dispersed radioisotopes undergoing β decay within the liquid xenon give an ER background that cannot be mitigated through self shielding. This is the dominant background for the low energy electron recoil searches in LZ. As described in Section 4.3.3, Rn and Kr isotopes can undergo naked β decays which are not accompanied by γ-ray emission (which would allow tagging). The ^{222}Rn, ^{220}Rn and ^{85}Kr isotopes are of particular importance and the conservative goal is to keep the sum of these below three times the pp solar neutrino background rate. The Rn level in the detector is minimised by reducing the surface contamination, as outlined above, so that levels of Rn emanation are as low as possible. The LZ background model assumes 1.8 μBq/kg of ^{222}Rn, based on emanation measurements of materials and estimates of dust levels — this is an order of magnitude improvement from LUX [193]. Gas charcoal chromatography is used to remove Kr from the xenon, using the process developed in LUX, aiming to reduce the total Kr concentration to less than 0.015 ppt ($\sim 10^7$ lower than research grade Xe and an improvement on the 3.5 ppt in LUX). However, there is some uncertainty in the level of Rn, Kr that will be present in LZ and the effect of the variation of projected sensitivity is examined in Section 5.4.4. In real data the semi-naked decay of ^{214}Pb to ^{214}Bi in the ^{222}Rn decay chain can be tagged using the subsequent ^{214}Po α decay, allowing indirect measurement of the ^{222}Rn level. The background spectra arising from ^{222}Rn, ^{220}Rn and ^{85}Kr have a flat spectral shape in the region of interest, with the spectra and estimated rates shown in Fig.

5.3b and Table 5.1. The pie chart in Fig. 5.3a demonstrates that the combined component from these isotopes is the single largest contributor to the electron recoil background.

Physics backgrounds

Tight control of radioisotope backgrounds means that it is important to consider new backgrounds from physics processes, which were not considered in LUX. These backgrounds are: neutrino nucleus scattering (NR), neutrino electron scattering (ER) of solar neutrinos, ^{136}Xe $2\nu\beta\beta$ decay and ^{124}Xe double electron capture.

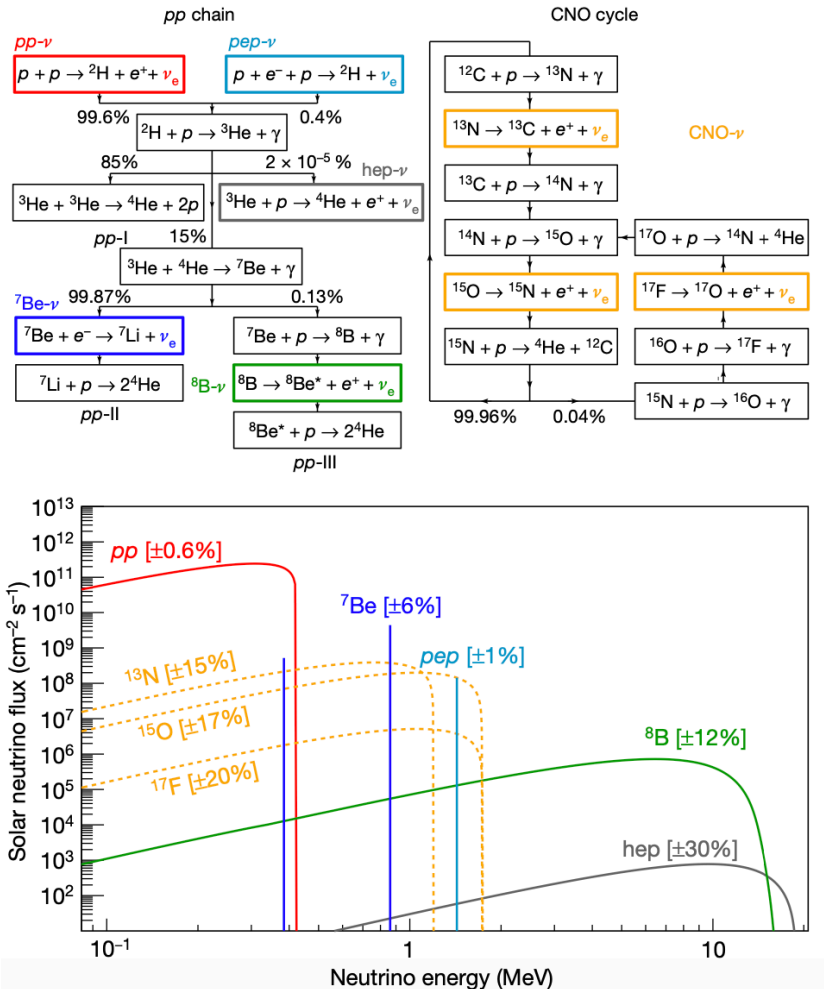

Figure 5.2 *Top: schematic of the pp and CNO nuclear fusion chains. Bottom: solar neutrino energy spectra for the different components. Figure taken from Ref. [203]*

Neutrinos are produced in the two fusion chains which power stars: the proton-proton (pp) chain and carbon nitrogen oxygen (CNO) cycle. The relative importance of the chains depends on the stellar mass and metal abundances in the core. For the Sun and other low mass stars, the pp chain dominates producing 99% of solar energy. In the pp chain most neutrinos are produced in the initial pp fusion step: $p + p \rightarrow^2 H + e^+ + \nu_e$, with a small number also produced in the three-body pep process, shown in Fig. 5.2. In the later stages further neutrinos are also produced by ^{7}Be electron capture and ^{8}B positron emission. The pp and ^{8}B neutrinos have continuous energy spectra, as shown in Fig. 5.2, with 420 keV and 15 MeV end points respectively. Neutrinos from captures give spectral lines: ^{7}Be at 0.384 MeV and 0.862 MeV and pep at 1.44 MeV. In the CNO chain the proton fusion is catalysed by heavier elements, via a series of proton capture and positron decays. Neutrinos produced in the positron decays of ^{13}N, ^{15}O and ^{17}F, result in continuous energy spectra extending up to 1.74 MeV. The flux depends on the choice of solar model: in the Standard Solar Model pp and ^{7}Be neutrinos make up 98% of the total solar neutrino flux [204, 205]. Neutrino oscillations are also important in the determining the events detected on Earth, occurring both within the solar medium and in the vacuum in between the Sun and Earth. LZ uses oscillation parameters from Ref. [109].

Solar neutrinos can undergo both ER and NR interactions in the detector via either neutrino-electron elastic scattering or coherent elastic neutrino-nucleus scattering CEνNS, introduced in Section 3.2.1. The Standard Model (SM) CEνNS process was first observed by the COHERENT collaboration in 2017 [206], four decades after it was first theorised in Ref. [117]. COHERENT used a CSI[Na] scintillator to detect neutrinos from a spallation source, observing CEνNS with 6.7σ significance.

Nuclear recoils from CEνNS from the ^{8}B and hep solar neutrinos are important in LZ, whilst interactions due to the other components would be below the energy threshold. Atmospheric neutrinos, produced by muon and pion decays, and neutrinos from distant supernovae, can result in NR events at higher energies, but with much lower flux. The ^{8}B neutrinos also provide a signal that LZ can study, with $\sim$ 36 events expected in the full exposure [167] (with a 4 keV NR threshold) and threshold lowering techniques can increase this significantly [186].

Elastic scattering of lower energy solar pp, ^{7}Be and CNO neutrinos with electrons give an irreducible ER background. For low energy ER searches the pp neutrino background is particularly important, with the ^{7}Be and ^{13}N only becoming

important at higher energies which only affect the highest mass ALP/HP searches. It is important that this irreducible solar neutrino background is accurately modelled in our study.

For low energy scatters the energy transfer begins to overlap with atomic energy scales, so it is important to account for atomic binding effects rather than treating the xenon electrons as free. The relativistic random phase approximation (RRPA) provides a method for first principles calculations of the structure, photoionization and neutrino-ionization of xenon [207]. This accounts for relativistic effects and two electron correlations, giving more accurate xenon wavefunctions. In Ref. [207] the wavefunctions and resulting event rate in xenon are calculated for 100 eV – 30 keV recoil energies. In this energy range the rate is 25% lower than in the free electron model. Above 30 keV the RRPA calculations have not been done, so a stepping approximation is used to account for the atomic energy levels. This uses a stepping function to give the number of electrons participating in a scattering interaction — only the electrons with binding energy less than the energy deposited by the incoming neutrino. The stepping function is scaled to match the RRPA rate at 30 keV. The resulting energy spectrum is shown in Fig. 5.3b, with the steps seen below 40 keV due to these atomic shell effects.

In addition to being a background, pp and ^{7}Be neutrinos could be measured as a signal in multi-tonne detectors at the precision level of current solar models. Extensions to the SM which result in additional neutrino cross section terms can also be probed, as described in Section 5.1.3. The Borexino experiment carried out a complete measurement of the pp chain energy spectrum, measuring the ^{7}Be, pep, ^{8}B and pp neutrinos, successively [203]. In 2020 the experiment also observed the first direct experimental evidence for CNO neutrinos [208].

Further physics backgrounds arise from nuclear physics processes of xenon isotopes, including the two neutrino double beta decay of ^{136}Xe. In this decay two neutrons in the nucleus are simultaneously converted to protons with two electrons plus two neutrinos being emitted. The second order SM process is observable in even-even nuclei, where single β emission is energetically forbidden. It is distinct from the neutrinoless double beta decay process, which is forbidden by the SM, and can be used to probe the possible Majorana nature of neutrinos [187]. The ^{136}Xe isotope makes up 8.9% of naturally occurring xenon, so a significant mass is expected in LZ. As an even-even nucleus it undergoes $2\nu\beta\beta$ decay giving a continuous energy spectrum with a 2458 keV end point, shown in the 0–100 keV energy range in Fig. 5.3b. This process for ^{136}Xe has been

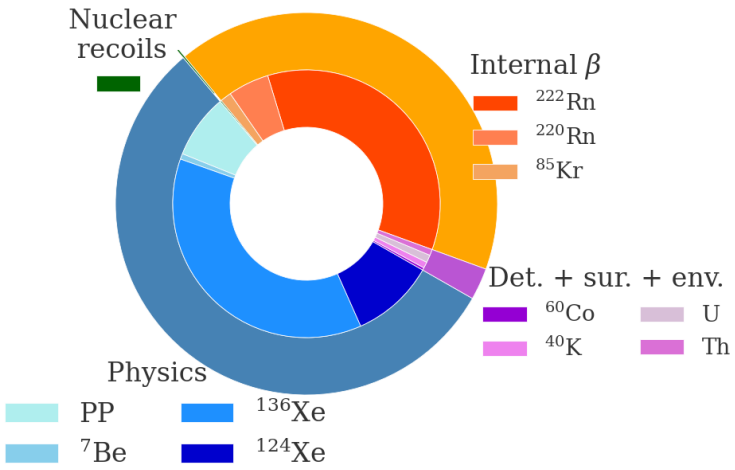

(a) *Relative contributions of LZ background components in the 0–100 keV energy range.*

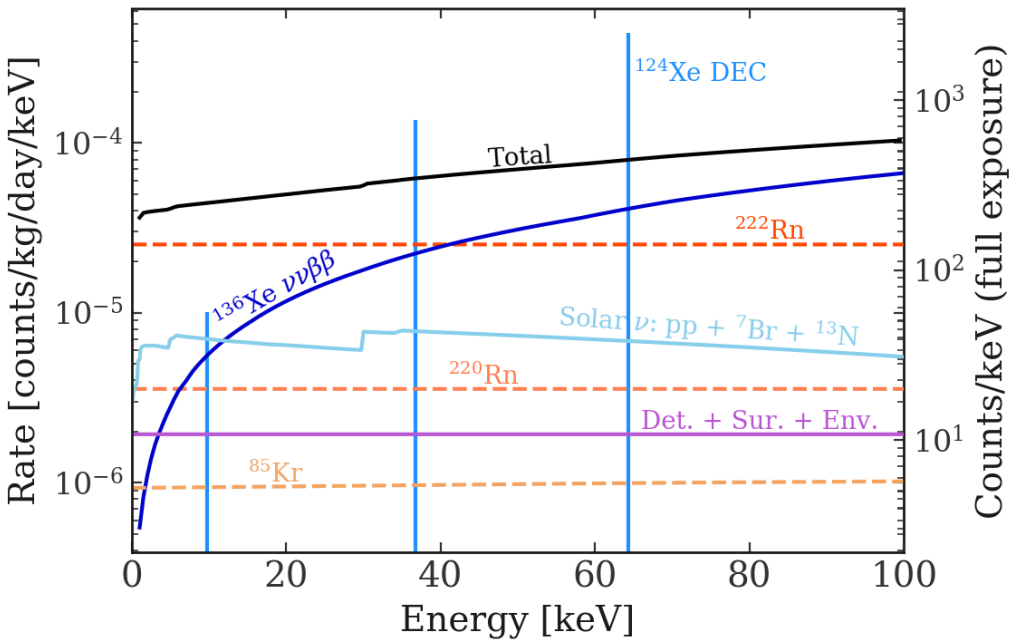

(b) *Energy spectra of electron recoil backgrounds in LZ.*

Figure 5.3 *LZ background components in the 0–100 keV energy range considered for low energy electron recoil searches.*

observed by EXO-200 and KamLAND-Zen [209, 210], with the measurements used to calculate the expected rate in LZ. However, there is a large uncertainty in the event rate for this decay due to uncertainties in the spectral shape at low

energies. As the spectrum overlaps significantly with the pp neutrino spectrum it is the main factor limiting the measurement of the pp neutrino flux. This background could be reduced by reducing the atomic abundance, however this would be in conflict with searches for ^{136}Xe neutrinoless double beta decay [187].

The second nuclear physics process considered is double electron capture by the ^{124}Xe nucleus. Simultaneous capture of two electrons results in conversion of two protons to two neutrons in the nucleus, accompanied by emission of two neutrinos. This SM process is again distinct from the zero neutrino version, which only occurs if the neutrino is a Majorana particle. After capture of electrons (mostly K shell), a cascade of X-rays and Auger electrons are emitted as the atom de-excites, with electrons from higher energy shells filling the vacancies. The neutrinos carry most of the nuclear binding energy from the process, so the resulting signal is monoenegetic peaks with energy depending on the shell(s) from which the electrons are captured. The three most frequent K and L shell capture combinations are: KK 64.3 keV (76.6%), KL 36.7 keV (23%) and LL 9.8 keV (1.7%). Two neutrino double electron capture on ^{124}Xe was first observed directly in the XENON1T experiment at a 4.4σ significance level, with a half life of $1.8 \pm 0.5 \pm 0.1 \times 10^{22}$ years [211]. This background was not included in the WIMP sensitivity study [167], but we include it here with rate calculated using the XENON1T half life measurement, as shown in Fig. 5.3b.

Production of ^{125}I by ^{124}Xe neutron capture (mostly on the unshielded xenon outside the water tank) was also considered. The rate depends on the iodine purification time scale, assuming a 10 day purification half life gives $\sim$100 ^{125}I decays in the 5.6 tonne $\times$ 1000 day exposure. This number is much smaller than the expected ^{124}Xe KK-shell background and nearly degenerate in energy (67.3 keV), so it is not included in the background model.

Unexpected backgrounds

Another difference from the WIMP sensitivity study is the inclusion of two "unexpected but possible" background components, motivated by the recent excess that the XENON1T experiment saw evidence for at $\sim$ keV energies [141]. One component, considered by XENON1T, is tritium which could arise from cosmogenic activation of xenon during above ground exposure, or emanation from detector materials (with cosmogenic or anthropogenic origin). The β decay of tritium results in a continuous spectrum with a 18.6 keV end point and a

Table 5.1 *Expected mean counts for each background component in a 5.6 tonne × 1000 day exposure after the application of single scatter, veto, and fiducial volume selections.*

	Expected counts in 5.6 t 1000 d				
Component	Energy range [keV]		S1c range [phd]		Unc.
	1.5-10	1.5-70	0-100	0-570	(%)
^{222}Rn	1216	9873	2504	11998	
^{220}Rn	171	1394	353	1694	24
^{85}Kr	45	378	93	462	
^{136}Xe	166	8796	603	13186	50
^{124}Xe	38	3287	56	3299	30
Solar ν	336	2418	670	2845	—
Det. +Surf. +Env. γ	93	754	191	916	20
TOTAL	2065	26900	4470	34400	

broad peak at $\sim$ 3 keV. The second background component is ^{37}Ar, which is produced cosmogenically either from fragmentation of Xe atoms in the detector or by neutron induced reactions in the atmosphere, which could enter the detector via air leaks. Electron capture decay of ^{37}Ar results in X-ray and Auger electron cascade emission, giving a mono-energetic peak at 2.8 keV. The short 35 day half life of ^{37}Ar means that even if this background is present in early data it should be negligible in LZ after a few months.

These components are not included in the background model used in the electron recoil sensitivity studies, however they are included as unconstrained nuisance parameters in the statistical analysis as described in Section 5.3. A similar approach was taken in LUX, after observation of an unexplained excess at 2.8 keV, which was attributed to ^{37}Ar.

5.1.3 Signal Models

Figure 5.4 shows the low energy electron recoil signal models studied for LZ, arranged by source, particle type and motivation. Particles originating in the Sun can be used to study extensions to the SM — solar axions and neutrino electromagnetic interactions, whilst dark matter halo particles arise from both bosonic and fermionic dark matter models. The axion, axion-like particle and hidden photon models arise from a broken U(1) group which generates a

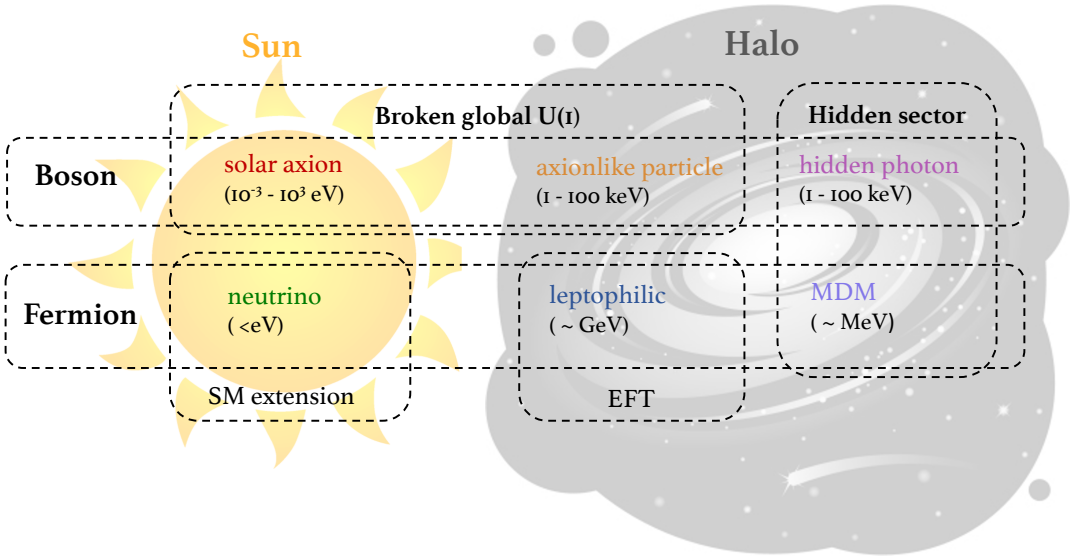

Figure 5.4 *Schematic showing the low energy electron recoil signal models considered for LZ, organised by particle type, origin and motivation.*

boson. Bosons are absorbed by the Xe electron in some effect analogous to the photoelectric effect, whilst the fermion dark matter and neutrinos scatter off the electrons.

Different beyond the SM and dark matter models have been motivated in Chapter 3: here the phenomenology and expected rates in LZ will be presented. This author was responsible for the solar axion and mirror dark matter analyses, so these will be discussed in detail, whilst the other models which used the same common analysis framework will be briefly summarised.

Solar Axion

As described in detail in Section 2.2.3, the Peccei-Quinn solution to the strong CP problem, introduces an additional U(1) chiral symmetry that is spontaneously broken at some scale f_a, producing Nambu-Goldstone bosons — axions. As shown in Eq. 2.11, 2.13, 2.15 the couplings of axions to leptons, hadrons and photons are inversely proportional to f_a and the smallest values have been ruled out by experimental searches ($f_a \geq 10^9$ GeV) [212]. Therefore, axions are expected to be very weakly interacting and very light, since axion mass is also inversely proportional to f_a.

Axions have the required characteristics for dark matter candidates (neutral, non-

baryonic and weak SM interactions) and could be produced in sufficient quantities by a non-thermal realignment mechanism [213]. Axions could also be produced by nuclear reactions and thermal processes in the interiors of stars which are known to produce weakly interacting particles, such as neutrinos.

Axion-electron interactions would occur via the axio-electric effect, which is analogous to the photoelectric effect. This could produce ERs in LZ from solar axions emitted by the Sun. The solar axion flux, resulting from production of axions by reactions in the solar plasma, depends on the coupling of axions to electrons, g_{ae}, photons, g_{ag}, and nucleons, g_{an}, as described in 2.2.3. There are three solar axion production mechanisms associated with each of these couplings:

1. Axion-electron coupling — Atomic, Bremsstrahlung and Compton (ABC) [214]
2. Axion-photon coupling — Primakoff effect [39]
3. Axion-nucleon coupling — ^{57} Fe de-excitation [215]

The relative importance of these production mechanisms depends on the axion model — for hadronic models, such as KSVZ, [44, 45] the axion has no tree level coupling to hadrons or leptons, so the Primakoff production dominates. However, for general axion models such as DFSZ [46, 47] the ABC processes, due to the electron coupling, will dominate production. Here no model is assumed and the three components are treated independently.

The ABC reactions, driven by the axion-electron coupling, comprise: atomic axio-recombination and axio-deexcitation (A), electron ion and electron electron bremsstrahlung (B) and Compton scattering (C) [214]. Despite A having the largest cross section it only contributes for metal ions, which are less abundant in the Sun than hydrogen, helium and electrons. Therefore B dominates with the ratio of solar fluxes: $\phi_A : \phi_B : \phi_C = 27.6 : 64.9 : 7.6$.

The total ABC axion emission rate from axion-electron coupling is given by [214].:

$$\Gamma_a(\omega) = \frac{g_{ae}^2 \omega^2}{e^2 m_e^2} \frac{k(\omega)}{e^{\omega\ T} - 1} + \frac{e^{w/T} - 2}{2(e^{w/T} - 1)} \Gamma_a^C + \Gamma_a^e e. \tag{5.1}$$

The first term gives the A, electron-ion B and part of C contribution which can be scaled from the equivalent photon production processes. Here, g_{ae} is the axion-electron coupling, $k(\omega)$ is the absorption coefficient, ω is the axion energy

and T is the local solar temperature. The second term gives the remaining C contribution, where Γ_a^C is the Compton scattering rate. The third term gives the electron-electron B, for which there is no equivalent photon process. The flux is found by integrating the sum of emission rates from ABC, multiplied by the phase space density, over the volume of the Sun:

$$\frac{d\Phi_a}{d\omega} = \int_{Sun} dV \frac{4\pi\omega^2}{(2\pi)^3}\Gamma_a(\omega). \tag{5.2}$$

Tabulated values of this flux, provided in Ref. [214], are used to calculate the signal spectrum.

The axion-photon coupling drives Primakoff production, in which particles with a two photon vertex can be produced from thermal photons in an external field. The strong magnetic fields and thermal photons in the Sun enable this production mechanism, with flux [39]:

$$\frac{d\Phi}{dE} = 2.481 \times g_{10}^2 E e^{-E/1.205} [6 \times 10^{10} \mathrm{cm}^{-2}\mathrm{s}^{-1}\mathrm{keV}^{-1}], \tag{5.3}$$

where $g_{10} = g_{a\gamma}/10^{-10}$ GeV^{-1}.

The axion-nucleon coupling can lead to axion emission from nuclear M1 transitions. This requires an isotope which has an accessible first excited state with an M1 transition to the ground state and a high natural abundance in the Sun. The ^{57}Fe isotope fulfils these conditions, with a 14.4 keV first excited state (compared to solar temperature $\sim$ 1.3 keV) and 2.6% solar abundance by mass fraction. Deexcitation of thermally excited ^{57}Fe, via nuclear M1 transitions, results in monochromatic axions produced with flux [216]:

$$\Phi_a = \left(\frac{k_a}{k_\gamma}\right)^3 \times 4.56 \times 10^{23} (g_{an}^{eff})^2 cm^{-2} s^{-1}, \tag{5.4}$$

where g_{an}^{eff} is the effective axion-nucleon coupling. The CAST [216] and CUORE [217] experiments have carried out dedicated searches for this type of axions.

All of the above fluxes must be multiplied by the axion-electron cross section, σ_{ae}, to find the expected event rate in liquid xenon:

$$\frac{dR}{dE} = \sigma_{ae} \times \frac{d\phi}{dE} \times N_{Xe}, \tag{5.5}$$

where N_{Xe} is the atomic density. The photoelectric cross section, σ_{pe}, can be

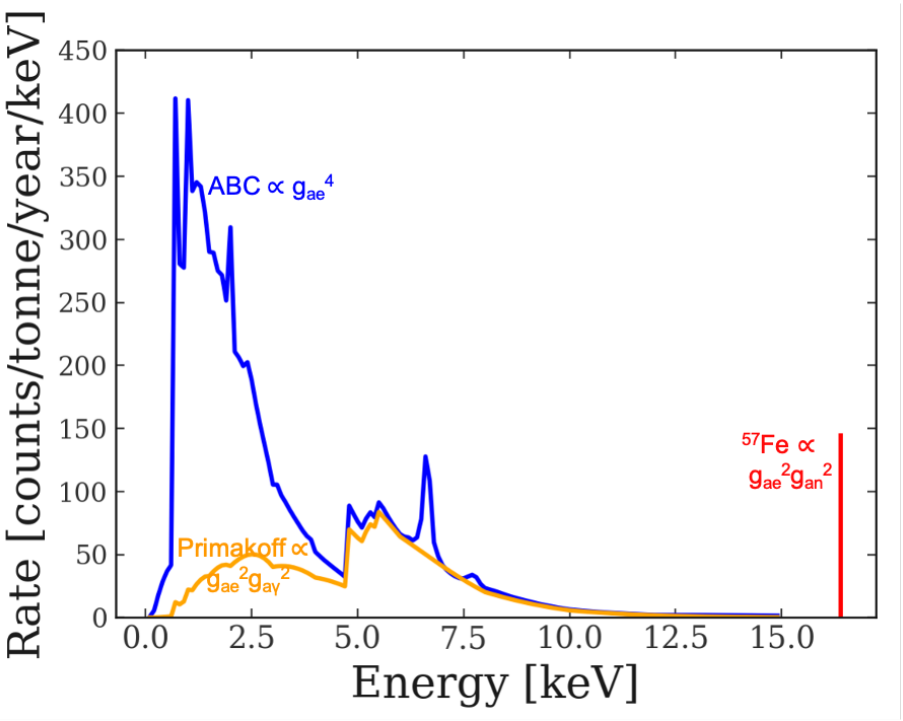

Figure 5.5 *Energy spectra of the three solar axion components, labelled with proportionality to the axion couplings, set to* $g_{ae} = 5 \times 10^{-12}$, $g_{a\gamma} = 2 \times 10^{-10}$, $g_{an} = 1 \times 10^{-6}$.

scaled to find the axion-electron cross section:

$$\sigma_{ae} = \sigma_{pe} \frac{g_{ae}^2}{\beta} \frac{3\omega^2}{16\pi\alpha m_e^2}, \tag{5.6}$$

where ω is the axion energy, β is the axion velocity, α is the fine structure constant and m_e is the electron mass.

The coupling dependence for the rate of each solar axion component comes from both the flux and the cross section: the ABC component is proportional to g_{ae}^4, the Primakoff component is proportional to $g_{ae}^2 g_{a\gamma}^2$ and the ^{57}Fe component is proportional to $g_{ae}^2 g_{an}^2$. The expected energy spectra for the three different components incident on xenon are shown in Fig. 5.5, with couplings set to $g_{ae} = 5 \times 10^{-12}$, $g_{a\gamma} = 2 \times 10^{-10}\text{GeV}^{-1}$, $g_{an} = 1 \times 10^{-6}$. Liquid xenon direct detection experiments have typically used the only ABC component to probe g_{ae}. In this study a projected sensitivity to g_{ae} will be calculated using the ABC component, however the overlapping Primakoff component will be accounted for in the statistical analysis, as described in Section 5.3. The ^{57}Fe component is not included as it is outside of the energy region of interest and does not overlap with

the ABC signal.

The lower middle panel of Fig. 5.6 has a dashed line showing the theoretical input energy spectrum for the ABC component. A solid line shows the reconstructed energy following LZ simulations and it can be seen that experimental resolution smooths out atomic shell effects.

Mirror Dark Matter

As introduced in Chapter 2, then described in detail in Chapter 4, mirror dark matter (MDM) is a hidden sector dark matter model where the hidden sector is isomorphic to the SM [55]. This symmetry means the hidden sector contains a mirror partner of each SM particle, with the same masses, lifetimes and self interactions. Kinetic mixing between mirror and SM particles would allow mirror electrons in the halo to scatter off Xe atomic electrons in the LZ detector, inducing ERs. The rate of ERs depends on the kinetic mixing strength ϵ and the local mirror electron temperature T, as shown in Eq. 4.10. There is also a non-negligible terrestrial effect from the capture and subsequent shielding of incoming mirror electrons, calculated in Section 4.1.1.

Significant modulation, both annual and sidereal, is expected for plasma dark matter models, including MDM. For the LUX analysis the modulation factor was calculated based on the dates and times at which data was taken (see Section 4.1.2, since these are not yet known for LZ a modulation factor must be estimated. The modulation terms are calculated for a given date — with maximum daily variations of approximately $\pm$ 60% seen on the 7th June and 8th December. These variations average out over the course of a year and for 1000 live days we find a maximum variation of 7% in total event number. However, there may be greater variation depending on any gaps in data-taking. Since the exact dates are not known yet, a factor of 1.0 is used for these two terms in the rate calculations.

The resulting theoretical energy spectra and corresponding reconstructed energy spectra are shown in the upper left panel of Fig. 5.6. Here, mirror electron temperatures 0.3 keV and 0.7 keV are shown, with the kinetic mixing parameter at the sensitivity level determined in Section 5.4. The rate is dominated by the detector threshold behaviour, which cuts off the sharply falling exponential part of the signal at very low energies.

Other signal models

Five other signal models were also studied using the same analysis framework outlined in Fig. 5.1, probing unanswered SM questions of neutrino mass or dark matter. All models give electron recoil interactions with energies below 100 keV, as show in Fig. 5.6.

The SM must be extended to explain neutrino mass and in many models neutrinos acquire electromagnetic properties through loop effects. The size of the electromagnetic couplings depends on the particular SM extension making tests of these properties a powerful way to search for a fundamental theory beyond the SM. For models where the neutrino is a Dirac particle any enhancement in electromagnetic properties must be accompanied by an enhancement in neutrino mass, which is already well constrained. However, if the neutrino is a Majorana particle (indistinguishable from its own antiparticle) there is no requirement for increased mass, so observation of enhanced electromagnetic properties would suggest this is the case [218]. The neutrino electromagnetic properties considered here are magnetic moment and effective milli-charge [219], both of which would add terms to the total neutrino-electron scattering cross section. Additional components of the solar neutrino energy spectrum would therefore be expected and these form the signal model. Rates for neutrino electromagnetic scattering on xenon atoms via magnetic moment or millicharge are calculated in Ref. [220], accounting for atomic binding effects using RRPA, as described in Section 5.1.2. The upper right panel of Fig. 5.6 shows the sharply falling spectral shape that is added to the SM solar neutrino interactions in the case of an electromagnetic enhancement.

The most general dark matter model we consider is one in which the the dark matter particle couples only to leptons, via an axial-vector interaction. Here, the signal in LZ is generated by WIMPs scattering off electrons with sufficient recoil energy to liberate the electron from its host atom. This can be treated using an effective field theory approach, as described in Section 2.3.3. Considering all interactions between dark matter and leptons, loop-induced interactions with quarks are allowed, which would dominate the experimental signature. These vanish if only the axial-vector interactions are considered [221], so the signal model here consists of the axial vector WIMP electron interaction only. Non-zero momentum of bound electrons means that some electron recoil events can exceed the detector threshold energy, for typical WIMP velocities. The resulting energy

spectra expected in the detector is determined by integrating over the momentum wave function of each electron shell and summing over shells, as in Ref. [58]. The lower left panel of Fig. 5.6 shows expected event rate in LZ, with the dominant contribution to the signal arising from scattering off electrons in the 3s shell.

A more specific class of dark matter models are hidden sector dark matter models, with the dark matter in a new sector that does not interact with SM particles though known SM forces, as described in Section 2.3.1. The hidden photon (HP) is a hypothetical U(1)' gauge boson in such models, which may be able to interact with the visible sector via loop induced kinetic mixing [222]. If HPs are non-thermally produced via the misalignment mechanism in the early universe they can reproduce the present day dark matter relic abundance. An electron recoil event in LZ would be induced by absorption of a HP, in an effect analogous to the photoelectric effect, with the two cross sections related by some model dependent constant which is proportional to the square of the kinetic mixing κ^2 [223]. The entire HP rest mass is converted into energy absorbed by the electron, resulting in a signal which is a monoenergetic peak at the HP mass. In reality this will be smeared by the energy resolution of the detector, giving a peak centred on the incoming HP mass.

There is also a general class of axion-like particles (ALPs), introduced in Section 2.2.3. These additional light scalar or pseudoscalar ALPs also arise from broken U(1) symmetries and couple to ordinary matter in the same way as axions, but with f_a replaced by the ALP decay constant. There is no a-priori relationship between the coupling strength and mass, so $m_{ALP}f_{ALP}$ is much less constrained that $m_a f_a$ for axions, giving a much wider parameter space [39]. The ALP particles do not solve the strong CP problem, but they may be CDM candidates if produced non-thermally. As with solar axions, the ALPS can interact with electrons via the axio-electric effect, with cross section proportional to the square of the axion-electron coupling g_{ae}^2. However, for these relic particles in the halo the full ALP rest mass energy is absorbed by the atom, resulting in a monoenergetic signal peak at the ALP mass, similar to that for HPs.

For both of these monoenergetic signals the lowest mass considered is 2.0 keV, limited by the $\sim$1 keV detector threshold, and the maximum extends up to 70.0 keV. The HP and ALP signals have the same shape — a peak with width dependent on the detector energy resolution and only the amplitude varying, depending on model parameters. The lower right panel of Fig. 5.6 shows monoenergetic peaks for 20.0 keV and 70.0 keV HP or ALP masses, at the

amplitude of the projected 90% CL exclusion sensitivity.

5.2 Simulations

The LZ simulation chain, as described in Ref. [224], was used to simulate the expected distributions of detector observables for each of the background components and the signal models.

For the background components with either non-uniform spatial distribution or possibility to register as multiple scatters this begins with BACCARAT — a GEANT4 based package which tracks particles as they propagate through the detector recording energy depositions, timing and position. The timing and spatial information are used to apply cuts to the simulated data: veto, single scatter and fiducial volume cuts are applied. Interactions are accepted as 'single scatter' events if there is no coincident energy deposition in the active skin or outer detector volumes and any additional energy depositions in the LXe are within a small spatial extent. This spatial extent requirement is defined as an energy-weighted standard deviation <3 cm in the radial direction and <0.2 cm in the vertical direction, imitating selection cuts based on S2 light distribution and pulse shape.

For event types which are spatially uniform and always appear as single scatters, theoretical energy spectra are used rather than BACCARAT. These are calculated analytically in terms of the number of expected events per unit mass and time, which can then be scaled to exposure. This approach is used for all of the signal models and the simplest background components: ^{136}Xe decay, ^{124}Xe decay and both ER and NR neutrino scatters.

The resulting energy spectra for both backgrounds and signals are then used as input to the Noble Element Simulation Technique (NEST) software [173, 174]. This translates ER and NR energy deposits into distributions of detector observables. This accounts for the position-dependence of signal collection efficiencies, which is then is removed by applying position-dependent 'corrections', to form the final analysis quantities S1c and S2c. Other detector response and efficiency effects are accounted for, using detector response parameters specific to the LZ detector (for example g_1, g_2, and electric field amplitude). Following this, data selection criteria are applied, which mimic those that will be applied to real

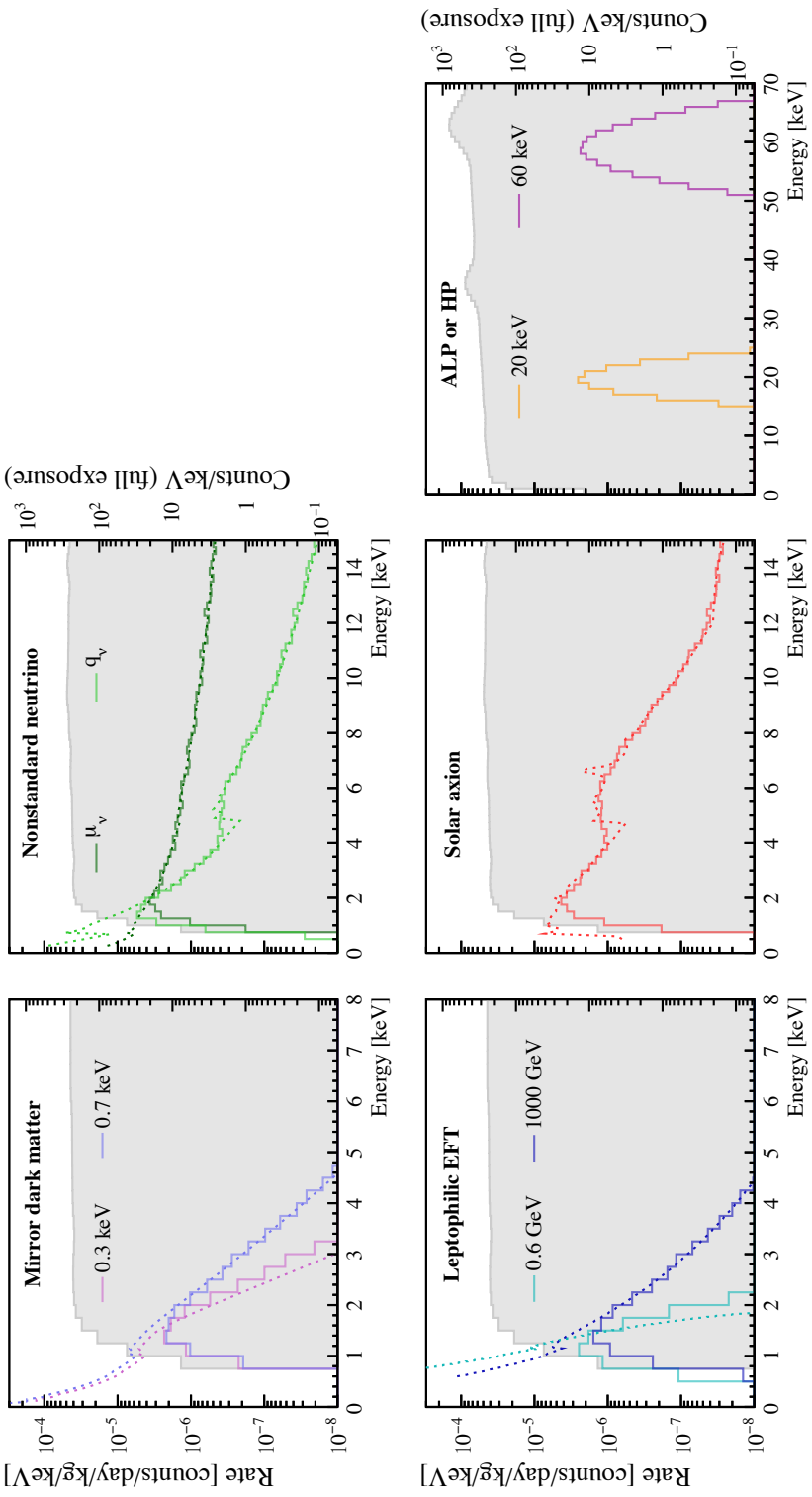

Figure 5.6 *ER spectra for the signal models studied. Solid lines show true deposited energies and dashed lines show energies reconstructed from simulated detector observables. The grey region shows the expected ER background, reconstructed energy from simulation.*

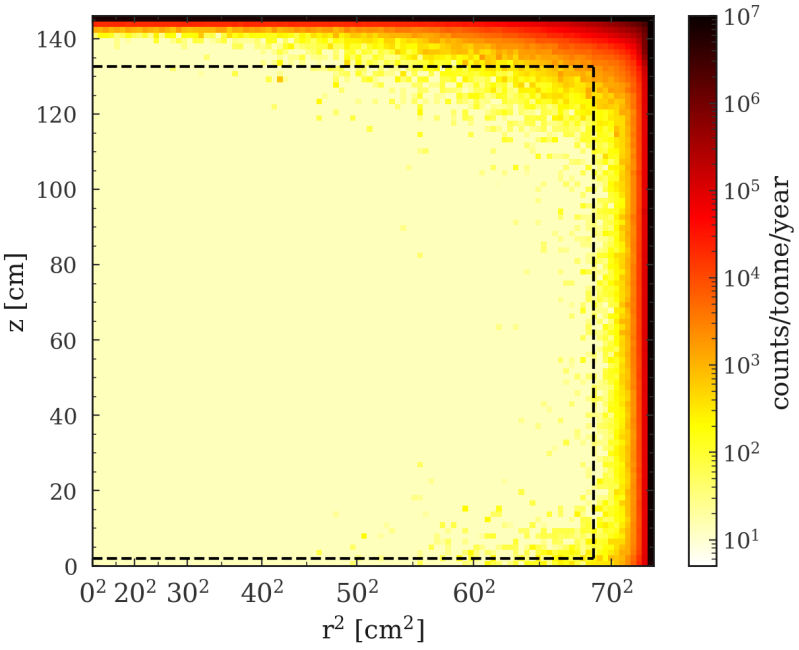

Figure 5.7 *Spatial distribution of electron recoil background expected in LZ, dashed black line shows the fiducial volume.*

data. Events must meet the three-fold coincidence requirement — having an S1 which registers a single photon in at least 3 PMTs. The uncorrected S2 signal must be greater than $\sim$ 415 phd ($\sim$ 5 electrons emitted from the liquid surface) to ensure accurate position reconstruction. Fiducial volume cuts of $r < 68.8$ cm from the center and $1.5 < z < 132.1$ cm above the cathode are also applied, as shown in Fig. 5.7, defining a 5.6-tonne fiducial mass as used in Ref. [167].

5.2.1 NEST Electron Recoil Models

The distributions of detector observables were generated using the NEST version 2.0.0 [174], calculating light and charge yield from a particle interaction, for a given interaction energy, drift field and liquid xenon density. This version of NEST takes a new approach of using sum of sigmoids for the yields rather than theoretical models used previously. For ERs the sum of two sigmoids is used, with the sigmoid shapes controlled by ten free parameters:

$$Q_y = m_1 + \frac{m_2 - m_1}{\left(1 + \left(\frac{E}{m_3}\right)^{m_4}\right)^{m_9}} + m_5 + \frac{m_6 - m_5}{\left(1 + \left(\frac{E}{m_7}\right)^{m_8}\right)^{m_{10}}}. \tag{5.7}$$

The free parameters m_i are tuned using empirical fits to all existing light and charge yield data taken with xenon experiments. This model reproduces the first principles yield models — the Thomas Imel box model for low energy ERs and the Doke Birks model for high energy particle tracks. The first sigmoid controls the low energy behaviours and the second sigmoid controls the high energy behaviour, allowing a smoother transition between the two regions.

Background sources of ERs in a LXe experiment are β and γ-ray interactions. Any difference in yields between the two is due to the energy dependent photo-absorption component of γ-ray interactions. Different models are available in NESTv2.0.0 for ERs caused by β and γ-ray interactions, with different m_i values from different calibration data sets. Compton scatters of γ-rays should not have any significant photo-absorption component, giving yields similar to those for β interactions. Therefore, the β model is appropriate for both β interactions and some low energy γ-ray interactions, if the scatter is at a single site, where the Compton effect dominates. The γ model is appropriate for X-ray and γ-ray photo-absorption in addition to unresolved multiple scattering of γ-rays.

The intermediate energy at which monoenergetic γ-ray peaks or similar signals should switch from using the β to γ model is not well defined. In LUX an 'ER

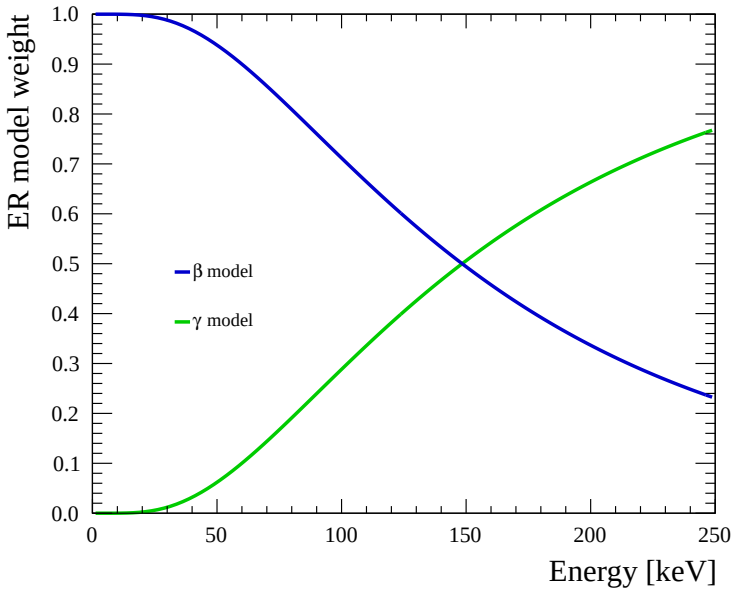

Figure 5.8 *NEST ER model weights for the β and γ yield models as a function of energy, with model parameters tuned from fits to LUX data.*

model', which is a weighted sum of these two models, was used — giving a single model to deal with the energy transition for γ-ray interactions. The resulting light and charge yields are given by:

$$\begin{aligned} Ly &= w_\gamma Ly_\gamma + w_\beta Ly_\beta, \\ Qy &= w_\gamma Qy_\gamma + w_\beta Qy_\beta. \end{aligned} \tag{5.8}$$

The model weights are given by:

$$\begin{aligned} w_\gamma &= 0.5 + 0.5\mathrm{erf}(A\log(E[\mathrm{keV}]), \\ w_\beta &= 0.5 - 0.5\mathrm{erf}(B\log(E[\mathrm{keV}]). \end{aligned} \tag{5.9}$$

where the A, B parameters are constants taken from fits to data. In LUX these best fit values where $A = 1.0$, $B = 5.0$, however there is a large uncertainty in these values across different experiments. Figure 5.8 shows the weights as a function of energy: the β yield dominates below $\sim$ 150 keV and above this the γ yield dominates.

Accurate modelling of the detector ER response is vital for low energy ER searches. The ER model was implemented in the LZ NEST interface by this author and compared to the β and γ models for two different cases. The first case considered was the detector, surface and environment ER background component — a flat energy spectrum in the 0–100 keV range. Figure 5.9 shows the resulting S1, log(S2) distributions. For this low energy continuous spectrum the ER model

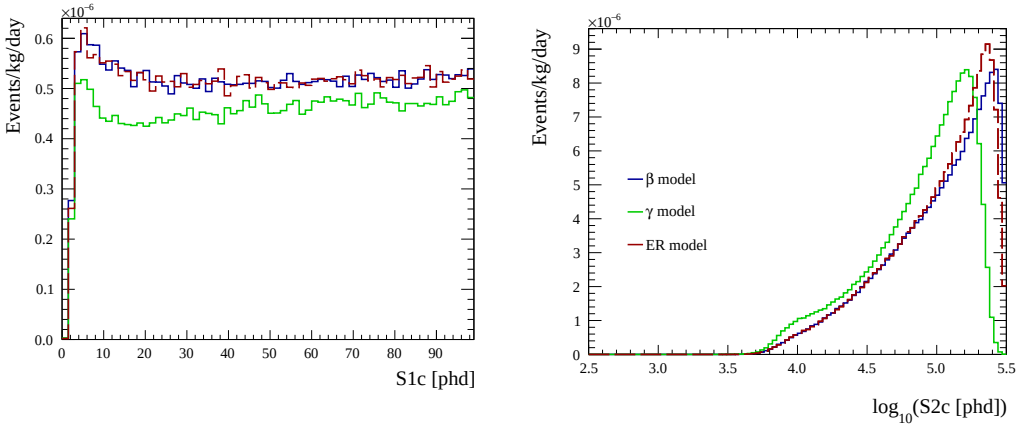

Figure 5.9 *Comparison of S1 and log(S2) distributions for a flat energy spectrum in the 0–100 keV energy range using the NEST β, γ and ER models for ER yields.*

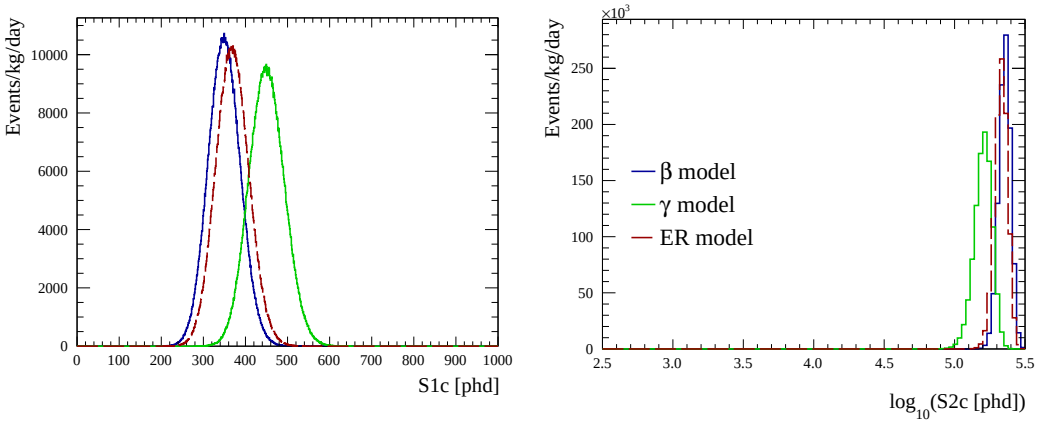

Figure 5.10 *Comparison of S1 and log(S2) distributions for an 80 keV monoenergetic signal using the NEST β, γ and ER models for ER yields.*

is a close match to the β model, as expected from Fig. 5.8.

The second case considered was an 80 keV monoenergetic peak — the signal expected for an ALP or HP of this mass. The S1 and log(S2) distributions from NEST for the three different models are shown in Fig. 5.10. As expected from Fig. 5.8 at 80 keV the ER model is closer to β model.

However, there are large uncertainties in the values of the A, B parameters. Here, the values from LUX have been used, but ZEPLIN and XENON have different values and LZ will likely have different values again. The maximum variation expected is: A: 0.5–1.5 and B: 3.0–5.0, these ranges can be used to estimate the

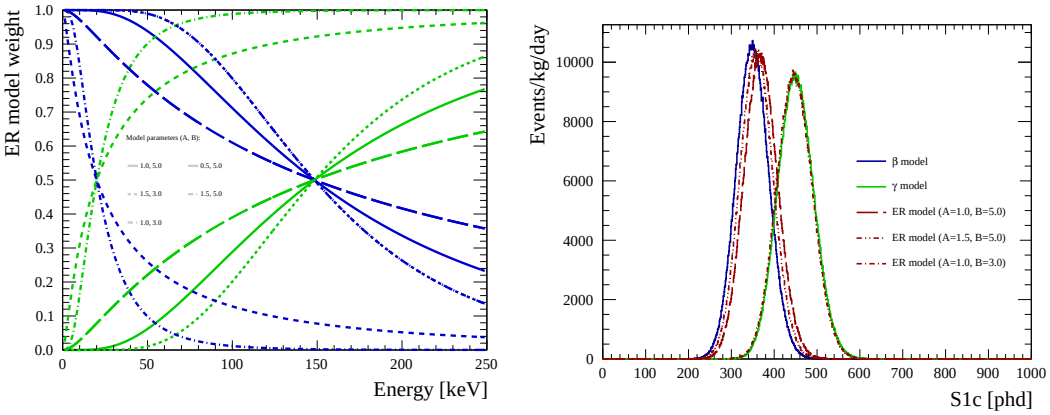

Figure 5.11 *Uncertainty in the A, B parameters in the β and γ model weights (left) and the resulting variation in S1 signal for a 80 keV monoenergetic signal (right).*

uncertainty for LZ. Figure 5.11 shows the variation in weights resulting from the variation in these parameters. The impact on the simulated S1 distribution for an 80 keV monoenergetic signal is also shown for the most extreme two cases: $A = 0.5$, $B = 3.0$ and $A = 1.5$, $B = 5.0$, with γ dominating for the former case and β dominating for the latter.

For the A, B values taken from LUX data the β model should be sufficient for our study, with all backgrounds and signals, except the highest energy monoenergetic peaks, well modelled by this. However, the large possible variation in A, B shows that depending on the detector the ER model may be more appropriate for intermediate energies. In LUX NESTv2.0.0 with minimal tuning was able to reproduce ER calibration data across different time periods where detector parameters varied and it should be possible to tune LZ simulations in a similar way.

5.2.2 Threshold Efficiency

The intrinsic scintillation properties of liquid xenon, plus light detection requirements, mean there is a minimum interaction energy that can be detected, giving a finite energy threshold. Minimum possible detected energy is determined by the

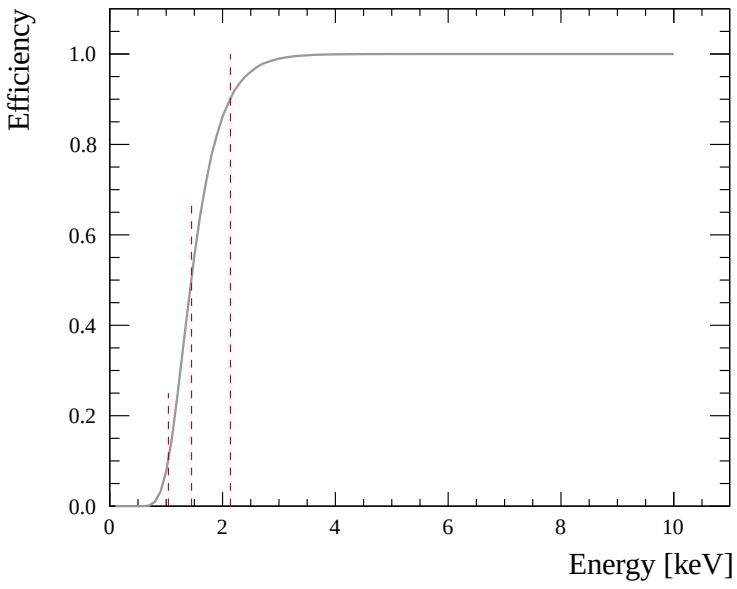

Figure 5.12 *Simulated LZ ER detection efficiency, vertical lines indicate the 10%, 50% and 90% threshold energies.*

S1 threshold, which is down to the three PMT coincidence requirement in LZ. For LZ, the projected detection efficiency can be determined using NEST. To find the efficiency mono energetic energy depositions from 0–10 keV are simulated, then the proportion of events that give a detectable S1, S2 in the detector is found. These efficiencies, and the energies corresponding to 10%, 50% and 90% (1.04, 1.45 and 2.14 keV respectively), are shown in Fig. 5.12.

Once data has been taken, the simulated detection efficiency can be compared to detection efficiency determined from calibrations. For low energy NRs this can be done using DD-neutron data and for low energy ERs tritium data is used, as demonstrated in LUX [191] (see Section 4.3.1 and Fig. 4.8). The energy spectra reconstructed from measured S1, S2 is compared to reconstructed energy spectra from simulated NEST events passing all analysis cuts used. For the final simulations NEST will have been tuned with calibration data and include measured values of detector parameters to reproduce the detector response as accurately as possible.

5.3 Statistical Analysis

In order to determine the sensitivity of the LZ experiment to exclude or observe the signal models in Section 5.1.3, a frequentest profile likelihood ratio (PLR) test is used. This uses the same approach to hypothesis testing as described in Section 4.5 for the LUX analysis, however this study gives the projected exclusion sensitivity of LZ compared to the exclusion limit found for LUX in Chapter 4. Projected sensitivity is a property of an experiment — the parameter space it will be able to explore, whilst the exclusion limit is a property of data — the parameter space that is ruled out by observations. The projected sensitivity can be exclusion sensitivity or discovery/evidence sensitivity.

5.3.1 Exclusion Sensitivity

As described in detail in Section 4.5, a null hypothesis of signal plus background is used for limit setting and a hypothesis test will either reject of fail to reject

this. The PLR method uses a test statistic:

$$t(\mu) = -2\ln\left(\frac{\mathrm{L}(\mu,\hat{\hat{\nu}})}{\mathrm{L}(\hat{\mu},\hat{\nu})}\right), \qquad \mathrm{q}(\mu) = \frac{\mathrm{L}(\mu,\hat{\hat{\nu}})}{\mathrm{L}(\hat{\mu},\hat{\nu})}. \tag{5.10}$$

Here, μ is the parameter of interest and $L(\mu,\hat{\hat{\nu}})$ is the conditional/profile maximum likelihood for a given value of μ and $L(\hat{\mu},\hat{\nu})$ is the global maximum likelihood with both μ and ν varying. The distribution of this test statistic $f(t|\mu)$ is used to calculate the p-value:

$$p_\mu = \int_{t_{obs}}^{\infty} f(t|\mu)dt_\mu. \tag{5.11}$$

A low p-value indicates poor agreement between the hypothesis and data, leading to the rejection of the hypothesis. In general $t(\mu)$ is a two sided test statistic, where a low p-value can result from $\hat{\mu}$ being much bigger or smaller than the value μ being tested (i.e. much more or less data than expected is observed). A one sided test statistic can be defined such that $t = 0$ for $\hat{\mu} > \mu$, so that the signal plus background hypothesis cannot be rejected due to an over fluctuation of data (only when less data than predicted for μ is observed).

5.3.2 Evidence and Discovery Sensitivity

In order to test for evidence or discovery a null hypothesis of background only is used. The projected evidence or discovery potential gives the smallest values of a parameter for which it would be possible to exclude the background only hypothesis at some level. The p-value is often converted to significance, defined as the number of standard deviations above the mean of a Gaussian distribution such that the upper tail probability is equal to the p-value:

$$Z = \Phi^{-1}(1-p). \tag{5.12}$$

Here, Φ is the cumulative distribution of the standard Gaussian and Φ^{-1} is the inverse. In particle physics the convention is that $Z > 3\sigma$ (p-value 1.3×10^{-3}) signifies *"evidence"* and $Z > 5\sigma$ (p-value 2.87×10^{-7}) signifies *"discovery"* [109].

5.3.3 LZ Analysis

Studies were carried out to find the projected 90% exclusion sensitivity of the LZ experiment for all seven of the signal models and projected 3σ evidence for two. Comparison between signal and background used two dimensional PDFs, generated as described in Section 5.2 with observables $S1$, $logS2$. These were used to generate an extended unbinned likelihood function, with the event probability model consisting of a signal plus eleven background components. The number of signal events was the parameter of interest and the number of background events for each component were Gaussian constrained nuisance parameters.

Table 5.1 shows the electron recoil background components and their uncertainties, used in the likelihood. The internal β emitting ^{85}Kr, ^{220}Rn and ^{222}Rn have the same spectral shapes in the region of interest, so they were grouped together as a single background component with their uncertainties added in quadrature. The uncertainties in the ^{220}Rn and ^{222}Rn backgrounds arise from uncertainties in the branching ratios of ^{214}Pb and ^{212}Pb respectively. For ^{85}Kr and ^{136}Xe the uncertainties arise from uncertainty in the spectral shape at low energies. Uncertainty on the ^{124}Xe double electron component arises from the half life. The uncertainty on the detector, surface and environment ER component is estimated using counting and simulation results. No uncertainty is shown or included for the solar neutrino component, as this has a comparatively much smaller uncertainty of 2–3%. Nuclear recoil background are also included in the event model, but remain fixed at their normalisations (with no uncertainty), due to their negligible contribution in the ER signal region. In the solar axion analysis the ABC component, described in Section 5.1.3, is used as the signal and the Primakoff component is included as an additional unconstrained nuisance parameter that floats in the fit.

For the projected 3σ evidence sensitivity the two unexpected backgrounds (^{37}Ar and ^{3}H) described in Section 5.1.2 are included. The presence of a signal consistent with these unexpected but possible backgrounds would not be compelling evidence for new physics. Rates of these backgrounds are expected to be negligible in LZ, so they are not included in the background model but they are included as unconstrained nuisance parameters in the fit in case of some unexplained source. Inclusion of these nuisance parameters means that evidence or discovery for signals with spectral shape identical to that of either ^{37}Ar or ^{3}H is not possible and the sensitivity to similar shapes is much reduced. In a real

experiment, following data taking in known conditions, a constraint on ^{37}Ar and ^{3}H concentrations or rates may be applied.

5.4 Projected Sensitivities

Projected exclusion limits were calculated for all signal models introduced in Section 5.1.3, whilst projected 3σ evidence was determined for the solar axion and neutrino magnetic moment. This was motivated by the fact that these two signals were proposed as an explanation for the excess of low energy electron recoil events observed by XENON1T [141]. As presented in Ref. [2], the sensitivities for all seven signal models show improvements on the current best experimental limit. The following will focus on the solar axion and mirror dark matter models, followed by a brief review of the other results.

5.4.1 Solar Axion

For solar axions, the projected sensitivity to the axio-electric coupling g_{ae} is shown in Fig. 5.13. This includes the projected 90% CL exclusion (1.58×10^{-12}) and 3σ evidence (1.84×10^{-11}). The current most stringent limit is the indirect detection constraint from the observed brightness of the tip of the Red Giant (RG) branch [225–227]. Thermal production of axions in the RG core would increase energy loss, delaying helium ignition and increasing the luminosity of the tip of the RG branch. Axion production in RGs is expected to be dominated by Bremsstrahlung processes, so comparison of the predicted and observed luminosity allows g_{ae} to be constrained. In Ref. [227] photometric measurements of 22 galactic globular clusters, using the Hubble space telescope and ground based telescopes, are compared to the predictions from solar models which include axion energy losses. The observed absolute magnitudes were found to be consistent with neutrino energy loss only, being ~ 0.04 mag higher on average than the prediction. A maximum likelihood fit of this difference gives $g_{ae} = 0.6^{+0.32}_{-0.58} \times 10^{-13}$, and an upper limit of $g_{ae} < 1.48 \times 10^{-13}$ can be set. The other indirect limit is from the constraint on solar cooling from the SNO all flavour solar neutrino measurement [228], which constrains nonstandard energy losses to <10% of the Suns photon luminosity. Also shown is a constraint from a model which includes a "stellar basin" of gravitationally bound axions, giving a second component of the flux

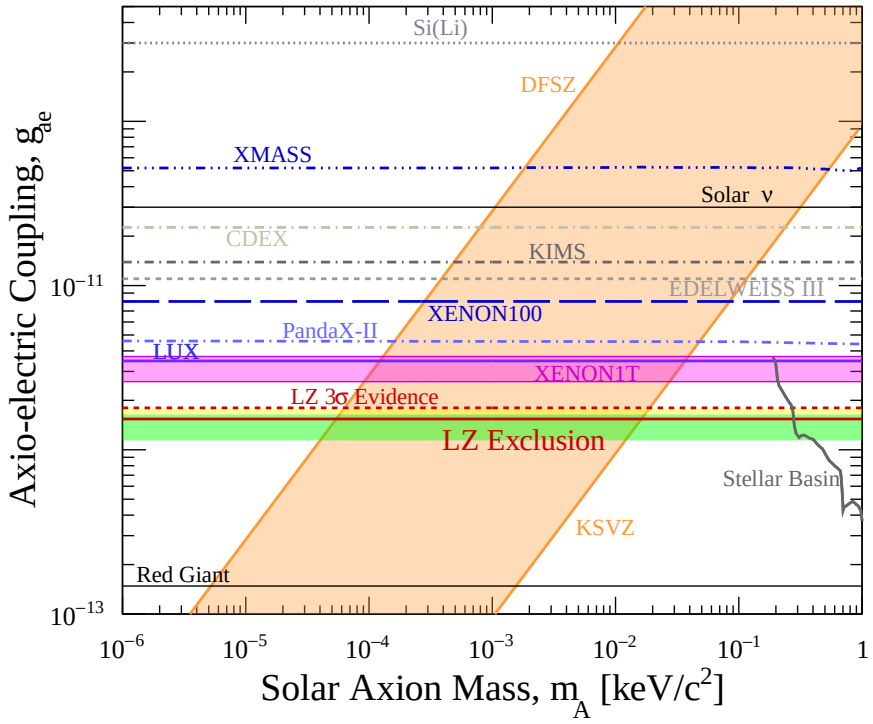

Figure 5.13 *Projected 90% CL exclusion sensitivity and 3 σ discovery potential for solar axions. Results from other xenon experiments are shown in blue, other detectors in grey and astrophysical constraints in black. The XENON1T confidence volume is indicated by the purple shaded region.*

[229]. This result is obtained by recasting previous experimental limits, but there is a large uncertainty from calculation of the ejection time of particles from the solar system.

Figure 5.13 also shows limits from solid state experiments: CDEX germanium crystals [230], EDELWEISS III germanium bolometers [137] and KIMS CsI(TI) crystals [231]. Limits from other xenon experiments PandaX [232] and LUX [140] are shown, with the projected LZ exclusion sensitivity showing a factor ~ 2.5 improvement the previous best 90 %CL from LUX. The XENON1T experiment recently reported an excess of electron recoil events in the few keV region [141], which can be interpreted as a solar axion signal with 3.5σ significance. A 90% volume gives $g_{ae} < 3.7 \times 10^{-12}$, which LZ will be able to test robustly given these sensitivity projections. This analysis and correlated limits on the different axion couplings will be studied further in Chapter 6.

5.4.2 Mirror Dark Matter

The projected exclusion sensitivity to mirror dark matter kinetic mixing for various local mirror electron temperatures is shown in Figure 5.14. As in Chapter 4 the theory limit of: $10^{-11} \leq \epsilon \leq 4 \times 10^{-10}$, from astrophysical arguments, is shown, along with the experimental constraint from orthopositronim decays. The LZ projection shows that, in the event of no signal, LZ would be able to exclude mirror electron temperatures down to 0.25 keV for this model, giving an improvement over the first direct detection search carried out by LUX [1]. This is a relatively small improvement despite the increased exposure, due to the higher threshold energy in LZ which means that a lot of the sharply falling signal at low energies is lost.

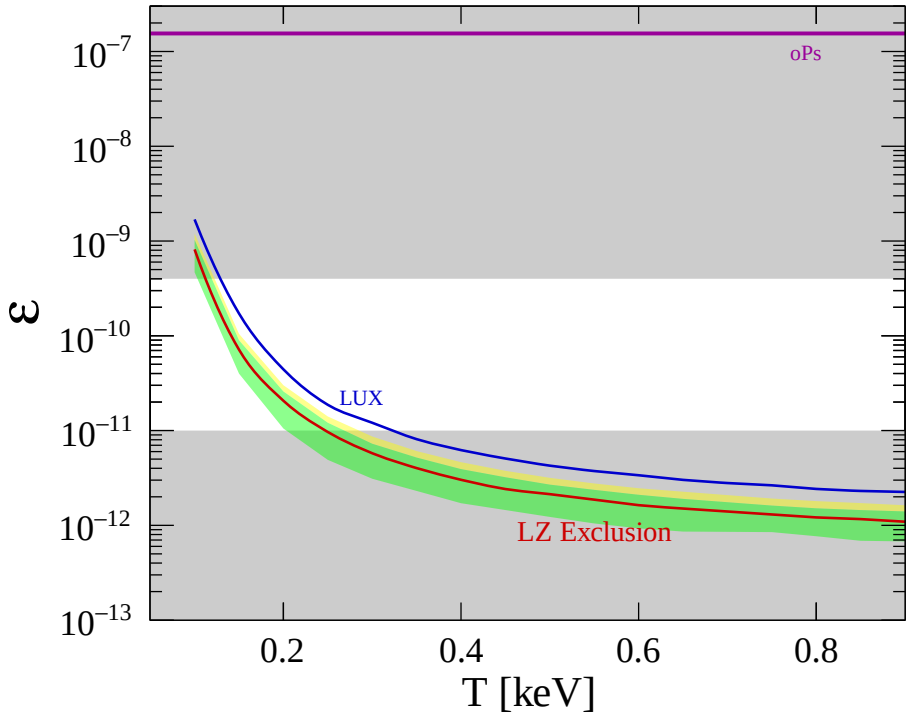

Figure 5.14 *Projected 90% CL exclusion sensitivity to mirror dark matter kinetic mixing for mirror electron temperatures from 0.1 to 0.9 keV. The grey region is disallowed by astrophyiscal constraints on the theory, the red line shows oPs experimental constraint and the blue line is the LUX limit found in Chapter 4.*

5.4.3 Other Results

The same framework was used to find the sensitivity to the other signal models. Signal pdfs in the S1, logS2 were simulated, then statistical analysis performed, to find a projected 90% confidence limit on the number of signal events which was converted to a projected limit on some model parameter.

For the solar neutrino electromagnetic interactions, the full LZ exposure will be capable of rejecting magnetic moments greater than $6.2 \times 10^{-12}\mu_B$ and millicharges greater than $1.4 \times 10^{-13}e_0$, at 90% CL. Sensitivity to 3σ evidence was found to be $9.5 \times 10^{-12}\mu_B$ and $1.9 \times 10^{-13}e_0$, for the magnetic moment and millicharge respectively. Figure 5.15 shows these sensitivities along with existing constraints from solar neutrinos and $\bar{\nu}_e$ neutrinos from reactor based experiments. The XENON1T electron recoil excess can be explained as a neutrino magnetic moment signal with 3.2σ significance and a confidence interval of $\mu_\nu \in (1.4, 2.9) \times 10^{-11}\mu_B$ at 90% CL is reported [141], which LZ will be able to test. More stringent astrophysical constraints, not shown here, also exist on the neutrino properties, see Ref. [233] for a review.

Figure 5.15 shows the projected exclusion sensitivity to the axial-vector WIMP-

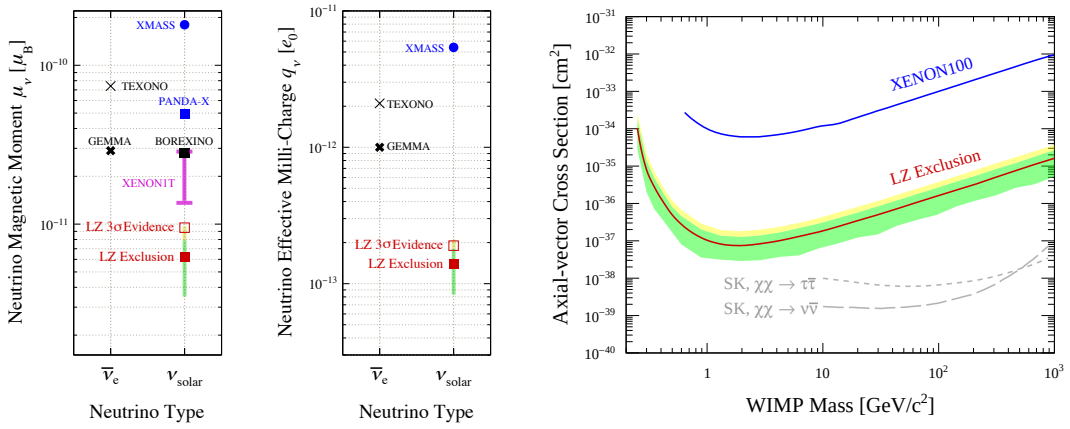

(a) *Neutrino electromagnetic interaction sensitivities, experimental limits using $\bar{\nu}_e$ alongside solar neutrino limits, with the XENON1T confidence region indicated.*

(b) *Leptophilic EFT axial-vector interaction sensitivity, with indirect limits from the SuperKamiokande experiment shown in grey.*

Figure 5.15 *Projected 90% CL exclusion and 3σ sensitivities to neutrino electromagnetic properties and axial-vector WIMP-electron scattering cross section, for the full LZ exposure. Existing results from xenon experiments are shown in blue.*

electron cross section, which is as low as 6×10^{-38} cm^2 for a WIMP mass of 2 GeV/c^2. This shows an improvement of three orders of magnitude on the XENON100 [198] limit, which is the best direct detection constraint to date. At WIMP masses above 10 GeV/c ^{2} there is a more stringent indirect detection constraint from dark matter anniliation in the Sun using Super Kamiokande data [234]. There is also an upper limit of $\sim 10^{-47}$ cm^2 from relic density constraints [235], which is well beyond the reach of the current generation of experiments.

For the monoenergetic searches, a single analysis was carried out — finding the projected 90% CL exclusion sensitivity for monoenergetic peaks in the 2–70 keV range. The limit on the number of signal events can then be converted to a limit on either HP kinetic mixing or ALP axio-electric coupling.

A scan over HP masses 2–70 keV/c^2 gives projected 90% CL exclusion sensitivity on kinetic mixing squared, κ^2, shown in Fig. 5.16. This is no larger than 7.4×10^{-28} at $\sim$ 64.3 keV, the energy of the ^{124}Xe KK peak. For intermediate energies, 10–30 keV, the indirect limit on κ^2 from RG cooling is still the most stringent, whilst LZ is expected to give a better limit for masses above and below this. Existing direct detection constraints from XMASS [236] and XENON100 [198] are also shown. There are also XENON1T constraints from the ionisation (S2-only) analysis [136] and a phenomenology constraint [237] derived using Ref. [141]. The projected LZ exclusion sensitivity shows an order of magnitude

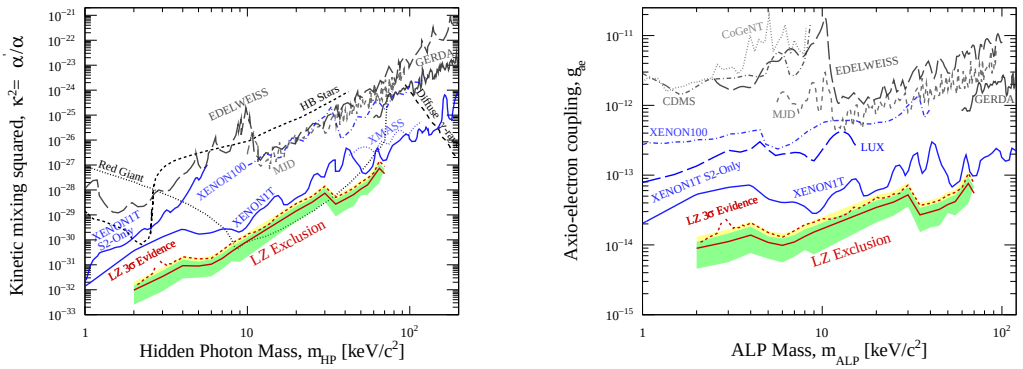

(a) *Hidden photon projected sensitivities.*

(b) *Axion-like particle projected sensitivities.*

Figure 5.16 *Projected 90% CL exclusion and 3σ evidence sensitivity for monoenergetic signals. Results from other xenon experiments are shown in blue, other detectors in grey and astrophysical limits in black.*

improvement over the current best limits and the projected 3σ evidence is below any existing experimental constraint. Since the projected 3σ evidence contains an unconstrained ^{37}Ar component there is no sensitivity to monoenergetic signals at the 2.8 keV energy of the ^{37}Ar decay, as shown by the discontinuity at this energy.

A scan over ALP masses 2–70 keV/c^2 gives a projected exclusion sensitivity to axio-electric coupling, g_{ae}, shown in Fig. 5.16, which is no larger than 7.6×10^{-14} at $\sim$ 64.3 keV. Experimental limits from XMASS [236], LUX [140], XENON100 [198] and the XENON1T S2-only analysis [136] are shown, along with a phenomenology constraint [237] derived using Ref. [141]. The projected LZ exclusion sensitivity shows an improvement of two orders of magnitude from the LUX limit, with both the projected exclusion and evidence sensitivities lying below all existing constraints.

5.4.4 Variation with Intrinsic Background Levels

As discussed in Section 5.1.2, and shown in Figure 5.3a, the intrinsic radon and krypton isotopes contaminants in the xenon are the dominant ER background in LZ at low energies. The rate of this dominant background depends strongly on the amount of radon entering the detector from radon emanation of components in the cold xenon environment and dust acquired on surfaces during construction. There is a large uncertainty in both of these factors, so it is important to investigate how projected sensitivity varies under differing radon contamination scenarios. In order to study this, the same analysis as above was carried out with different levels of the grouped betas component (^{222}Rn + ^{220}Rn + ^{85}Kr). This was varied by different factors from 10 times smaller to 10 times greater than the baseline expectation and the 90% sensitivity projections were found as above. The result of this study for mirror dark matter is shown in Fig. 5.17, with the projected 90% CL exclusion sensitivity plotted as a function of the dominating ^{222}Rn part of the varied background.

Given the 1000-day exposure time assumed, any possible signal competes with a large number of background counts, typically $\sim$hundreds of events per keV. In this regime, sensitivity to signal counts changes in proportion to the square root of the background counts in the relevant signal region. Studies with varied background levels confirm this expectation at low energies when ^{222}Rn forms the dominant background. However, the square root scaling weakens in two regimes: when the

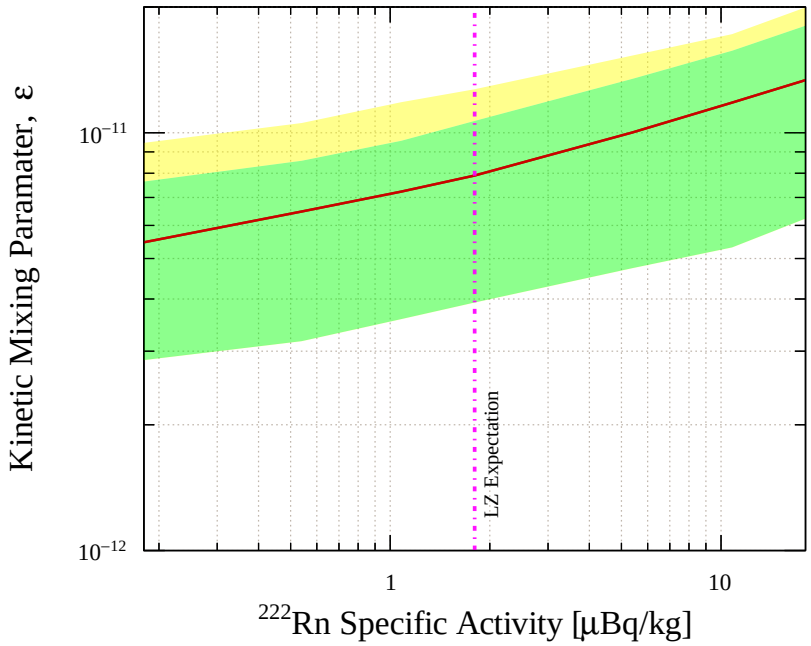

Figure 5.17 *Variation of 90% CL exclusion sensitivity to mirror dark matter kinetic mixing (for local mirror electron temperature 0.3 keV) with activity of the dominant ^{222}Rn β emitting intrinsic Xe contaminant.*

^{222}Rn is reduced by a significant factor, where the solar neutrino scattering rate begins to dominate, and when the signal model is constrained to higher energies, above $\sim$ 40 keV, where the $2\nu\beta\beta$ decay of ^{136}Xe begins to dominate.

The shapes of the β decay spectra that dominate the low energy background have recently been subject to new theoretical calculation, which results in a suppression of their rates at energies in the region of interest for these searches. For the dominant ^{214}Pb species the rate is reduced by $\sim$19% and smaller amounts for the other sub-dominant species ^{212}Pb and ^{85}Kr [238]. The reduction in low-energy background beta decay rate shifts 'LZ Expectation' line in Figure 5.17 to the left, from 1.8 μBq/kg to 1.46 μBq/kg. Therefore, the overall impact on the projected LZ sensitivity as a result of this can be seen to be less than 10%.

5.5 Outlook

The low energy electron recoil sensitivity studies, presented in Ref. [2], show that LZ will be able to probe a number of different new physics models which result in additional low energy ERs. These may be new particles, such as axions, or new mechanisms of interaction, such as enhanced loop-induced neutrino electromagnetic properties. For each of the seven models tested LZ is projected to have world leading sensitivity. In particular, LZ will thoroughly test any new physics explanation of the recent XENON1T excess. Chapter 6 will continue this discussion, investigating the possibility of characterising a signal in the case of detection.

Chapter 6

Bayesian Approach to Signal Characterisation

6.1 Motivation

The XENON1T experiment observed a low energy excess of electron recoils at 2 – 3 keV, with one explanation being a solar axion signal favoured at 3.5σ significance [141]. This possibility raises questions about signal characterisation and being prepared for detection, in addition to limit setting, with the next generation of xenon experiments.

If a signal is observed the number of events does not constrain the new physics model, for this we need to constrain the model parameters. There are often more than one model parameters to constrain simultaneously, so a statistical analysis which can handle multiple parameters of interest and set a multi-dimensional interval is needed. In a frequentist analysis, such as the profile likelihood test, used in Chapter 4 and 5, adding extra parameters of interest is computationally expensive and going beyond two becomes prohibitively slow. However, Bayesian analysis provides an alternative method for signal characterisation which is investigated below, using the test case of a solar axion signal.

6.2 Bayesian Inference

The frequentist definition of probability is the proportion of times an outcome occurs for an infinite number of identical trials. By contrast in Bayesian statistics probability is fundamentally different — it is the degree of belief for an outcome to occur.

In Bayesian statistics the posterior gives the probability of model/parameter set m given observed data x. This is calculated by using the likelihood from data to update a prior probability, according to Bayes theorem:

$$P(m|x) = \frac{P(x|m)P(m)}{P(x)}. \tag{6.1}$$

Here, $P(x|m)$ is the likelihood — the probability of the data given the model and $P(m)$ is the prior probability of the model — the degree of belief for the model before carrying out the measurement. The denominator $P(x)$ is the normalisation obtained by integrating over the likelihood for all possible model values weighted by the prior.

If the set of model parameters contains both parameters of interest (POI) θ and nuisance parameters (NP) ν; $m = \{\theta, \nu\}$, the posterior in terms of the parameters of interest is found by marginalising over the nuisance parameters:

$$P(\theta|x) = \int P(\theta, \nu|x) d\nu. \tag{6.2}$$

These integrals are typically not possible to compute in closed form due to complicated structure and standard Monte Carlo methods may not work for high dimensions, so Markov Chain Monte Carlo (MCMC) techniques are often used. These numerical methods aim to create a sequence of points, a Markov chain (MC), in parameter space which have density proportional to the posterior. The sequence is constructed from probabilistic steps, with the transition probability at step depending only on the current variable(s) and not the history. Different sampling algorithms can be used to construct the MC, a common choice is the Metropolis Hastings algorithm [110, 239]. A proposal function $Q(\alpha'|\alpha)$ is used to get the next proposed point in parameter space α', given the current position/value α. The algorithm proceeds as follows:

1. generate a value α' using the proposal density $Q(\alpha'|\alpha)$,
2. calculate the Hastings ratio: $r = \min\left[1, \frac{P(\alpha')Q(\alpha|\alpha')}{P(\alpha)Q(\alpha'|\alpha)}\right]$,
3. generate a random value, u, from a random distribution in [0,1],
4. if $u \leq r$ append the step to the chain and set the current position to $\alpha = \alpha'$, otherwise stay at $\alpha = \alpha$.

These steps are repeated many times to build up the MC. If the proposal density is symmetric, i.e. $Q(\alpha'|\alpha) = Q(\alpha|\alpha')$, the Hastings ratio is $r = \min[1, P(\alpha')/P(\alpha)]$. This means that if the probability of the proposed variable α is greater than that of α' the step is always taken and if it is lower the step is taken probabilistically.

Figure 6.1 shows the evolution of all model parameters projected to one dimension, in an MC with 10^5 steps. These plots show the value of each of the parameters (in a model with three POI and six NPs) after each accepted step in the chain. Burn-in steps at the beginning, shown in red, take the MC from the starting point to a high probability region, mixing the parameters efficiently. These initial steps are discarded from the chain when the posterior is given, so that the starting point does not affect the result even if it is in a lower probability region.

Performance of the algorithm should be optimised so that the proposal acceptance is high enough to make the algorithm efficient, but not so high that structure in the posterior is undefined. This is achieved by adjusting the proposal function, often a Gaussian centred on α' is used — varying the width of this will vary the proposed step size and therefore the proposal acceptance rate. Figure 6.2 shows scatter plots of the Markov chain evolution, with these examples showing a single parameter of interest plotted against each nuisance parameter (note that similar plots can be made for all parameters of interest in an analysis). Different choices of proposal Gaussian width are shown, which result in different acceptance fractions. A smaller width gives smaller proposed steps, which are more likely to be accepted. However, as shown in Fig. 6.2a this can lead to poor sampling of the parameter space. Conversely, if the width is too large very few steps will be accepted and the algorithm becomes inefficient, as shown in Fig. 6.2b. The aim is to achieve 10–20% proposal acceptance, as shown in Fig. 6.2c, this has the proposal Gaussian width used in the subsequent analysis.

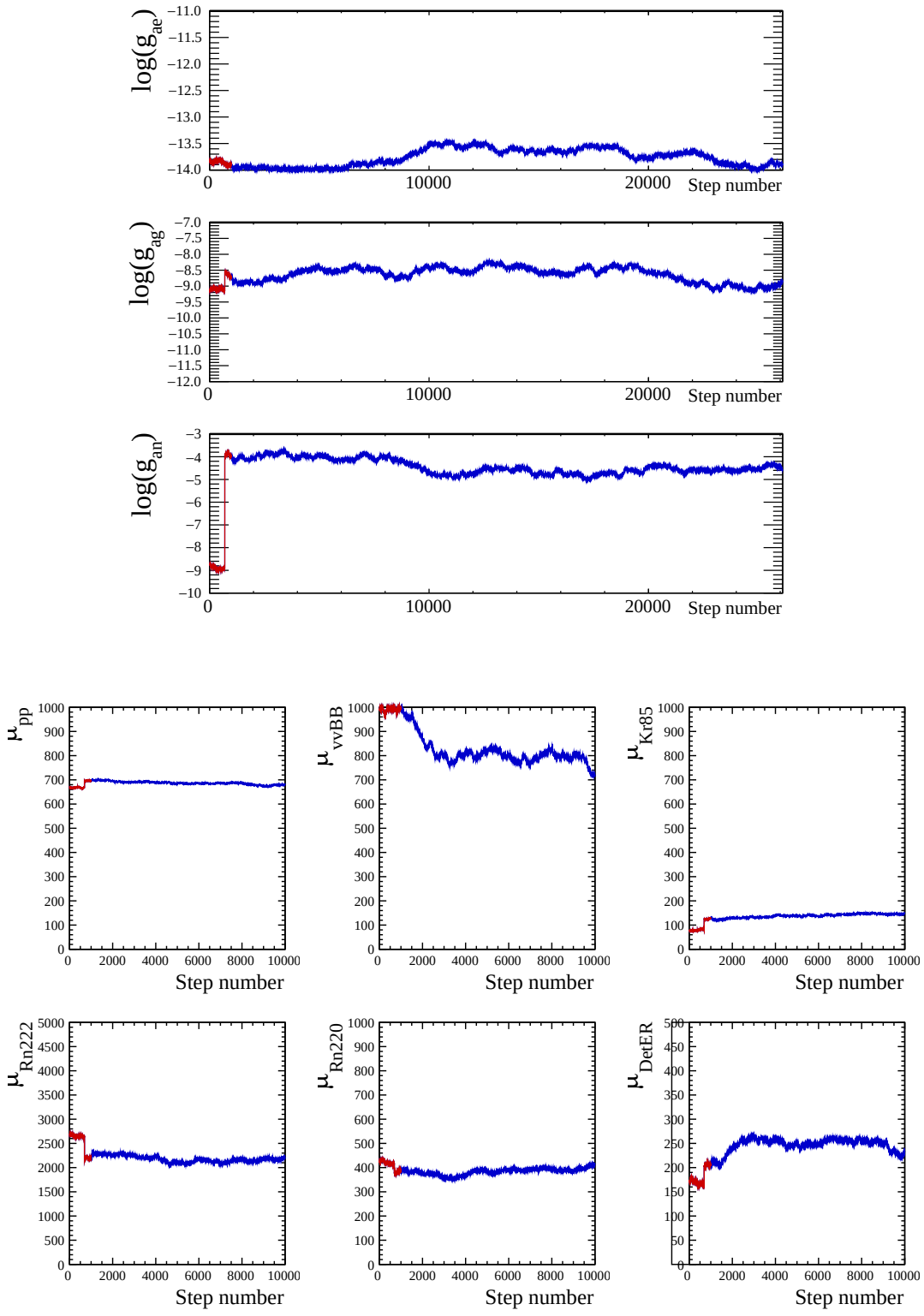

Figure 6.1 *Evolution of the parameters of interest (top) and nuisance parameters (below) in* 10^5 *steps of the Markov Chain, with burn-in steps shown in red.*

.

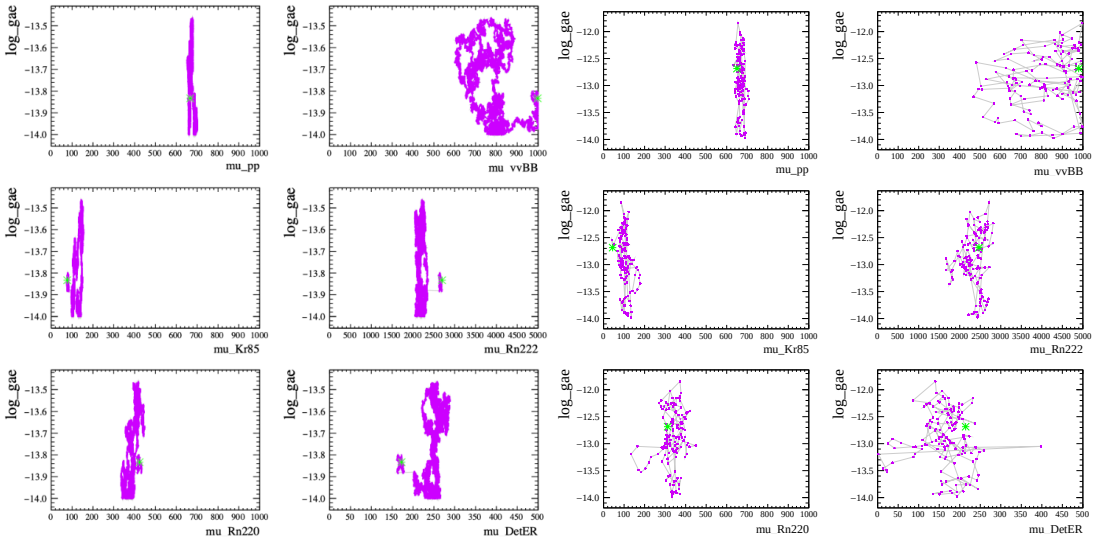

(a) *Smallest Gaussian width: acceptance fraction too high — 86.286%.*

(b) *Largest Gaussian width: acceptance fraction too low — 0.136%.*

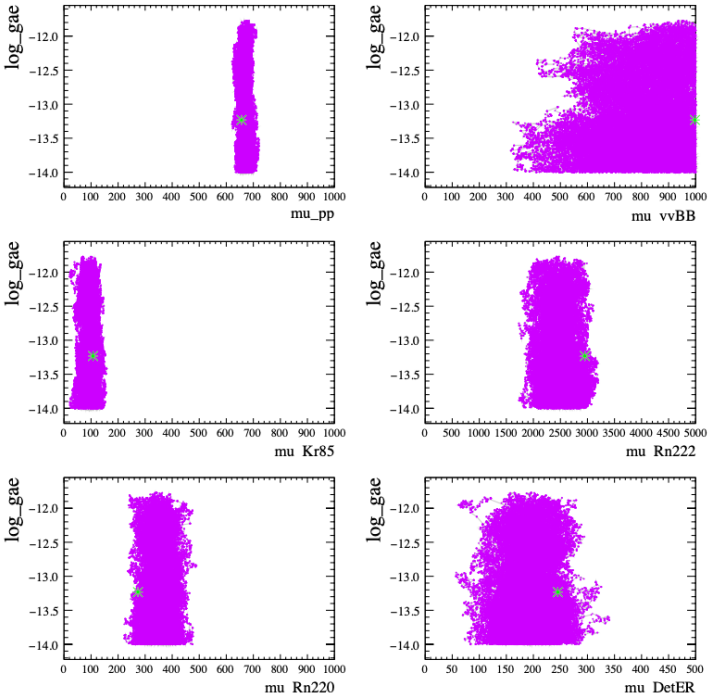

(c) *Acceptance fraction 18.410% as used in study.*

Figure 6.2 *Scatter plots showing evolution of the Markov chain in two dimensions, with the parameter of interest, $\log(g_{ae})$, plotted against all nuisance parameters, electron recoil background counts, for different choices of proposal function width.*

6.3 Credible Intervals

Once the Bayesian posterior probability distribution has been determined it can be used to find regions which have a given probability of containing the true value of the parameter — these are called credible intervals. In the one dimensional single parameter case, a credible interval containing a $1 - \alpha$ fraction of the posterior probability can be found:

$$1 - \alpha = \int_{\theta_{low}}^{\theta_{up}} p(\theta|x)d\theta. \tag{6.3}$$

The credible interval is not unique for a posterior distribution. For instance it can be chosen to be the narrowest possible interval (in one dimension this is the highest posterior density interval), have equal probability in the upper and lower tails outside the interval or have the mean as the central point inside the interval. Highest posterior density intervals can be generalised to higher dimensions, so this is the method chosen for this analysis. In higher dimensions this will not necessarily be the narrowest possible interval, but the method of beginning at the highest posterior density and moving downwards until a specified proportion of the posterior density is contained remains the same.

The idea of the credible interval differs from that of the confidence interval found using a frequentist analysis. In the frequentist approach the parameter is considered to have a fixed true value and the confidence interval constructed is random, as it depends on the random sample. For a large number of repeated measurements the confidence interval will contain the true value a specified n% of the time, this property is called coverage. In the Bayesian approach a fixed credible interval is constructed and the parameter is a random variable. The credible interval is interpreted as having a specified n% probability to contain the true value. The difference comes from the fact that the frequentist confidence interval depends only on data, whilst the Bayesian credible interval depends on prior information about the problem which is updated using data. In the two approaches nuisance parameters are also treated in different ways: maximum likelihood removes them using differentiation in the frequentist case and marginalisation removes them using integration in the Bayesian case.

6.4 Solar Axion Test Case

As introduced in Section 6.1, the XENON1T experiment considered the interpretation of an excess of low energy electron recoil events as a solar axion signal. In order to constrain the axion model, a three dimensional analysis was carried out, with three solar axion components from different production mechanisms that depend on different couplings. The ratio of these couplings varies in different models, so probing multiple couplings allows the axion model to be constrained. Multi-dimensional analysis becomes computationally expensive in a frequentist approach, so here Bayesian methods are used to study the three dimensional credible interval for the model parameters. This provides a test case for any higher dimensional model or comparing components of different models.

As described in Section 5.1.3, the three components are solar axions produced by: ABC interactions (g_{ae}), Primakoff interactions ($g_{a\gamma}$) and ^{57}Fe de-excitation (g_{an}). In the same way as in Chapter 5, simulated distributions of the detector observables S1, log(S2) are generated for the signal components using NEST. The resulting signal contours for these three components are show in Fig. 6.3, along with the resulting reconstructed energy spectra compared to the input energy spectra for validation.

These distributions, along with those for the background components, are used to construct the likelihood, as detailed in Section 4.5, with the observables S1 and log(S2) being used. As in Section 5.3, the nuisance parameters are the number of events of each of the background components, with auxiliary functions for these included in the likelihood as constraint terms.

Similarly to the analysis described in Section 5.3, the electron recoil background components are used as nuisance parameters. The internal β emitting ^{85}Kr, ^{220}Rn and ^{222}Rn, ^{136}Xe two neutrino double beta decay, ^{124}Xe double electron capture and detector+surface+environment γs are all included with Gaussian constraint terms. These have central values and widths equal to the expected values and uncertainties given in Table 5.1. The solar neutrino electron recoil component and all nuclear recoil components are included as constant components in the background model.

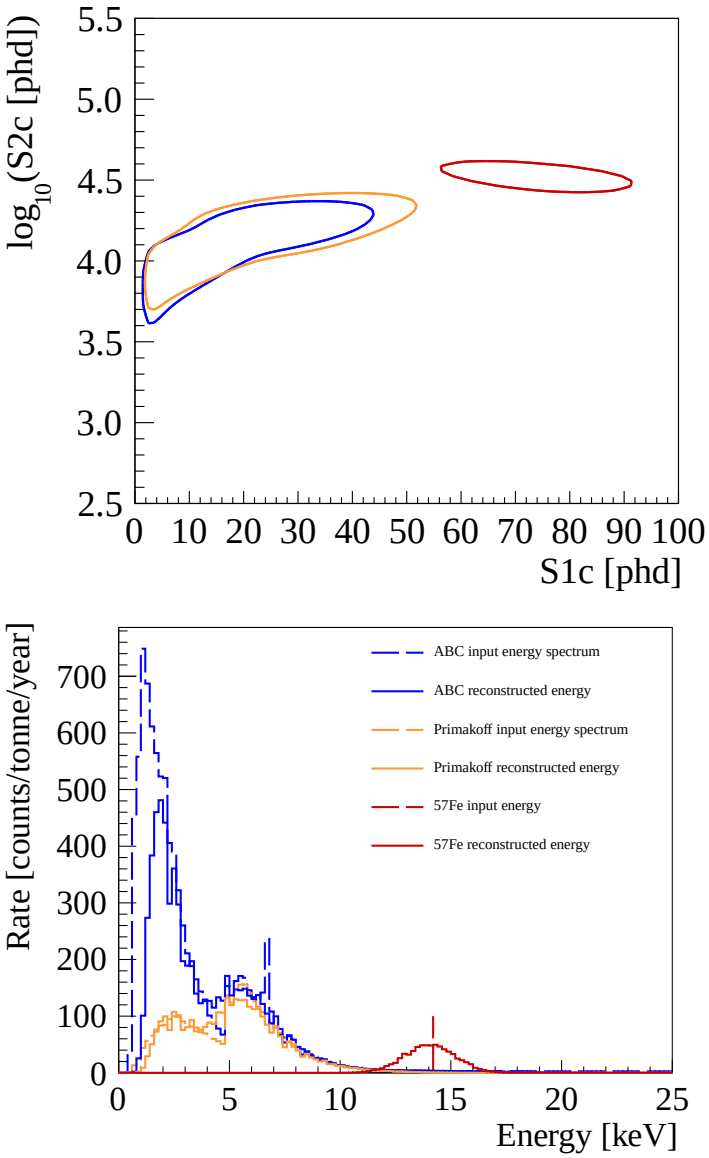

Figure 6.3 *Contours (top) and reconstructed energy (below) of the three solar axion components: ABC* $\propto g_{ae}^4$*, Primakoff* $\propto g_{ae}^2 g_{a\gamma}^2$ *and* $^{57}Fe \propto g_{ae}^2 g_{an}^2$*. The couplings are fixed to* $g_{ae} = 5 \times 10^{-12}$*,* $g_{a\gamma} = 2 \times 10^{-10}\text{GeV}^{-1}$*,* $g_{an} = 1 \times 10^{-6}$*.*

6.4.1 Choice of Priors

The prior probability for a parameter or model is the degree of belief about its value before carrying out a measurement. As shown by Eq. 6.1, this is an essential part of Bayesian inference, which can either be seen as an advantage — the posterior accounts for relevant prior information, or a disadvantage — it can be subjective if little is known. Due to the strong dependence of the posterior on

the prior, it is important to consider the choice of prior in an analysis and study how different priors will impact the result.

A common choice is to take a uniform or "flat" prior which represents ignorance about the value of the parameter in the physically allowed parameter range, assigning all values equal probability:

$$P(\theta) = \begin{cases} \frac{1}{\theta_{max} - \theta_{min}} & \theta_{min} \leq \theta \leq \theta_{max}, \\ 0 & \text{otherwise.} \end{cases} \tag{6.4}$$

The problem of this approach is that a prior which is flat in one parameter θ may not transform to a flat prior in another parameter, if it is a non-linear function of θ. For example, in the solar axion case, a flat prior in the ABC axion interaction rate μ_{ABC} would not be flat in the axion electron coupling g_{ae} since $\mu_{ABC} \propto g_{ae}^4$. An alternative approach is to use an objective prior, which does not reflect the current degree of belief, but is constructed using a formal set of rules. One type of objective prior is Jeffrey's prior, which is designed to be invariant under reparametrization of the observables and covariant under reparametrization of the model parameters [239]. According to Jeffrey's rule, the prior is:

$$P(\theta) \propto \sqrt{det(I(\theta))}, \tag{6.5}$$

where the Fisher information matrix $I(\theta)$ is determined from the second derivative of the likelihood function. The Jeffrey's prior for the mean of a Gaussian distribution is a constant, whilst the Jeffrey's prior for the mean μ of a Poisson distribution is $P(\mu) \propto 1/\sqrt{\mu}$. Neither of these reflect the degree of belief in the parameter, but they provide a consistent way to define the prior. Other types of objective prior can also be defined using different sets of rules, such as the reference prior by Bernardo and Berger [110].

In this study, initially the same type of POIs were used as for the frequentist analysis in Chapter 4 — the number of signal events for each of the axion components ($\mu_{ABC}, \mu_{Prim}, \mu_{Fe}$). Flat priors in these parameters will not transform to flat priors in the couplings, so three different choices of prior were investigated in order to determine their effect on the result. The three priors considered were:

1. Flat priors in the number of signal events.

2. Priors which transformed to flat in the couplings.

3. Objective Jeffrey's priors.

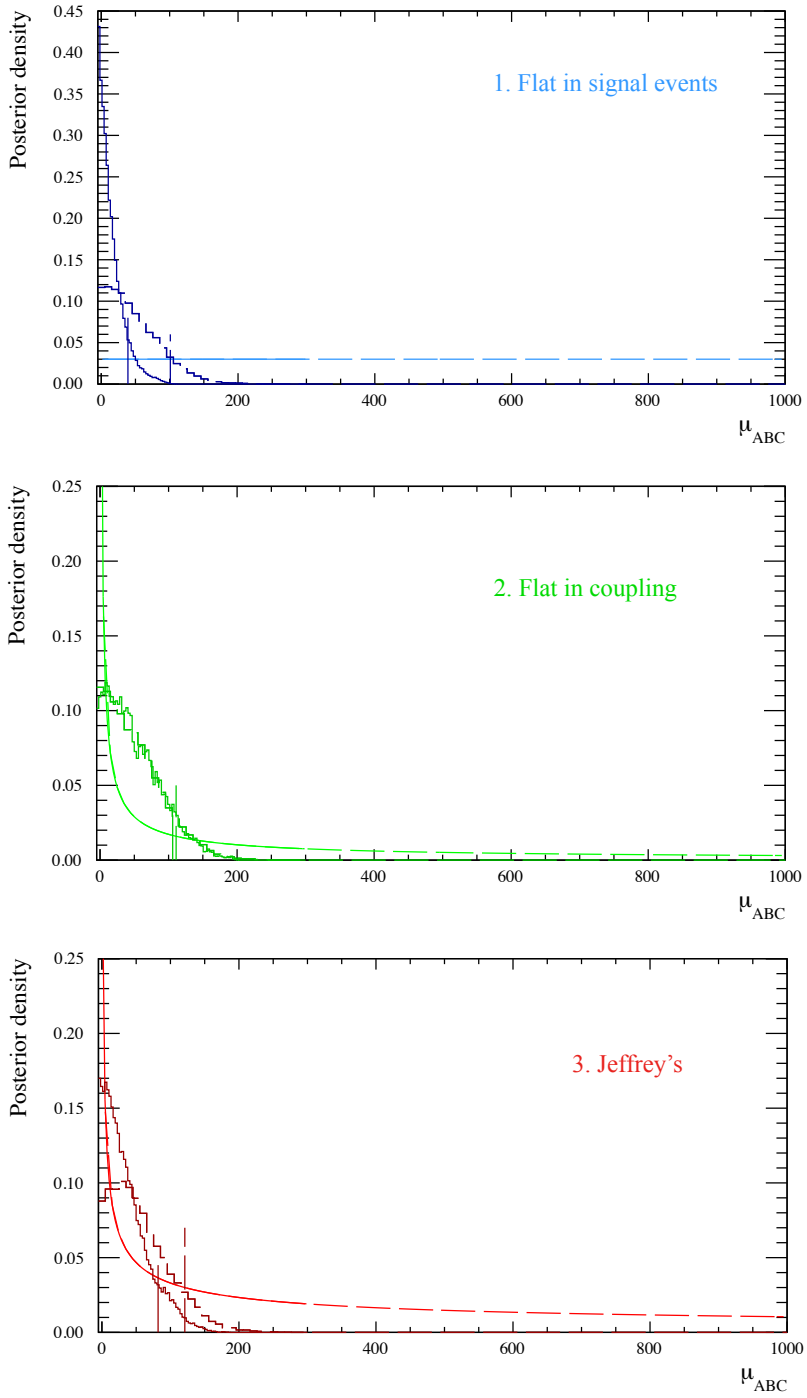

Figure 6.4 *Priors and resulting posteriors in the number of ABC signal events. Top flat in μ_{ABC}, middle flat in g_{ae}, bottom Jeffrey's prior. Smooth lines show the priors and darker histograms show the posterior, with vertical lines indicating the 90% credible interval.*

.

Probability density functions transform as: $P(a) = P(b)db/da$. In order to give flat priors in the couplings the priors in the POI must take the form:

$$P(\mu_{ABC}) = 1/\mu_{ABC}^{3/4}, \quad P(\mu_{Prim}) = 1/\mu_{Prim}^{1/2}, \quad P(\mu_{Fe}) = 1/\mu_{Fe}^{1/2}. \tag{6.6}$$

To find the Jeffrey's prior for a counting experiment the result for Poisson counts can be used: $P(\mu) = \sqrt{1/\mu}$, to construct an objective prior for each of the components.

For each of these three priors the analysis was carried out using two different parameter ranges of 0–300 and 0–1000 events (for the parameters $\mu_{ABC}, \mu_{Prim}, \mu_{Fe}$). All other parameters relating to the analysis and Markov chain (number of steps, burn in steps, acceptance fraction) were kept the same and 90% credible intervals constructed in each case. Figure 6.4 shows the three priors and resulting posteriors in the number of ABC axion signal events parameter μ_{ABC}. The smooth lines show the input priors, with the dashed line extending to the 1000 signal events. Resulting posteriors for the two parameter ranges are shown by the darker coloured histograms in each panel, with the vertical lines indicating the 90% credible interval (note that the posterior normalisations are not equal). This shows that for the flat prior the range makes a bigger difference to the resulting posterior, as the distribution can spread rather than being concentrated at the lowest values. The second prior being the steepest distribution, the posterior is affected very little by the change in parameter range. It can also be seen that for the 0–1000 parameter range the choice of prior has only a small effect on the resulting credible interval.

6.4.2 Choice of Parameter of Interest

In addition to choosing suitable priors, it is important to choose appropriate POI(s) for the analysis. For a one dimensional solar axion analysis it is straightforward to map a number of signal events to the physical model parameter, in this case the coupling. For ABC solar axions this is done using: $g_{ae}(CI) = g_{ae}(0)\big(\mu_{ABC}(CI)/\mu_{ABC}(0)\big)^{1/4}$, where $g_{ae}(0)$, $\mu_{ABC}(0)$ are the input coupling and number of signal events and $\mu_{ABC}(CI)$ is the computed interval. However, since the Primakoff component depends on both g_{ae} and $g_{a\gamma}$, mapping between the signal event and coupling spaces becomes more complicated. At the point where there are zero ABC solar axion events this implies $g_{ae} = 0$, which in turn would

mean zero Primakoff events, implying $g_{a\gamma} = 0$. This correlation is not true for the number of signal event parameter space, which comes from the two separate component shapes in the analysis. But the conversion where $g_{a\gamma} \propto 1/g_{ae}$ means that $g_{ae} = 0$ can never be covered after the mapping, which incorrectly would imply a non-zero signal. In order to solve this mapping problem, the analysis was instead carried out using the couplings as the parameters of interest. A further consideration here is that there are very few concrete theoretical constraints on the coupling values, so several orders of magnitude can be probed. Therefore, in order to sample the parameter space effectively the logarithm of the coupling was chosen as the POI.

If we want to constrain the model using the couplings, then the POI must be log(coupling) in the solar axion case and using a model parameter or its logarithm may be useful for other models. But the analysis can still be carried out in terms of number of signal events, this might be more useful when looking at distinguishing multiple models/model components rather then constraining the model itself.

6.5 Asimov Data

Similarly to Section 5.3, we want to find the projected LZ result in the case of no observed signal, in the frequentist analysis this was a projected 90% confidence interval whereas here it is a projected 90% credible interval.

Here, the aim is to characterise the sensitivity of the experiment to a given hypothesis. The frequentist confidence interval will cover the true value 90% of the time, therefore this projected sensitivity can be calculated using a single random data set and we expect that for many repeated ensembles there will be coverage. However, the Bayesian credible interval, introduced in Section 6.2, is a statement about the region where there is 90% probability to find the true value. This should not be dependent on a single random dataset, as it is a projection for the experiment, so we need a median sensitivity. In order to estimate the median sensitivity a single representative data set can be used. This is the Asimov data set, defined such that the observed parameter values are set to be equal to their expected values, i.e. estimators evaluated for this data set will return the "true" values. Other examples of Bayesian sensitivity studies using the Asimov data set can be found for multi component dark matter in Ref. [240] and neutrino mass hierarchy in Ref. [241].

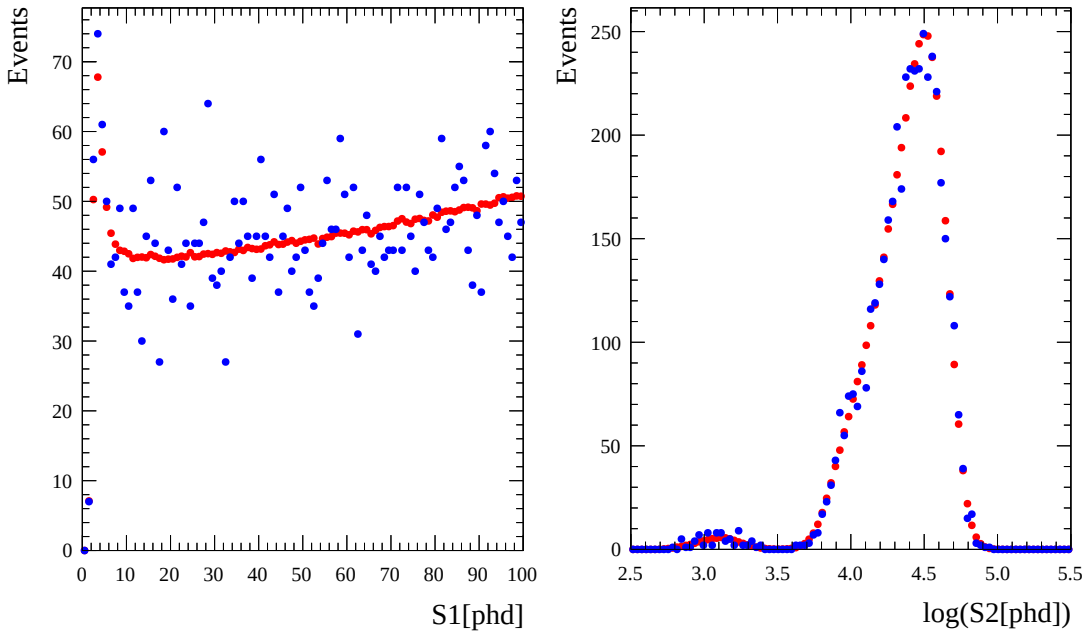

(a) *Projections of the Asimov dataset (red) and a randomly generated dataset (blue) in the observable S1 (left) and log(S2) (right).*

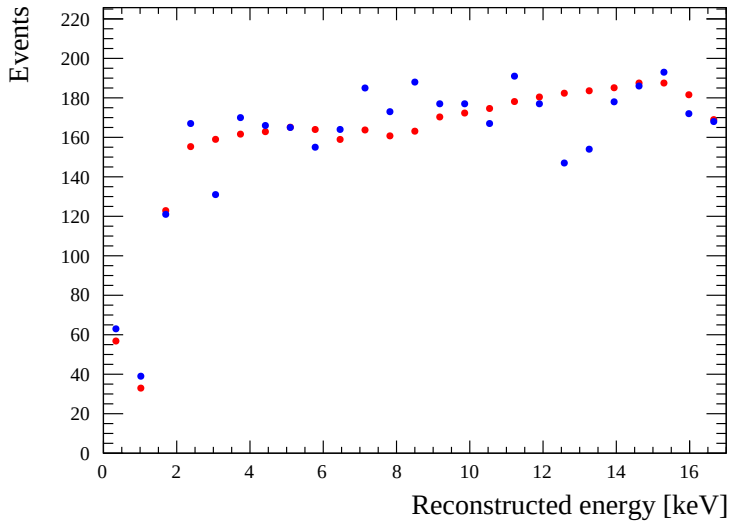

(b) *Reconstructed energy of the Asimov dataset (red) and a randomly generated dataset (blue).*

Figure 6.5 *Comparison of the Asimov dataset and a randomly generated dataset.*

Figure 6.5 shows the Asimov data generated for the LZ solar axion sensitivity study, under the background only hypothesis. This will be used to find the projected sensitivity of the Bayesian analysis for solar axions in LZ.

6.6 LZ Sensitivity Study

The Bayesian sensitivity analysis for the three solar axion components in LZ was carried out using $\log(g_{ae})$, $\log(g_{a\gamma})$, $\log(g_{an})$ as parameters of interest and background components as nuisance parameters, with observables S1, log(S2). To compute the posterior 100 independent Markov Chains with 10^5 steps were constructed. For each Markov chain the first 1000 burn-in steps were removed then the chains were stitched together to find the posterior distribution in three dimensions. Figure 6.6 shows the one and two dimensional projections of this posterior distribution, in each coupling individually plus each possible pair of couplings. The top centre panel shows the correlation between the axion-photon and axion-electron couplings, due to the overlap in the energy spectra of the ABC and Primakoff components. Projections of these two with the axion-nucleon coupling show much lower correlation as the ^{57}Fe component has a very different

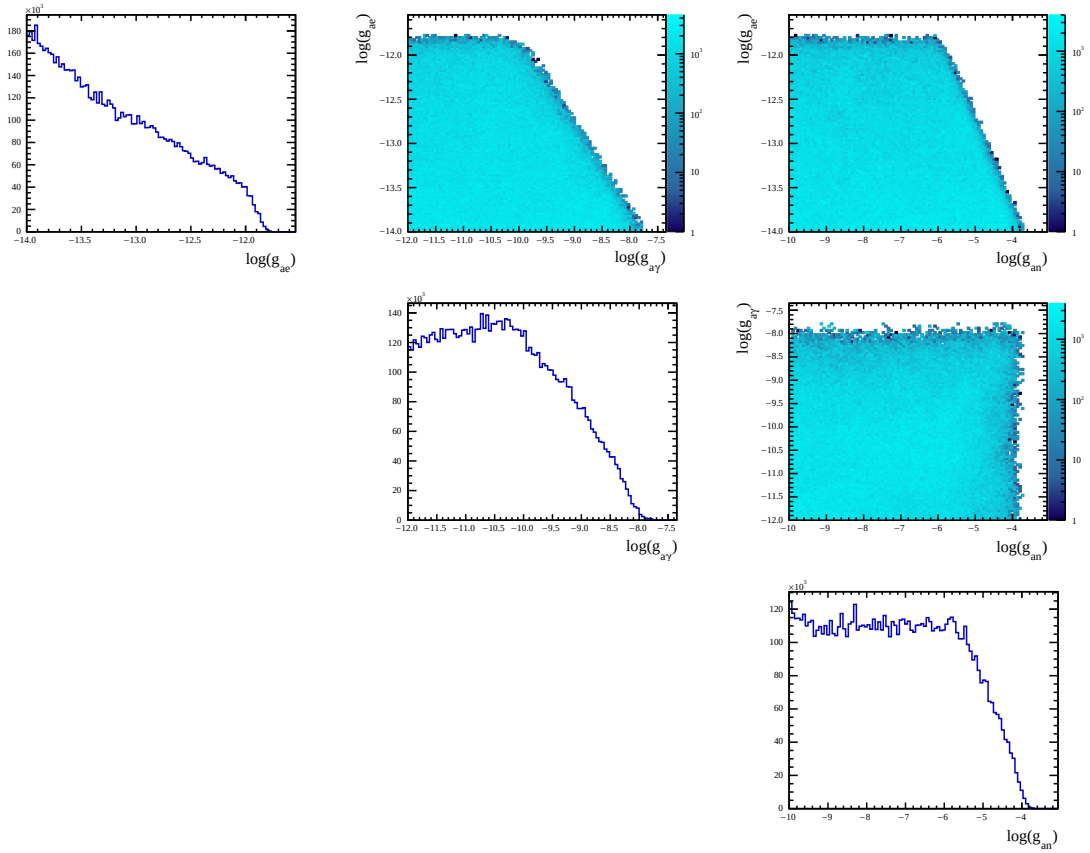

Figure 6.6 *Projections of the three dimensional posterior density in each of the parameters of interest individually and as pairs. Note that the posterior densities are not normalised and have arbitrary units.*

energy spectrum.

Using the three dimensional posterior a 90% credible interval was determined using the highest posterior density method. This credible interval is shown for the $\log(g_{a\gamma})$ vs $\log(g_{ae})$ plane in Fig. 6.7. The red "LZ bayesian" line indicates the parameter space which is favoured in the event of no observed signal for the full LZ exposure of 5.6 tonnes $\times$ 1000 live days, with the expected nominal background levels.

Existing experimental limits shown in Fig. 6.7 come from CAST (green line) and LUX (blue line). The CAST analysis constrains the product of the couplings: $g_{ae}g_{a\gamma} \leq 8.1 \times 10^{-23}$ GeV^{-1} for axion masses $m_a \leq 10$ meV [242], with the parameter space above the line excluded. This is a 95% confidence limit constructed using a maximum likelihood method. LUX set the leading direct

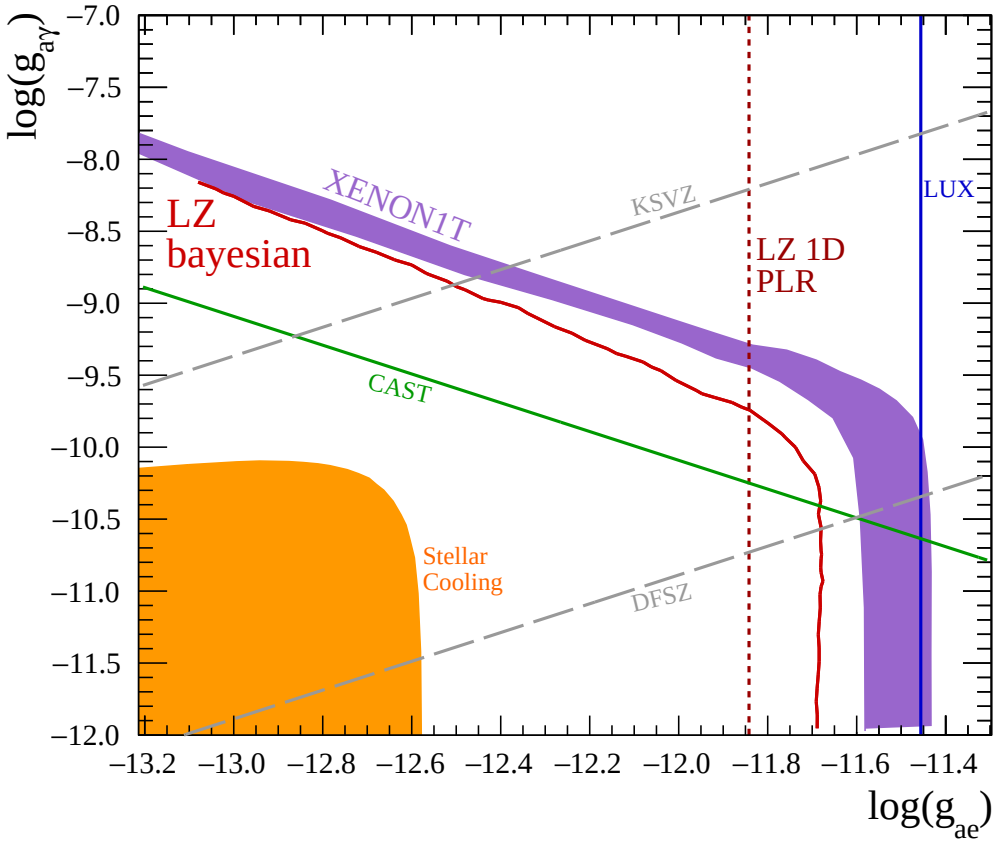

Figure 6.7 *Projection of the 90% credible interval in the axion-photon and axion-electron couplings. Experimental 90% confidence limits from LUX and CAST are shown in addition LZ projection. The preferred regions from the stellar cooling global fit and the 90% confidence volume constructed in the XENON1T analysis are also shown.*

detection limit on ABC solar axions, constraining $g_{ae} \leq 3.5 \times 10^{-12}$, at 90% confidence level using the profile likelihood method described in Section 4.5. The ABC solar axion component has flux proportional to g_{ae}^2 and a further factor of g_{ae}^2 arises in the rate for LUX from the axion-electron cross section. In CAST the ABC component is also considered but the detection via Primakoff conversion of axions into X-ray photons in a strong magnetic field introduces a factor of $g_{a\gamma}^2$ to the rate. Note that CDMS carried out the first direct detection search for solar axions in 2009. This analysis considered the Primakoff component only, resulting in a limit: $g_{a\gamma} < 2.4 \times 10^{-9}\text{GeV}^{-1}$ (95% C.L) [243].

The "LZ 1D PLR" line in red shows the projected 90% exclusion limit, calculated in Chapter 5, using a frequentist profile likelihood ratio analysis with the same exposure and background levels as this Bayesian analysis. In the PLR analysis there is only one parameter of interest, the ABC solar axions with the Primakoff component is included as a nuisance parameter and ^{57}Fe component is not included. The Bayesian projection is slightly more conservative, due to the use of a different statistical approach and a higher number of dimensions.

The two filled regions in Fig. 6.7 show areas of parameter space that are favoured by two analyses: orange from a global fit to stellar cooling constraints [244] and purple from the XENON1T observed excess [141].

Current astrophysical observations show hints for excess energy losses in stars at different evolutionary stages: red giants, supergiants, He core burning stars, white dwarfs and neutron stars. One possible explanation for this cooling anomaly is the production of axions which can transport energy out of the stars. Large systematics in stellar modelling and observations mean that individual cooling hints have small statistical significance, but a global fit can be used to determine the significance of the axion explanation for the combined hint. Accounting for axion production by Bremsstrahlung (g_{ae}) and Primakoff ($g_{a\gamma}$) processes, a combined fit of the white dwarf, red giant branch and horizontal branch observations gives the best fit values: $g_{ae} = 1.5 \times 10^{-13}$, $g_{a\gamma} = 1.4 \times 10^{-11}\text{GeV}^{-1}$ [244]. The combined fit is also used to construct 1/2/3 σ hinted areas in the $g_{a\gamma}$, g_{ae} parameter space, with the 2σ region shown here. The future IAXO helioscope and ARIADNE fifth range force experiments should be able to probe this parameter space, which the next generation of xenon direct detection experiments are not expected to reach.

The purple region shows the projection in $g_{a\gamma}$, g_{ae} space of the 90% confidence

volume for a solar axion signal created in the XENON1T analysis using a frequentist Neyman construction [141]. Since these two preferred regions do not overlap, they are in tension and it will be important for other experiments to test these regions of parameters space.

The two dashed grey lines show the predicted relations between the axion-photon and axion-electron couplings in the benchmark hadronic KSVZ and general DFSZ axion models, described in Section 2.2.3. In the KSVZ model there are no tree level interactions with standard model quarks and leptons, whilst in the DFSZ model there are. As a result, the expected $g_{a\gamma}$ values are higher in the KSVZ model for a given value of g_{ae}.

6.7 Outlook

In this chapter a framework for carrying out Bayesian inference for multi-component models, using multiple parameters of interest, has been established. The test case of solar axions is of particular interest, due to the recent XENON1T result. It is shown that LZ will have the capability to probe the parameter space favoured by the XENON1T analysis. The Bayesian sensitivity projection is slightly more conservative than the one dimensional frequentist projection, but it improves on existing experimental constraints. The intersection with the expected couplings for KSVZ and DFSZ can constrain the axion model, indicating whether or not it is hadronic. None of the next generation of direct detection experiments is expected to test the region favoured by stellar cooling hints. A useful further study for solar axions would be to create an Asimov dataset with a solar axion signal injected at the level of the XENON1T excess. This would test the prospects of this analysis for characterising this signal in LZ.

Analysis with multiple POI may also be useful for characterising other models with multiple components. For example effective field theories, introduced in Section 2.3.3, have many separate operators, which would become computationally expensive with a frequentist approach. It is also possible that the components do not come from the same model, e.g. dark matter consisting of both axions and WIMPs. In this case it might be more useful to use the number of signal events rather than any model parameters as the parameter of interest in order to quantify what amount of each signal is present in the data.

Chapter 7

Summary and Conclusions

In this thesis, dark matter searches beyond the standard WIMP paradigm have been presented, highlighting the capability of direct detection experiments to carry out a range of physics searches.

The big question

In Chapter 1 the dark matter problem was motivated, with evidence on a range of astrophysical scales that most of the matter in the universe is non luminous and non baryonic. The current Standard Model of particle physics does not contain a valid dark matter candidate, suggesting that it is incomplete. A growing number of issues in theoretical and experimental particle physics embolden this claim — a *new theory* of fundamental physics is needed.

Chapter 2 describes different approaches to model building and some of the resulting models. Weakly Interacting Massive Particles (WIMPs) have been the most studied candidate, followed by much lighter axions. No conclusive evidence for either of these has been seen after several decades of searches, so the theoretical landscape remains wide open to a broad range of models. This leaves a *big question* facing particle physics and cosmology today; *what is the nature of dark matter and how does this fit into a new theory of physics beyond the Standard Model*?

The smaller question

Complimentary searches across many different disciples are key to resolving this problem, covering as much parameter space as possible and confirming

any observations. Chapter 3 discusses the direct detection approach — aiming to detect dark matter particles scattering off atoms in a terrestrial detector. In particular the LUX liquid xenon time projection chamber experiment, and next generation LZ experiment, are described. Designed to search for nuclear recoils arising from WIMP-nucleon interactions, these experiments can also detect electron recoils, which can be utilised in non WIMP searches.

This work aims to address one *small* part of the *big question* introduced above; *how can direct detection experiments be used to probe a broad range of new physics models?* More specifically; *what is the reach of new physics searches using low energy electron recoils in direct detection experiments?*

Key results and contributions

Low energy electron recoil searches using the LUX and LZ experiments are studied in this work — with analysis of existing data, preparation for future data and consideration of the longer term prospects for discovery.

The LUX analysis, presented in Chapter 4, was the first dedicated direct detection search for mirror dark matter. To test this model detailed phenomenology was needed and this author carried out the first calculation of the effects of mirror dark matter capture and shielding for xenon direct detection experiments. Then using LUX data, the first ever direct detection limit on mirror dark matter kinetic mixing was found. Much of the theoretically allowed parameter space was ruled out, leaving only a narrow parameter space where the simplest mirror dark matter model can exist.

Chapter 5 considers the sensitivity of the next generation LZ experiment to such models. In LZ a more general and comprehensive approach will be taken — with a common analysis framework, developed by this author, used for all low energy electron recoil searches. Studies of key electron recoil backgrounds and their simulation were also undertaken. Different electron recoil models were implemented and tested using the NEST package, in order to validate the detector electron recoil response at different energies. This author carried out sensitivity studies for mirror dark matter and solar axion models, finding the projected exclusion limit, discovery potential and impact of varying internal β background levels. The common analysis framework was also used to study five other signal models.

Low energy electron recoil searches are of particular interest in light of the excess

in of $\sim$ keV electron recoils observed by the XENON1T experiment [141]. Solar axion and neutrino magnetic moment signals were proposed as explanations, by the XENON1T collaboration. Our sensitivity studies show that LZ will be able to; firstly determine the existence of an excess and secondly probe the relevant parameter space in these signal models. In the case of no detection LZ will be able to set world leading limits on all seven signal models considered. These analyses are complimentary to conventional low mass dark matter searches using cryogenic experiments (e.g. SuperCDMS [132], EDELWEISS [138] and CRESST [135]) and axion searches using helio- or halo- scopes (e.g. ADMX [146] and IAXO [101]).

In the final part of this work, Chapter 6 considers the prospects for signal characterisation, using Bayesian methods, in the case of signal discovery. For a model with multiple parameters or signal components this provides an efficient way to carry out analysis with multiple parameters of interest. A test case of a solar axion analysis was used, however these tools are now part of the core LZ statistical analysis package and could be used for any model or distinguishing different models.

In summary this work has presented searches for new physics using low energy electron recoils in direct detection experiments. A framework to carry out these analyses in LZ has been developed and sensitivity studies carried out. Prior to this a specific mirror dark matter search was done using LUX data and subsequently work was done on signal characterisation. As part of the LUX and LZ collaboration this author has also worked on simulations, data quality and hardware commissioning.

Future outlook

Further studies could extend the work described above; mirror dark matter phenomenology could be developed further and different models could be studied with the Bayesian analysis. Once the LZ experiment has taken data the low energy electron recoil analysis framework can be used for analysis — a natural progression from the sensitivity projections. If a signal is observed the work on Bayesian signal characterisation lays the foundations for determining what has actually been discovered.

Going back to the *big question*, complimentary approaches are key to probing a broad range of parameter space for dark matter and new physics beyond the Standard Model, leaving no stone unturned. This moves beyond conventional WIMP searches in direct detection experiments and this thesis aims to address a

small part of this effort. The next generation of searches will maximise potential for achieving a *big answer*. Whilst it is unclear how or where dark matter will be found, what is clear is that its discovery will mark the start of a new era in fundamental physics.

Appendix A

The First Appendix

A.1 Mirror Dark Matter Capture Calculations

A.1.1 Capture Energy Loss

In order to find the cutoff velocity, below which collisions of incoming mirror electrons with captured mirro helium is important the energy from these interactions must be calculated (Section 4.1.1).

Energy loss per unit distance travelled for mirror electrons, due to collisions with captured mirror helium, is given by:

$$\frac{dE'}{dl} = -n_{He'} \int_{E_{min}}^{E} \frac{d\sigma}{dE_R} E_R dE_R, \tag{A.1}$$

where $n_{He'}$ is the number density of captured mirror helium. For $E_R \leq E_b$ the energy is insufficient to ionize helium so we take $E_{min} = E_b$.

$$\begin{aligned} \frac{dE'}{dl} &= -n_{He'} \frac{\lambda}{v^2} \int_{E_b}^{E} \frac{\lambda}{E_R} dE_R, \\ \frac{dE'}{dl} &= -n_{He'} \frac{\lambda}{v^2} ln\Big(\frac{E}{E_b}\Big) \end{aligned}$$

Find total energy loss:

$$\begin{aligned}
\int v^2 dE' &= -\lambda ln\Big(\frac{E}{E_b}\Big)\int n_{He'}dl \\
\frac{m}{2}\int E' dE' &= -\lambda ln\Big(\frac{E}{E_b}\Big)\int n_{He'}dl \\
\frac{E'^2}{m} &= -\frac{2g_T\pi\alpha^2}{m} ln\Big(\frac{E}{E_b}\Big)\int n_{He'}dl \\
E'^2 &= -4\pi\alpha^2\Sigma ln\Lambda.
\end{aligned}$$

To find cutoff velocity set the integrated energy loss equal to the incoming mirror electron energy $E' = 1/2mv_{cut}^2$, which gives:

$$\frac{1}{4}m^2 v_{cut}^4 = -4\pi\alpha^2\Sigma log\Lambda \tag{A.2}$$

$$v_{cut}^4 = \frac{16\pi}{m^2}\alpha^2\Sigma log\Lambda. \tag{A.3}$$

$$\tag{A.4}$$

A.1.2 Modified Velocity Distribution

Below the cutoff velocity, collisional scattering alters the mirror electron velocity distribution. The velocity dispersion v_0 is replaced by an energy dependent term:

$$\frac{1}{v_c^0} = \frac{1}{N}\int_{|v|>y}^{\infty} \frac{e^{-v^2/v_0^2}}{v_0^3\pi^{3/2}|v|} d^3v. \tag{A.5}$$

This is changed to polar coordinates: $d^3v = v^2 \sin\psi d\theta d\psi dv$.

$$\frac{1}{v_c^0} = \frac{1}{Nv_0\sqrt{\pi}}\int\int\int \frac{e^{-v^2/v_0^2}}{v_0^2\pi|v|}v^2 = \frac{2}{Nv_0\sqrt{\pi}}\int\int \frac{e^{-v^2/v_0^2}}{v_0^2\pi|v|}v^2\sin\psi d\psi d|v| \tag{A.6}$$

$$= \frac{2}{Nv_0\sqrt{\pi}}\int\int e^{-q^2}\frac{q^2}{|v|}v_0\sin\psi d\psi dq, \tag{A.7}$$

$$= \frac{2}{Nv_0\sqrt{\pi}}\int\int e^{-q^2}q\sin\psi d\psi dq, \tag{A.8}$$

$$= \frac{2}{Nv_0\sqrt{\pi}}\int \frac{e^{-y^2/v_0^2}}{2}\sin\psi d\psi, \tag{A.9}$$

$$= \frac{-2}{Nv_0\sqrt{\pi}}\int e^{-y^2/v_0^2}d\cos\psi. \tag{A.10}$$

$$\tag{A.11}$$

Bibliography

[1] D. S. Akerib et al. First direct detection constraint on mirror dark matter kinetic mixing using LUX 2013 data. *Phys. Rev. D*, 101(8):012003, Jan 2020.

[2] D. S. Akerib et al. Projected sensitivities of the LUX-ZEPLIN (LZ) experiment to new physics via low-energy electron recoils. *arXiv:2102.11740 [hep-ex]*, Feb 2021.

[3] G. Bertone and D. Hooper. A History of Dark Matter. *Rev. Mod. Phys.*, 2016.

[4] J. Ford V. Rubin and N. Thonnars. Extended rotation curves of high-luminosity spiral galaxies. *Astrophys. J.*, 225:107–111, 1978.

[5] F. Zwicky. Die Rotverschiebung von extragalaktischen Nebeln. *Helv. Phys. Acta*, 6:110–127, 1933.

[6] F. Zwicky. On the Masses of Nebulae and of Clusters of Nebulae. *Astrophys. J.*, 86:217, October 1937.

[7] S. Smith. The Mass of the Virgo Cluster. *Astrophys. J.*, 83:23–30, 1936.

[8] J.P. Hughes. The Mass of the Coma Cluster: Combined X-Ray and Optical Results. *Astrophys.J.*, 337:21, February 1989.

[9] A. H. Gonzalez, S. Sivanandam, A. I. Zabludoff, and D. Zaritsky. Galaxy Cluster Baryon Fractions Revisited. *Astrophys. J.*, 778:14, 2013.

[10] J. Wambsganss P. Schneider, C. Kochanek. *Gravitational Lensing: Strong, Weak and Micro.*

[11] D. Clowe et al. A direct empirical proof of the existence of dark matter. *Astrophys. J.*, 648(2):L109L113, Aug 2006.

[12] D. Hooper G. Bertone and J. Silk. Particle dark matter: evidence, candidates and constraints. *Phys. Rep.*, 405(5):279 – 390, 2005.

[13] A. A. Penzias and R. W. Wilson. A Measurement of excess antenna temperature at 4080-Mc/s. *Astrophys. J.*, 142:419–421, 1965.

[14] D. J. Fixsen, E. S. Cheng, J. M. Gales, J. C. Mather, R. A. Shafer, and E. L. Wright. The Cosmic Microwave Background Spectrum from the Full COBE/FIRAS Data Set. *Astrophys. J.*, 473(2):576587, Dec 1996.

[15] G. Hinshaw et al. Nine-year Wilkinson Microwave Anisotropy Probe (WMAP) Observations: Cosmological Parameter Results. *Astrophys. J. Supple. Ser.*, 208(2):19, Sep 2013.

[16] N. Aghanim et al. Planck 2018 results. *Astron. Astrophys.*, 641, Sep 2020.

[17] V. Springel et al. Simulations of the formation, evolution and clustering of galaxies and quasars. *Nature*, 435(7042):629636, Jun 2005.

[18] L. J. Hall, K. Jedamzik, J. March-Russell, and S. M. West. Freeze-in production of FIMP dark matter. *J. High Energy Phys.*, 2010(3), Mar 2010.

[19] G. Aad et al. Observation of a new particle in the search for the Standard Model Higgs boson with the ATLAS detector at the LHC. *Phys. Lett. B*, 716(1):129, Sep 2012.

[20] S. Chatrchyan et al. Observation of a new boson at a mass of 125 GeV with the CMS experiment at the LHC. *Phys. Lett. B*, 716(1):3061, Sep 2012.

[21] S. Fukuda et al. Solar B8 and hep Neutrino Measurements from 1258 Days of Super-Kamiokande Data. *Phys. Rev. Lett.*, 86(25):56515655, Jun 2001.

[22] Q. R. Ahmad et al. Measurement of the Rate of $\nu_e + d \rightarrow p + p + e^-$ Interactions Produced by ^8B Solar Neutrinos at the Sudbury Neutrino Observatory. *Phys. Rev. Lett.*, 87(7), Jul 2001.

[23] K. andothers Abe. Indication of electron neutrino appearance from an accelerator-produced off-axis muon neutrino beam. *Phys. Rev. Lett.*, 107:041801, Jul 2011.

[24] M. Aker et al. First direct neutrino-mass measurement with sub-eV sensitivity, 2021.

[25] G. W. Bennett et al. Final report of the e821 muon anomalous magnetic moment measurement at bnl. *Phys. Rev. D*, 73:072003, Apr 2006.

[26] B. Abi et al. Measurement of the positive muon anomalous magnetic moment to 0.46 ppm. *Phys. Rev. Lett.*, 126(14), Apr 2021.

[27] S. D. McDermott, H. Yu, and K. M. Zurek. Turning off the lights: How dark is dark matter? *Phys. Rev. D.*, 83(6), Mar 2011.

[28] B. Audren, J. Lesgourgues, G. Mangano, P. D. Serpico, and T. Tram. Strongest model-independent bound on the lifetime of dark matter. *J. Cosmol. Astropart. Phys.*, 2014(12):028028, Dec 2014.

[29] D. Harvey, R. Massey, T. Kitching, A. Taylor, and E. Tittley. The nongravitational interactions of dark matter in colliding galaxy clusters. *Science*, 347(6229):14621465, Mar 2015.

[30] P. Tisserand et al. Limits on the Macho content of the Galactic Halo from the EROS-2 Survey of the Magellanic Clouds. *Astro.*, 469(2):387404, Apr 2007.

[31] A. M. Green and B. J. Kavanagh. Primordial black holes as a dark matter candidate. *J. Phys. G*, 48(4):043001, Feb 2021.

[32] B. P. Abbott et al. Observation of gravitational waves from a binary black hole merger. *Phys. Rev. Lett.*, 116(6), Feb 2016.

[33] S. Dodelson and L. M. Widrow. Sterile neutrinos as dark matter. *Phys. Rev. Lett.*, 72(1):1720, Jan 1994.

[34] K. Olive. T. Falk and M. Srednicki. Heavy sneutrinos as dark matter. *Phys. Lett. B*, 339(3):248–251, 1994.

[35] D. Hooper and S. Profumo. Dark matter and collider phenomenology of universal extra dimensions. *Phys. Rep.*, 453(2-4):29115, Dec 2007.

[36] N. Arkani-Hamed, A. G. Cohen, E. Katz, and A. E. Nelson. The littlest higgs. *J. High Energy Phys.*, 2002(07):034034, Jul 2002.

[37] S. Weinberg. The u(1) problem. *Phys. Rev. D*, 11:3583–3593, Jun 1975.

[38] G. 't Hooft. Symmetry Breaking through Bell-Jackiw Anomalies. *Phys. Rev. Lett.*, 37:8–11, Jul 1976.

[39] G. Raffelt M. Kuster and B. Beltra. *Axions: Theory, Cosmology and Experimental Searches*, volume 1. Springer, 7 2008.

[40] J. M. Pendlebury et al. Revised experimental upper limit on the electric dipole moment of the neutron. *Phys. Rev. D*, 92:092003, Nov 2015.

[41] R. D. Peccei and Helen R. Quinn. CP conservation in the presence of pseudoparticles. *Phys. Rev. Lett.*, 38:1440–1443, Jun 1977.

[42] M. Gorghetto and G. Villadoro. Topological susceptibility and qcd axion mass: Qed and nnlo corrections. *J. High Energy Phys.*, 2019(3), Mar 2019.

[43] F. C. Porter and K. C. Königsmann. Unambiguous test for the axion. *Phys. Rev. D*, 25:1993–1996, Apr 1982.

[44] J. E. Kim. Weak-interaction singlet and strong CP invariance. *Phys. Rev. Lett.*, 43:103–107, Jul 1979.

[45] M. A. Shifman, A. I. Vainshtein, and V. I. Zakharov. Can confinement ensure natural cp invariance of strong interactions? *Nucl. Phys. B*, 166(3):493 – 506, 1980.

[46] M. Dine, W. Fischler, and M. Srednicki. A Simple Solution to the Strong CP Problem with a Harmless Axion. *Phys. Lett. B*, 104:199–202, 1981.

[47] A. Zhitnitsky. A Simple Solution to the Strong CP Problem with a Harmless Axion. *Sov. J. Nucl. Phys.*, 31:206, 1980.

[48] F. Chadha-Day, J. Ellis, and D. J. E. Marsh. Axion dark matter: What is it and why now?, 2021.

[49] J. Feng, H. Tu, and H. Yu. Thermal relics in hidden sectors. *J. Cosmol. and Astropart. Phys.*, 2008(10):1–20, 2008.

[50] J. Alexander et al. Dark sectors 2016 workshop: Community report, 2016.

[51] S. Alekhin et al. A facility to search for hidden particles at the CERN SPS: the SHiP physics case. *Rep. Prog. Phys.*, 79(12):124201, Oct 2016.

[52] J. M. Cline, P. Scott, K. Kainulainen, and C. Weniger. Update on scalar singlet dark matter. *Phys. Rev. D.*, 88(5), Sep 2013.

[53] B. Holdom. Two U(1)'s and charge shifts. *Phys. Lett. B*, 166(2):196–198, 1986.

[54] R. Foot, H. Lew, and R. Volkas. A model with fundamental improper spacetime symmetries. *Phys. Lett. B*, 272(1-2):67–70, 1991.

[55] R. Foot. Mirror dark matter: Cosmology, galaxy structure and direct detection. *Int. J. Mod. Phys. A*, 29, 2014.

[56] J.D. Clarke and R. Foot. Plasma dark matter direct detection. *J. Cosmo. Astropart. Phys.*, 2016(01):029029, Jan 2016.

[57] A. L. Fitzpatrick, W. Haxton, E. Katz, N. Lubbers, and Yiming Xu. The effective field theory of dark matter direct detection. *J. Cosmol. Astropart. Phys.*, 2013(02):004004, Feb 2013.

[58] J. Kopp, V. Niro, T. Schwetz, and J. Zupan. Dama/libra data and leptonically interacting dark matter. *Phys. Rev. D*, 80:083502, Oct 2009.

[59] H. Zhang, Q. H. Cao, C. R Chen, and C. S. Li. Effective dark matter model: relic density, CDMS II, Fermi LAT and LHC. *J. High Energy Phys.*, 2011(8), Aug 2011.

[60] J. Abdallah et al. Simplified models for dark matter searches at the LHC. *Phys. Dark Universe*, 9-10:823, Sep 2015.

[61] C. Alpigiani. Searches for Dark Matter in ATLAS. 2017.

[62] S. Lowette. Search for Dark Matter at CMS. *Nucl. Part. Phys. Proc.*, 273-275:503–508, 2016.

[63] P. Fox, R. Harnik, J .Kopp, and Y. Tsai. LEP shines light on dark matter. *Phys. Rev. D*, 84(1):1–20, 2011.

[64] J. Beacham et al. Physics beyond colliders at cern: beyond the standard model working group report. *J. Phys. G*, 47(1):010501, Dec 2019.

[65] D. Banerjee et al. Search for Invisible Decays of Sub-GeV Dark Photons in Missing-Energy Events at the CERN SPS. *Phys. Rev. Lett.*, 118(1), Jan 2017.

[66] S. Andreas, C. Niebuhr, and A. Ringwald. New limits on hidden photons from past electron beam dumps. *Phys. Rev. D*, 86:095019, Nov 2012.

[67] M. Battaglieri et al. Dark matter search in a Beam-Dump eXperiment (BDX) at Jefferson Lab, 2014.

[68] G. Inguglia. Belle II studies of missing energy decays and searches for dark photon production. *Proc. Sci.*, 11-15-April-2016:0–5, 2016.

[69] E. C. Gil et al. Search for production of an invisible dark photon in $\pi 0$ decays. *J. High Energy Phys.*, 2019(5), May 2019.

[70] P. Ilten, J. Thaler, M. Williams, and W. Xue. Dark photons from charm mesons at LHCb. *Phys. Rev. D*, 92, Dec 2015.

[71] A.M. Sirunyan et al. Search for invisible decays of a Higgs boson produced through vector boson fusion in proton-proton collisions at s=13TeV. *Phys. Lett. B*, 793:520551, Jun 2019.

[72] E. C. Gil and others. Search for heavy neutral lepton production in K^+ decays. *Phys. Lett. B*, 778:137145, Mar 2018.

[73] P. A. N. Machado, O. Palamara, and D. W. Schmitz. The Short-Baseline Neutrino Program at Fermilab. *Annu. Rev. Nucl. Part. Sci.*, 69(1):363387, Oct 2019.

[74] S. Archambault et al. Dark matter constraints from a joint analysis of dwarf Spheroidal galaxy observations with VERITAS. *Phys. Rev. D*, 95(8):1–14, 2017.

[75] A. Acharyya et al. Sensitivity of the Cherenkov Telescope Array to a dark matter signal from the Galactic centre. *J. Cosmol. Astropart. Phys.*, 2021(01):057057, Jan 2021.

[76] M. Ackermann et al. Searching for Dark Matter Annihilation from Milky Way Dwarf Spheroidal Galaxies with Six Years of Fermi Large Area Telescope Data. *Phys. Rev. Lett.*, 115(23), Nov 2015.

[77] M. Ackermann et al. The Fermi Galactic Center GeV Excess and Implications for Dark Matter. *Astrophys. J.*, 840(1):43, may 2017.

[78] R. Bartels, F. Calore, E. Storm, and C. Weniger. Galactic binaries can explain the Fermi Galactic centre excess and 511 keV emission. *Mon. Not. R. Astron. Soc.*, 480(3):38263841, Aug 2018.

[79] R. K. Leane and T. R. Slatyer. Revival of the Dark Matter Hypothesis for the Galactic Center Gamma-Ray Excess. *Phys. Rev. Lett.*, 123(24), Dec 2019.

[80] J. Kndlseder et al. The all-sky distribution of 511 keV electron-positron annihilation emission. *Astron. Astrophys.*, 441(2):513532, Sep 2005.

[81] A. C. Vincent, P. Martin, and J. M Cline. Interacting dark matter contribution to the galactic 511 keV gamma ray emission: constraining the morphology with INTEGRAL/SPI observations. *J. Cosmol. Astropart. Phys.*, 2012(04):022022, Apr 2012.

[82] R. M. Bandyopadhyay, J. Silk, J. E. Taylor, and T. J. Maccarone. On the origin of the 511-keV emission in the Galactic Centre. *Mon. Not. R. Astron. Soc.*, 392(3):11151123, Jan 2009.

[83] E. Bulbul et al. Detection of an unidentified emission line in the stacked x-ray spectrum of galaxy clusters. *The Astrophysical Journal*, 789(1):13, Jun 2014.

[84] M. E. Anderson and J. N. Churazov, E.and Bregman. Non-detection of x-ray emission from sterile neutrinos in stacked galaxy spectra. *Mon. Not. R. Astron. Soc.*, 452(4):39053923, Aug 2015.

[85] IceCube Collaboration. Search for annihilating dark matter in the Sun with 3 years of IceCube data: IceCube Collaboration. *Eur. Phys. J. C.*, 77(3):1–14, 2017.

[86] A. Albert et al. Combined search for neutrinos from dark matter self-annihilation in the Galactic Center with ANTARES and IceCube. *Phys. Rev. D.*, 102(8), Oct 2020.

[87] K. Abe et al. Indirect search for dark matter from the Galactic Center and halo with the Super-Kamiokande detector. *Phys. Rev. D.*, 102(7), Oct 2020.

[88] O. Adriani et al. An anomalous positron abundance in cosmic rays with energies 1.5–100 GeV. *Nature*, 458(7238):607–609, 2009.

[89] M. Aguilar et al. First Result from the Alpha Magnetic Spectrometer on the International Space Station: Precision Measurement of the Positron Fraction in Primary Cosmic Rays of 0.5–350 GeV. *Phys. Rev. Lett.*, 110:141102, Apr 2013.

[90] G. Elor, N. L. Rodd, T. R. Slatyer, and W. Xue. Model-independent indirect detection constraints on hidden sector dark matter. *J. Cosmol Astropart. Phys.*, 2016(06):024024, Jun 2016.

[91] M. Doro et al. Dark matter and fundamental physics with the Cherenkov Telescope Array. *Astropart. Phys.*, 43:189214, Mar 2013.

[92] K. Ehret et al. New alps results on hidden-sector lightweights. *Phys. Lett. B*, 689(4-5):149155, May 2010.

[93] R Bhre et al. Any Light Particle Search II — Technical Design Report. *J. Instrum.*, 8(09):T09001–T09001, sep 2013.

[94] A. Ejlli, F. Della Valle, U. Gastaldi, G. Messineo, R. Pengo, G. Ruoso, and G. Zavattini. The PVLAS experiment: a 25 year effort to measure vacuum magnetic birefringence, 2020.

[95] A. A. Geraci et al. Progress on the ARIADNE axion experiment, 2017.

[96] L. Badurina et al. AION: an atom interferometer observatory and network. *J. Cosmol. Astropart. Phys.*, 2020(05):011–011, May 2020.

[97] Y. A. El-Neaj et al. AEDGE: Atomic Experiment for Dark Matter and Gravity Exploration in Space. *EPJ Quantum Technol.*, 7(1), Mar 2020.

[98] T. Braine et al. Extended search for the invisible axion with the axion dark matter experiment. *Phys. Rev. Lett.*, 124:101303, Mar 2020.

[99] S. Beurthey et al. MADMAX Status Report, 2020.

[100] V. Anastassopoulos et al. New CAST Limit on the Axion-Photon Interaction. *Nature Phys.*, 13:584–590, 2017.

[101] E Armengaud et al. Conceptual design of the International Axion Observatory (IAXO). *J. Instrum.*, 9(05):T05002T05002, May 2014.

[102] I. G. Irastorza and J. Redondo. New experimental approaches in the search for axion-like particles. *Prog. Part. Nucl. Phys.*, 102:89159, Sep 2018.

[103] A. Andrianavalomahefa and others. Limits from the FUNK experiment on the mixing strength of hidden-photon dark matter in the visible and near-ultraviolet wavelength range. *Phys. Rev. D.*, 102(4), Aug 2020.

[104] A. Drukier and L. Stodolsky. Principles and applications of a neutral-current detector for neutrino physics and astronomy. *Phys. Rev. D*, 30:2295–2309, Dec 1984.

[105] M. Goodman and E. Witten. Detectability of certain dark-matter candidates. *Phys. Rev. D*, 31:3059–3063, Jun 1985.

[106] A. Drukier, K. Freese, and D. Spergel. Detecting cold dark-matter candidates. *Phys. Rev. D*, 33:3495–3508, Jun 1986.

[107] J. Silk et al. *Particle Dark Matter: Observations, Models and Searches.* Cambridge Univ. Press, Cambridge, 2010.

[108] M. Schumann. Direct detection of wimp dark matter: concepts and status. *J. Phys. G.*, 46(10):103003, Aug 2019.

[109] M. Tanabashi and other. Review of particle physics. *Phys. Rev. D*, 98:030001, Aug 2018.

[110] M. Tanabashi et al. Review of Particle Physics. *Progress of Theoretical and Experimental Physics*, 2020(8), 08 2020. 083C01.

[111] J. Buch, S. Leung, and J. Fan. Using Gaia DR2 to constrain local dark matter density and thin dark disk. *J. Cosmol. Astropart. Phys.*, 2019(04):026026, Apr 2019.

[112] L. Vietze, P. Klos, J. Menndez, W.C. Haxton, and A. Schwenk. Nuclear structure aspects of spin-independent wimp scattering off xenon. *Physical Review D*, 91(4), Feb 2015.

[113] P. Klos, J. Menndez, D. Gazit, and A. Schwenk. Large-scale nuclear structure calculations for spin-dependent wimp scattering with chiral effective field theory currents. *Physical Review D*, 88(8), Oct 2013.

[114] R. Essig, J. Mardon, and T. Volansky. Direct detection of sub-GeV dark matter. *Phys. Rev. D*, 85(7), Apr 2012.

[115] M. Pospelov, A. Ritz, and M. Voloshin. Bosonic super-WIMPs as keV-scale dark matter. *Phys. Rev. D*, 78(11), Dec 2008.

[116] M. Battaglieri et al. US Cosmic Visions: New Ideas in Dark Matter 2017: Community Report, 2017.

[117] D. Z. Freedman. Coherent effects of a weak neutral current. *Phys. Rev. D*, 9:1389–1392, Mar 1974.

[118] S. Ahlen et al. Limits on Cold Dark Matter Candidates from an Ultralow Background Germanium Spectrometer. *Phys. Lett. B*, 195:603–608, 1987.

[119] C. E. Aalseth et al. CoGeNT: A search for low-mass dark matter using p-type point contact germanium detectors. *Phys. Rev. D*, 88(1), Jul 2013.

[120] H. Ma et al. CDEX Dark Matter Experiment: Status and Prospects. *J. Phys.*, 1342:012067, jan 2020.

[121] Q. Arnaud et al. First results from the NEWS-G direct dark matter search experiment at the LSM. *Astropart. Phys.*, 97:5462, Jan 2018.

[122] J. Battat et al. Low threshold results and limits from the DRIFT directional dark matter detector. *Astropart. Phys.*, 91:6574, May 2017.

[123] R. Bernabei et al. First model independent results from DAMA/LIBRA-phase2. *Nucl. Phys. At. Energy*, 19(4):307325, Dec 2018.

[124] J. Amar et al. First Results on Dark Matter Annual Modulation from the ANAIS-112 Experiment. *Phys. Rev. Lett.*, 123(3), Jul 2019.

[125] G. Adhikari et al. Search for a Dark Matter-Induced Annual Modulation Signal in NaI(Tl) with the COSINE-100 Experiment. *Phys. Rev. Lett.*, 123(3), Jul 2019.

[126] J. Amar et al. Annual modulation results from three-year exposure of ANAIS-112. *Phys. Rev. D*, 103(10), May 2021.

[127] K. Abe et al. A direct dark matter search in XMASS-I. *Phys. Lett. B*, 789:4553, Feb 2019.

[128] R. Ajaj et al. Search for dark matter with a 231-day exposure of liquid argon using DEAP-3600 at SNOLAB. *Phys. Rev. D*, 100(2), Jul 2019.

[129] C. Amole. Dark matter search results from the PICO-60 CF_3I bubble chamber. *Phys. Rev. D*, 93(5):1–14, 2016.

[130] D. S. Akerib et al. Exclusion limits on the WIMP-nucleon cross section from the first run of the Cryogenic Dark Matter Search in the Soudan Underground Laboratory. *Phys. Rev. D*, 72:052009, Sep 2005.

[131] R. Agnese et al. Projected sensitivity of the SuperCDMS SNOLAB experiment. *Phys. Rev. D*, 95:082002, Apr 2017.

[132] R. Agnese et al. Results from the Super Cryogenic Dark Matter Search Experiment at Soudan. *Phys. Rev. Lett.*, 120(6), Feb 2018.

[133] R. Agnese et al. Search for low-mass dark matter with CDMSlite using a profile likelihood fit. *Phys. Rev. D.*, 99(6), Mar 2019.

[134] L. Hehn et al. Improved EDELWEISS-III sensitivity for low-mass WIMPs using a profile likelihood approach. *Eur. Phys. J. C*, 76(10), Oct 2016.

[135] A.H. Abdelhameed and others. First results from the CRESST-III low-mass dark matter program. *Phys. Rev. D*, 100(10), Nov 2019.

[136] E. Aprile et al. Light Dark Matter Search with Ionization Signals in XENON1T. *Phys. Rev. Lett.*, 123(25), Dec 2019.

[137] E. Armengaud et al. Searches for electron interactions induced by new physics in the EDELWEISS-III germanium bolometers. *Phys. Rev. D*, 98(8), Oct 2018.

[138] Q. Arnaud et al. First Germanium-Based Constraints on Sub-MeV Dark Matter with the EDELWEISS Experiment. *Phys. Rev. Lett.*, 125(14), Oct 2020.

[139] K. Abe et al. Search for solar axions in XMASS, a large liquid-xenon detector. *Phys. Lett. B*, 724(1-3):4650, Jul 2013.

[140] D.S. Akerib et al. First Searches for Axions and Axionlike Particles with the LUX Experiment. *Phys. Rev. Lett.*, 118(26), Jun 2017.

[141] E. Aprile et al. Excess electronic recoil events in XENON1T. *Phys. Rev. D*, 102(7), Oct 2020.

[142] Y. Hochberg, T. Lin, and K. Zurek. Absorption of light dark matter in semiconductors. *Phys. Rev. D*, 95(2), Jan 2017.

[143] T. Aralis et al. Constraints on dark photons and axionlike particles from the SuperCDMS Soudan experiment. *Phys. Rev. D*, 101(5), Mar 2020.

[144] Y. Hochberg, T. Lin, and K. Zurek. Detecting ultralight bosonic dark matter via absorption in superconductors. *Phys. Rev. D*, 94(1), Jul 2016.

[145] K. Abe et al. Search for dark matter in the form of hidden photons and axion-like particles in the XMASS detector. *Phys. Lett. B*, 787:153158, Dec 2018.

[146] T. Braine et al. Extended Search for the Invisible Axion with the Axion Dark Matter Experiment. *Phys. Rev. Lett.*, 124(10), Mar 2020.

[147] A. Wagner et al. Search for Hidden Sector Photons with the ADMX Detector. *Phys. Rev. Lett.*, 105(17), Oct 2010.

[148] V. Anastassopoulos et al. New CAST limit on the axionphoton interaction. *Nature*, 13(6):584590, May 2017.

[149] S. A. Hertel, A. Biekert, J. Lin, V. Velan, and D.N. McKinsey. Direct detection of sub-GeV dark matter using a superfluid ^{4}He target. *Phys. Rev. D*, 100(9), Nov 2019.

[150] M. Ibe, W. Nakano, Y. Shoji, and K. Suzuki. Migdal effect in dark matter direct detection experiments. *J. High Energy Phys.*, 2018(3), Mar 2018.

[151] D.S. Akerib and others. Results of a Search for Sub-GeV Dark Matter Using 2013 LUX Data. *Phys. Rev. Lett.*, 122(13), Apr 2019.

[152] V. Chepel and H. Arajo. Liquid noble gas detectors for low energy particle physics. *J. Instrum.*, 8(04):R04001R04001, Apr 2013.

[153] Martin Berger, J Hubbell, Stephen Seltzer, J Coursey, and D Zucker. Xcom: Photon cross section database (version 3.1), 2010-11-01 2010.

[154] P. Agnes et al. First results from the DarkSide-50 dark matter experiment at Laboratori Nazionali del Gran Sasso. *Phys. Lett. B*, 743:456466, Apr 2015.

[155] P. Agnes et al. Results from the first use of low radioactivity argon in a dark matter search. *Phys. Rev. D*, 93(8), Apr 2016.

[156] P. Agnes et al. Low-Mass Dark Matter Search with the DarkSide-50 Experiment. *Phys. Rev. Lett.*, 121(8), Aug 2018.

[157] C. E. Aalseth et al. DarkSide-20k: A 20 tonne two-phase LAr TPC for direct dark matter detection at LNGS. *Eur. Phys. J.*, 133(3), Mar 2018.

[158] Qiuhong W. et al. Results of dark matter search using the full pandax-ii exposure. *Chin. Phys. C*, 44(12):125001, Nov 2020.

[159] H. Zhang et al. Dark matter direct search sensitivity of the PandaX-4T experiment. *Sci. China Phys., Mech.*, 62(3), Aug 2018.

[160] J. Angle et al. First Results from the XENON10 Dark Matter Experiment at the Gran Sasso National Laboratory. *Phys. Rev. Lett.*, 100(2), Jan 2008.

[161] E. Aprile et al. XENON100 dark matter results from a combination of 477 live days. *Phys. Rev. D*, 94(12), Dec 2016.

[162] E. Aprile et al. Dark Matter Search Results from a One Ton-Year Exposure of XENON1T. *Phys. Rev. Lett.*, 121(11), Sep 2018.

[163] E. Aprile et al. Projected WIMP sensitivity of the XENONnT dark matter experiment. *J. Cosmol. Astropart. Phys.*, 2020(11):031031, Nov 2020.

[164] G.J. Alner et al. First limits on WIMP nuclear recoil signals in ZEPLIN-II: A two-phase xenon detector for dark matter detection. *Astropart, Phys.*, 28(3):287302, Nov 2007.

[165] D.Yu. Akimov et al. WIMP-nucleon cross-section results from the second science run of ZEPLIN-III. *Phys. Lett. B*, 709(1-2):1420, Mar 2012.

[166] D.S. Akerib et al. Results from a Search for Dark Matter in the Complete LUX Exposure. *Phys. Rev. Lett.*, 118(2), Jan 2017.

[167] D.S. Akerib et al. Projected WIMP sensitivity of the LUX-ZEPLIN dark matter experiment. *Phys. Rev. D*, 101(5), Mar 2020.

[168] J Lindhard, M Scharff, and H E Schioett. Range concepts and heavy ion ranges (notes on atomic collisions, ii). *Kgl. Danske Videnskab. Selskab. Mat. Fys. Medd.*

[169] A. Hitachi. Properties of liquid xenon scintillation for dark matter searches. *Astropart. Phys.*, 24(3):247 – 256, 2005.

[170] P. Sorensen and C. Dahl. Nuclear recoil energy scale in liquid xenon with application to the direct detection of dark matter. *Phys. Rev. D*, 83(6), Mar 2011.

[171] C. Dahl. *The physics of background discrimination in liquid xenon, and first results from Xenon10 in the hunt for WIMP dark matter.* PhD thesis, Princeton U., 2009.

[172] G. Anton et al. Measurement of the scintillation and ionization response of liquid xenon at MeV energies in the EXO-200 experiment. *Phys. Rev. C*, 101(6), Jun 2020.

[173] M. Szydagis et al. NEST: a comprehensive model for scintillation yield in liquid xenon. *J. Inst.*, 6(10):P10002–P10002, Oct 2011.

[174] M. Szydagis et al. Noble Element Simulation Technique v2.0, July 2018.

[175] D. S. Akerib et al. Calibration, event reconstruction, data analysis and limits calculation for the LUX dark matter experiment. *Phys. Rev. D*, 97:1–36, 2018.

[176] D.S. Akerib et al. The Large Underground Xenon (LUX) experiment. *Nucl. Instrum. Methods Phys. Res. A*, 704:111126, Mar 2013.

[177] D. S. Akerib et al. First results from the LUX dark matter experiment at the sanford underground research facility. *Phys. Rev. Lett.*, 112(9), 2014.

[178] D.S. Akerib et al. Improved limits on scattering of weakly interacting massive particles from reanalysis of 2013 LUX data. *Phys. Rev. Lett.*, 116(16), Apr 2016.

[179] D. S. Akerib et al. Results from a Search for Dark Matter in the Complete LUX Exposure. *Phys. Rev. Lett.*, 118:021303, Jan 2017.

[180] D.S. Akerib et al. Limits on Spin-Dependent WIMP-Nucleon Cross Section Obtained from the Complete LUX Exposure. *Phys.l Rev. Lett.*, 118(25), Jun 2017.

[181] D. S. Akerib et al. Effective field theory analysis of the first lux dark matter search. *Phys. Rev. D*, 103:122005, Jun 2021.

[182] D. S. Akerib et al. *Phys. Rev. Lett.*, 122(7):131301, 2019.

[183] D. S. Akerib and others. Extending light WIMP searches to single scintillation photons in LUX. *Phys. Rev. D*, 101:042001, Feb 2020.

[184] B. J. Mount et al. LUX-ZEPLIN (LZ) Technical Design Report. 2017.

[185] D.S. Akerib et al. Identification of radiopure titanium for the LZ dark matter experiment and future rare event searches. *Astropart. Phys.*, 96:110, Nov 2017.

[186] D. S. Akerib et al. Enhancing the sensitivity of the LUX-ZEPLIN (LZ) dark matter experiment to low energy signals. *arXiv:2101.08753 [astro-ph]*, Jan 2021.

[187] D. S. Akerib et al. Projected sensitivity of the LUX-ZEPLIN experiment to the $0\nu\beta\beta$ decay of ^{136}Xe. *Phys. Rev. C*, 102:014602, Jul 2020.

[188] R. Foot and R.R. Volkas. Spheroidal galactic halos and mirror dark matter. *Phys. Rev. D*, 70(12):6, 2004.

[189] P. Ciarcelluti and R. Foot. Primordial He abundance implied by the mirror dark matter interpretation of the DAMA/LIBRA signal. *Phys. Lett. B*, 690(5):462–465, 2010.

[190] R. Foot. Shielding of a direct detection experiment and implications for the DAMA annual modulation signal. *Phys. Lett. B*, 789(June):592–597, 2019.

[191] D. S. Akerib et al. Tritium calibration of the LUX dark matter experiment. *Phys. Rev. D*, 93(7):1–12, 2016.

[192] E. Aprile and T. Doke. Liquid xenon detectors for particle physics and astrophysics. *Rev. Mod. Phys.*, 82:2053–2097, Jul 2010.

[193] D. S. Akerib et al. Radiogenic and muon-induced backgrounds in the LUX dark matter detector. *Astropart. Phys.*, 62:33–46, 2015.

[194] D.S. Akerib et al. Chromatographic separation of radioactive noble gases from xenon. *Astropart. Phys.*, 97:8087, Jan 2018.

[195] K. Cranmer. Kernel estimation in high-energy physics. *Comput. Phys. Commun.*, 136(3):198207, May 2001.

[196] G. Cowan, K. Cranmer, E. Gross, and O. Vitells. Asymptotic formulae for likelihood-based tests of new physics. *Eur. Phys. J. C*, 71(2):1554, 2011.

[197] C. Vigo, L. Gerchow, L. Liszkay, A. Rubbia, and P. Crivelli. First search for invisible decays of orthopositronium confined in a vacuum cavity. *Phys. Rev. D*, 97:092008, May 2018.

[198] E. Aprile et al. Exclusion of leptophilic dark matter models using XENON100 electronic recoil data. *Science*, 349(6250):851–854, 2015.

[199] R. Bernabei et al. Final model independent result of DAMA/LIBRA–phase1. *Eur. Phys. J. C*, 73(12):2648, Nov 2013.

[200] J. Clarke and R. Foot. Mirror dark matter will be confirmed or excluded by XENON1T. *Phys. Lett. B*, 766:29–34, 2017.

[201] D. S. Akerib et al. The LUX-ZEPLIN (LZ) radioactivity and cleanliness control programs. *Eur. Phys. J. C.*, 80(11), Nov 2020.

[202] D.S. Akerib et al. Measurement of the gamma ray background in the Davis cavern at the Sanford Underground Research Facility. *Astropart. Phys.*, 116:102391, Mar 2020.

[203] M. Agostini et al. Comprehensive measurement of *pp*-chain solar neutrinos. *Nature*, 562(7728):505–510, 2018.

[204] J. N. Bahcall and C. Pea-Garay. Solar models and solar neutrino oscillations. *New J. Phys.*, 6:6363, Jun 2004.

[205] A. M. Serenelli, W. C. Haxton, and C. Pea-Garay. Solar models with accretion. I. Application to the solar abundance problem. *Astrophys. J.*, 743(1):24, Nov 2011.

[206] D. Akimov et al. Observation of coherent elastic neutrino-nucleus scattering. *Science*, 357(6356):1123–1126, 2017.

[207] J. W. Chen, H. C. Chi, C. P. Liu, and C. P. Wu. Low-energy electronic recoil in xenon detectors by solar neutrinos. *Phys. Lett. B*, 774:656661, Nov 2017.

[208] M. Agostini et al. Experimental evidence of neutrinos produced in the CNO fusion cycle in the Sun. *Nature*, 587:577–582, 2020.

[209] N. Ackerman et al. Observation of Two-Neutrino Double-Beta Decay in ^{136}Xe with the EXO-200 Detector. *Phys. Rev. Lett.*, 107(21), Nov 2011.

[210] A. Gando and others. Measurement of the double-beta decay half-life of ^{136} Xe with the KamLAND-Zen experiment. *Phys. Rev. C*, 85(4), Apr 2012.

[211] E. Aprile et al. Observation of two-neutrino double electron capture in ^{124}Xe with XENON1T. *Nature*, 568(7728):532–535, 2019.

[212] J. E. Kim and G. Carosi. Axions and the strong CP problem. *Rev. Mod. Phys.*, 82:557–601, Mar 2010.

[213] J. Preskill, M. Wise, and F. Wilczek. Cosmology of the invisible axion. *Physics Letters B*, 120(1):127 – 132, 1983.

[214] J. Redondo. Solar axion flux from the axion-electron coupling. *J. Cosmol. and Astropart. Phys.*, 2013(12):008008, Dec 2013.

[215] Shigetaka Moriyama. Proposal to search for a monochromatic component of solar axions using ^{57}fe. *Nucl. Phys. B*, 72:183186, Mar 1999.

[216] S. Andriamonje et al. Search for 14.4 keV solar axions emitted in the M1 transition of ^{57}Fe nuclei with CAST. *J. Cosmol. Astropart. Phys.*, 2009(12):002002, Dec 2009.

[217] F. Alessandria et al. Search for 14.4 keV solar axions from M1 transition of ^{57}Fe with CUORE crystals. *J. Cosmol. Astropart. Phys.*, 2013(05):007–007, May 2013.

[218] C. Giunti and A. Studenikin. Neutrino electromagnetic interactions: A window to new physics. *Rev. Mod. Phys.*, 87:531–591, Jun 2015.

[219] N. F. Bell, V. Cirigliano, M. J. Ramsey-Musolf, P. Vogel, and M. B. Wise. How magnetic is the dirac neutrino? *Phys. Rev. Lett.*, 95:151802, Oct 2005.

[220] C. C. Hsieh et al. Discovery potential of multiton xenon detectors in neutrino electromagnetic properties. *Phys. Rev. D*, 100:073001, Oct 2019.

[221] N. F. Bell, Y. Cai, R. K. Leane, and A. D. Medina. Leptophilic dark matter with $Z^{'}$ interactions. *Phys. Rev. D*, 90:035027, Aug 2014.

[222] S. A. Abel, M. D. Goodsell, J Jaeckel, V. V. Khoze, and A. Ringwald. Kinetic mixing of the photon with hidden U(1)s in string phenomenology. *J. High Energy Phys.*, 2008(07):124–124, Jul 2008.

[223] M. Pospelov, A. Ritz, and M. Voloshin. Bosonic super-WIMPs as keV-scale dark matter. *Phys. Rev. D*, 78:115012, Dec 2008.

[224] D. S. Akerib et al. Simulations of events for the LUX-ZEPLIN (LZ) dark matter experiment. *Astropart. Phys.*, 125:102480, Feb 2021.

[225] N. Viaux et al. Neutrino and axion bounds from the globular cluster M5 (NGC 5904). *Phys. Rev. Lett.*, 111:231301, Dec 2013.

[226] O. Straniero, I. Dominguez, M. Giannotti, and A. Mirizzi. Axion-electron coupling from the RGB tip of Globular Clusters. In *13th Patras Workshop on Axions, WIMPs and WISPs*, pages 172–176, 2018.

[227] O. Straniero et al. The RGB tip of galactic globular clusters and the revision of the axion-electron coupling bound. *Astron. Astrophys.*, 644:A166, Dec 2020.

[228] P. Gondolo and G. G. Raffelt. Solar neutrino limit on axions and keV-mass bosons. *Phys. Rev. D*, 79(10), May 2009.

[229] K. Van Tilburg. Stellar basins of gravitationally bound particles. *Phys. Rev. D*, 104:023019, Jul 2021.

[230] Y. Wang et al. Improved limits on solar axions and bosonic dark matter from the CDEX-1B experiment using the profile likelihood ratio method. *Phy. Rev. D*, 101(5), Mar 2020.

[231] Y. S. Yoon et al. Search for solar axions with CsI(Tl) crystal detectors. *arXiv:1604.01825 [hep-ex]*, 2016.

[232] C. Fu et al. Limits on Axion Couplings from the First 80 Days of Data of the PandaX-II Experiment. *Phys. Rev. Lett.*, 119(18), Nov 2017.

[233] C. Giunti and A. Studenikin. Neutrino electromagnetic interactions: A window to new physics. *Rev. Mod. Phys.*, 87:531–591, Jun 2015.

[234] J. Kopp, V. Niro, T. Schwetz, and J. Zupan. Dama/libra data and leptonically interacting dark matter. *Phys. Rev. D*, 80:083502, Oct 2009.

[235] S. Dutta, B. Rawat, and D. Sachdeva. Signals of leptophilic dark matter at the ilc. *Eur. Phys. J. C*, 77(9), Sep 2017.

[236] K. Abe et al. Search for dark matter in the form of hidden photons and axion-like particles in the xmass detector. *Phys. Lett. B*, 787:153–158, 2018.

[237] H. An, M. Pospelov, J. Pradler, and A. Ritz. New limits on dark photons from solar emission and kev scale dark matter. *Phys. Rev. D*, 102:115022, Dec 2020.

[238] S. J. Haselschwardt, J. Kostensalo, X. Mougeot, and J. Suhonen. Improved calculations of decay backgrounds to new physics in liquid xenon detectors. *Phys. Rev. C*, 102(6), Dec 2020.

[239] K. Cranmer. Practical Statistics for the LHC. In *2011 European School of High-Energy Physics*, 2014.

[240] J. Herrero-Garcia, A. Scaffidi, M. White, and A. G. Williams. On the direct detection of multi-component dark matter: sensitivity studies and parameter estimation. *J. Cosmol. Astropart. Phys.*, 2017(11):021021, Nov 2017.

[241] X. Qian, A. Tan, W. Wang, J. J. Ling, R. D. McKeown, and C. Zhang. Statistical evaluation of experimental determinations of neutrino mass hierarchy. *Phys. Rev. D.*, 86(11), Dec 2012.

[242] K. Barth et al. CAST constraints on the axion-electron coupling. *J. Cosmol. Astropart. Phys.*, 2013(05):010–010, may 2013.

[243] Z. Ahmed et al. Search for axions with the CDMS experiment. *Phys. Rev. Lett.*, 103(14), Oct 2009.

[244] M. Giannotti, I. G. Irastorza, J. Redondo, A. Ringwald, and K. Saikawa. Stellar recipes for axion hunters. *J. Cosmol. Astropart. Phys.*, 2017(10):010–010, Oct 2017.